The copyright of this thesis rests with the University of Cape Town. No quotation from it or information derived from it is to be published without full acknowledgement of the source. The thesis is to be used for private study or non-commercial research purposes only.

University of Cape Town

Synthesis, Characterisation and Device Application of Silicon Nanoparticles produced by Mechanical Attrition

Ayodele Odo

University of Cape Town

Thesis Presented for the Degree of
DOCTOR OF PHILOSOPHY
in the Department of Physics
UNIVERSITY OF CAPE TOWN

September 12, 2009

Abstract

Nanostructured silicon is a promising materials for research because it serves as building blocks for nanotechnological applications, such as nano and quantum electronics, sensors and energy applications. However, many of the synthesis methods come with an increased level of sophistication, and thus the unit cost of material produced is high. The study shows that cheap and mass production of silicon nanoparticles can be achieved efficiently with a top-down process of mechanical attrition, particularly using an orbital pulveriser. The inclusion of the powder in a polymeric binder resulted in a new class of nanocomposite whose electrical properties are promising for devise applications using simple printing processes. Scanning and transmission electron microscopy studies reveal that the powders consist of a wide range of size and shape distribution, with large faceted particles with sizes between $1-3\mu m$ and relatively small particles of sizes $40-100nm$. The variation of the average particle size with milling time fits well with a first order exponential decay model which was used to evaluate the limiting particle size as about $120nm$.

The structural properties of the nanocomposites was investigated using small angle X-ray scattering, while the electrical properties were investigated by conducting $I-V$ measurements on a metal-nanocomposite-metal structure. Further tests for electronic properties like field effect mobilities were achieved by using the nanocomposite as the active layer in an insulated gate field effect transistor structure. Electrical characterisation reveals that the carrier injection and transport is determined by two main factors: the concentration of particles constituting the composite, and the level of external bias voltage on the structure. The nanocomposite systems show a clear percolation threshold for charge conduction. Below the percolation threshold, transport is mainly limited by the matrix or insulating binding medium. Direct tunneling and field emission (FE) are the major transport mechanism for all concentrations at low voltages, while thermally activated processes, such as hopping and thermionic emission are major contributors at low concentrations. At higher concentrations and field, Poole-Frenkel and Richardson-Schottky conduction mechanisms, resulting from barrier limiting process in the interface, of the metal contact to an interfacial insulator is dominant. Similar pronounced contribution from space charge limited current process resulting from accumulation of charges at the interface, and traps in the bulk, is pronounced at concentrations above the percolation threshold.

The transistors function as ambipolar devices, where the dominance of either carrier is deter-

University of Cape Town

mined by the sign and swing direction of the gate potential. The best transistors fabricated have a hole mobility of $2.63 \times 10^{-5} cm^2/Vs$ and electron mobility $7.81 \times 10^{-7} cm^2/Vs$.

University of Cape Town

Acknowledgements

This research has resulted from the moral, academic, and financial assistance giving by many people and organizations. I am very grateful for the assistance and directions given by my supervisors Professors D.T. Britton and M. Härting. I am grateful to the Department of Physics, and the National research foundation (NRF) South Africa for the financial support. I owe sincere gratitude to the Deutscher Akademischer Austausch Dienst (DAAD), Germany for covering the financial needs of my study. I am greatly indebted to my institute, Engineering Materials Development Institute (EMDI) Akure Nigeria, for the study leave, and also to the director general of the National Agency for Science and Engineering Infrastructure (NASENI) Abuja Nigeria, Prof O.O. Adewoye for the care and understanding. Many thanks also to my present boss Dr. B. Babatope for the understanding and to my friends and colleague in the research and development unit of EMDI. I thank greatly Profs Buffler, Aschman, Comrie and other members of the Physics department for their encouragement and support during the trials of this Ph.D. study. Thanks also to all my colleagues, Girma Goro, Batsirai Magunje, Raji Abdulrafiu, Wole Solana, Emmanuel Jonah and more worth mentioning, whose endurance are source of encouragement and hope to face the future with unflagging enthusiasm. I would also like to thank Dr. Tunde Ojumu for his encouragement. And for my brothers and sisters who were all concern about my failing health, and cared for me and my family at all time, Justin and Lisa Fullstone I say thanks very much for your care. I also thank greatly my parents Mr and Mrs Odo for ensuring I get the secure foundation upon which the structures of of this achievement sits. To Funmi Badmus, Olamide, Tola, Segun and all the Odo-Alawaye's family, I say thanks for your understanding. I also thank my in-laws Mr and Mrs Ehinju for their care, prayers and support for me and my family over these years. To Mr and Mrs Eluma, Caleb, Bola and Peace Ehinju, I say thank you very much for your support. Lastly I would like to thank my beloved wife Olayinka, and my son Ayodeji for the understanding and support, for holding closely together with hope even through tribulations, and rejoicing in the relieve that awaits us soon through Jehovah's promise of a new world. I owe you greatly and will always love you.

University of Cape Town

Ecc.12:11-14

11. The words of the wise ones are like oxgoads, and just like nails driven in are those indulging in collections [of sentences]; they have been given from one shepherd. 12. As regards anything besides these, my son, take a warning: ***To the making of many books there is no end, and much devotion [to them] is wearisome to the flesh****. 13. The conclusion of the matter, everything having been heard, is: Fear the [true] God and keep his*

commandments. For this is the whole [obligation] of man. 14. For the [true] God himself will bring every sort of work into the judgment in relation to every hidden thing, as to whether it is good or bad.

University of Cape Town

Contents

Abstract i

Acknowledgements iii

1 Introduction 1

2 Synthesis and characterisation of silicon nanoparticles 4

2.1 Basics of nanostructured silicon 5

2.1.1 Structural properties of silicon nanoparticles 5

2.1.2 Electronic and optical properties of nanoparticles 6

2.1.3 Methods of silicon nanoparticle fabrication 7

2.2 Experimental Methods 15

2.2.1 Milling using a laboratory disc mill 15

2.3 Characterisation of milled silicon nanoparticles 19

2.3.1 X-ray diffraction study of nanostructured silicon produced using a laboratory disc mill 19

2.3.2 Morphological and elemental compositional study of silicon nanoparticles 25

2.3.3 Transmission electron microscopy (TEM) and electron diffraction study of silicon nanoparticles 31

2.3.4 Raman spectroscopy study of silicon nanoparticle produced using laboratory disc mill 40

3 Functional Nanocomposite of Silicon 47

3.1 Nanocomposites: an overview 48

3.2 Structural characterisation of nanocomposites using SAXS 50

University of Cape Town

3.3 Experimental Methods 56
3.3.1 Silicon nanocomposite layer production and characterisation 56
3.4 Results and Discussion 59
3.4.1 Morphological study of silicon nanocomposites 59
3.4.2 SAXS study of nanocomposite of silicon using Guinier's analysis . . . 62
3.4.3 SAXS study of nanocomposite of silicon using Porod's law analysis . 66
3.4.4 Analysis of deviation from Porod's law 69
4 Charge carrier transport mechanisms in silicon nanocomposites 72
4.1 Background theory of charge carrier transport 73
4.1.1 Schottky barrier 73
4.1.2 Interface states 76
4.2 Charge transport in a nanoparticulate semiconductor network 79
4.3 Current transport process across a metal semiconductor interface 81
4.3.1 Thermionic emission theory. 83
4.3.2 Field emission/tunneling current theory. 84
4.3.3 Diffusion theory. 84
4.3.4 Space charge-limited current (SCLC) theory. 86
4.4 Experimental procedure 89
4.4.1 Materials and sample preparation 89
4.4.2 Forward and reverse I-V measurement 90
4.5 Results and Discussion 93
4.5.1 Assumptions for the determination of carrier transport type. 93
4.5.2 Temperature dependence of the forward I-V characteristics 94
4.5.3 Characteristic I-V behaviour at 295K 99

University of Cape Town

4.5.4 Contribution of charge carrier transport due to thermionic emission (TE) . . . 102
4.5.5 Contribution of thermionic field emission (TFE) to charge carrier transport in silicon nanocomposites . . . 109
4.5.6 Contribution of field emission (FE) to carrier transport . . . 110
4.5.7 Contribution resulting from lowering of the columbic potential barrier by the external electric field: Richardson-Schottky and Poole-Frenkel emission process . . . 118
4.5.8 Evaluation of the contribution from space charge limited current (SCLC) to the overall transport . . . 124
4.5.9 Contribution from hopping conduction to charge carrier transport in silicon nanocomposites. . . . 129
4.6 Summary of carrier transport mechanism . . . 131

5 Devices application of silicon nanocomposites 133

5.1 Hybrid organic-inorganic materials for printed electronics devices . . . 134
5.2 Review of nanocrystalline silicon based transistors . . . 134
5.3 Thick-film deposition and patterning . . . 136
5.3.1 Printed electronics . . . 136
5.3.2 Principle of pad printing . . . 138
5.4 Transistor structure . . . 142
5.5 Basic TFT operation . . . 142
5.5.1 Linear region . . . 144
5.5.2 Saturation region . . . 145
5.5.3 Determination of device parameters . . . 145
5.5.4 MISFET's with non ohmic source and drain contacts . . . 147
5.6 Experimental Method . . . 148

University of Cape Town

5.6.1 Fabrication of Transistor structures 148
5.6.2 Deposition of active nanocomposite layer and transistor characterisation 150
5.7 Results and discussion 151
5.7.1 All printed thick film nanocomposite transistor on plastic substrate . 151
5.7.2 Thick film nanocomposite transistor formed on standard silicon wafer TFT structures 156

6 Conclusions 161

Reference 164

A Appendices 189

University of Cape Town

1. Introduction

Materials whose structural elements, clusters, crystallite or grains have dimension in the 100nm range are classified as nanostructured materials [1, 2, 3, 4]. These materials have been studied extensively in recent time, because of the interesting properties many of these object exhibit at this length scale. At these sizes, nanostructured materials can exhibit interesting and useful physical behaviour based on quantum phenomena like electron confinement [4]. Another reason for the characteristic behaviour of nanostructured materials, which differs from their bulk properties in many respects, has been attributed to the high surface to volume ratio, resulting in a high percentage of the constituent atoms residing at the surface or an interface [1, 4]. Thus by varying the size of nanostructured materials, it is possible to vary or tune their properties to a desired one. For example, the colour of colloidal gold depends on both the size and shape of the particles [5]. As gold is reduced in size to about $90nm$ its colour changes to blue, and at about $30nm$, its colour is red [6]. Similar dependence of size on colour of nanoparticle of cadmium sulphide (CdS) has been reported [7].

Nanostructured silicon has been a major focus of nanostructured materials research because it serves as building blocks for nanotechnological applications such as nano and quantum electronics, sensors and energy applications [8]. With the present problems associated with the downscaling of CMOS transistor technology, such as short-channel effects and physical thickness limits of the bulk dielectric SiO_2 [9, 10, 11], the application of nanostructured silicon may become a major alternative for further increase in transistor density or functionality per unit chip area. A wide variety of methods have been developed for the synthesis of nanostructured silicon. These include gas phase condensation, chemical processing, crystallisation of amorphous and mechanical attrition [12]. However, many of the synthesis methods come with an increased level of sophistication and thus the unit cost of material produced is high. Application of nanostructured silicon or nanoparticles of silicon for wide area applications such as solar cells and pixel array drivers are the pressing issues in nanotechnology today [13, 14]. This dissertation presents the adaptation of an orbital pulveriser for cheap and efficient synthesis of doped nanoparticles/nanostructured silicon powder.

Nanocomposites are materials formed by inclusion of nanoparticles into a macroscopic sample material [15]. In general, nanocomposites involve inclusion of the nano or molecular domain sized particles into an organic polymer, metal or ceramic matrix materials [16]. The resulting nanocomposite may exhibit drastically enhanced mechanical, optical, electrical, magnetic as well as chemical properties. In all works involving nanocomposites as identi-

University of Cape Town

fied by Yong et al. [17], the technical challenge is the need to obtain intimate blending of the nanoparticles into the polymer matrices, which in most cases is restricted by induced chemical incompatibility, i.e. lack of adhesion between the fillers and the polymer media. The dispersion of semiconductor nanoparticles in polymeric binders have resulted in a new class of semiconductor nanocomposites, and devices based on the use of these composites are aimed at low cost large area fabrication via simple solution coating or printing [18, 19].

Solution-based printing of semiconductor materials, on flexible substrates for example, has traditionally employed organic semiconductor materials and methods like spin coating, self alignment, high resolution inkjet printing and vacuum deposition for fabrication of field effect transistors demonstrating field effect mobility of about $0.1cm^2V^{-1}s^{-1}$ [20, 21, 22]. There is a strong indication that the transport properties of organic based solution process semiconductors cannot be improved beyond the limit of amorphous silicon $1-2cm^2V^{-1}s^{-1}$. Inorganic semiconductors on the other hand have intrinsic motilities of the order of $1000cm^2V^{-}s^{-1}$, and a *life time* of over 50 years [23]. However inorganic semiconductors are not soluble in any convenient solvents and do not offer any easy way of adjusting their solubility [23].

Composites of polymers and metals have been widely used in electronics to make interconnections between components. Such composites are usually composed of a random distribution of the metal into a dielectric phase and the final electrical property is strongly related to the proportion of metal dispersed in the polymer phase [24]. There exists a threshold concentration that marks an abrupt transition from a dielectric state to a conductive state. The critical concentration that defines such transition is called the percolation threshold. Composites of polymers and semiconductor nanoparticles have not received as much attention until recently, when the possibility of solution processed electronic devices became apparent.

A new type of nanocomposite material produced from inks made from inclusion of the milled powders into linseed oil and acrylic paste will be presented. To understand the mechanism of charge carrier transport in such nanocomposites, a study of the electrical characteristics of a metal-nanocomposite-metal structure was carried out. Application of this nanocomposite as active layer in printed transistor structures has been implemented. This dissertation is arranged with chapters two to five addressing specific subjects relating to the synthesis, characterisation and application of nanoparticulate silicon inks. Each of these chapters begins with sections on background study, followed by sections on materials and method, results and discussion of important deductions from the analysis of the different results. Chapter two addresses the synthesis, structural and morphological characterisation of silicon nanoparticles produced by mechanical attrition. Results of morphological and

University of Cape Town

structural characterisation of the milled powder using standard characterisation tools such as Scanning Electron Microscopy (SEM), Transmission Electron Microscopy (TEM), Raman Spectroscopy, X-Ray and electron diffraction will be discussed with a view of evaluating mechanical attrition as a viable means of producing crystalline silicon nanoparticles.

Chapter three covers the structural study of nanocomposites formed by inclusion of the powders in polymeric binders using small angle X-ray scattering (SAXS). This is aimed at understanding the dispersion and the aggregate type formed by the nanoparticles in the different binders. Results from the SAXS experiments will be interpreted using Guinier and Porod's laws for the extraction of useful parameters needed to quantify the microstructures of the nanocomposite formed. Chapter four covers the study of charge carrier transport in a metal-nanocomposite-metal structure formed using the nanocomposites produced above. Different transport models, with emphasis on electric field dependent models, will be used with a view to determining the dominant processes governing charge carrier transport.

Chapter five covers printed electronics applications, where two types of the nanocomposite namely acrylic and linseed oil based nanocomposites, are employed as active layers in a transistor structure. These all printed field effect transistors formed on a plastic substrate have been characterised with a view of deducing important parameters such as field effect mobility. The active nanocomposite layer was also tested on a standard TFT structures formed on silicon wafer with gold electrode and SiO_2 gate dielectric for comparison.

Chapter six will conclude with the restatement of important results from the research and recommendations on the different avenues for further development in research relating to the use of powder of silicon produced from mechanical attrition and in general nanoparticles of other materials.

University of Cape Town

2. Synthesis and characterisation of silicon nanoparticles

As noted earlier, nanostructured semiconductor materials, including silicon, have been key players, with the most interest and intense research effort in nanotechnology because of their great potential for engineering and scientific applications. Due to the promising role of nanostructured semiconductors for device applications, many techniques have been developed for their fabrication. In particular free nanoparticles can be produced by either a bottom-up chemical synthesis route, or a top-down size reduction of bulk material [8, 25].

Bottom-up methods generally employ the production of isolated and uncontaminated particles either from inert gas condensation or through chemical reaction of a precursor. In the case of silicon, this has traditionally meant one of two forms of thermal processing: pyrolysis of silanes [26, 27, 28, 29], or evaporation of bulk silicon in an inert atmosphere [30, 31]. The most widely used method is decomposition of silane gas, which can be achieved using simple thermal pyrolysis [26, 27] or laser decomposition [28], to produce particles with sizes in the range of $100nm$. Smaller particles, less than $10nm$, can be produced through cluster generation in processes similar to hot-wire chemical vapour deposition (HW-CVD) [29] or plasma-enhanced CVD [27]. The application of soft chemical synthesis methods for silicon nanoparticles, is limited by their complexity, involving multi-stage synthesis [32], or growth in inverse micelle structures [33], as well as by their low yield [34].

Top-down approaches, using high energy mechanical milling or chemical reduction are widely used as an effective process for industrial production of metal and ceramic powders. These methods have been successfully employed for silicon and other notable semiconductor materials [35, 36], and thus look promising for large scale production of silicon nanoparticles. However, many reports have suggested that these production methods often introduce contaminants into the processed materials, and in the case of high energy mechanical milling, the induction of strain and dislocations in the final material [37, 38].

The objectives of this work are twofold, firstly to investigate the suitability of mechanical attrition as a method of producing nanostructured silicon in a top-down fashion from wafers and other bulk materials, and secondly, to investigate via standard techniques, the dependence of morphological properties (size and shape of the particles), structural properties (atomic arrangement within the particle) and chemical composition on the milling process and milling time of the powder.

University of Cape Town

Notable processes that have been employed for nanoparticle production, and particularly the synthesis of metallurgical (M) grade and P-type silicon nanoparticles using an orbital pulverizer, in a top-down approach from their respective bulk form will be discussed in detail. The different experimental methods employed to characterise the nanoparticles with respect to their size, morphology and structure, will be explained. Results of the different experiments will be presented and discussed with relation to how the size and structure of these nanoparticles may influence the electronic properties of the resulting nanoparticles.

2.1 Basics of nanostructured silicon

2.1.1 Structural properties of silicon nanoparticles

University of Cape Town

The physical properties of a material are strongly dependent on its microstructure and morphology. Fig. 2.1 shows three different types of microstructures which silicon, for example, can assume. In a single crystal, the atoms or molecules are arranged in a regular repetitive pattern or lattice in three dimensional space. Crystalline silicon therefore has a long range order as shown in Fig. 2.1(a). Polycrystalline materials as shown in Fig. 2.1(b) on the other hand, consist of crystalline grains, separated by grain boundaries, which are heavily disordered and may contain impurities. In macroscopic materials, because each grain represents a different nucleation centre or seed, most crystalline solids are polycrystalline. When the arrangement of atoms or molecules does not have a specific pattern or order, or is random, then the material is amorphous, as shown in Fig. 2.1(c). Intermediate forms also exist: for example nanocrystalline silicon (nc-Si) thin films produced by CVD, have small grains of crystalline silicon within an amorphous matrix [39].

Although the same structural forms exist for nanoparticles as well as macroscopic materials, there exists a size effect on the resulting structure. In many cases, X-ray diffraction experiments reveal a reduction in the intensity and a broadening of the Bragg peak with decrease in size [41, 42]. Also the crystalline fraction as measured from Raman spectroscopy often decreases with size reduction [43]. This is generally interpreted as a shift from the crystalline to the amorphous phase [43]. As particle size reduces, grain refinement and amorphorization set in. There is also an increase in surface area to volume ratio, and hence an increase in the free energy, leading to changes in interatomic spacing [25].

For semiconductors in general, grain refinement and amorphorization arise from compressive strain induced by the surface tension from the small radius of curvature of the nanoparti-

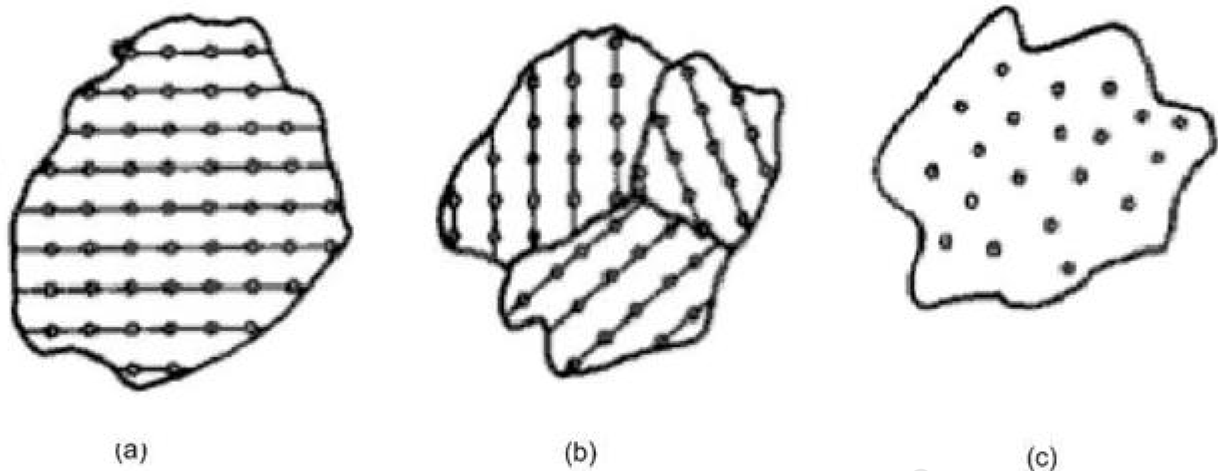

Fig. 2.1: Classification of nanoparticles based on structural arrangement of atoms. (a) In crystalline system, (b) polycrystalline system and (c) an amorphous system [40].

University of Cape Town

cle [1]. Depending on the synthesis method, nanoparticles of materials with a crystalline bulk structure may assume an amorphous state, or, in other cases, could undergo a phase transition to a new structure which is macroscopically unstable [44, 45].

2.1.2 Electronic and optical properties of nanoparticles

Recent trends in silicon nanoparticle and nanostructure research have been geared by the exhibition of visible luminescence as the size of the particles reaches the $100nm$ range. This change from a bulk indirect band gap property to a quasi-direct band gap has been attributed to quantum confinement [46, 47]. Quantum confinement results from electrons and holes being squeezed into a dimension that approaches a critical quantum measurement, called the exciton Bohr radius [48, 49].

A theoretical model generally used to describe the effect of quantum confinement was suggested by Efros and Efros [50] and has become the most acceptable concept for describing the size effect properties of materials [3, 49, 51, 52, 53]. They assume a spherical microcrystallite with infinite potential at its boundary. Accordingly, the mechanism for this luminescence have been modeled on the presence of oxides at the surface of the nanoparticles, i.e., the Si/SiO_2 interface state, defects in the SiO_2 or Si nanocrystallites embedded in an oxide with a resultant larger band gap due to quantum confinement [54].

In the nanometre range, the band gap of a Si crystal increases with decreasing size. Assuming

a spherical nanoparticle of radius R, as the radius reduces, the energy levels of the carrier change from a continuous band structure to a set of discrete levels [49][55]. The relationship between the band gap energy and the size of the nc-Si can be written as [25]

$$E = E_g + \Delta E, \tag{2.1}$$

where E_g is the band gap of bulk silicon, and ΔE is the additional energy due to quantum confinement of the electronic states.

The boundaries of the band gap of nc-Si can therefore, be tuned by adjusting the size of the particle, in essence controlling the number of atoms that constitute the particle. Since the emission frequency is dependent on the band gap, the wavelength of the luminescence can therefore be controlled by changing the radius of the particle. The smaller the dot the bluer the emission colour.

Other optical properties that can be affected by size include, photo-catalysis, photoconductivity, photo-emission and electroluminescence [25]. As the size of particle reduces, in many cases the energy bands cease to overlap and a conducting material can become insulating below a critical length scale [56]. Transport of free carriers between adjacent nanostructures becomes one of tunneling, and application of an external voltage between two nanostructures could lead to resonance tunneling [25]. Another notable influence of size becomes pronounced when a particle has a dimension smaller than the mean free path for inelastic scattering, in which case carriers can travel within the nanostructure without scattering and transport becomes purely ballistic [25].

University of Cape Town

2.1.3 Methods of silicon nanoparticle fabrication

Numerous ways have been devised for the fabrication of silicon nanoparticles and nanostructures with various degrees of quality, speed and cost. The production process of nanoparticles in general can be classified into either the category *bottom-up* process, involving atom by atom agglomeration, or the category *top-down* process which involves the removal of materials to create the desired structure [25], as illustrated in Fig. 2.2.

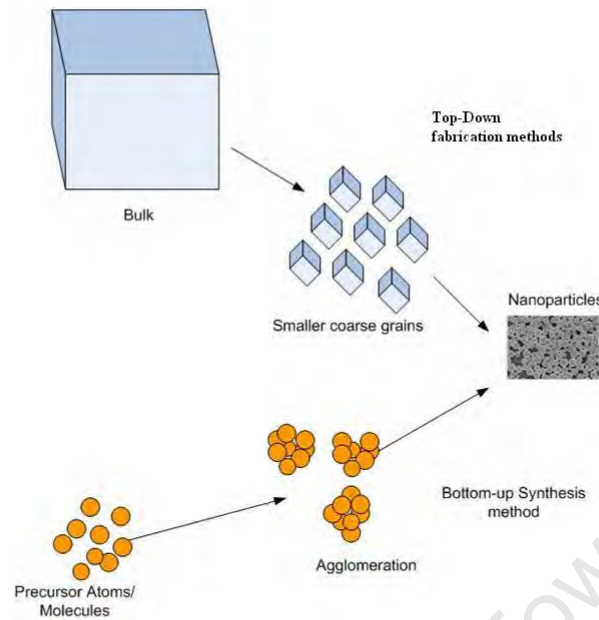

Fig. 2.2: Schematic representation of the two major production routes for nanoparticles and nanostructured materials. The top arrows represent the top-down method while the bottom arrows represent the bottom-up process. Adapted from [25].

University of Cape Town

Bottom-up processes of silicon nanoparticle and nanostructure fabrication

In principle, the bottom-up process for producing nanoparticles involves the aggregation of building blocks like atoms, molecules, or relatively small nanoparticles to form a complex nanostructure, usually via chemical synthesis. This could either be through solid, liquid or gas phase reaction, resulting in decomposition and deposition, self-assembly, and positional assembly of nanostructured materials [25].

For the production of silicon nanoparticles and nanostructures, the commonly used methods employed in the bottom-up process are itemised below.

- **Molecular Beam Epitaxy (MBE):** MBE generally involves the use of an ultra-high precision, ultra clean evaporator combined with a set of spectroscopy tools for in-situ characterisation of deposited material [25]. This technique is generally used for epitaxial growth via the interaction of one or several molecular or atomic beams on a surface of a heated crystalline substrate. The process exploits the evaporation process of condensed materials as a molecular flux source in a vacuum [57]. In a typical MBE process, the nanostructure is an extended single-crystal film formation on top of a crystalline substrate. In the case of silicon where preservation of periodicity is important, the film and substrate are the same material (homoepitaxy) [58]. The most important

characteristic of such nanostructures is that the epilayer is generally freer of defects, purer than the substrate, and can be independently doped [58]. When the epilayer and substrate crystal are identical, the lattice parameters are perfectly matched and there is no interfacial bond straining. On the other hand for heteroepitaxy, where the epilayer is different from the substrate, the lattice parameters are necessarily unmatched [58]. While MBE may be useful in producing defect free nanostructured silicon surfaces, the process is limited with respect to production of free nanoparticles.

- **Solid-phase crystallisation (SPC):** Solid phase crystallisation is generally used to produce nanostructured silicon in two stages. First is the deposition of an amorphous silicon a-Si or a multilayer a-Si/a-SiO_2 on a suitable substrate and secondly the crystallisation of these layer in a two step thermal process [59]. The crystallisation is initiated in the first step by rapid thermal annealing at $800-900^oC$ for $40-60sec$, and then a higher temperature of 1050^oC is slowly ramp down at a rate of $10^oC/min$, thus allowing the growth of seed crystals formed during the first stage [59, 60]. Solid phase crystallisation (SPC) is carried out because of its best uniformity of silicon nanocrystals ($2-25nm$) and it illustrates an excellent result in reproducibility among the various crystallization methods [61]. The SPC process also offers the advantage of producing a high density of nanocrystal silicon. Like MBE, SPC is applicable only for nanostructured silicon synthesis, but unlike MBE only partial crystallization of amorphous layers produced by any deposition method has been achieved [62].

- **Chemical Vapor Deposition (CVD):** This is one of the easiest methods of silicon nanostructure as well as nanoparticle production. In this technique, silane (SiH_4) is decomposed to nucleate on substrate. The entire process involving nanocrystal nucleation, growth, and deposition occurs within the same chamber [59]. Most commonly used CVD methods are hot wire chemical vapor deposition (HWCVD) and plasma enhanced chemical vapor deposition (PECVD) [63, 64]. Nanostructured silicon layers produced using HWCVD for example are usually highly amorphous, and in most cases are further processed, e.g. via rapid thermal annealing to improve the crystallinity. Recently many workers are using HWCVD to produce free standing silicon nanoparticles. For example Fig. 2.3 shows a highly porous agglomeration of a-Si nanoparticles of primary size in the order of $40nm$ produced using HWCVD process by Scriba et al. [65]. The particles created using this means have fairly circular shapes and a small size distribution between $20-70nm$ [65]. This method has the advantage of been scalable, with the potential of producing device quality silicon nanoparticles at a high deposition rate. The added advantage is the possibility of doping the nanocrystals in

University of Cape Town

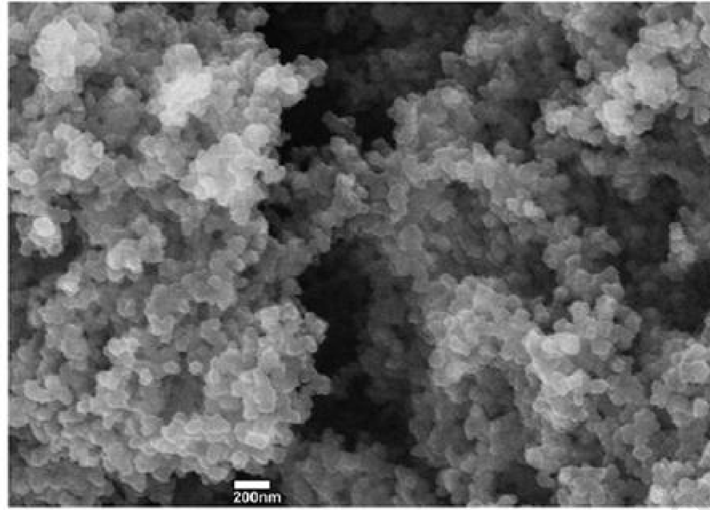

Fig. 2.3: Shows highly porous agglomeration of *a*-Si nanoparticles of primary size in the order of $40nm$ produced using HWCVD process [65].

University of Cape Town

the gas phase [64, 66].

- **Aerosol synthesis:** Aerosol synthesis process is another widely used bottom up approach for nanostructured silicon fabrication. In this technique, an aerosol of spherically shaped silicon nanocrystals is formed by pyrolytic decomposition of diluted silane (SiH_4) gas at 950^oC [59, 67]. The process usually starts with the nucleation of clusters in a gas phase, which are then oxidized in a furnace resulting in an amorphous SiO_2 shell ($\approx 2nm$) grown on the nanoparticles [68]. The oxidized aerosol is then passed through a chamber heated to 200^oC and collected on the surface of a substrate maintained at 23^oC. The nanocrystals migrate to the substrate and are deposited to attain monolayer surface coverage with planar densities as large as $10^{13}cm^{-2}$ [59]. The method can be easily adapted for the production of free standing silicon nanoparticles by using a differential mobility analyzer [59]. Onischuk et al. [68] for example, have used this process to produce silicon nanoparticle aggregates consisting of small primary particles of $10nm$.

- **Liquid Phase Methods:** This method generally involves the precipitation of an ultra fine nanoparticulate from a solution in a mixed precipitation reaction. Semiconductor clusters have traditionally been prepared by the use of colloids, micelles, polymers or a crystalline host [1]. The difficulty of producing solution based silicon compounds and the fact that clusters produced using this technique have poorly defined surfaces and a broad size distribution, which is detrimental to the properties of the semiconductor materials, makes the method a less popular means of nanostructure and nanoparticle

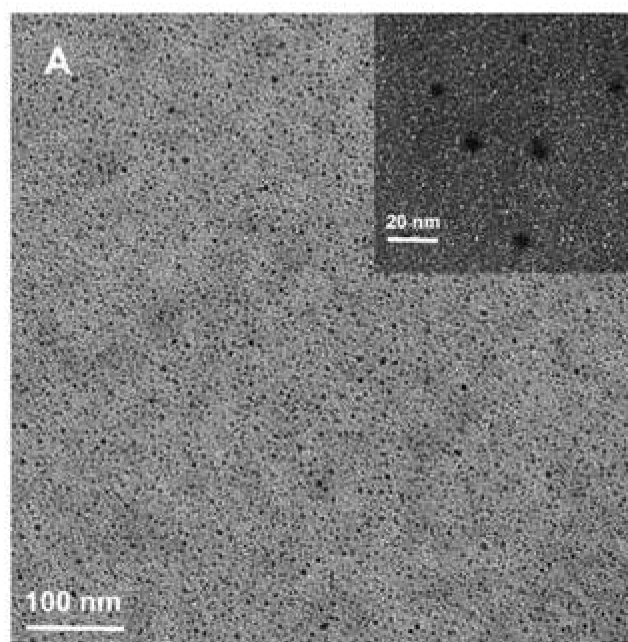

Fig. 2.4: TEM image of silicon nanoparticles prepared by, liquid phase synthesis method [69].

University of Cape Town

production [1].

However Zhang et al. [69] and Warner et al. [70] have demonstrated the possibility of overcoming these challenges by synthesizing hydrogen-capped silicon nanoparticles with strong blue photoluminescence by the metathesis reaction of sodium silicide (NaSi), with NH_4Br. The hydrogen-capped Si nanoparticles were further terminated with octyl groups and then coated with a polymer to render them water-soluble. Fig. 2.4 shows a typical transmission electron (TEM) micrograph of silicon nanoparticles with an average diameter of $3.9 \pm 1.3nm$ produced using this method. No aggregation is observed in the TEM image [69].

- **Self-assembly and positional assembly:** These are new methods developed to manipulate and position nanomaterials into two and three dimensional structures based on packing considerations [25]. In general the use of an atomic force microscope (AFM) tip and other direct manipulating tools for positional assembly has become popular [71]. Tanaka et al. [72] for example, demonstrated a new bottom-up technique of forming silicon nanostructures based on self assembly of nanocrystalline (nc) Si dots from a solution. In their method nc-Si dots with a diameter of $8nm$ were dispersed in methanol and then evaporated from the surface of a substrate. During the evaporation, the nc-Si dots were assembled in the solution via the lateral capillary meniscus force which works as an attractive force between the dots [72].

Although bottom-up synthesis methods gives the advantage of controlled size and quality grade nanostructured and nanoparticles of Si production, it is not suited for large scale low cost production purposes because of the cost of the equipment and precursors used in the synthesis. Also, in some processes the chemistry is complex and hazardous.

Top-down processes for silicon nanostructure and nanoparticle fabrication

Top-down methods generally involve physical or chemical reduction of bulk materials, either by milling, laser ablation or etching into the desired structure. The basic advantage of this approach is their simplicity and the operation of the technique for large scale production. Some of the notable top-down methods generally used to produce nanostructures as well as nanoparticles of silicon are given below.

University of Cape Town

- **Milling:** The most widely applied physical method employed in the top-down production of silicon nanoparticle is milling. This is generally achieved through high energy ball milling. High energy ball milling is of industrial importance because it enables low cost production of nanostructured materials with an added advantage of simplicity and effectiveness [43]. Fig. 2.5 shows the schematic representation of a high energy ball milling process of bulk materials to smaller particulate sizes. As illustrated in the figure, coarse grains are trapped between two colliding balls resulting in rearrangement and re-stacking of the particles in the powder [37]. Usually this is carried out under controlled environment to prevent unwanted reactions such as oxidation [25]. Repeated plastic deformation, results in the creation of grain boundaries within a particle, which then act as lines of dislocation allowing reduction in size upon further crushing. The resulting particles formed in this way are characteristically fine, irregularly shaped and full of defect states [37]. These powders can exhibit nanostructural characteristics on at least two levels. Firstly, the particles themselves may normally possess a distribution of sizes less than $100nm$, and secondly the particles may possess a grain structure such that the crystallite (grain) size after milling is often between $1 - 10nm$ in diameter [37].

  High-energy milling, like other non-equilibrium methods, has a potential to distort the lattice and produce amorphous silicon. Study of milled powder using Raman spectroscopy often reveals, grain refinement, lattice transformation and amorphorization [73]. Other possible effect of milling on the microstructure produced by high energy ball milling include dislocations and stacking faults as well as mechanical alloying of

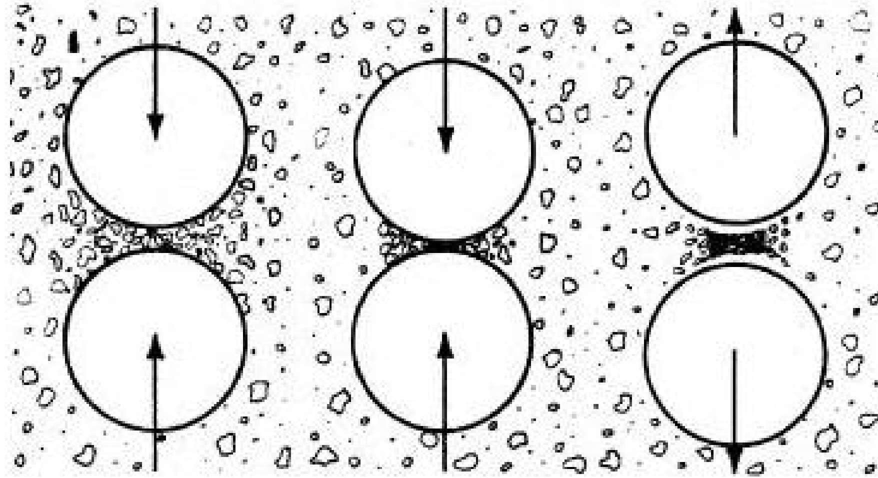

Fig. 2.5: Typical high energy ball milling of bulk materials to nanoparticulate grains. In this process two or more balls are randomly agitated resulting in trapping, reduction and compaction of particles [37].

University of Cape Town

the primary content with the milling medium [73]. High energy ball milling of single-crystal silicon also leads to significant broadening of the X-ray diffraction peaks due to the refinement of the microstructure, induced by the heavy plastic deformation experienced during the processing [41]. Other types of mechanical milling, including using a planetary mill at room temperature have been reported [74]. The silicon nanoparticles produced using this method have range of sizes from $10 - 25nm$, and high resolution electron microscopy (HREM) experiment of this powder showed similar defects to those produced using high energy ball milling.

- **Lithographic process:** Conventional lithographic processes can be used to create nanostructures by the formation of pattern on a substrate via the creation of resist on the substrate surface [25]. The variants of lithography are based on the exposure mechanism, using either visible or ultraviolet (UV) light, X-rays, electrons or ions to project an image of the desired pattern onto a surface coated with photoresist material. These different techniques are termed photolithography, X-ray lithography, electron beam lithography and ion beam lithography, depending on the radiation type employed [25]. The principle of all these processes is that the photoresist, usually a polymer, is chemically changed upon irradiation. The resist can then be used as a template or as an etch mask [25]. The wavelength of the radiation used in the lithography determines the details in the resist and hence the final planar structure [25]. Lithography has enabled the lateral dimensions of devices to be scaled down far below $100nm$.

  Recently however, soft lithography through the use of a mold or stamp rather than by

radiation has been applied for fabricating nanostructured devices. In many cases, the stamp is coated with a chemical that reacts with the resist solely at the edge of the stamp [25]. This process, termed nanoimprinting, can produce patterned structures in the size range of $10nm$ [25]. In UV-nanoimprint lithography for example, a transparent stamp with nano/micro-scale patterns is pressed onto a thin resin layer or resin droplets. The resin is then cured by exposing it to UV light from above the stamp. After tens of seconds, the stamp is separated from the patterned layer on the substrate. Finally, anisotropic etching is used to transfer the patterns onto the substrate [75].

- **Laser induced ablation:** Laser induced ablation from a solid target is known as a good method for nanoparticle production. In this method, the target, usually a bulk single crystal is immersed in a liquid such as water, hexane or toluene, and a laser beam is focused on the target with a lens to irradiate the target at a fluence of about $10mJ/cm^2$. This process reduces the bulk material into small nanoparticles which are then dispersed in the solvent [76]. Umezu et al. [76] used pulsed laser ablation of a silicon target in liquid environment, to prepare a silicon colloid solution. A similar approach by Makino et al. [77] using pulsed laser ablation in a hydrogen background gas, produced nanoparticles which are spherical, and have characteristic log-normal size distribution with a mean diameter of $4.6nm$ [77]. In both cases cited above, structural studies using Raman spectroscopy revealed that the silicon nanoparticles have a high degree of crystallinity.

- **Chemical Reduction:** Top down chemical reduction of bulk materials to nanoparticles generally involves exposing of the bulk materials to corrosive vapour (chemical vapor-etching (CVE)) [78] or immersion into a solution. Valenta et al. [79] for example, used an electrochemical etching on Si wafers in a mixture of HF (50%), ethanol (UV grade) and hydrogen peroxide (30% aqueous solution). By continuous stirring and applying relatively low etching current density of $2.3mA/cm^2$ during the etching, with additional post-etching in hydrogen peroxide for $20min$, a smaller mean diameter of Si nanoparticles was obtained. These approach is now widely used for the fabrication of porous silicon [80, 81, 82].

University of Cape Town

2.2 Experimental Methods

This section details the experimental techniques used for the production, sample preparation and characterisation of silicon nanoparticles.

2.2.1 Milling using a laboratory disc mill

For this research, batch grinding of bulk silicon was achieved by using a Siebtechnik 800W TS laboratory disc mill shown in Fig. 2.6, equipped with a 52100 chrome steel pestle and mortar [34]. The central feature is the vibrating disc unit, powered by a three phase electric motor. The clamp and fixture are placed on opposite sides of the vibrating unit and its function is to hold the milling medium in place during milling. For this experiment two sets of milling media was used. The first set **A**, shown in Fig. 2.7(a), consist of four sets of 52100 chrome steel pestles and mortars, with a cover lid fitted with rubber seal. The combination of the mortar, with the pestle placed inside, and thereafter covered with the lid, sits in a bottom rack which holds the four mortars for simultaneous milling. This bottom rack includes two pins for securing a top rack with four plastic studs to secure the lid over the mortar through the clamp shown in Fig. 2.6. The second set **B**, shown in Fig. 2.7(b) consists of a single large 52100 chrome steel pestle, mortar and also a ring, which sits inside the mortar between the inner wall of the mortar and the pestle. Set **B**, unlike **A**, sits directly on the vibrating disc through a bottom ring shown in Fig. 2.6 and is secured through the cover lid with the clamp and fixture.

The principle of milling in this system is by means of predominantly horizontal vibration, the material is ground by impact and friction, usually in minutes, and at the same time homogenised [83]. For the arrangement **A**, this will mean impact between the pestle and the mortar, crushing any materials trapped in between, and grinding any material underneath the pestle as it makes its way back and forth in the grinding medium. For **B**, however, impaction occurs between the pestle and the ring's inner wall and between its outer wall and the mortar inner wall, while grinding of the material occurs underneath the pestle as well as the ring as it makes its way back and forth in the grinding medium.

University of Cape Town

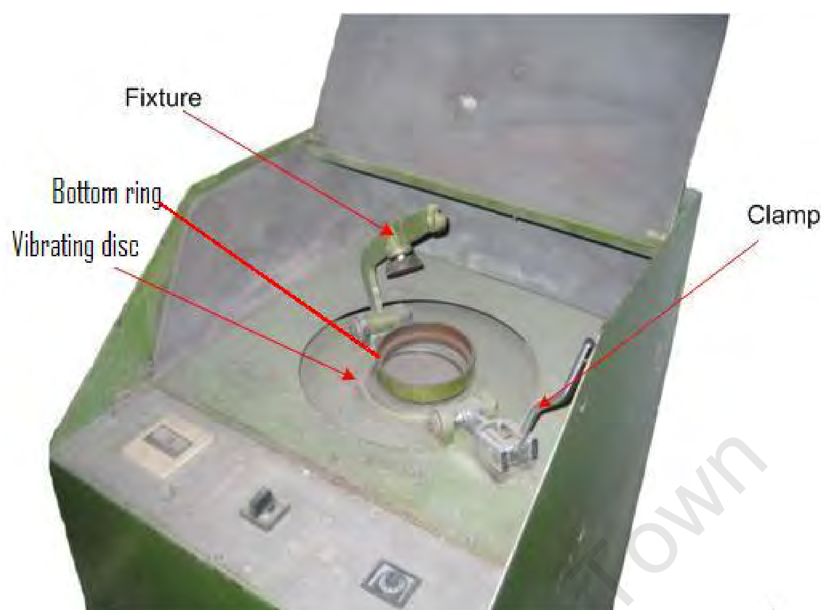

Fig. 2.6: The Siebtechnik 800W laboratory disc mill, with a central vibrating disc, fixture and clamp to secure the milling medium as indicated with the arrows.

University of Cape Town

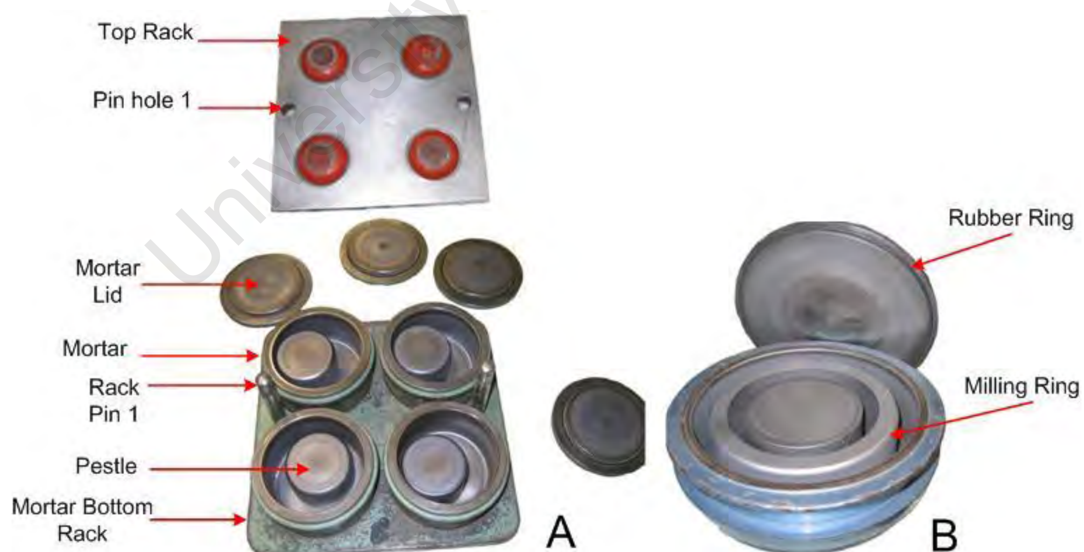

Fig. 2.7: Showing the two type of milling medium, (A) is a set of four small mortar with pestle and lid fitted with a rubber ring to ensure a proper sealing and (B) the large mortar with bigger pestle and inner ring for crushing on the wall of the mortar as well as on the pestle.

Feedstock and milling process

The two main bulk silicon materials milled in the laboratory disc mill consist of p-type single crystalline boron doped silicon wafers, and 2503 grade polycrystalline silicon metal, provided by Silicon Smelters (PTY) Ltd. Polokwane, South Africa. Table 2.1 shows the main properties of the as received starting materials. The purity of the p-type silicon wafer is nominally 99.99%, while the metallurgical grade silicon, according to the manufacturers analysis, is 99.40%. Table 2.2 shows a list of the known elemental impurities constituting 0.60% of the metallurgical grade silicon.

Table 2.1: Table showing the different materials used as starting feedstock for the production of nanoparticles of silicon and some of the manufacturer labeled properties.

Silicon type	Dopant	Orientation	Resistivity	Mass milled	Tag
P	Boron	$< 111 >$	$2-5\Omega cm$	$20.05g$	P*
Metallurgical	Unknown	Polycrystalline	unknown	$50g$	M

Table 2.2: Showing list of impurities contained in the as received metallurgical grade silicon from manufacturers analysis.

Impurities	Fe	Al	Ca	Ti	Cr	P	Ni
%	0.21	0.14	0.23	0.01	0.06	0.04	0.02

The milling of the p-type wafer was achieved using set-up **A** described above, under normal laboratory conditions. Five wafers with total mass $20g$, without further treatment, were placed in one of the mortar and initially broken into larger fragments by means of the pestle, while an equivalent amount of quartz sand, was placed in the other three mortars to balance the mill. For the metallurgical grade silicon, $50g$ of the as received granules were poured between the pestle and the ring in a mortar of the type **B** system, with the cover lid secured by the clamp attached to the vibrator on the disc mill.

In the case of the p-type wafer, the milling was carried out for 5 hours in sessions of 1 hour. Each milling session is characterised by a continuous crushing and grinding of the wafer into smaller free particles or compaction into small clusters. The milling resulted in the generation of heat within the medium, with temperatures reaching about 120^oC after one hour. As such, each milling session is followed by a hold time of about five hours, long enough to bring the medium back to room temperature.

A small quantity of the P* powder in particular was taking from the mortar before the start of a new milling session. This powders were sealed in a labeled plastic container, which was then kept in a safe place awaiting characterisation. At the completion of five hours of milling

University of Cape Town

in the case of the wafers, and three hours for the metallurgical silicon, the entire powder comprising of loose as well as compacted clusters was scooped out of the mortar into different plastic containers and then sealed. At a later time, however a second batch of metallurgical silicon powder milled for 5 hours was produced using same procedure.

University of Cape Town

2.3 Characterisation of milled silicon nanoparticles

This section details the principle of operation, sample preparation and characterisation techniques used for examining the structural, morphological and elemental composition of the two main silicon powders produced by milling p-type single crystalline wafers and bulk metallurgical silicon respectively, as described in section 2.2.1. The result of the different analysis will focuss on how the features mentioned above vary with the milling time of the powders, and the differences that may exist between the two batches of powders.

For the purpose of this analysis the P* powder milled for $1-5$ hours will be labeled P^*1 to P^*5, where the number indicates the milling time in hours. For the case of the metallurgical powder, the label $M3$ and $M5$ will be used to indicate powders milled for three and five hours respectively.

University of Cape Town

2.3.1 X-ray diffraction study of nanostructured silicon produced using a laboratory disc mill

X-ray diffraction is a set of techniques which reveal information about the crystallographic structure, chemical composition, and physical properties of materials [84]. It is based on observing the scattered intensity of an X-ray beam, hitting a sample, as a function of incident and scattered angle [84], and it is used normally to distinguish between single crystal, polycrystalline or amorphous materials [85].

For a cubic crystal with cell lattice parameters a, b and c, the Von Laue equation relating the incident wavevector $\mathbf{k_i}$ with the diffracted wavevector $\mathbf{k_o}$ is given by [86]

$$a.(\mathbf{k_o} - \mathbf{k_i}) = 2\pi h, \tag{2.2}$$

$$b.(\mathbf{k_o} - \mathbf{k_i}) = 2\pi k, \tag{2.3}$$

$$c.(\mathbf{k_o} - \mathbf{k_i}) = 2\pi l. \tag{2.4}$$

Where h, k, and l are integers. By taking $\mathbf{k_o} - \mathbf{k_i} = \mathbf{G}$, where $\mathbf{G}$ is the reciprocal lattice

vector, equation 2.4 can be related to the well know Bragg equation through,

$$|\mathbf{G}| = \frac{4\pi}{\lambda}\sin\theta = \frac{2\pi}{d_{hkl}}, \tag{2.5}$$

which is then reduced to

$$\lambda = 2d_{hkl}\sin\theta, \tag{2.6}$$

Where θ is the angle between the diffracted beam and the plane of reflection and d_{hkl} is the interplanner spacing.

Bragg's law states the condition for a sharp diffraction peak from an infinite crystal with perfect 3 dimensional order [87]. Usually the diffraction peak has a finite width which is associated with imperfection in some of the Bragg parameters [87]. X-ray peaks are broadened due to (1) instrumental effects (2) small particle size and (3) lattice strain in the materials. For mechanically milled powder the lattice strain is an important parameter [88].

The Scherrer equation relates the peak broadening represented by the Full Width at Half Maximum in radian β_{FWHM}, to the size of the grain as [89],

$$t = \frac{K\lambda}{\beta\cos\theta_B}, \tag{2.7}$$

where t is the coherent scattering length (crystallite size), θ_B is the Bragg angle, K is a constant which depends on both apparatus and studied sample. It is taken as $1.0 < K < 1.3$ when integral breadths are used, and $K = 0.9$ when a gaussian function (rather than a triangle function) is used to describe the peak [87]. The Scherrer equation is useful when crystals are smaller than $100nm$ in size. For grains larger than this size, other statistical means should be employed [87].

For the purpose of determining the structural features of the milled powders, X-ray diffraction was carried out on the different powders using a Huber G670 Guinier imaging plate X-ray diffractometer. The diffractometer has a 2θ range of $4 - 100^o$ in step of 0.05^o. The Huber G670 uses an image plate detection method where the image storage foil is positioned in the Guinier camera 670, with the sensitive side facing inward precisely on the focal circle with a radius of $90mm$. After exposure, the image plate is scanned by a vertical linear red diode laser beam within 5 seconds. The X-ray wavelength used for this diffraction experiment is $1.5405\mathring{A}$. The powders $P^{*}1$ to $P^{*}5$, produced from milling p-type wafers for $1 - 5$ hours, as well as the $M3$ powder, produced from milling metallurgical grade silicon for 3 hours, were

University of Cape Town

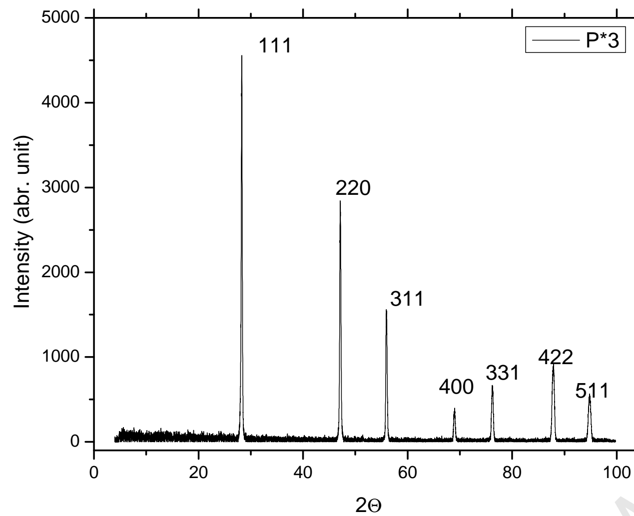

Fig. 2.8: XRD pattern for $P^{*}3$ silicon powder milled for 3 hours using the laboratory disc mill after background subtraction.

University of Cape Town

used to fill different $1mm$ capillary glass tubes. First a background X-ray diffraction was carried out with an empty capillary tube for 15 minutes, after which measurement was done on each sample filled capillary tube, for another 15 minutes. The reading of the recorded diffraction spots on the imaging plate was done internally by an image scanning instrument 10 time to improve on the recorded intensities.

Analysis of the diffraction data was performed with Origin data analysis software. First, correction to the data was made by subtracting the background diffraction data measured for the empty capillary tube. Indexing of the different peaks was done by using structure factor and the lattice parameter $a = 0.543nm$ for silicon. Fig. 2.8 shows the X-ray diffraction patterns of the $P^{*}3$ silicon powder milled for 3 hours as an example. The diffraction patterns for the different milling times are similar and show seven basic peaks corresponding to reflections from the planes (111), (220), (311), (400), (331), (422) and (511), with the most intense peak been the (111) reflection. Other phases that may arise due to contamination from the milling medium and oxidation from the atmosphere were below the detection limit of the instrument. The diffraction patterns for all milling times are characterised by sharp peaks, which is an indication of the high crystallinity of the milled powder and a small broadening of the peaks, which may arise from build up of lattice strain or from reduction in grain size of the powder [88, 87]. A similar plot for the milled metallurgical grade powder $M3$ as shown in Fig. 2.9, also shows seven basic peaks, with characteristics similar to those shown by the $P^{*}3$ milled wafer, shown earlier in Fig. 2.8.

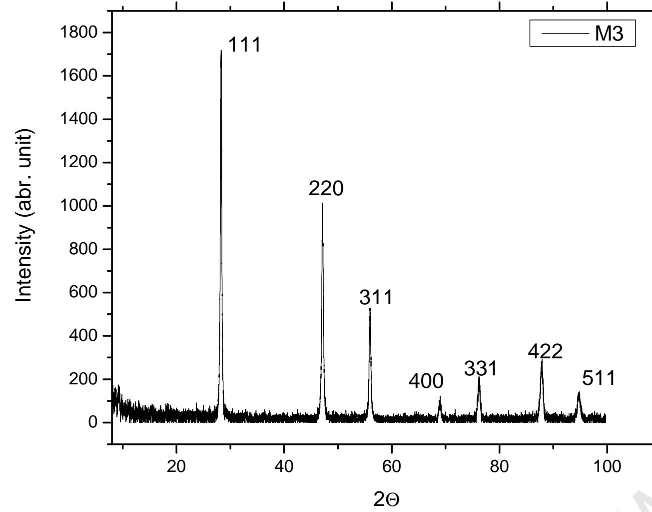

Fig. 2.9: XRD pattern for $M3$ silicon powder milled for 3 hours using the laboratory disc mill after background subtraction.

University of Cape Town

A close examination of the (111) peak for the $P^{*}5$ as well as the $M3$ powder (the longest milling time powders at the time of this experiment) shown in Fig. 2.10 and 2.11 respectively, clearly shows a characteristic small broadening of the peaks around the peak center $2\theta \approx 28.29$ as indicated on the plots, and the absence of a broad $\geq 2^{o}$ background characteristic of an amorphous phase [90] in both cases. Similar broadening of the diffraction peaks width have been reported by Diaz-Guerra et al., for powders produced via mechanical milling of p-type silicon wafer in a Spex-8000 mixer-mill equipped with a hardened steel for up to 50 hours [41]. The broadening of the Bragg peaks is suggested to be due to the refinement of the microstructure induced by the heavy plastic deformation experienced during the processing [41]. In other cases, study have shown a structural transformation from single crystalline to polycrystalline silicon induced by high energy ball milling in which two phase amorphous and nanocrystalline silicon particles were produced [91]. The powders produced in this study have only shown a small broadening of the diffraction peaks for milling time up to 5 hours in case of the milled wafers and 3 hours for the metallurgical powder. This may be due to reduction in grain size as well as induced lattice strain as indicated above. Interesting, however, is the absence of any indication of significant amorphorisation.

An attempt was made to determine the effect of milling time on the crystallite or average grain size of the powder by applying the Scherrer equation, taking $K = 0.9$, $\lambda = 0.154nm$. The FWHM deduced from fitting a gaussian function to the (111) peak after correction for instrumental broadening, yields crystallite sizes which have a small dependence on the

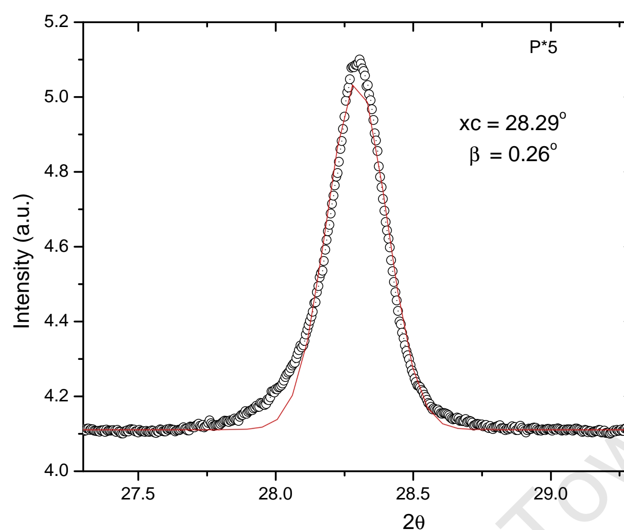

Fig. 2.10: Plot showing a gaussian function fit to the (111) peak for $P^{*}5$, indicating a small broadening $\beta = 0.26$ with no indication of a broad hump suggesting the presence of an amorphous phase.

University of Cape Town

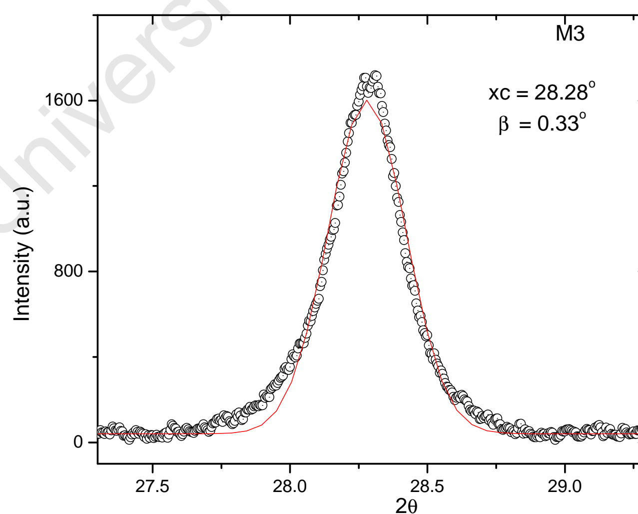

Fig. 2.11: Plot showing a gaussian function fit to the (111) peak for $M3$, indicating a small broadening $\beta = 0.33$ with no indication of a broad hump suggesting the presence of an amorphous phase.

Table 2.3: Showing the calculated crystallite sizes using the Scherrer method with the β_{FWHM} derived from fitting a gaussian function to the different (111) peaks after correction for instrumental broadening.

Powder type	$P^{*}1$	$P^{*}2$	$P^{*}3$	$P^{*}4$	$P^{*}5$	$M3$
Crystallite size (nm)	39.66	37.59	36.11	36.27	34.64	25.68

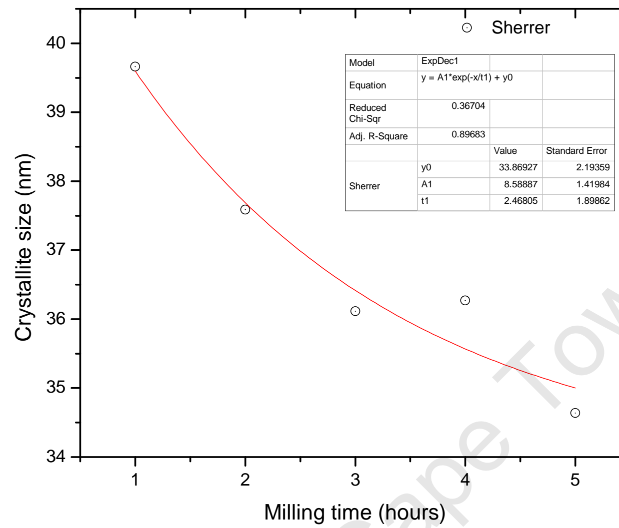

Fig. 2.12: Plot showing the dependence of the crystallite size calculated from the (111) peak using the Scherrer method on the milling time.

University of Cape Town

milling time. Table 2.3 shows the calculated crystallite sizes for the powders $P^{*}1$ to $P^{*}5$ as well as for the $M3$ powder, assuming all broadening is due to size effect. The calculated values are all within the $100nm$ range for which Eqn.2.8 is valid [87]. The dependence of the crystallite size on milling time is shown in Fig. 2.12. The plot indicate a first order exponential reduction in crystallite sizes with milling time. A comparison between the p-type powders and the $M3$ powder shows that the calculated crystallite size for the $M3$ powder is much smaller than even the $P^{*}5$ powder. This is an indication of a difference in the manner in which grain or crystallite formation propagates in the two powder types.

It is therefore reasonable to suggest that the process of top-down milling of silicon, using the laboratory disc mill for producing nanostructured/nanoparticle silicon is effective, as the produced nanoparticles remain highly crystalline for the entire milling period. The preservation of crystallinity is important for the device application of the produced silicon powder, as this will ensure preservation to a large extent of the electronic features (carrier mobility) of the particles.

2.3.2 Morphological and elemental compositional study of silicon nanoparticles

Scanning Electron Microscopy (SEM), is an extremely useful surface and subsurface imaging tool. It creates various images by focusing a high energy beam of electrons onto the surface of a sample and then detecting signals from the interaction of the incident electrons with the samples. The signals gathered in a SEM can include secondary electrons, characteristic x-rays, and back scattered electrons [92]. SEM is therefore suitable for the study of size, shape and other physical features of materials.

Most SEM instruments have facilities to carry out elemental compositional study from X-ray emission from the interaction of the sample with the incident electron beam. When energetic electron interacts with material, electrons from the outermost shell of the atoms may be knocked out and a possible de-excitation, results in X-ray emission. The energy of the emitted X-ray is characteristics of the atomic level present in the material. By measuring the energy of the X-ray emitted from the surface of the material, it is possible to identify different elemental composition, from a particular section of the electron beam. This is the basis for the energy dispersive X-ray (EDX) analysis technique [93, 94, 95]. Since EDX is due to ionization and subsequent emission of X-rays from materials, caused by energetic electrons, most SEM and TEM are equipped to carry out EDX analysis in conjunction with their primary purpose. This is particularly useful for quality control of materials or for monitoring the synthesis of material with desired composition.

For the purpose of this study, small quantities of the powders, namely P^*1 to P^*5 were dispersed in ethanol contained in a plastic bottle. The contents of the bottles were then sonicated in an ultra sonic bath for 1 hours in 2 session of 30 minutes. This ensured that much of the clustered lumps are properly broken down. Two drops each of the dispersed powder in ethanol were placed using a pipette, on a carbon coated surface of a sample holder made of aluminum. The sample was then placed under a $100W$ electric bulb to vapourise the ethanol before measurement. A similar study of powder $M3$ and $M5$ was carried out on pellets of the powder formed by compressing the $M3$ and $M5$ powders.

The study of the morphology, which includes the sizes distribution and shape, as well as the elemental composition of the nanostructured silicon produced above, was performed using a Leica Stereoscan S440i. The dependence of these features on milling time was also investigated. For imaging, the operating beam energy used is $20KeV$, and a probe current of $50 - 100pA$ which gives an estimated resolution for images of about $10nm$ in secondary

University of Cape Town

electron mode. SEM micrographs of each sample were taken for three different regions at magnifications ranging from low (×10000) to high (×50000). For the elemental composition study, different areas of the sample were examined for their elemental composition, with a focus on silicon, as the primary constituent, and oxygen, chromium and iron from possible contamination, using a beam energy of $20KeV$ and a beam current of $1000pA$ with a working distance of $25.0mm$. Measurement of particle size distribution was carried out on the micrograph using an image processing software Digimizer, version 3.1.2.0 from MedCalc [96].

Fig. 2.13(a)-(e) shows the micrographs of the powder $P^{*}1$ to $P^{*}5$ milled for $1-5$ hours, while Fig. 2.13(f) shows the micrograph for $M3$ powder milled for 3 hours. The morphology of the powder $P^{*}1$, after an hour of milling as seen from Fig. 2.13(a), shows that the powder consist of particles with wide range of sizes and two main shape types. The obvious ones are large faceted particles, cleaved along close packed planes, whose size varies between $1-3\mu m$. The other types of particles are relatively smaller particles of sizes $100-400nm$ with an overall spherical shape. The size distribution from random measurement of 150 particles with clearly defined boundaries along their longest axis shows a typical log-normal distribution with the population of the smaller more spherical particles dominating as shown in the inset of Fig. 2.13(a).

After 2 hours of milling, the morphology of the powder $P^{*}2$, exhibits a similar wide size distribution as seen in Fig. 2.13(b). However the powder now consists of much more smaller particles in the range $100-400nm$ (see inset), when compared to $P^{*}1$. A comparison of the morphology of the 1 hours to 5 hours milling of the powder Fig. 2.13(a)-(e), shows a progressive increase in the population of the particles with sizes in the range $100-400nm$ and a relative reduction of the population of the larger faceted ones due to further attrition with milling time.

Fig. 2.13(f) shows the SEM micrograph for the $M3$ metallurgical powders milled for 3 hours. The powder is seen to have similar size distribution of particle. The particles are all to a large degree rounder in shape with size distribution showing a predominantly round particles in the size range $100-400nm$ as seen in the inset of Fig. 2.13(f). Similar feature was observed in the $M5$ powder shown in Fig. 2.14 for the 5 hours milled metallurgical powders. This single particle shape for all size distribution is a marked difference between the milled wafers and the metallurgical grade silicon.

Fig. 2.15 shows the plot of the intensity versus X-ray energy on a semilog scale for the EDX analysis carried out *in-situ* for powder P*1 as an example. From the spectra, silicon at $K_{\alpha 1} = 1.739KeV$ is clearly the dominant element in the powder $\approx 95a.t\%$, with oxygen at

University of Cape Town

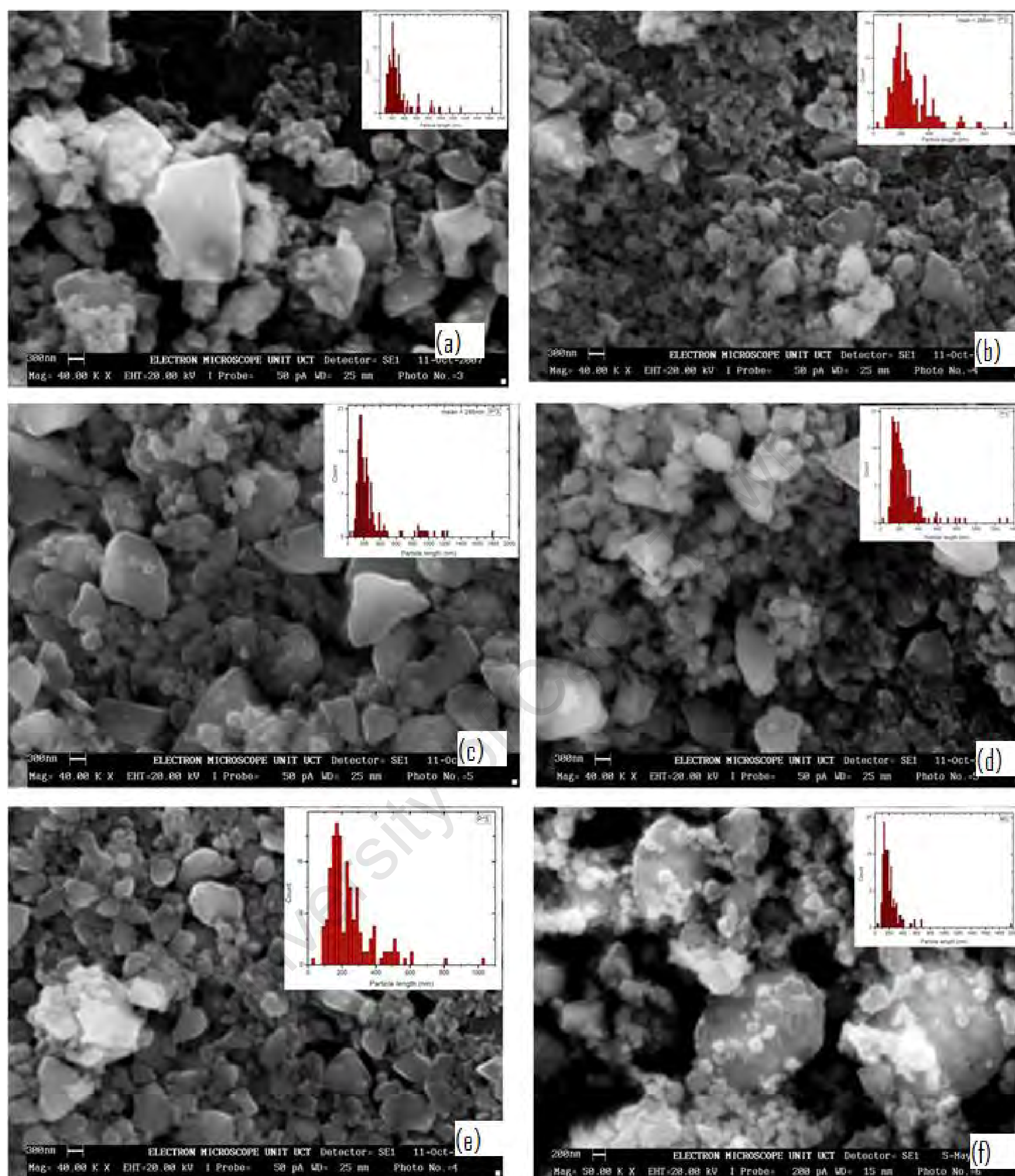

Fig. 2.13: Showing SEM micrographs of milled nanostructured silicon for (a) $P^{*}1$,(b) $P^{*}2$,(c) $P^{*}3$,(d) $P^{*}4$,(e) $P^{*}5$ and (f) a pellet formed by compressing nanostructured silicon of $M3$ powder.

$K_{\alpha 1} = 0.525 KeV$, iron at $K_{\alpha 1} = 6.398 KeV$ and chromium at $K_{\alpha 1} = 5.40 KeV$ constituting only trace amounts in the powder, as no clear peak was observed at the different energy positions corresponding to their energy levels as seen in Fig. 2.15. Similar trends were

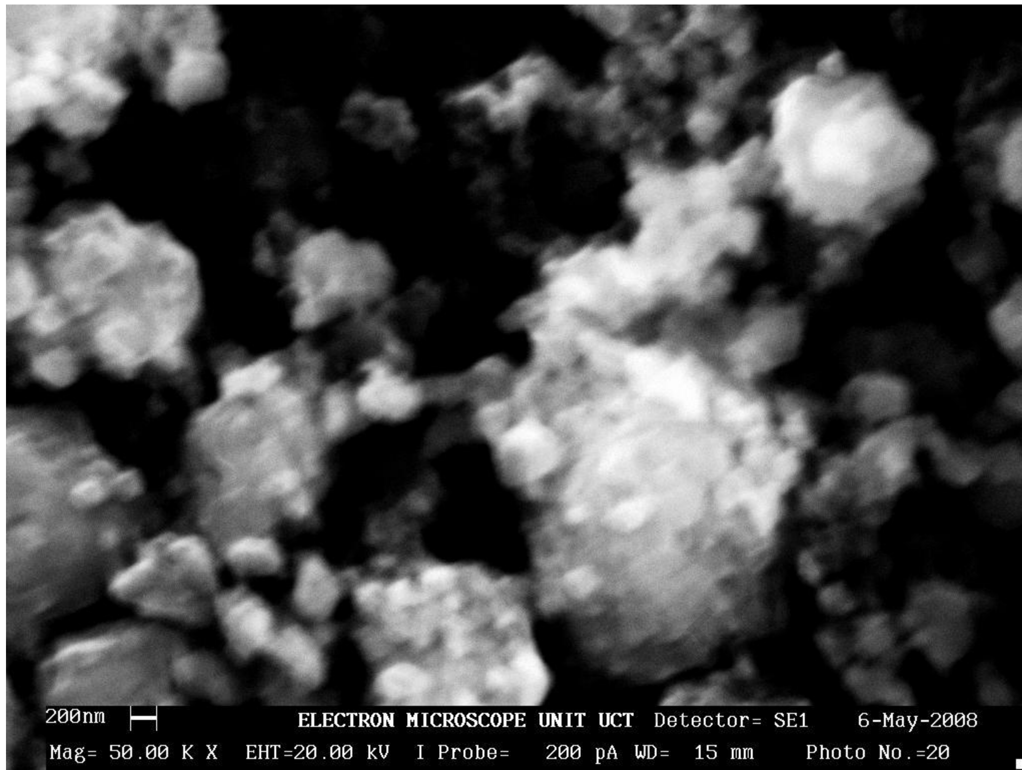

Fig. 2.14: Showing SEM micrographs a pellet formed by compressing nanostructured silicon of (a) $M5$ powder.

University of Cape Town

observed for the other powders P*2 to P*5, indicating that the contamination from the milling medium and atmospheric oxidation due to the milling process is minimal. The observed peaks from copper and aluminum may have resulted from the detector coil and the aluminum sample holder of the instrument, while the source of calcium ($L\alpha1$) is not known.

Fig. 2.16 shows the variations with milling time of the concentration of the above mentioned contaminants estimated from the spectra intensity plots, using a standard software installation for the instrument. From Fig. 2.16 oxygen appears to be the most contaminating element, but this level of oxygen may be associated with an initial wafer surface oxidation rather than oxidation during milling since the oxygen level remains fairly constant through out the period of milling. The other two possible contaminants chromium and iron both have no significant change with milling time.

The metallurgical powder $M3$, examined for the presence of a list of suspected impurities like iron, aluminium sulphur, indium and the like as specified by the manufacturer reveals the presence of this impurities in relatively small amounts compared to silicon as shown in table 2.4. This level of impurities is from the bulk manufacturing process rather than from the milling.

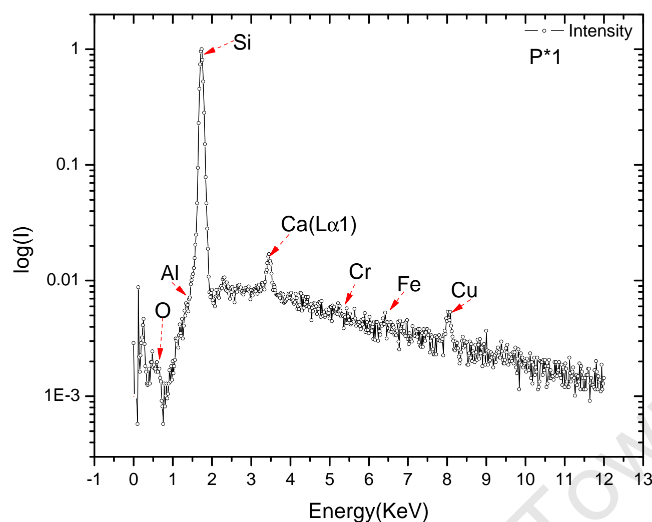

Fig. 2.15: EDX spectra for powder $P^{*}1$ on a semilog scale, showing silicon at $K_{\alpha 1} = 1.739KeV$ as the dominant detectable element. Possible contaminant like oxygen, chromium, and iron at energies indicated by the arrows are relatively insignificant.

University of Cape Town

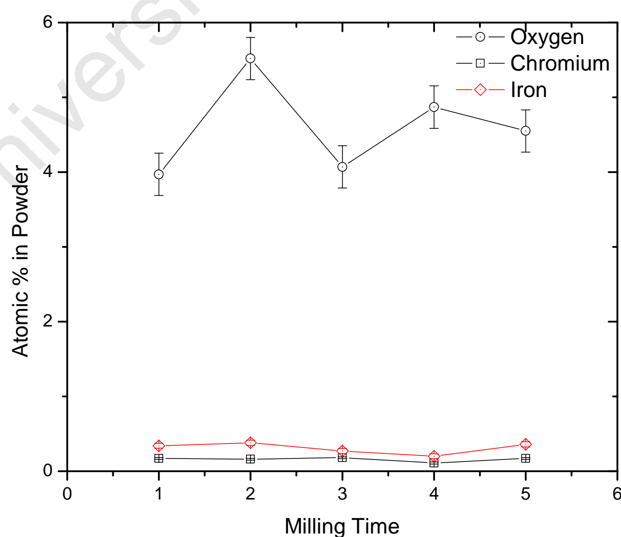

Fig. 2.16: Variation of contaminant level in $at\%$ with milling time for the $P^{*}1$ to $P^{*}5$ silicon powder, Showing a relative constant measured level for all the contaminant with time.

Table 2.4: Table of elemental analysis for Metallurgical silicon $M3$.

Element	Atomic%	Error
Al	1.12	0.05
Si	96.99	0.48
Fe	0.33	0.01
As	0.69	0.02
In	0.22	0.01
Sb	0.14	0.00
S	0.52	0.00

From the above it is reasonable to suggest that the production of silicon powder from single crystalline silicon wafer using an the laboratory disc mill in a top-down nanostructured silicon route, starts with cleavage of the wafer along their preferred orientation followed by a gradual wearing off of the particle surface toward smaller particle size, reaching a fairly constant size distribution after about 3 hours of milling. Further milling only reduces the larger particles to within the range $100-400nm$. While cleavage, and later attrition is true for the wafers, the same may not be the case for the metallurgical silicon. Comparison through observation of the shape of the larger particles from the micrographs Fig. 2.13(c) for $P^{*}3$, and Fig. 2.13(f) for $M3$, shows the presence of sharp edges on the $P^{*}3$ particles while larger $M3$ particles have much rounder features. This suggest that the process of reduction of particle size in the metallurgical powder may be due to attrition alone. However the size distribution after 3 hours of milling is comparable for both starting feedstock. In general production of silicon nanoparticles using this process, irrespective of the type of single crystalline silicon wafer or bulk silicon, should show a continuous reduction of particle size with milling time. The shape and size distribution, as observed for the two main powders after five hours milling of the respective bulk, is comparable to those obtained from high-energy ball milling of silicon single crystals for 50 hours reported by C. Diaz-Guerra et. al. [41]. This suggest that the present method is a fast and efficient method for silicon nanoparticle production from its bulk state.

From this study, it is reasonable to say that the effect of milling time on the contaminant level is negligible. The level of contaminants introduced by milling high grade silicon in an orbital pulverizer for up to five hours is minimal, the detected oxygen level is seen to remain fairly constant for the entire milling period, suggesting minimal silicon oxidation from the process. The impurity level will be further investigated by other methods to be discussed in the following section.

University of Cape Town

2.3.3 Transmission electron microscopy (TEM) and electron diffraction study of silicon nanoparticles

TEM, like SEM uses accelerated electrons, but in this case the image of a specimen is formed from the beam of electrons transmitted through an ultra thin specimen. The electron beam passes through regions with differences in density or chemistry as it traverses the specimen. Thus the transmitted beam contains information about these differences, and this information is used to form an image of the sample [97]. The popularity of the TEM comes from the ability to modify it for other purpose such as in scanning transmission electron microscope (STEM), by the addition of a system that rasters the beam across the sample to form the image. It can also be modified as an analytical TEM by equipping it with detectors that can determine the elemental composition of the specimen by analysing its X-ray spectrum or the energy-loss spectrum of the transmitted electrons [97].

Transmission Electron Microscopy can also be used in diffraction mode to examine the atomic arrangement of a material. For an amorphous material a diffuse diffraction rings are formed as shown in Fig. 2.17(a). The ring separation is related to the average inter-atomic distances in a radial distribution function of atoms [25]. Crystalline materials with periodic atomic arrangement, give scattering at well defined angles defined by Bragg's Law. For polycrystalline materials, diffraction produces a pattern of narrow concentric rings as shown in Fig. 2.17(b). For single crystalline material the diffraction pattern will consist of points spaced at distance inversely proportional to the lattice spacing, aligned in a direction perpendicular to the orientation (hkl) as shown in Fig. 2.17(c) [25].

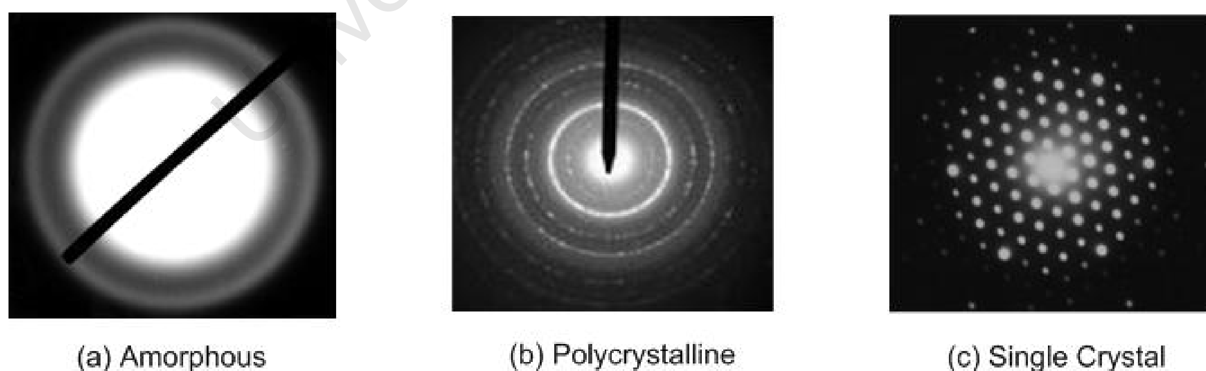

Fig. 2.17: Electron diffraction patterns for: (a) an amorphous, (b) polycrystalline and (c) single crystal materials [25].

To further study the shape, variation of size distribution with milling time, as well as the internal structures of the silicon nanoparticles, TEM was carried out on the different powders. The sample preparation for this TEM studies follows the same procedure to that described

University of Cape Town

for the SEM study. Two drops, from each of the different dispersion was placed with a pipette on holey carbon coated copper TEM grids. The study was carried out using a LEO 912 transmission electron microscope operating at 120 keV. To ensure that enough particles were viewed for particle size distribution analysis, pictures of four different areas of a given sample were taken at the same magnification and later merged at their common boundaries to produce a wide view micrograph. For electron diffraction, selected area diffraction on isolated particles or clusters of particle suspended across the holes in the carbon coated copper grid was carried out.

Fig. 2.18(a)-(e) shows the TEM images of the silicon nanoparticles P^*1 to P^*5 and Fig. 2.18(f) shows the TEM image of $M3$ powder, all at the same magnification. The TEM micrograph for the 1 hour milled powder P^*1 (Fig. 2.18(a)), shows a similar result to the SEM analysis. The powder is composed of large faceted particles of cross section $600nm < d < 1500nm$ and a clustering of relatively smaller particles in the range $60nm < d < 100nm$ with the smallest measured particle being $20nm$, where d is the length of the longest cross section of the particle. A closer look at the larger particles however, shows darker areas either overlaying or embedded in the particle. These may be either small particles, or the result of deformation of the particle giving rise to stacks of planes with orientation different from that of the main particle. Such deformation would introduce a large density of defects within the particles which may act as trap centers hindering the movement of free carriers under electrical bias [41].

University of Cape Town

A comparison of the 1 to 2 hours milled powder as seen in Fig. 2.18(a) and Fig. 2.18(b), shows a clear reduction in the average particle size with milling time. The distribution of particles consists predominantly of smaller and rounder particles, with relatively few larger and faceted ones in both cases. However the 2 hours milled powder is seen to have a much smaller particle population. As the milling time reaches 5 hours, as seen in Fig. 2.18(e), the population of the smaller and spherically shaped particles in the size range of $70nm < d < 200nm$ dominates the size distribution. The $M3$ powder shown in Fig. 2.18(f) also exhibits a distribution of particle sizes similar to that observed for the P^*3 powder.

To accurately determine how the average particle size and hence the particle size distribution varies with milling time, each of the micrograph Fig. 2.18(a)-(e) was analysed using the image processing software Digimizer, version 3.1.2.0 from MedCalc [96]. With a length measurement tool, the longest axis of each clearly identified (having well defined boundaries) particle or cluster was measured. For the purpose of this measurement, in regions where there was no clear boundaries, clusters were taken as a single particles.

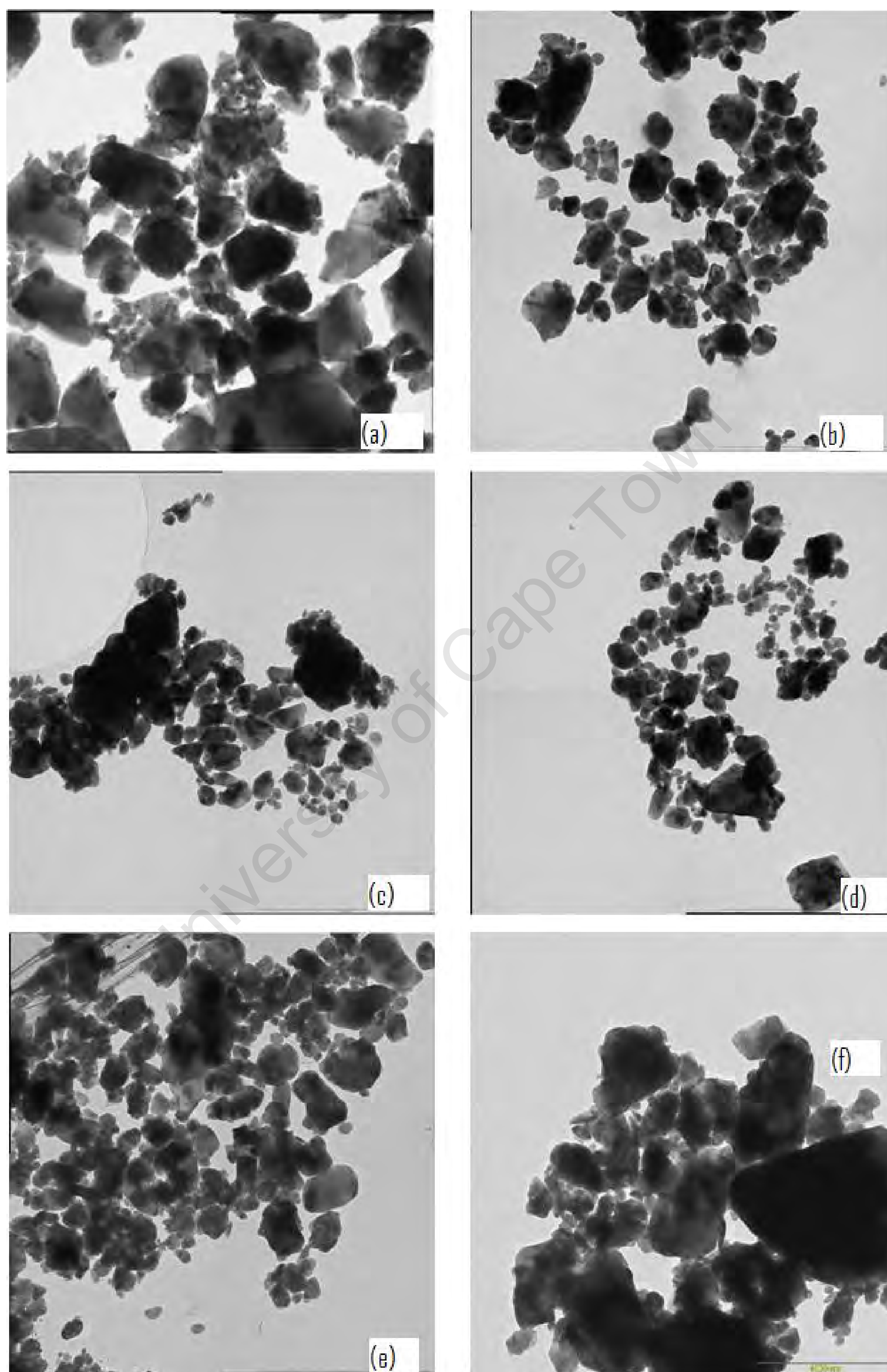

University of Cape Town

Fig. 2.18: TEM micrographs of milled nanostructured silicon powder dispersed in ethanol and then deposited on carbon coated copper grid for (a) $P^{*}1$,(b) $P^{*}2$,(c) $P^{*}3$,(d) $P^{*}4$,(e) $P^{*}5$ and (f) $M3$ powder.

Fig. 2.19 shows the size distribution of the milled silicon particles for P^*1 to P^*5 in Fig. 2.19(a)-(e) and the $M3$ powder in Fig. 2.19(f). The distribution of the measured cross sectional length of the particles can be described by a log-normal function, with a tail observed to decrease with milling time.

$$f(d;\mu,\sigma) = \frac{1}{d\sigma\sqrt{2\pi}} \exp\left(-\frac{[\ln(d)-\mu]^2}{2\sigma^2}\right), \tag{2.8}$$

where $d > 0$ is the cross sectional length of the particle, μ and σ are the logarithmic mean and standard deviation respectively. The fit of equation 2.8 to the size distribution histogram was used to derive the mean particle size for each of the powder.

The centre position of the fitted function, which corresponds to the average cross sectional length, is plotted against milling time in Fig. 2.20. The plot shows that the decrease in average particle size follows a first order exponential reduction pattern with milling time t, and may be represented by

$$d(t) = d(0)\exp\left(-\frac{t}{\tau}\right) + d^*, \tag{2.9}$$

where $d(t)$ describes the particle diameter after milling for a time t, $d(0)$ is the initial particle diameter, τ defines a time constant and d^* is a constant representing the limiting particle diameter after a very long milling time. The fit of equation 2.9 to the data yields $d^* = 126.49$. One can reasonably conclude that with the process used for this work, the average size of particle that can be achieved after long time of milling will be $\approx 126 \pm 6nm$. A similar analysis carried out on the metallurgical silicon (M) powder milled for 3 hours is shown in Fig. 2.19(f). As seen in the plot the particle size distribution can also be represented by a log-normal distribution function, centre at $127.0 \pm 0.6nm$.

For diffraction, isolated particles or clusters overlapping the holes of the carbon coated copper grid were identified, and selected area diffraction carried out with beam energy $120KeV$ and camera length $288mm$. Fig. 2.21(a)-(e) shows the selected area diffraction for regions defined by the circles shown in the insets for the P^*1 to P^*5 powder. As seen from the figure the diffraction patterns are made up of continuous rings containing discrete reflections spots for all the powders. Since the diffraction was carried out on an isolated clearly defined particle, the observed diffraction pattern may be reasonably interpreted as resulting from a polycrystalline particle, suggesting that the particles derived, originally from single crys-

University of Cape Town

talline wafer, had been induced with crystallites oriented in different preferred directions. Electron diffraction experiment on the $M3$ silicon powder (not shown) exhibits similar ring structure typical of polycrystalline silicon like the ones observed for the three hours milled wafer.

Fig. 2.22(a) shows the magnified images of the area isolated for diffraction for sample P^*5 powder. These images show possible crystallite or embedded grains marked with dashed boundaries, suggesting that the milling process had cause a refinement of the microstructure of the starting materials due to high energy induced dislocation of the particles, thus creating grain boundaries around small crystallites. This measurement is in agreement with the X-ray experiment from which crystallite size of $\approx 44nm$ was estimated.

Indexing of the diffraction pattern was carried out using the JECP/PCED Polycrystalline Electron Diffraction software version 8.0 as described in [98]. The first 7 rings of the diffraction pattern was compared with a simulated diffraction ring pattern of polycrystalline silicon in the software. Fig. 2.22(b) shows the identification of the major planes associated with polycrystalline silicon for the P^*5 silicon powder, the absence of diffuse rings structure suggest that amorphorisation of the powder due to the milling process does not occur. This is in agreement with the reported XRD analysis discussed earlier.

University of Cape Town

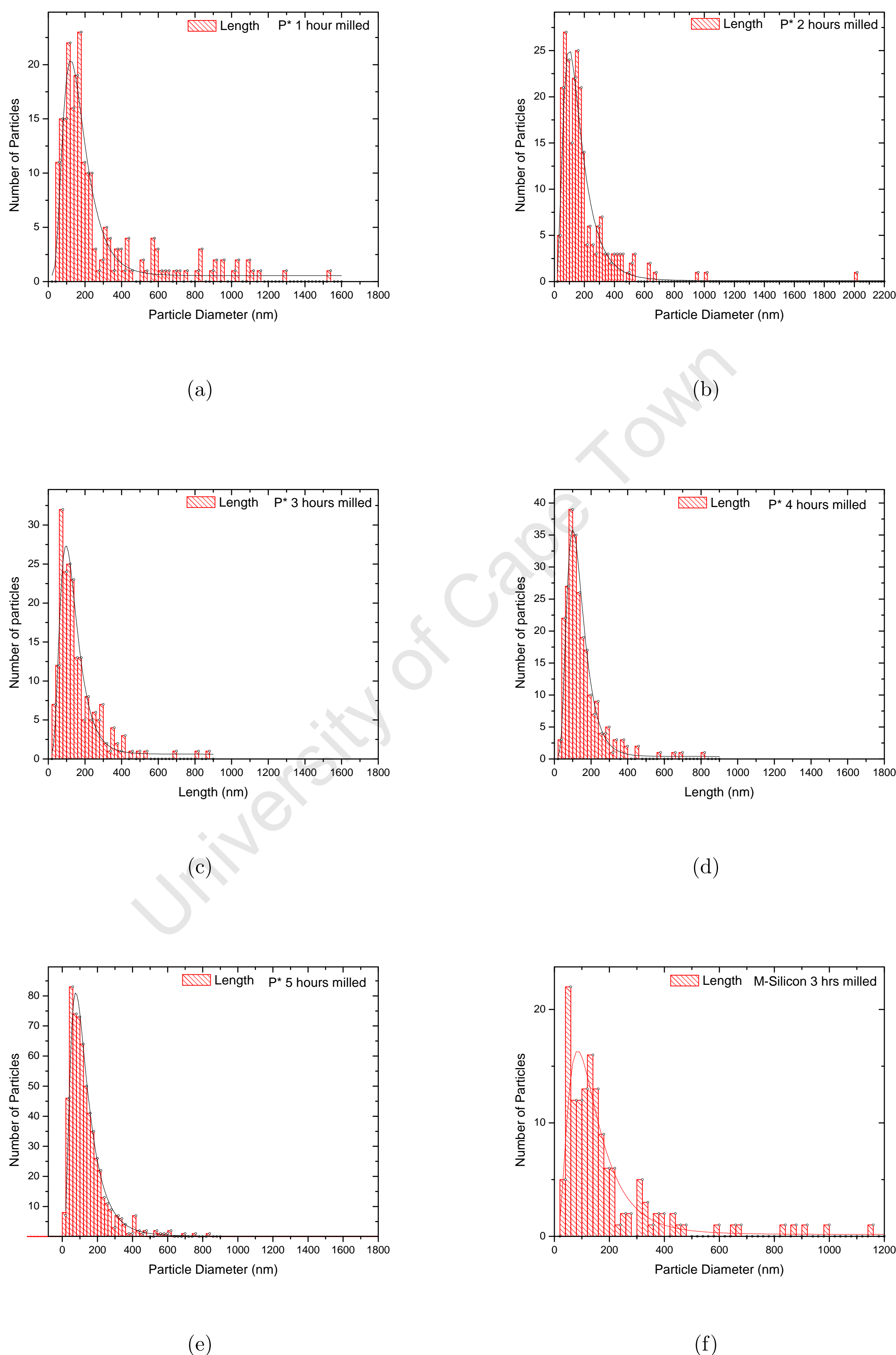

University of Cape Town

Fig. 2.19: Particle size distribution for (a)$P^{*}1$ (b) $P^{*}2$ (c) $P^{*}3$ (d) $P^{*}4$ (e) $P^{*}5$ and (f) $M3$ powders.

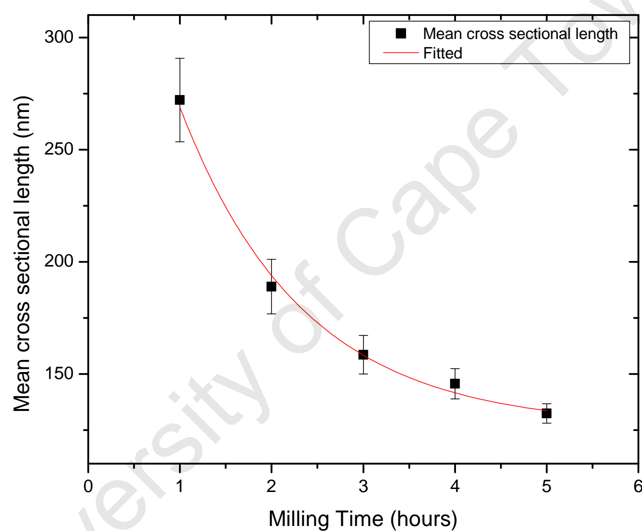

University of Cape Town

Fig. 2.20: Variation of mean particle size X_C from the fitted function with milling time.

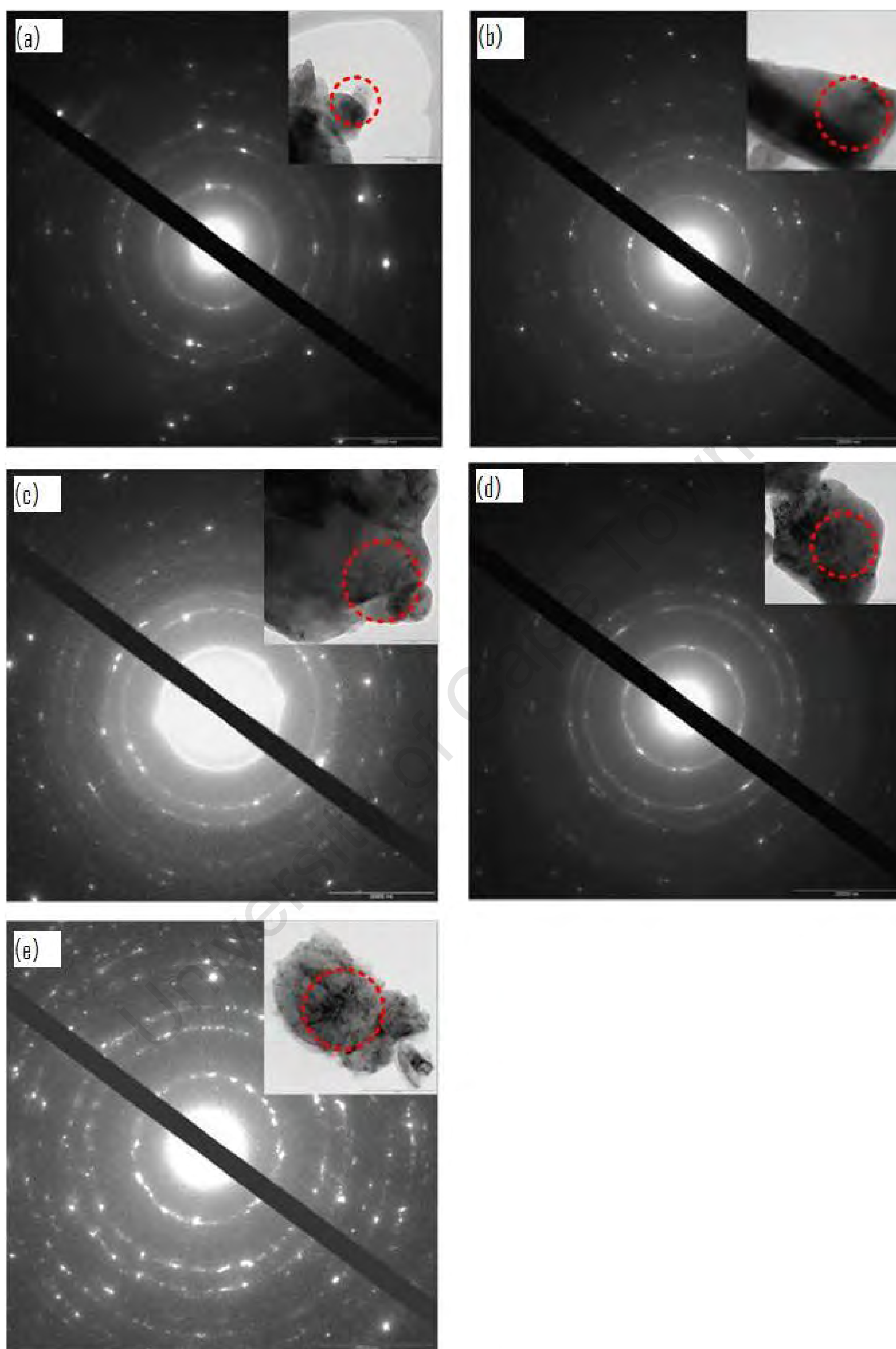

Fig. 2.21: Electron diffraction pattern showing concentric rings in the zero order Laue zone with inset showing the area where the selected area diffraction was carried out for (a)$P^{*}1$ (b) $P^{*}2$ (c) $P^{*}3$ (d) $P^{*}4$ and (e) $P^{*}5$ powders.

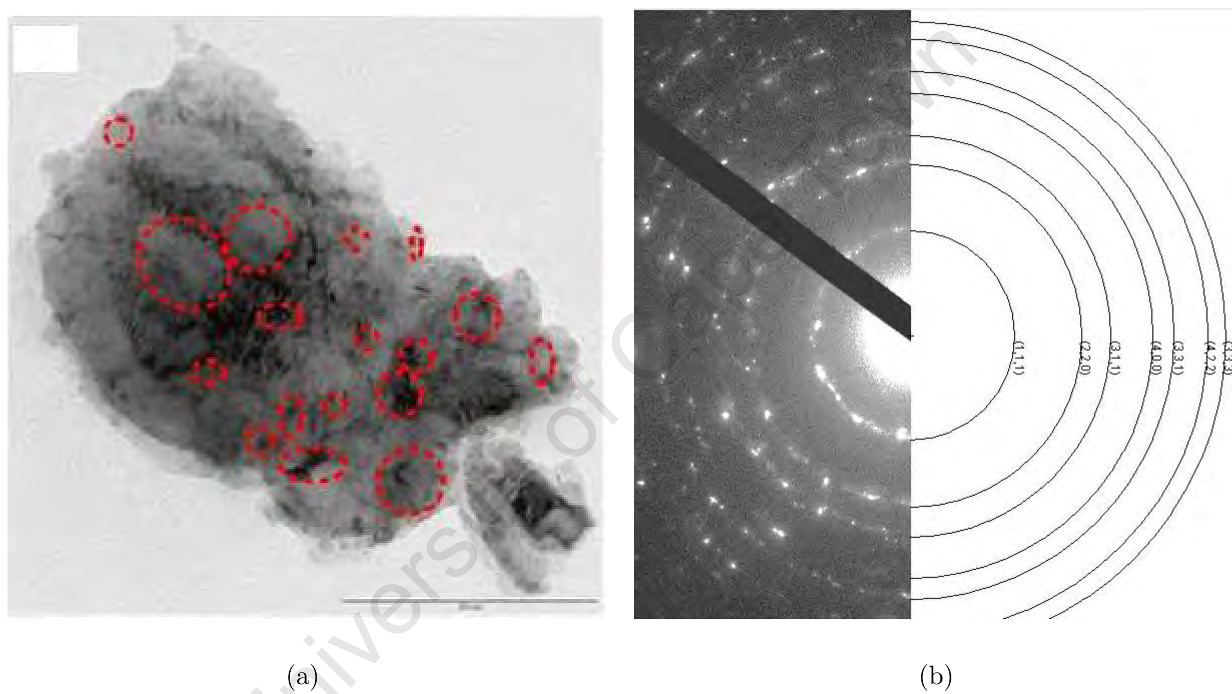

(a) (b)

Fig. 2.22: (a) Shows the magnified image of the area isolated for diffraction for the P*5 powder and (b) Phase identification for $P^{*}5$ silicon powder using JECP/PCED Polycrystalline Electron Diffraction software.

University of Cape Town

2.3.4 Raman spectroscopy study of silicon nanoparticle produced using laboratory disc mill

The technique of mechanical attrition, for the production of the silicon nanoparticles, has been observed to induced heavy plastic deformation. This causes a refinement of the microstructure [41] or distortion of the ordered lattice, possibly leading to a total loss of defined periodicity [73]. The degree of crystallinity of the silicon nanoparticles is an important factor that determines the overall performance of devices made from silicon nanocomposites. A commonly used experimental technique for quantifying crystallinity, is Raman spectroscopy, which is used to study vibrational, rotational, and other low-frequency modes [99]. Raman spectroscopy is a useful tool for examining the crystal structures of different materials and recently it has been employed for determining the micro structure of nanoparticles [100, 101, 102]. It relies on inelastic scattering of monochromatic light, usually from a laser in the visible, near infrared, or near ultraviolet range. The laser light interacts with phonons or other excitations in the system, resulting in the energy of the emitted photons being shifted up or down. The shift in energy gives information about the phonon modes in the system [99].

Fig. 2.23 shows the two basic Raman scattering mechanisms, that may result when light shines upon a molecule and interacts with the electron cloud of a bond. In **Stokes scattering**, an electron may be excited from the ground state to a virtual energy state, and then relax into a vibrational excited state, absorbing a phonon. If however the system was already in an elevated vibrational energy state, **anti-Stokes scattering** occurs with the emission of a phonon. The amount of deformation of the electronic cloud around the atom of a material is related to the polarizability, which determines the intensity of the scattering, while the Raman shift is equal to the vibrational level that is involved [103, 104].

Raman spectroscopy measurement using a DeltaNu (Advantage 532) Raman spectrometer was carried out on the milled silicon powders $P^{*}1$ to $P^{*}5$ as well as powders $M5$ with the aim of examining the effect of high energy milling on the Raman spectra of the powders when compared to the spectra from their respective bulk (feedstock). The spectrometer uses a $532nm$ (green) solid state laser with a peak power of $200mW$ with a $35\mu m$ diameter focused beam. The principle of operation of this instrument involves a direct focusing of the laser beam on the sample surface and collection of the shifted Raman light through a prism onto a multi-pixel CCD array. The array bins the intensity of light at each wavelength and this is recorded on a computer using the Nuscope software installation for the instrument [105]. The measurement procedure involves a recording of a reference spectrum with the laser off

University of Cape Town

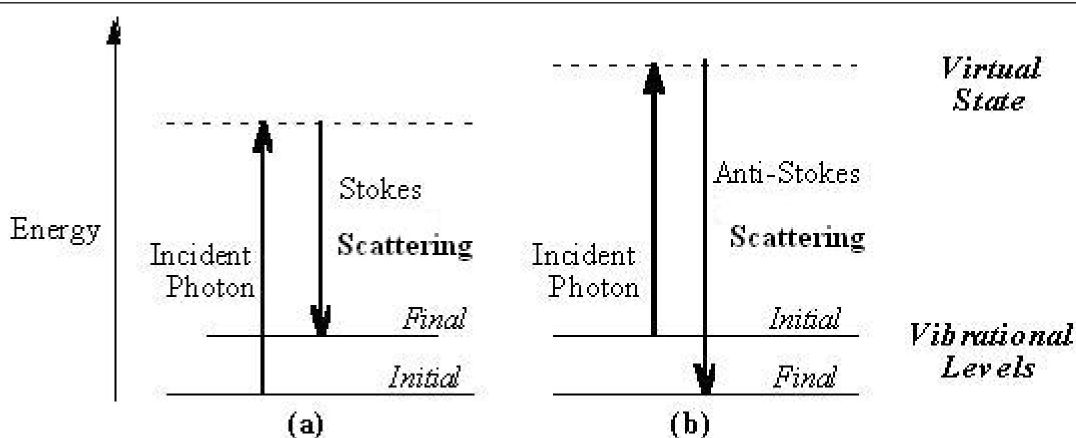

Fig. 2.23: Energy level diagram for Raman scattering (a) Stokes Raman scattering (b) anti-Stokes scattering [104].

University of Cape Town

for a given integration time. This record is then subtracted from the actual measurement with the laser beam on for the same integration time automatically by the software. For the purpose of this measurement, the different powders were filled into separate small plastic cups. With the aid of an attached video microscope, the surface of the sample was brought into focus of the multi-pixel CCD array. The measurement time for both the background and sample measurement was set at 60 seconds. Using Origin Software the method described by [73] in which a lorentz/gaussian function may be fitted to the experimental data to obtained the individual peak centre and full width at half maximum (FWHM) was followed.

Fig. 2.24 shows the plot of the intensities in arbitrary units, of the Raman spectroscopy measurement from the powders P^*1 to P^*5 , as well as from a wafer in the same batch as that of the milled powders. From the plot, three main peaks indicated by the broken lines on the plot can be clearly identified. The first two prominent peaks at $520cm^{-1}$ and $880 - 1000cm^{-1}$ may be associated with crystalline silicon, having a face centered cubic (fcc) diamond structure [73], and to the symmetric and antisymmetric stretching vibrational modes of the oxide phase of silicon respectively [106]. Similarly, the peak at about $1396 - 1414cm^{-1}$ is also attributed to the stretching vibrations of a double bond oxide phase [107]. It is interesting to note from this plot that almost all peaks present in the spectra of the milled powders is also present in the spectrum from the silicon wafer (feedstock). This suggests that the milling process had not introduced a marked change in structure or composition of the silicon.

Of particular interest is the effect of milling time on the crystallinity of the silicon. Fig. 2.25 shows the Raman spectra covering the amorphous ($480cm^{-1}$) as well as the crystalline ($520cm^{-1}$) regions for the P^*1 to P^*5 powders compared with the feedstock. From the plot,

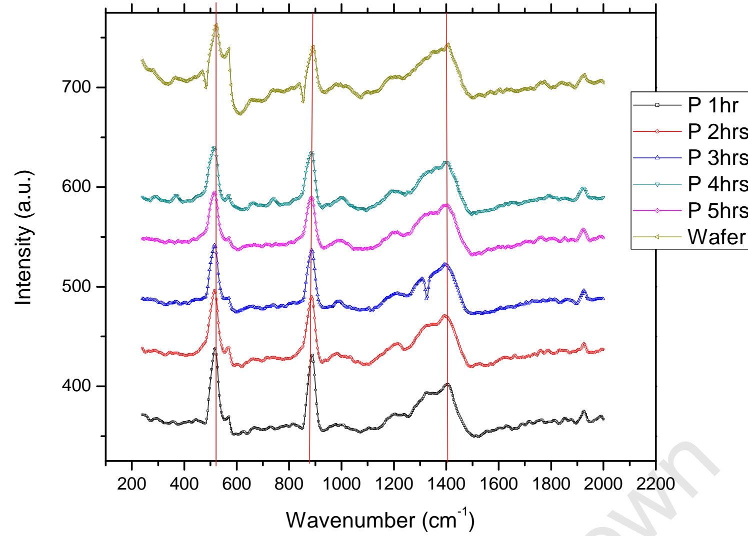

Fig. 2.24: Raman spectra from powder $P^{*}1$ to $P^{*}5$ and also from a p-type wafer taken from the same batch as the feedstock.

University of Cape Town

the position of the peak attributed to crystalline silicon is observed to shift toward the lower wavenumber region as milling time increases. By fitting a gaussian function to each of the peak in this region using Origin software, the peak centre and full width at half maximum (FWHM) were determined. The peak position for the wafer, taken as reference for this study was $521.43cm^{-1}$. Fig. 2.26 show the shift position with milling time.

In a typical Raman spectra for silicon, the amorphous silicon phase produces a broad peak centered at $470-480cm^{-1}$ [73], and the presence of nanocrystalline silicon phase results in an asymmetric peak centered at $520cm^{-1}$[101]. In the spectra of the different P* powders, only the $521\pm10cm^{-1}$ peak corresponding to the optical-phonon frequency at the Brillouin-Zone of silicon was clearly identified. The absence of a $470-480cm^{-1}$ peak shows that the milling process applied in this work introduces no amorphorisation of the structure. The broadening of the observed $521\pm10cm^{-1}$ peaks with milling time and the asymmetric about the central peak position for each milling time is a proof of the presence of nanometer range crystallite in the powders. A similar frequency down-shift and broadening of the $520\pm2cm^{-1}$ for silicon has been reported by many worker [108, 109, 110, 111]. This Raman scattering line shift and shape broadening has been related with the crystallite size reduction. In particular, decreasing crystallite size of nanocrystalline silicon below about $10nm$ has been explained in term of a phonon confinement model [100].

Examination of the Raman spectra from bulk metallurgical silicon and the $M5$ silicon pow-

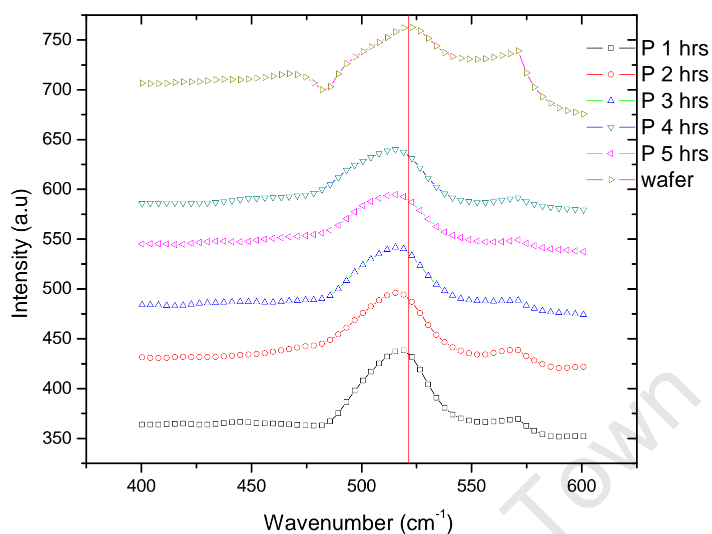

Fig. 2.25: A comparison of the Raman spectra from powder $P^{*}1$ to $P^{*}5$ with that from the feedstock in the regions covering the amorphous ($480cm^{-1}$) as well as the crystalline ($520cm^{-1}$) phase.

University of Cape Town

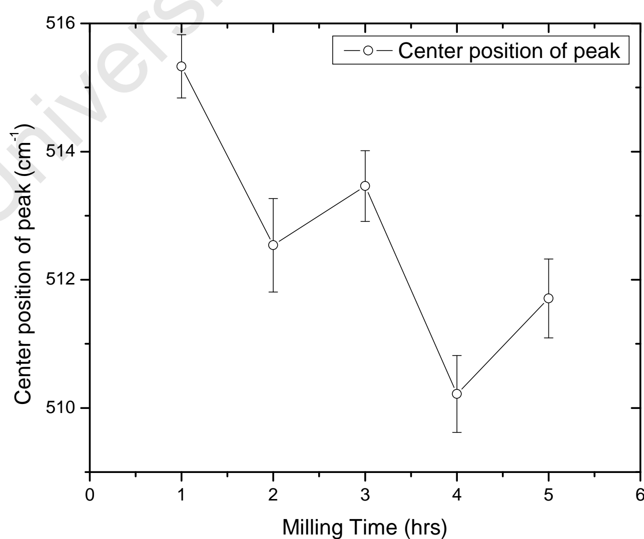

Fig. 2.26: The shift of the $521cm^{-1}$ peak position for the P* powder with milling time.

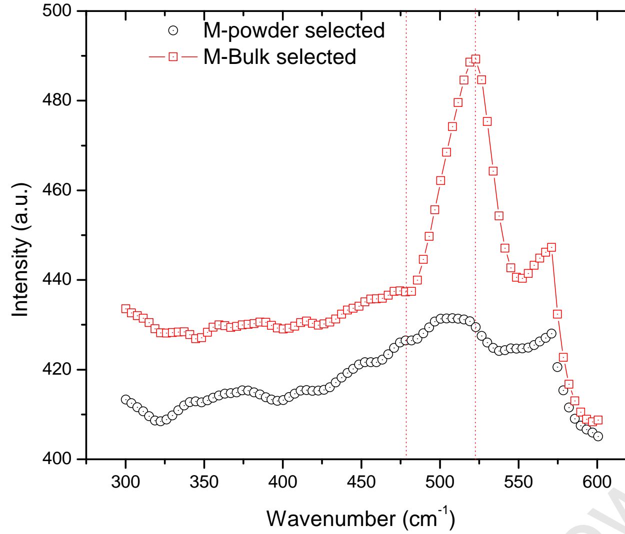

Fig. 2.27: Showing a comparison of the Raman spectrum from powder $M^{*}5$ with that from the feedstock in the regions covering the amorphous ($480cm^{-1}$) as well as the crystalline ($520cm^{-1}$) phase.

der, shows a similar pattern as those for the p-type powder. The three major peaks described above were also seen in the metallurgical samples. A comparison of the bulk metallurgical feedstock with the $M5$ powder in the regions defined by the crystalline $520 \pm 2cm^{-1}$ and the amorphous phase $470 - 480cm^{-1}$, shown in Fig. 2.27, reveals a marked shift in the central peak position from $518.32 \pm 0.32cm^{-1}$ in the bulk metallurgical silicon to $507.78 \pm 0.94cm^{-1}$ for the $M5$ metallurgical silicon powder. This shift of about $10cm^{-1}$ is comparable to the peak shift observed for the milled wafer. A broadening of the FWHM from $28.74 \pm 0.80cm^{-1}$ in the bulk metallurgical silicon to $38.46 \pm 3.11cm^{-1}$ for the $M5$ powder was also observed.

University of Cape Town

Of interest in the comparison of the bulk and the milled metallurgical Silicon in the region $470 - 480cm^{-1}$ representing the phase due to amorphous silicon. Fig. 2.28 shows a pronounced amorphous peak at about $475cm^{-1}$ in the $M5$ silicon powder when compared to the small indication in the bulk metallurgical silicon which could not be fitted as shown in Fig. 2.29. This shows that the metallurgical silicon bulk may contain the presence of a small fraction amorphous phase which is propagated by induced plastic deformation resulting from the milling process. To estimate the crystalline fraction for the $M5$ milled silicon powder from the gaussian fit to the spectral, the following equation was used [112]

$$X_c = \frac{I_c}{I_c + \gamma I_a}. \tag{2.10}$$

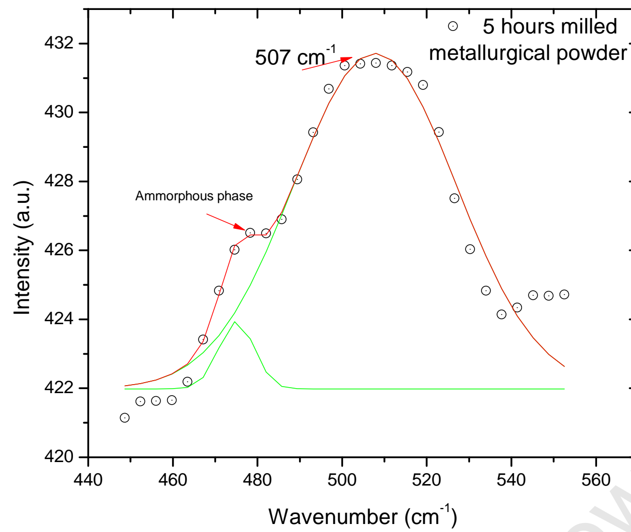

Fig. 2.28: Fitting a gaussian function to the spectral region defined by crystalline $520 \pm 2cm^{-1}$ and the amorphous region $470 - 480cm^{-1}$ for the $M5$ milled powder. The pronounced peak at position $475cm^{-1}$ suggest the presence of amorphous phase.

In this equation I_a and I_c are the amorphous and crystalline areas of the de-convoluted Raman spectra, and $\gamma = 0.8$ is a correction factor due to the different scattering cross sections of the amorphous and crystalline phases [112]. The calculated crystalline fraction for the $M5$ milled metallurgical silicon powder is $X_c = 96.61\%$. This level of crystallinity is very high, suggesting that the induced amorphorisation on the metallurgical silicon using the milling process for 5 hours is very small, and the consequence on the electrical property may be negligible.

University of Cape Town

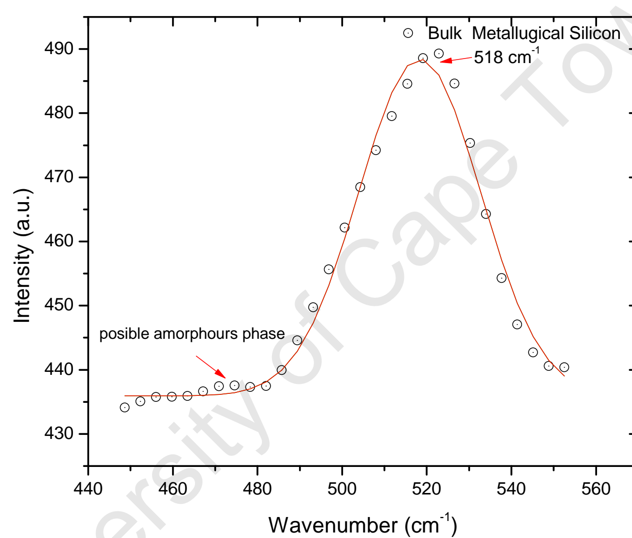

University of Cape Town

Fig. 2.29: Fitting a gaussian function to the spectral region defined by crystalline $520 \pm 2cm^{-1}$ for the bulk metallurgical silicon. The amorphous region $470 - 480cm^{-1}$ in this case is not pronounced peak as a fit to this region does not yield a reasonable result.

3. Functional Nanocomposite of Silicon

Nanocomposites are nanostructured materials composed of a combination of a nanoscale phase with a macroscopic material. In general, nanocomposites involve the inclusion of a nano or molecular domain sized filler into organic polymer, metal or ceramic matrix materials [16]. As mentioned in chapter 1, polymer nanocomposites have been attracting a lot of attention because these materials are novel alternatives to traditional composites and bulk materials in many applications, due to the multifunctional properties associated with the unique structure and size dependent properties of the embedded nanoscale fillers. The advances in synthetic techniques and the ability to readily characterize such materials are other reasons for the present interest [113]. Inclusion of semiconductor nanoparticles, for example silicon, in a polymeric matrix, will result in an active nanocomposite whose electronic properties can be tuned by varying the proportion of filler in the matrix. Semiconductor inks produced with silicon nanoparticles may be prepared for screen printing and inkjet printing. To obtain high efficiency for such systems, it is necessary to have an interpenetrating network of electron conducting or hole conducting components within the device to supply a free path for charge carriers [114].

For the reason that the properties of a nanocomposite may depend on its structure and morphology, many methods used primarily for study of nanoparticles have been adapted to study the different types of composites formed by their inclusion in polymer matrix. Apart from measurement of nanocomposite layer thickness, usually with a profilometer [115], other properties of interest usually include morphology, usually investigated with optical microscopy, scanning electron microscopy (SEM) and transmission electron microscopy (TEM). X-ray scattering is a common technique used to probe the structure of nanocomposites. It is used to measure characteristics distances in the composite nanostructure. Typical X-ray techniques employed for such characterisation include small angle X-ray scattering (SAXS) and X-ray diffraction to study particle size, correlation distances, and atomic spacing respectively [116].

This part of the research builds on previous studies of the synthesis and characterisation of silicon nanoparticles produced via mechanical attrition, by using the particles as fillers in nanocomposite structures. The morphology, structural and fractal properties of silicon nanocomposite layers produced from inks formed by the inclusion of the milled silicon powder

University of Cape Town

in four types of polymeric binders will be presented. The study comprises microscopic observation, using SEM, of the printed nanocomposite layer, and analysis of results from small angle X-ray scattering (SAXS) experiment carried out on different nanocomposite layers, printed on flexible plastic substrates.

3.1 Nanocomposites: an overview

A general classification of nanocomposites is based on the constituent materials and compatibility (adhesion) of the nanoparticles in a polymer matrix [117]. Another method of classification relates to their microstructures. Further classifications of nanocomposites are based on their material function, physical and chemical differences and formation [118]. Classification of nanocomposites based on functionality aims to exploit the following: (a) magnetic, (b) ferroelectric, (c) superconducting/ferroelectric, (d) dielectric, (e) conducting and semiconducting properties for useful applications [118].

A variety of applications can be considered with the multifunctional diversity which nanocomposites can offer. Depending on the application, one must determine the type of nanoparticles, the dispersion type and concentration needed to provide the desired effect [119]. The inclusion of silicon nanoparticles in polymeric binders has resulted in a new class of nanocomposites aimed at annexing the enhanced electronic properties exhibited by nanostructured silicon. The production of such nanocomposites with well-defined and well-reproducible properties depends largely on control over the particle size distribution, and particle-interface interactions in the chosen polymer matrix [120, 121].

Direct dispersion of electrically active silicon nanoparticles in a solution of insulating or polymeric binder followed by polymerisation for example, may result in either a randomly dispersed or ordered dispersion in the matrix. For example, direct dispersion of hydrophilic inorganic particles like silicon particles into hydrophobic polymers (e.g., polystyrene or polypropylene) may lead to phase separation or agglomeration of particles, resulting in poor mechanical, optical, and electrical properties [122]. For such systems the properties of the nanocomposite is dominated by the matrix properties. In some cases, the particles may form randomly distributed clusters and super-clusters in the matrix, which are direct consequences of the nanoparticles themselves [120] as shown in Fig. 3.1(a). In both cases the structure of the nanocomposites will depend largely on the particle-interface interactions in the chosen polymer matrix, as explained earlier, and on the production process [120, 122].

University of Cape Town

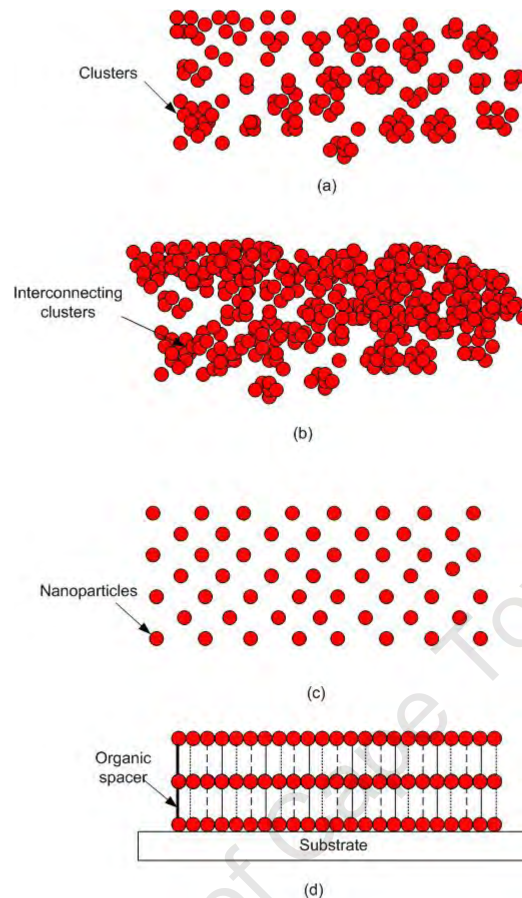

Fig. 3.1: Showing four major classes of nanocomposite that may result from direct dispersion of nanoparticles into a polymeric binder. (a) Shows a disordered nanocomposite structure, (b) disordered but interconnected nanocomposite structure (c) ordered nanocomposite structure (d) an ordered nanocomposite resulting in a 1-D superlattice. Adapted partly from [120].

University of Cape Town

For electrically active composites, the conducting nanoparticles or clusters must be distributed in the matrix such that the particle properties dominate, while retaining much of the properties that make the insulators useful for structural support. The proportion of filler for which the properties of the nanocomposite is dominated by that of the embedded filler is referred to as the percolation threshold (ρ_0). At this point, as shown in Fig. 3.1(b), the particles or clusters make physical interconnections, resulting in a path for transport of electrical charge for example.

The dispersion of a higher concentration ($\rho > \rho_0$) of the electrically active silicon nanoparticle in a given polymer matrix, will further reduce interparticle spacing, and thus increase interparticle contact for improved conductivity. The reduced binding strength resulting from the small proportion of binder may, however, void the intended performance of the composite due to lack of structural support. Thus an optimum ratio that allows for maximum induced

electronic properties without great loss in the binding strength of the matrix medium (insulator) is desired [117].

In some cases an ordered nanocomposite structure is desired. This is usually formed from an homogeneous distribution of the filler in the organic matrix, such that the fillers are arranged in well defined pattern as shown in Fig. 3.1(c). They may occur either in 1, 2 or 3 dimensions, or arranged such that planes formed by the fillers are separated by the polymer and are ordered in 3 dimension in the matrix resulting in a superlattice as shown in Fig. 3.1(d). Ordered arrays of nanocrystals, could be thought of as arrays of SETs (single-electron transistors), with electrostatic interaction between neighboring SETs separated by suitable insulating spacers. An electric field applied in one direction polarizes the strings into either the 0 or the 1 state [120]. One major reason for desiring an ordered nanocomposite structures, is that such interaction between nanocrystals could be well predictable, and any exhibition of novel properties arising out of such interactions could be predetermined. Many applications in photonics and electronics in general would require such ordered nanostructured properties.

3.2 Structural characterisation of nanocomposites using SAXS

The size, shape and clustering of nanoparticles in the nanocomposite are of fundamental interest to understand the microstructure of such a heterogeneous or composite material. When the contrast is sufficient, i.e. there is a clear difference in electronic density between the embedded particles and the matrix, small angle X-ray scattering gives valuable information about the structure of the composite. Apart from the size, shape and size distribution of scatterers, SAXS is also sensitive to the spatial fluctuation of electron density between the scatterer and the medium around it, but not on the degree of crystallization [123].

The SAXS intensity is determined experimentally as a function of the scattering vector q, given by $q = 4\pi \sin(\theta/2)/\lambda$. Where λ is the wavelength of the X-ray beam and θ is the scattering angle [124]. In general the SAXS intensity can be represented as [125]

$$I(q) = N_p(1/q)n_e^2(1/q), \tag{3.1}$$

where $N_p(1/q)$ is the number of scattering elements in an irradiated volume and $n_e^2(1/q)$ is the square of number of electrons in the scattering volume.

University of Cape Town

Two main features can be observed from the scattering pattern in the small angle regime. First, a typical plot of $log(I(q))$ versus $log(q)$ results in a power-law decay, and secondly this power-law decay begins and ends with an exponential regime that appears as knee or inflection reflecting a preferred size described by $r = 1/q$ [125]. Two basic theories exist for the analysis of the dependence of scattering intensity $I(q)$ on scattering vector q, usually derived from a SAXS experiment. They are namely Porod's law, for regions where $q > 1/r$, and Guinier's Law for regions where $q \leq 1/r$. An approach described as the unified Guinier/Power-law is a combination of the two basic theories. The different methods are described in detail below.

- The derivation of Porod's law, which assumes a well-defined smooth surface of particles, is achieved by decomposing the surfaces into spherical scattering elements that bisect the particle/matrix interface. In such systems, the number of such spheres is proportional to the area of the particle divided by the area presented by a scattering element r^2 or $1/q^2$, while the number of electrons per particle is proportional to r^3 or $1/q^3$. Applying equation 3.1 for this case, with $N_p(1/q) = Sq^2$ and $n_e^2(1/q) = 1/q^3$, the expression for Porod's law is given by [124]

$$I(q) = \frac{2\pi\Delta\rho^2 S}{q^4} \qquad (q \to \infty), \tag{3.2}$$

where $\Delta\rho$ is the electron density difference between the particulate domain and the matrix material, and S is the surface area of the interface between the two phases, usually defined for a q-range such that $\xi \gg q^{-1} \gg a_1$, where ξ is a characteristic length of the composite structure, and a_1 is the size of the primary particles composing the structure. Equation 3.2 is valid for any system of regular structures, including voids and other internal surfaces, as well as densely packed systems, and not just for isolated spheres [126]. A common approach in the analysis of SAXS patterns using the Porod law involves using the intensity $I(q)$ as a function of the wave vector q in the power-law region, and can be described by [127, 128]

$$I(q) \propto q^{-\alpha}. \tag{3.3}$$

The value of α derived from a plot of $log(I(q))$ versus $log(q)$ allows for the determination of the fractal-dimension which includes deduction of information about the fractal structure of the samples or interface formation.

Depending on the value of α, three general fractal categories can be distinguished. The

University of Cape Town

derived value gives information about the microscopic structure of the nanocomposite, whether it is organised as mass fractal, surface fractal or contains a diffused interface.

When $1 < \alpha < 3$ the scattering can be associated with mass fractal materials (whose mass and surface are characterised by fractal properties [129, 128]). Then $\alpha = D_m$, where D_m is the mass fractal dimension [130, 124]. The SAXS intensity from a surface fractal structure where only the surface are characterised by fractal properties [129], also follows a similar power-law dependence on q. However, in this case the exponent α assumes values in the range $3 < a < 4$, and is related to the surface fractal dimension D_s by [130]

$$\alpha = 6 - D_s. \tag{3.4}$$

The special case where $\alpha = 4$ corresponds to Porod's law, and $D_s = 2$ representing a smooth scattering surface. The size corresponding to the characteristic length ξ is the size of the fractal aggregate L_m [127], which is composed of particles of radius r_o deduced from knowledge of a_1. These values can be calculated from the upper (q_{max}) and the lower limit (q_{mim}) of the power-law regime given by [127]

$$r_o = \frac{\pi}{q_{max}}, \tag{3.5}$$

and

$$L_m = \frac{2\pi}{q_{min}}. \tag{3.6}$$

However for some systems, power laws with exponents greater than four can result from a higher reduction in intensity at high scattering vector due to one of two factors [126]. One is the influence of a gradient in the electron density at a diffuse interface [131, 132], and the other is a polydisperse size distribution of particles [128]. Both effects may also be present in small angle scattering from systems with fractal scaling, but are not immediately apparent. The scattering intensity from this structure can be modeled with

$$I(q) \propto q^{-\alpha} \quad \alpha = 4 + \beta, \tag{3.7}$$

where the Schmidt exponent β is a measure of the concentration decay of the diffused interface [125, 128].

Figure 3.2 illustrates a typical analysis from a plot of $log(I(q))$ versus $log(q)$ using the Porod law with information on the nature of the system's structure and size distribution. The plot shows three separate fractal regions and the determination of the fractal dimensions from point of change of the different slope regions from one value to the

University of Cape Town

other as indicated with the exponent of the power law region [133].

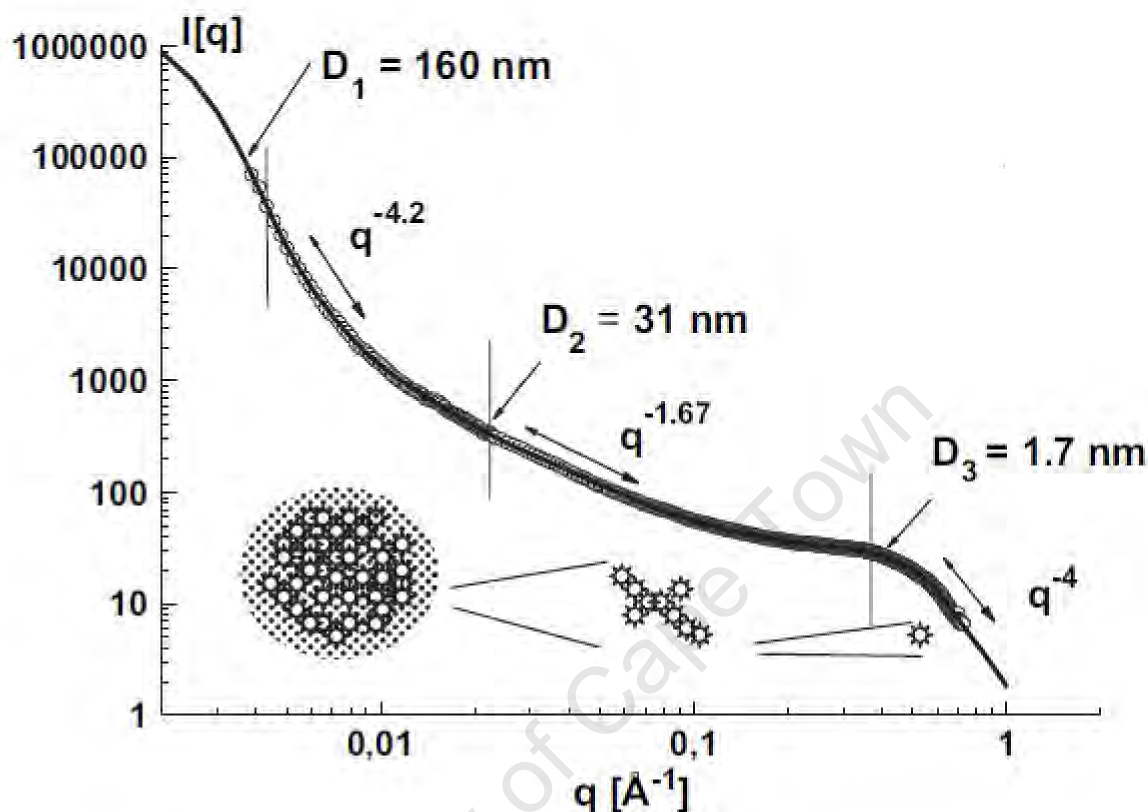

Fig. 3.2: A typical analysis from a plot $log(I(q))$ versus $log(q)$ using the Porod's law. The plot shows three separate fractal regions and the determination of the fractal dimensions from point of change of the different slope regions [133].

University of Cape Town

A further description of the aggregate geometry is provided for in the Porod analysis which is found experimentally for values of q such that $qR_g \geq 1 \geq qa_0$ for an ideal two phase system [134]. To determine the fractal behaviour and estimate the dimension of aggregates as well as the average size of individual particles constituting the aggregate, a plot of $log(I(q))$ versus $log(q)$ is employed. From such a plot, known as the Porod plot, a power law dependence of I on q is expected and the range of a fractal behaviour is dependent on the scattering length of self similar structure [134]. Estimation of the aggregate size or particle size as the case may be, is determined from the position of a knee or inflexion point, as illustrated in Fig. 3.2.

For a non-ideal two phase system, where there is a diffuse interface, there is a negative deviation from the Porod's law, which for a SAXS intensity collimated by slit system,

can be represented by [135]

$$\ln[I(q)q^3] = \ln K - \sigma^2 q^2, \tag{3.8}$$

where σ is a parameter related to the interface thickness. In other cases where the electronic density within any phase is non-uniform, for example electron density fluctuation within scatterers, a positive deviation from the Porod's law is always obtained. This case can be represented by [135, 136]

$$\ln[I(q)q^3] = \ln K + \sigma^2 q^2, \tag{3.9}$$

where σ in this case relates to the characteristic size of the electron density inhomogeneity [135].

- Guinier's Law assumes an isotropic system for which scattering from a particle will generally involve interference from waves coming out from two points separated by a distance $r = 1/q$. For a given set of points, the scattering intensity will involve averaging over these points, and also over the vectors r, similar to the determination of the moment of inertia. In this case when the electronic density is used as the weighting factor rather than the mass density, then the moment of inertia is referred to as the radius of gyration [125]. The Guinier law relates the SAXS intensity from a number of independent identical scatterers, which is given by [130]

$$I(q) = N(\Delta\rho)^2 v^2 \exp\left(\frac{-R_G^2 q^2}{3}\right), \tag{3.10}$$

where R_G is the gyration radius of the particles of volume v and $\Delta\rho$ is the difference in electronic density between the particles and the matrix. Guinier's law is valid for small **q** values so that $qR_G < 1$. Average values for R_G may be obtained usually from a plot of $log(I(q))$ versus q^2, known as the Guinier plot [130]. This plot will yield a straight line, and the q range covered in such plot will depends largely on the size and shape of the particles or clusters. From the slope of this straight line the radius of gyration R_g is determined.

Assuming a composite system with embedded homogeneous and spherical nanoparticles, the radius of gyration R_g is related to the radius of the particle R by the

University of Cape Town

expression.

$$R_g = \sqrt{\frac{3}{5}} R = 0.775R. \tag{3.11}$$

For highly polydisperse system (one in which the cluster mass is not uniform but varies over a size distribution), the q range over which the Guinier law holds is very small, and the plot in this case yields an average radius of gyration, far from the arithmetic average, with a bias toward the largest particle. In general R_g for a dilute solution reduces to the radius of gyration of scatterers, while for interacting or overlapped systems R_g is a correlation length [134].

The extrapolated intensity $I(0)$ is proportional to the average volume occupied by the cluster which is also dependent on the size and shape of the particles. The definition of the Guinier regime, a range for which the Guinier approximation is generally acceptable is given by $qR_g \leq 1$ [134].

- Guinier/Power-law: For a complex system, displaying morphological features covering a wide length scale, often a combination of absolute intensity measurement from ultra-low angle scattering, SAXS, and in some cases, small angle light scattering are employed. This method is able to resolve length scale features ranging from few Angstroms to hundreds of micrometres. For such measurements analysis based on the Porod and Guinier laws to independently give complete characteristics of the system becomes difficult [137]. Beaucage [137, 138] describes how a combined Guinier, and structural limited power-law may be applied to a complex system. The combined SAXS intensity for such a system may be represented as [137]

$$I(q) \approx G \exp\left(\frac{-q^2 R_g^2}{3}\right) + B \left[\frac{\left(erf\left(qR_g/\sqrt{6}\right)\right)^3}{q}\right]^{\alpha}, \tag{3.12}$$

where G is the Guinier prefactor, and B is a prefactor associated with the power law [137]. The fractal dimension can be estimated by fitting the above unified model to $I(q)$. The Porod law scattering indicated by $\alpha = 4$ defines scattering from sharp interfaces and $B = 2\pi\rho^2 S$. For a surface fractal $B = 4\pi^2\rho^2 R_g^{(6-\alpha)}\Gamma((\alpha-1)\sin(\pi(\alpha-3)/2)(\alpha-3)$, where R_g is the large particle radius of gyration and Γ is the gamma function [137, 138].

University of Cape Town

3.3 Experimental Methods

3.3.1 Silicon nanocomposite layer production and characterisation

Generally functional nanocomposites are formed into layers, either as a thin-film consisting of more than one phase, in which the dimensions of at least one of the phases is in the nanometer range [117], or as thick films in which a compact layer usually some microns thick is produced from an interconnected network of essentially free nanoparticles, held together by a polymeric binder [34]. Depending on the application as mentioned earlier, the choice of polymer matrix, the concentration of the fillers in the matrix, substrate material, and also the production method are important factors. Unlike the disperse composites being investigated for the optical properties of their localized states, there should be a direct semiconducting path through the layer, with the semiconducting behaviour provided by the particles themselves and not the matrix [34]. For this work, nanocomposites of silicon were produced by printing on plastic substrates. Two main categories of samples were produced for the morphological characteriusation using SEM and structural characterisation using SAXS as described below.

University of Cape Town

- Sample preparation and structural study using SAXS:

  The nanocomposites used for this study were prepared from ink formed by inclusion of nanopowder from P type wafer milled for one hour, and metallurgical grade silicon milled for 3 hours as described in chapter 2 in polymeric binder. Two classes of binder were used to form the nanocomposite inks: (1) soluble polymers, and (2) polymerizing monomers. Two materials from each class were selected. The soluble polymers were cellulose acetate butyrate (CAB), from Goodfellow Ltd. UK, and commercial quality low density polystyrene foam (PS). The polymerizing monomer binders were a commercial acrylic printing base (ACR), from Daler-Rowney, USA, and refined linseed oil (LIN) from Windsor and Newton, UK. The solvent used was trichloromethane, except for the acrylic base, which is only soluble in polar solvents for which ethanol was used. The compositions are designated according to the type of silicon nanoparticle and the binder used, for example PCAB refers to $P^{*}1$ powder in CAB binder.

  Table 3.1 shows the ink formulation and layer thickness after curing for the P type powder in the different binders as an example. The same composition was used for the metallurgical powder based nanocomposite inks. The different inks were mixed thoroughly in a preparation bottle with a stirrer until a smooth paste was achieved,

and then printing of the inks on a separate cellulose acetate sheet of thickness $25\mu m$ was achieved with a glass rod. The rod serves to spread the inks over the plastic sheet until an even thin layer of the nanocomposite is formed. Measurement of the layer uniformity was not carried out due to unavailability of a profilometer. However effort was made to ensure that the print was relatively thin and visibly uniform. The thickness of the layers measured using a micrometer screw gauge vary between $15\pm2\mu m$ to $45 \pm 2\mu m$, as shown in the table 3.1 for the different P type nanocomposites. The printed nanocomposites were then placed in a clean room and allowed to dry over a week before the measurement was carried out.

Table 3.1: The composition of the nanocomposite ink used in the SAXS study.

INK Type	Binder Type	Solvent Type	Silicon powder	Binder	Solvent	particle loading	Layer thickness (μm)
PCAB	CAB	Chloroform	0.40g	0.16g	4ml	71.43%	15
PACR	Acrylic	Ethanol	0.40g	0.32g	4ml	55.55%	15
PLIN	Linseed oil	Chloroform	0.40g	0.20g	300ul	66.66%	35
PPS	Styroform	Chloroform	0.40g	0.16g	4ml	71.43%	45

SAXS experiments were carried out, in transmission geometry, on beamline D11A at the National Synchrotron Light Laboratory (LNLS) facility located in Campinas, Sao Paulo, Brazil. The beamline is equipped with two kapton scattering films and detectors, positioned on each side of the sample holder, to monitor the primary beam intensity and absorption in the sample chamber. A detailed description of the LNLS SAXS beam-line can be found in [124, 139]. Air scattering and parasitic scattering, from the sample holder were determined by measuring with an empty sample chamber and empty sample holder respectively. Similarly, the substrate signal was measured using a blank cellulose acetate film in the sample holder. Three sets of slit collimators were used in this study. The incident X-ray wavelength λ was 0.1608 nm, and the scattering intensities were measured with sample-to-detector distance 1.077m, yielding and effective angular range of 5^0 above the primary beam. The corresponding range of q values over which the measurement was carried out was $0.007 < q < 0.304$Å.The measurement times were 3600s for each sample. Conversion from detector position in channels to scattering vector and standard corrections, were made on-site with software provided with the instrumentation. This program uses established algorithms and measured data to correct for the detector inhomogeneity, intensity variation and parasitic scattering. The measured substrate contribution was subtracted, as variable parameter in proportion to the measured attenuation, in the subsequent data analysis. It was found, however, that, because the scattering from silicon is much higher than that from the carbon-based substrate material, magnitude of this correction had little effect on the final results [126].

University of Cape Town

- Sample preparation and morphological study using SEM:

  This study was carried out using two nanocomposite types. In this case, however, $P^{*}5$ powder was dispersed in the same refined linseed oil (LIN) and acrylic printing medium (ACR) as those used for the SAXS experiment, described above, in a plastic bottle. In preparing the nanocomposite inks, in this case $0.20g$ of the $P^{*}5$ powder was mixed in $0.10g$ of linseed oil, after which $100\mu l$ of commercial lacquer thinners was added. The same quantity of powder was dispersed in $0.04g$ of the acrylic medium with $1000\mu l$ of ethanol added to form an acrylic based ink in a plastic bottle. The blends were then sonicated for 1 hour in an ultrasonic bath to ensure proper dispersion of the particles in the binder. The bottle was then opened to allow the solvent to vaporise.

  After 24 hours, the inks were printed on a cellulose acetate plastic sheet using the stencil and doctor blade method. First the area for printing was defined with transparent adhesive tape, with the aid of a glass rod, each type of ink was evenly spread to cover the defined area. The samples were then allowed to cure for 7 days after which small sections of the nanocomposite, suitable for mounting on an aluminium stud used as sample holder for SEM were cut out. Using carbon glue, the samples were held in place on the stud, with the glue making electrical connection between the surface of the printed nanocomposites and the aluminium stud.

  The study of the nanocomposites morphology was performed using a Leica Stereoscan S440i SEM. For imaging, the operating beam energy used was $20KeV$, and the probe current was maintained at $50pA$. Images of the samples were taken at magnifications of $\times 10,000$ and $\times 40,000$, in secondary electron mode. This magnifications ensures that a large area of the nanocomposite is covered for analysis of the cluster distribution.

University of Cape Town

3.4 Results and Discussion

3.4.1 Morphological study of silicon nanocomposites

Fig. 3.3 and 3.4 show the SEM micrographs of the PLIN and PACR nanocomposites respectively. This section compares qualitatively the two samples from their respective images at relatively (a) low and (b) higher magnifications.

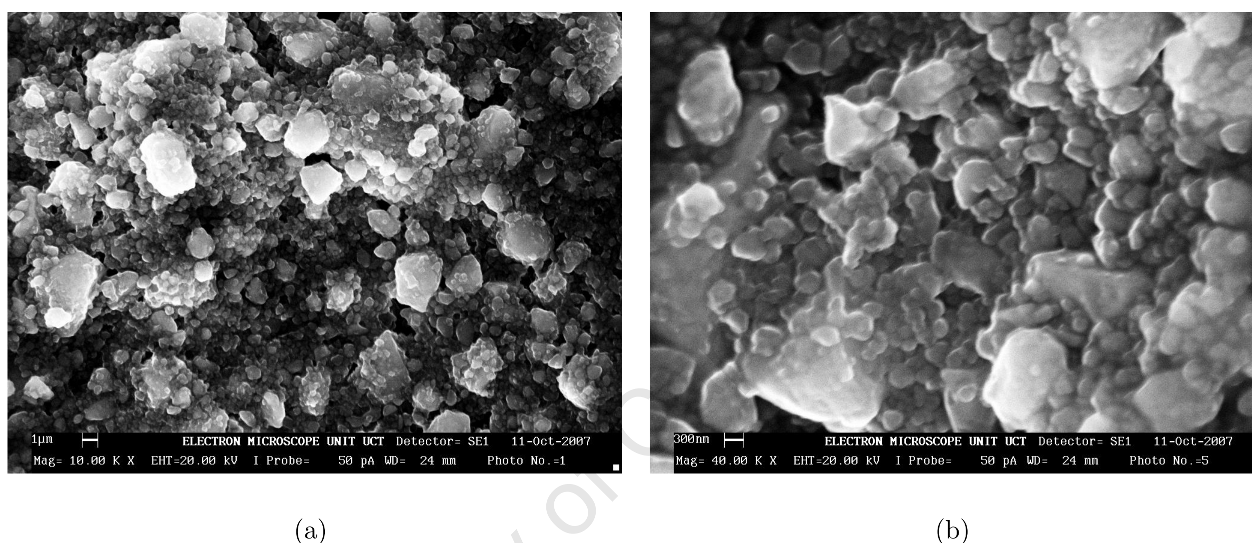

(a) (b)

Fig. 3.3: Showing SEM micrograph of PLIN nanocomposites at (a) low magnification and (b)at higher magnification.

University of

From the micrographs of the two nanocomposites, three types of clustering can be identified. The most obvious are the larger fairly round shaped clusters having cross-sectional length in the range $2-9\mu m$, formed by the aggregation of isolated and smaller clusters of particles on a larger particle. The second type of clusters have a cross-sectional length in the range $1-2\mu m$, while the third type of clustering results from the smaller particles trapped in the regions between the larger clusters. The characteristics of the clusters can be described as dense and polydisperse, as the clusters are composed of particles of varying sizes closely packed together.

The major difference between the PLIN and PACR nanocomposite is in the networking of the clusters. Considering the higher magnified image Fig. 3.3(b) for the PLIN and Fig. 3.4(b) for the PACR, the clusters in the PLIN appear closely knitted compared to those observed for the PACR nanocomposite which has much more open network of the larger clusters.

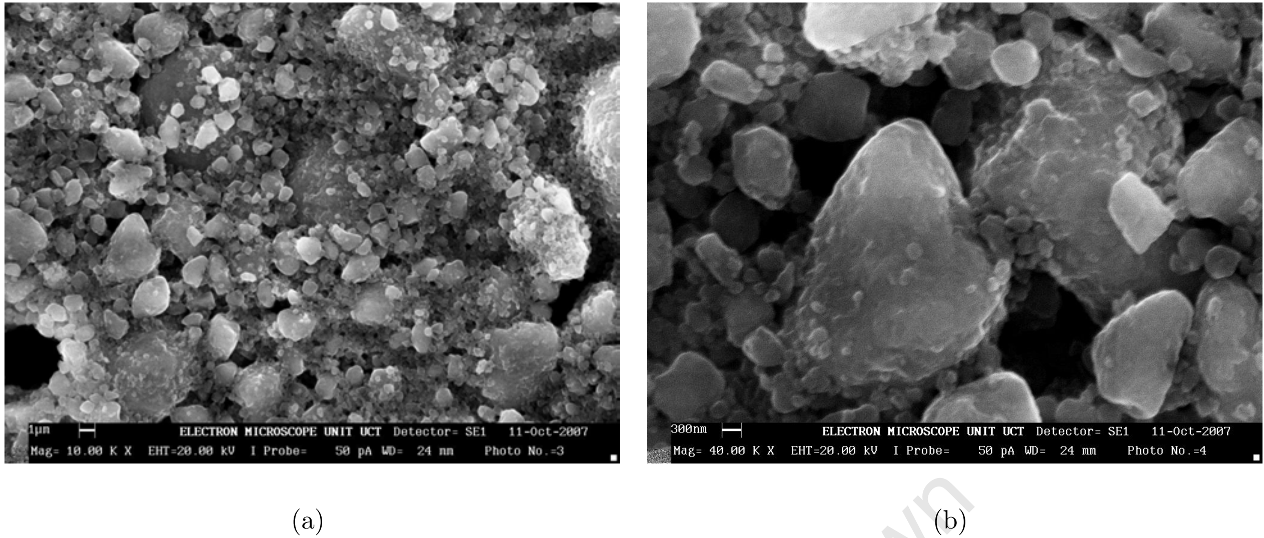

(a) (b)

Fig. 3.4: Showing SEM micrograph of PACR nanocomposites at (a) low magnification and (b) at higher magnification.

University of Cape Town

This feature is represented schmatically in Fig. 3.5. The reason for this may be due to the difference in the proportion of binder acting as support for the particles in the composites, with the PLIN nanocomposite having a greater mass fraction 33% compared to the PACR nanocomposite with 17% binder mass fraction. Since the acrylic medium is an emulsion, the open network may also have resulted from voids created by the evaporation of water from the acrylic medium during curing. The distribution of clusters in the PLIN nanocomposite structure, shows to a large extent the clusters are closely connected with gaps of $\approx 100nm$ between a few clusters. On the other hand for the PACR, the clusters are predominantly loosely connected with separation gaps up to $500nm$. In general, the nanocomposites can be further classified as disordered.

Fig. 3.6 shows the histogram of measured cluster cross sectional length distribution for PLIN and PACR nanocomposite respectively, using the image processing software Digimizer as described earlier in chapter 2. The plot in both cases shows that the nanocomposites consist of a wide distribution of cluster sizes, ranging from relatively smaller clusters of cross-sectional length $400nm$ to bigger ones of sizes up to $9\mu m$. The distribution in both cases follows a log-normal distribution pattern. The fit of equation 2.8 to the histogram, yield a mean clusters cross-sectional length of $1.15\mu m$ and $1.50\mu m$ for the PLIN and PACR nanocomposites respectively as shown in the inset of both plots.

The condition for good electrical conductivity within the bulk nanocomposite layer, is such that the embedded particles and clusters have intimate contact with each other, forming a

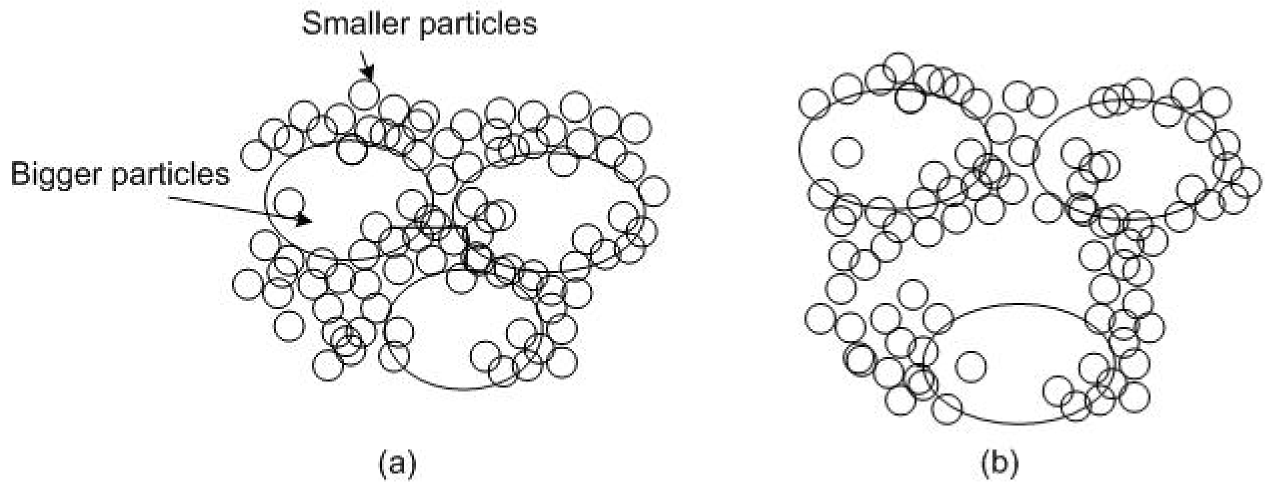

Fig. 3.5: Schematic representation of (a) the PLIN composite with closely linked network of bigger cluster and (b) PACR composite with relatively open network of clusters.

University of Cape Town

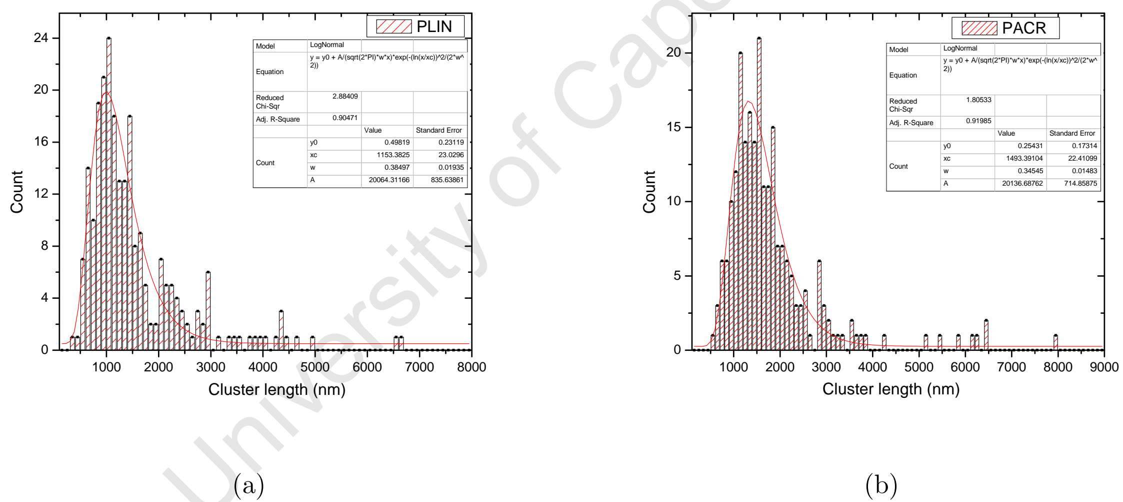

Fig. 3.6: Showing histogram of the clusters crosssectional for (a) PLIN nanocomposite and (b) PACR nanocomposite

path for continuity of free carriers from one end of an electrical connection to the other. On the other hand, for loosely packed clusters having gaps between the different clusters, no clear conduction path is provided for continuity of free carriers. In this case transport of carriers will more likely be dominated by tunneling rather than drift. For the two class of nanocomposite discussed in these work, electrical conduction of free carriers through the path created by the interconnection of cluster may possibly dominate that due to tunneling in the case of the PLIN composites, while the converse may be the case for the PACR

nanocomposite layer.

3.4.2 SAXS study of nanocomposite of silicon using Guinier's analysis

Fig. 3.7 shows the Guinier plot ($log(I(q))$ vs. q^2) for PACR, PCAB, PLIN and PPS samples, with derived parameters as shown in the inset of each graphs. Similar Guinier plots for MACR, MCAB, MLIN and MPS samples are also shown in Fig. 3.8. As seen from the plot for all the nanocomposite types, the shape of the curves does not show a linear dependence for the whole range of q. This suggests that the dispersion of both powders in the different binders consist of a broad distribution of size heterogeneities, i.e. a polydispersive system as defined earlier [134, 140]. However, a careful investigation of the Guinier plots reveals two linear regions; (1) in the low q regions with a short linear dependent region and (2) a wider linear region separated from each other by a transition region. For all the systems, the radius of gyration for the two linear regions, designated R_{1g} and R_{2g}, was calculated from the slope of the best linear fit to the regions as shown in Fig. 3.7 and Fig. 3.8, with the top and bottom inset displaying the different estimates of radius of gyration R_{xg}, aggregate radius R_x and the regions of validity derived using equation 3.11 for the two regions. Since the q values probe the structural features at various length scales, the larger value of the slope of the linear region (1) compared to (2) indicates a larger size of the scatterers in region (1) [141].

It is however well known that the estimated aggregate radius R from a Guinier plot is valid in the q range where qR_g is less than 1 [142, 141]. For all the case considered, the estimated R_1 values for the first observed linear region may not be valid for the region over which R_{1g} was calculated, because the range of qR_g in this region is greater than unity. The R_2 values on the other hand may be considered valid in each case for the small q region for which $q \leq 0.02\mathring{A}^{-1}$ as seen for the entire nanocomposite samples. The aggregate size, assuming the composites consist of spherical particles was estimated for the eight samples using the expression 3.11.

Table 3.2 shows the calculated values for radius of gyration for the second linear regions for which $qR_g \approx 1$ and the corresponding radius of aggregate R_2 derived from the linear fit to the second region. The smallness of the linear regions that defines the Guinier regime $q \leq 0.02\mathring{A}^{-1}$ confirms, as mentioned above, that the nature of PACR, PCAB, PLIN and PPS on the one hand, and MACR, MCAB, MLIN and MPS on the other hand are all

University of Cape Town

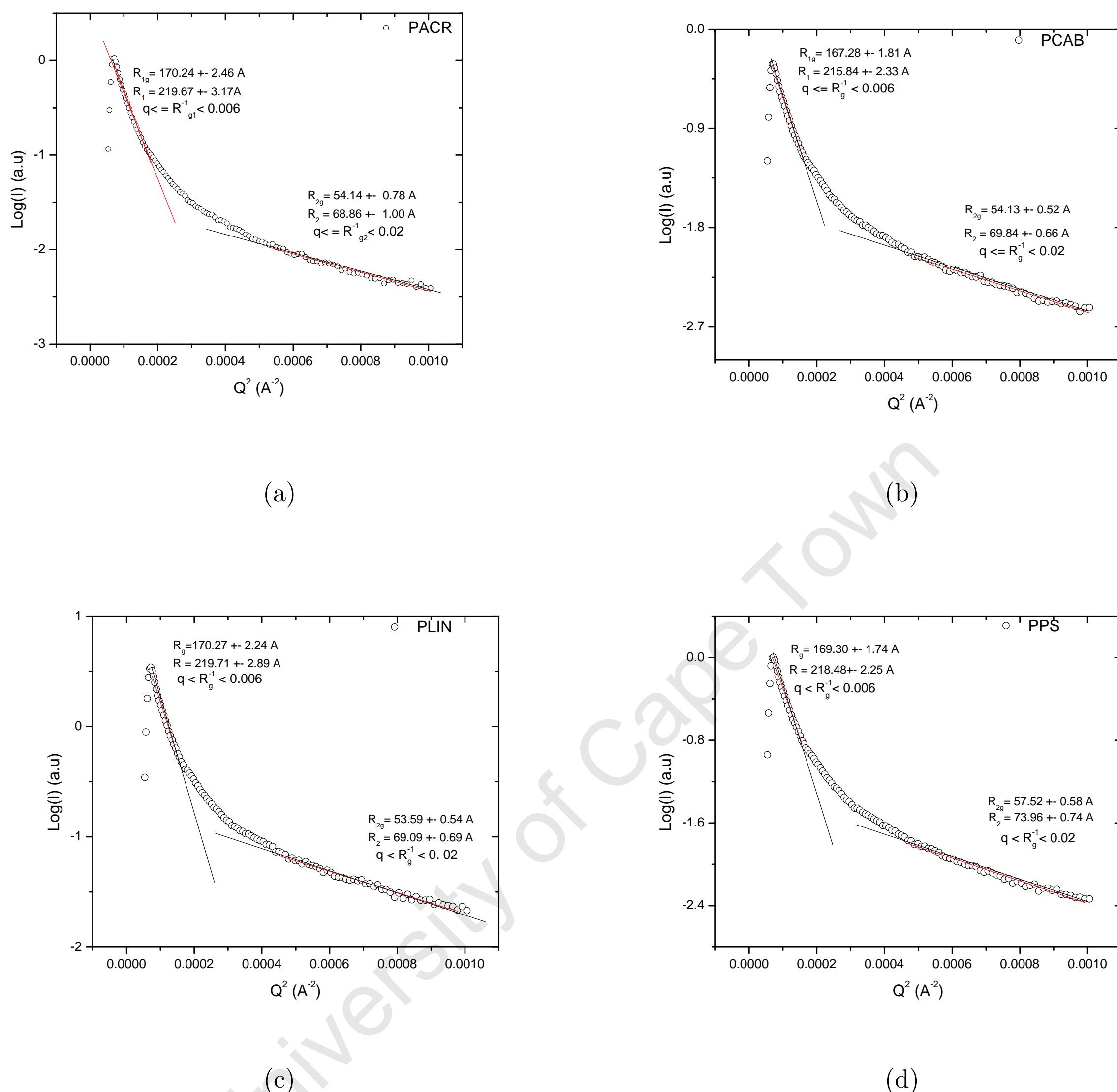

University of Cape Town

Fig. 3.7: Guinier plot showing two linear region from which radius of gyration R_{xg}, and corresponding aggregate size R_x was calculated for (a) PACR (b) PCAB (c) PLIN and (d) PPS nanocomposites.

polydispersive with interparticle interaction typical of overlapping systems, and the R_g values may represent a spatial correlation length or a measure of the mean cluster radius [134].

Comparing the different values of R_g and R_2 based on the powder type on the one hand and the binder type on the other, one does not see a clear trend, as the radius of gyration and radius of cluster is seen to fluctuate about the average values. The calculated R_2 values in all the cases is much lower than the average particle size derived from the TEM study of the P*1 powder in chapter 2. These may only suggest that the range of q values used in this experiment is only suitable for determining sizes of particle or aggregates of relatively larger

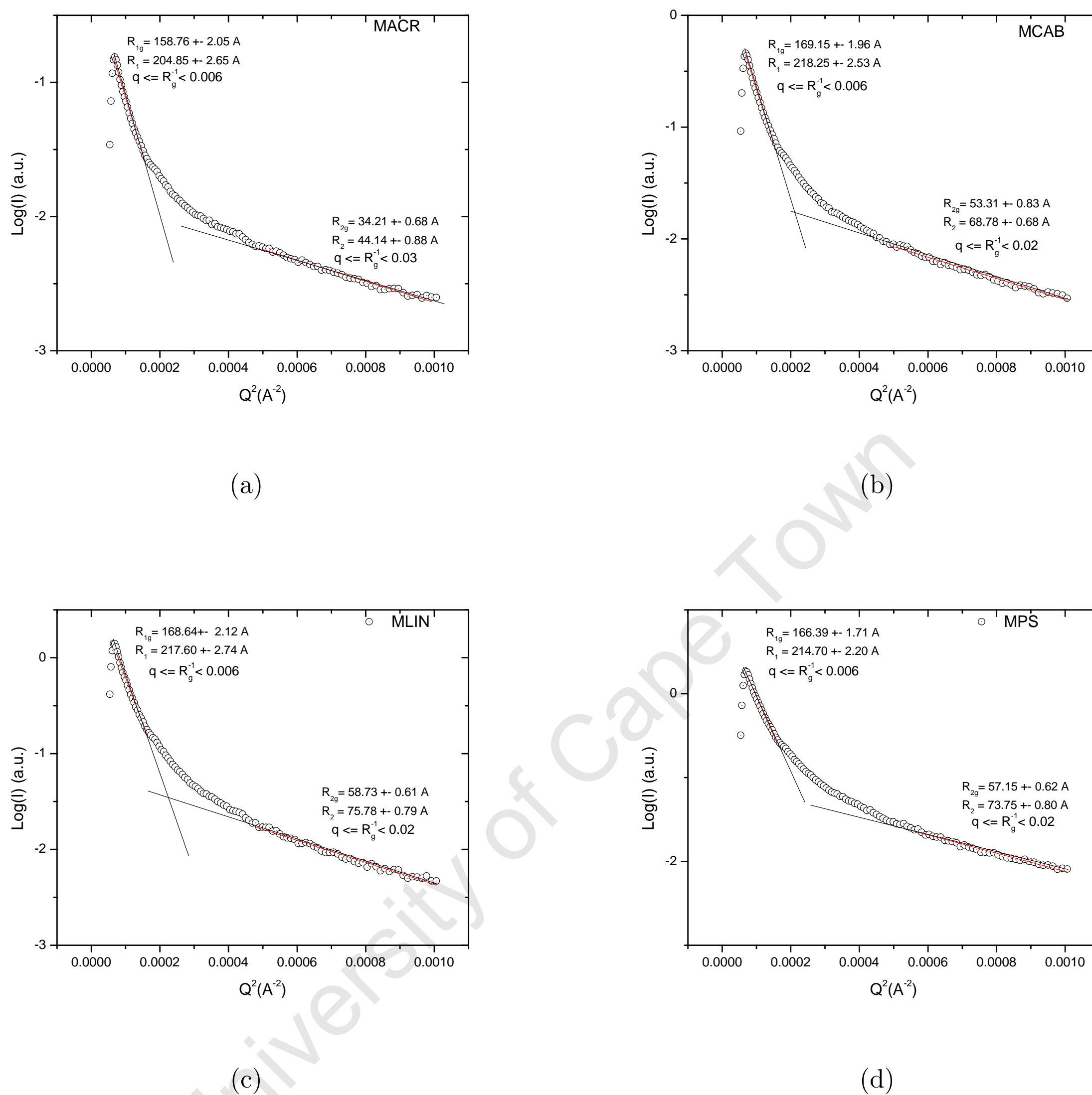

University of Cape Town

Fig. 3.8: Guinier plot showing two linear regions from which the radius of gyration R_{xg}, and corresponding aggregate size R_x was calculated for (a) MACR (b) MCAB (c) MLIN and (d) MPS nanocomposites.

sizes.

Table 3.2: Table of calculated values for radius of gyration R_g and corresponding radius of aggregate R_1 derived from the linear fit to the first region for both P and M based inks with the region of validity.

Sample	Radius of Gyration R_r (A)	Aggregate radius R_1 (A)	Region of validity q
PACR	54.14	68.86	≤ 0.02
PCAB	54.13	69.84	≤ 0.02
PLIN	53.59	69.09	≤ 0.02
PPS	57.52	73.96	≤ 0.02
MACR	34.21	44.14	≤ 0.02
MCAB	53.31	68.78	≤ 0.02
MLIN	58.73	75.78	≤ 0.02
MPS	57.15	73.75	≤ 0.02

University of Cape Town

3.4.3 SAXS study of nanocomposite of silicon using Porod's law analysis

Figs.3.9 and 3.10 shows the Porod plots, $log(I(q))$ vs. $log(q)$ for the eight samples discussed above. Just after the Guinier region discussed above, there is a region with a power law behaviour, with a slope greater than 3.0 except in the case of PLIN and MACR which exhibits a slope less than 3 in this region. Fractally rough surfaces, have a slope which varies between 3.0 and 4.0 and the surface-fractal dimension $D_s = 6 - \alpha$. Thus, samples PACR, PCAB and PPS possess a surface fractal behaviour, with the range of such fractal behaviour defined by $\xi^{-1} < q < l^{-1}$ [143]. From this region the sizes of the upper bound limit ξ^{-1} representing the size of the aggregate or cluster and the lower limit l^{-1} representing the size of the basic particles (the constituents of the aggregates) [143] was deduced using $D = 2\pi/q_{min/max}$, where q_{min} and q_{max} represent the upper and lower bound respectively. In the case of PLIN and MACR where the slope value in each case is less than 3.0, the structure is said to have a characteristics mass fractal behaviour with upper and lower bound limit similar to that discussed for surface fractal features of PACR, PCAB and PPS composites.

Table 3.3 shows the different characteristic values derived from the measurement of the slope of the straight line in the relatively high q Porod regime, and also listed is the possible fractal behaviour that can be associated with the different nanocomposite.

Table 3.3: Table showing the different characteristics value derived from the measurement of the intermediate straight line and the possible fractal behaviour that can be associated with the values for the different nanocomposite.

Sample	Slope (α)	Fractal Dimension			Fractality range		
	Porod's Region	β	D_m	D_s	$\xi(\mathring{A})$	$l(\mathring{A})$	Fractal type
PACR	-3.41	0.97		2.59	370.03	63.94	Surface
PCAB	-3.20	0.36		2.80	338.13	56.23	Surface
PLIN	-2.77	0.53	2.77		342.84	74.22	Mass
PPS	-3.38	0.59		2.62	354.41	61.66	Surface
MACR	-2.73		2.73		337.73	53.31	Mass
MCAB	-3.08	0.76		2.92	331.13	67.71	Surface
MLIN	-3.58	0.35		2.42	347.12	62.57	Surface
MPS	-3.57	0.74		2.43	258.20	49.25	Surface

University of Cape Town

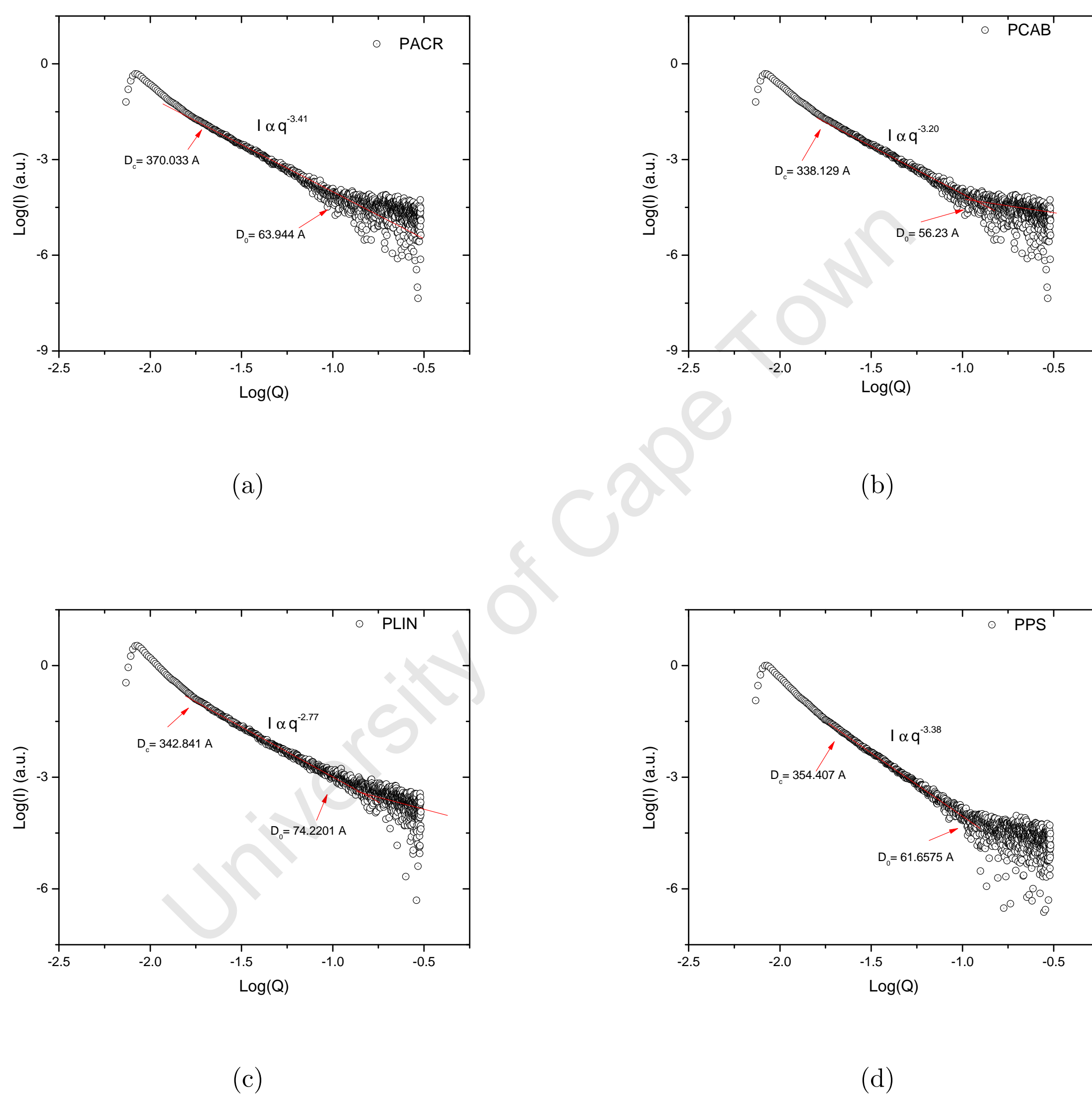

University of Cape Town

Fig. 3.9: Porod plot from which the fractal behaviour and aggregate size of the unit was calculated for (a) PACR (b) PCAB (c) PLIN and (d) PPS nanocomposites.

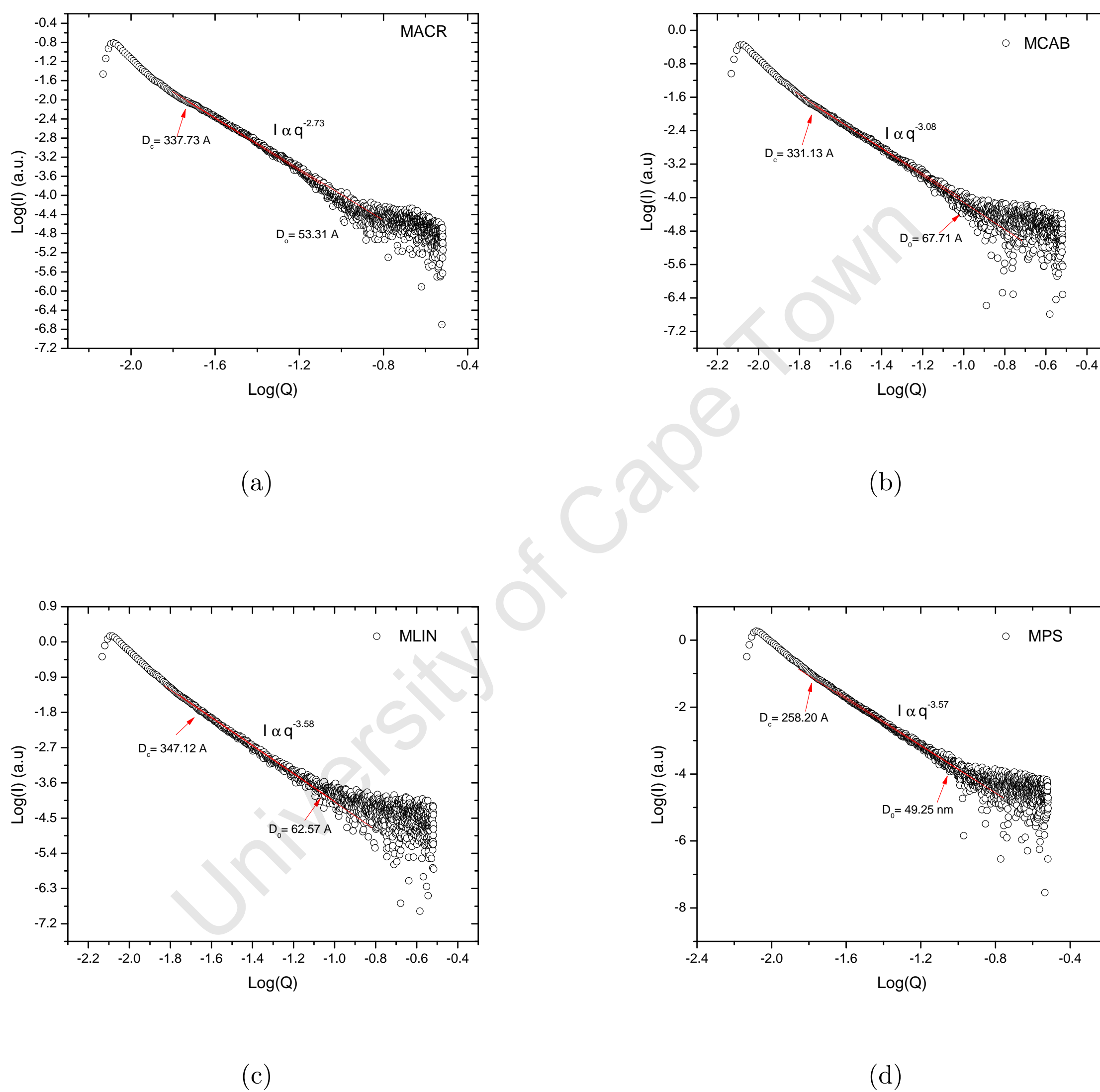

University of Cape Town

Fig. 3.10: Porod plot from which the from which fractal behaviour and aggregate size of the unit was calculated for (a) MACR (b) MCAB (c) MLIN and (d) MPS nanocomposites.

3.4.4 Analysis of deviation from Porod's law

Many two-phase materials can be described either with a sharp phase boundary having well defined step-like changes in the scattering length or electron density, which obeys Porod's law in the small-angle scattering vector asymptotic region, or the case of a diffuse interfacial region that causes deviation from Porod's law [144]. The nature of the phase boundary in a nanocomposite can be investigated by the plot of the Porod's law for slit collimated saxs intensity of $log(q^3 I(q))$ vs. $log(q^2)$ derived from equation 3.8 and restated here for convenience [135, 136].

$$\ln[I(q)q^3] = \ln K + \sigma^2 q^2, \tag{3.13}$$

where σ is a parameter related to the interface thickness or to the size of electron density inhomogeneity [135], which depends on whether this region shows a negative or positive deviation.

Fig. 3.11 and 3.12 shows the plot of $log(q^3 I(q))$ vs. $log(q^2)$ for the P* and M nanocomposites respectively. From these plots it is easy to see that all the samples exhibits a negative deviation from Porods law, characteristic of non-ideal two-phase system with a diffuse interface layer between the particle and matrix [135, 136], except for the PLIN and MACR sample that exhibit a positive deviation from Porods law. This positive deviation is characteristic of a two-phase systems with electron density inhomogeneity [135, 136] in the particles. This is probably unphysical when compared to the other samples and may be an artifact due to a residual background. Coincidentally these two systems are the only nanocomposite that exhibit mass fractal behavior in the Porod region, suggesting a possible correlation between sign of deviation from Porod's law and fractality.

By fitting the data in these regions to equation 3.8, describing negative deviation from Porod law, σ^2, representing the extent of deviation from and ideal Porod's law behaviour taking as the reference (zero line), was calculated from the slope of the best line of fit to this region as shown in the inset of each graph. Table 3.4 shows the deviation for each sample and the corresponding structures.

University of Cape Town

Table 3.4: Showing the extent of deviation from Porod's law for the different systems

Sample	σ^2	Deviation from Porod's law	Two phase Structure with
PACR	-14.10	-ve	diffuse interface
PCAB	-14.10	-ve	diffuse interface
PLIN	24.49	+ve	inhomogeneous electron density
PPS	-18.08	-ve	diffuse interface
MACR	3.75	+ve	inhomogeneous electron density
MCAB	-15.17	-ve	diffuse interface
MLIN	-5.02	-ve	diffuse interface
MPS	-20.50	-ve	diffuse interface

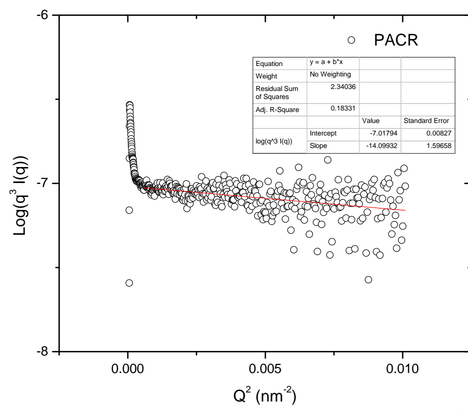

(a)

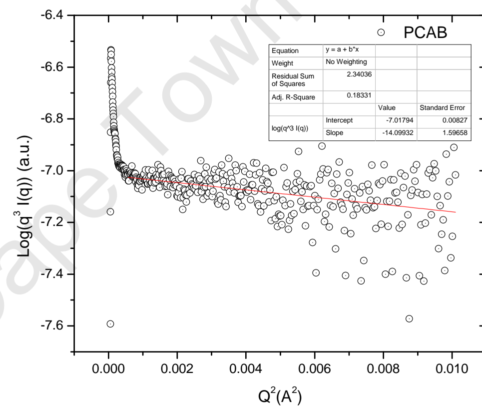

(b)

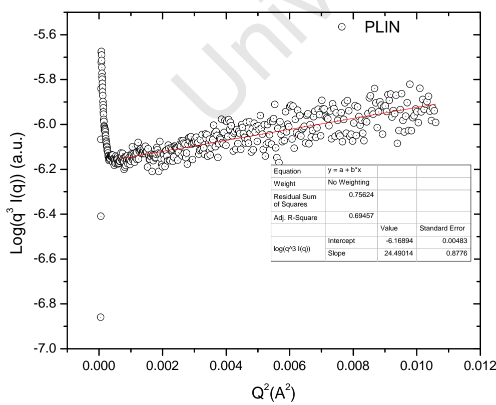

(c)

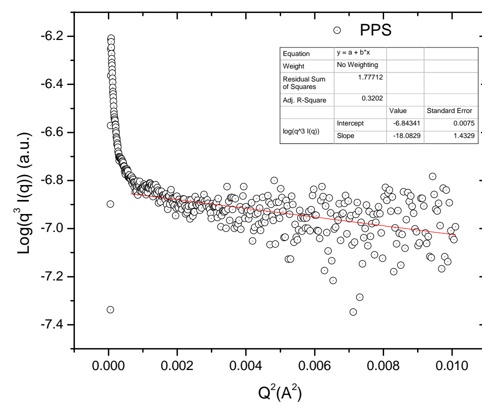

(d)

Fig. 3.11: Showing plot of $log(q^3 I(q))$ vs. $log(q^2)$ for the P based (a) PACR (b) PCAB (c) PLIN and (d) PPS nanocomposites.

University of Cape Town

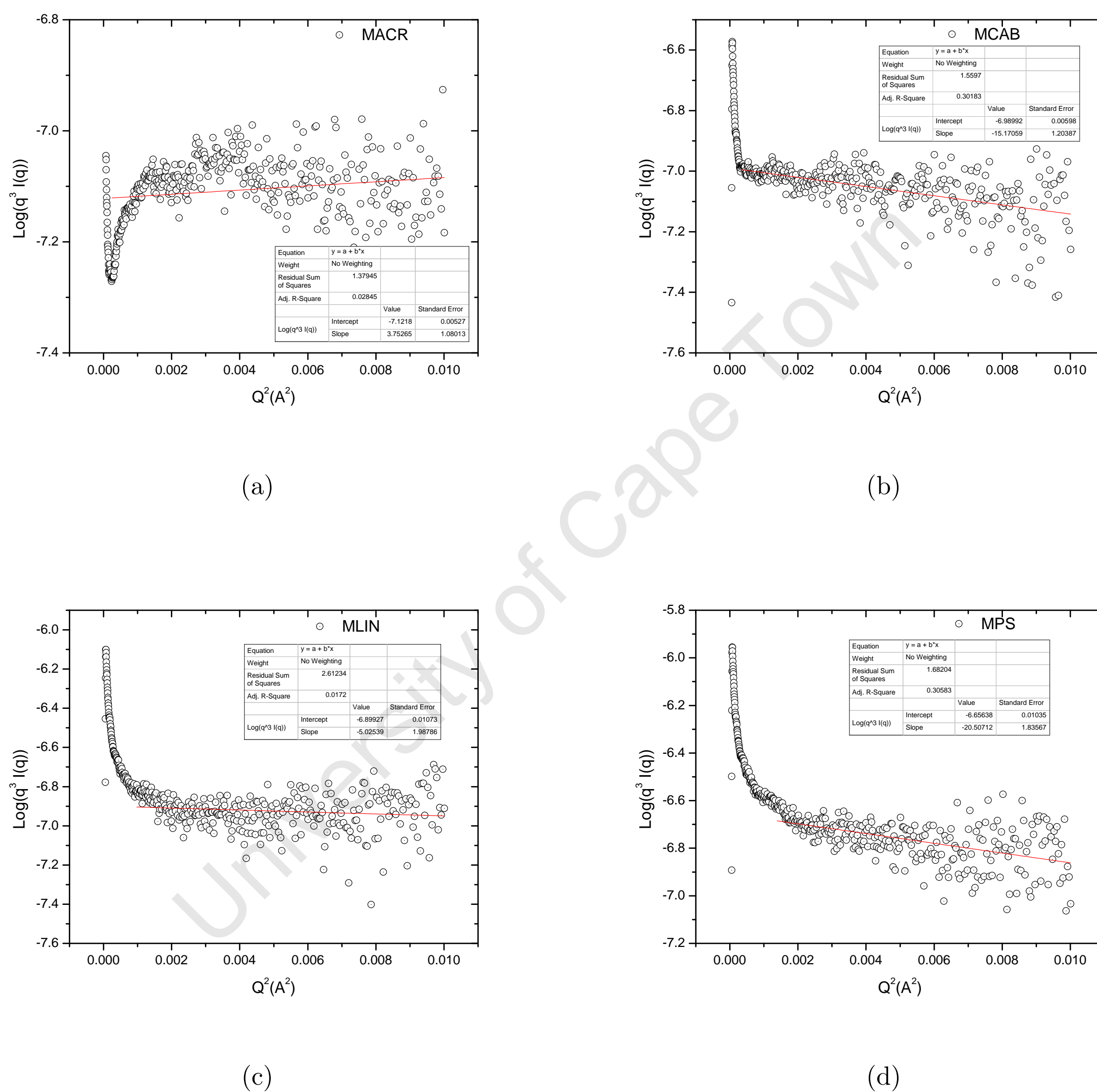

Fig. 3.12: Showing plot of $log(q^3 I(q))$ vs. $log(q^2)$ for the M based (a) MACR (b) MCAB (c) MLIN and (d) MPS nanocomposites.

University of Cape Town

4. Charge carrier transport mechanisms in silicon nanocomposites

Implementation of semiconductor devices usually requires placing metallic electrodes on such components for electrical connection. The desired interface is an ohmic type, which allows for easy transport of carriers from the metal into the semiconductor or vice-versa. When the metal makes contact with a semiconductor, a barrier is formed at the metal semiconductor interface, since the metal and semiconductor have different chemical potentials. This barrier is responsible for controlling the current conduction as well as the capacitance behaviour of the device [145]. In practice, many contacts have barriers resulting from either homogeneous or inhomogeneous distribution of Schottky barriers and interface states. In practice however, an ohmic interface is achieved usually by preferentially doping the semiconductor near the junction of the metal.

Of interest is the interface type and dominant charge carrier transport for systems formed from contact of a metal to nanocomposite of silicon nanoparticles in a polymeric binder. Although many works have been reported on silicon nanocrystals embedded in dielectrics like oxide and ceramic matrixes [14, 146, 147], the emphasis has been on the structural and morphological characteristics, with few reports on the electrical properties. Apart from the work by Ando et al. [18] on photoelectric properties of printed thin films of silicon nanocrystals dispersed in polymer binder, the only other such study of nanocomposites resulting from combining silicon powder in a dielectric like linseed oil or acrylic medium was our own work [34].

This part of the research presents the nature of the interface and the process of charge carrier transport between the metallic contact and the silicon nanocomposites developed earlier in Chapter 3. This is achieved by conducting $I-V$ characteristic experiments on a metal-nanocomposite-metal structure, where the metal is a printable silver paste. The results of the $I-V$ characteristics are tested with existing charge transport models for metal-semiconductor as well as metal-dielectric systems in order to determine how well a particular transport model describes the conduction process in the metal-nanocomposite-metal structures. For this purpose two main filler types, (a) $P^{*}5$ type and (b) M5 type earlier described, are used to form seven nanocomposite type, based on the proportion of filler in a given binder. This is aimed at investigating the dependence of the charge carrier transport type on the concentration of fillers in the nanocomposites.

University of Cape Town

4.1 Background theory of charge carrier transport

Metallic contacts to semiconductors or active layers in general, create a contact resistance to current flow at the physical junctions. The nature of such contact depends largely on the type of metal, type of interface layer formed, and also on type and structure of the semiconductor material [148]. In an ideal case, i.e. for junctions without surface states and other anomalies, two basic contact types can result from a connection of metal to a semiconductor, ohmic contacts and Schottky contacts. In reality however, the junction may result from a mix of the two types, or of one dominated by interfacial layer formation at the interface of the metal to the semiconductor. The following subsection describes an ideal types of contacts as occur in a metal-semiconductor as well as with metal-organic semiconductor or hybrids of organic-inorganic contacts. The effect of the presence of interface state between the metal-semiconductor for the ideal system will also be presented.

University of Cape Town

4.1.1 Schottky barrier

When a metal and semiconductor make intimate contact, a Schottky barrier may be formed at the interface of the metal and semiconductor. Fig. 4.1 shows the electronic energy relation for an ideal contact between a metal and a semiconductor assuming no interfacial layer, no chemical reaction and no physical strain at the interface of the metal and semiconductor. For a high work-function metal and an n-type semiconductor shown as separate systems in Fig. 4.1(a), if the two systems are then connection by an external wire for example, charge will flow from the semiconductor to the metal and thermal equilibrium is established as a single system as shown in Fig. 4.1(b) [145]. The Fermi level in the semiconductor is lowered by an amount equal to the difference between the two work functions.

The work function of a solid is defined as the energy difference between the vacuum level and the Fermi level [145]. This is denoted by $q\phi_m$ for the metal and $q\left(\chi + \phi_n\right)$ for the semiconductor. The potential difference between the two work functions $q(\phi_m - (\chi + \phi_n))$ is called the contact potential.

As the gap distance δ between the two systems decreases, as shown in Fig. 4.1(c), the electric field in the gap increases and an increasing negative charge is built up at the metal surface [145] with an equal opposite charge (positive) in the semiconductor depletion region. When δ is small enough to be comparable to the interatomic distances, the gap becomes transparent to electrons, and the limiting case shown in Fig. 4.1(d) may be assumed. The barrier height

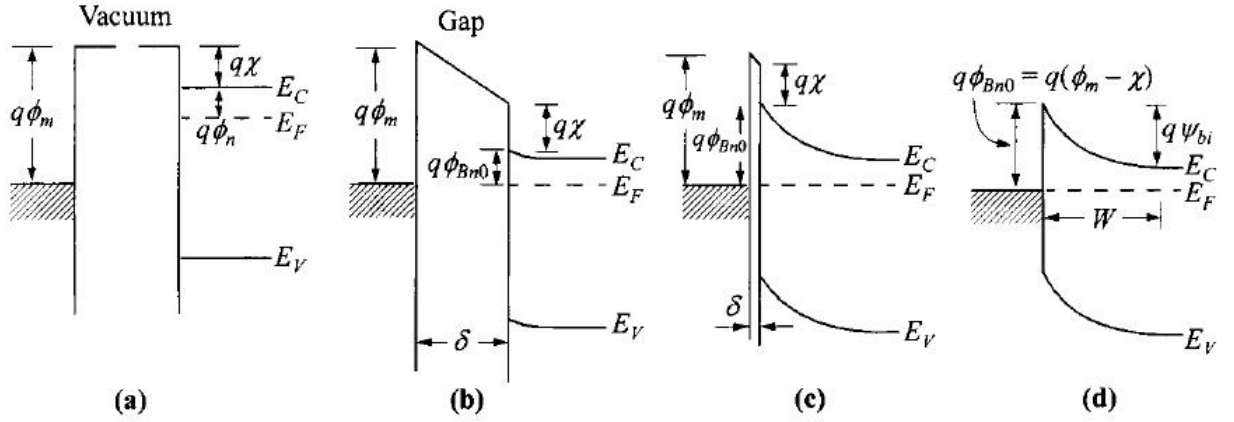

Fig. 4.1: Electronic energy band diagram of the metal and the semiconductor (a) before contact is made (b) after contact is established (c) with much reduced contact separation and (d) with no separation [149].

resulting from the contact in this model is given by [150, 145]

$$\phi_{B0} = \phi_m - \chi, \tag{4.1}$$

where:
ϕ_{B0} the barrier height at zero applied bias, is simply the difference between the metal work function and the electron affinity of the semiconductor contact;
ϕ_m is the metal work function, a measure of the energy required to remove an electron from the metal or equal to the deference between the fermi level of metal and vacuum; and
χ is the electron affinity of the semiconductor, a measure of the attractive potential energy for an electron in vacuum, which may be further expressed from Fig. 4.2 as

$$\chi = \frac{(q\phi_s - (E_c - E_f))}{q}, \tag{4.2}$$

where,
$q\phi_s$ is the semiconductor work function,
E_c is the conduction band energy level, and
E_f is Fermi energy level.

According to the Schottky theory for metal-semiconductor junction given in equation 4.1, the barrier height ϕ_B will only depend on the metal work function and the semiconductor electron affinity, but independent of the semiconductor doping density [151]. This implies that when the metal is carefully chosen for a given semiconductor type, three possible junction barriers may result at the metal semiconductor interface as shown in Fig. 4.2 [152, 145, 151].

University of Cape Town

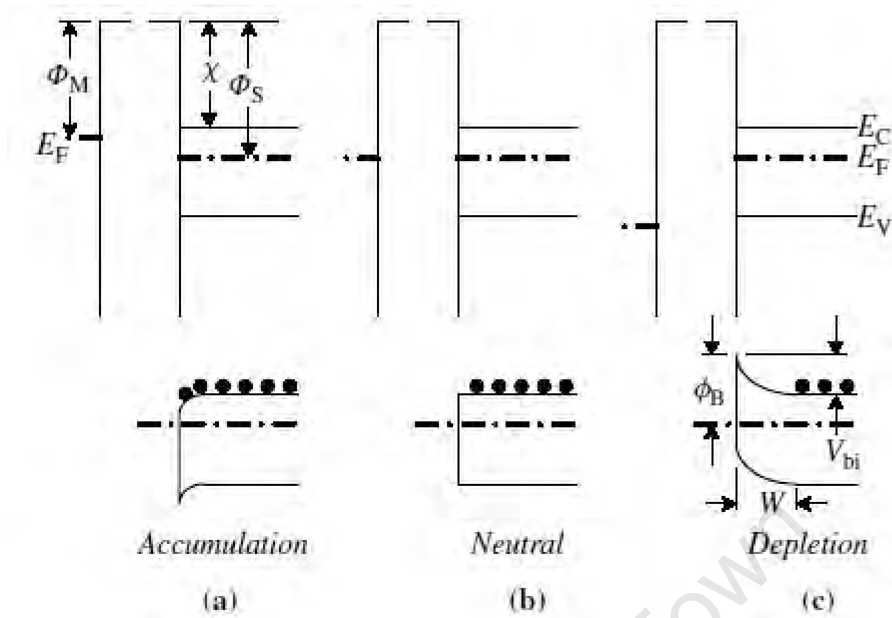

Fig. 4.2: Showing three possible metal Semiconductor junction type that can result from an intimate contact of a metal to a semiconductor [151].

University of Cape Town

The ohmic contact which is the desired type of connection in many applications results from generation and recombination of charges at the interface of the metal-semiconductor junction. For this contact often referred to as an accumulation contact type, electrons in the metal experience a negligible resistance to flow into and out of the semiconductor as shown in Fig. 4.2(a). An ideal ohmic contact is characterised by a linear current-voltage behaviour, the voltage drop at the contact is negligible compared to the drop across the active region of the device and usually there is no injection of carriers from the metal to semiconductor or vise versa [151]. The concept of a neutral barrier assumes that the metal and semiconductor have equal work functions and thus the formation of contacts does not result in any band bending as shown in Fig. 4.2(b).

In practice however, a Schottky contacts generally is formed when a metal make intimate contact with a semiconductor. This contact poses a barrier to the flow of current into or out of the semiconductor depending on the polarity of the applied potential as shown in Fig. 4.2(c). Schottky contacts are depletion type contacts, and the most common contacts in a metal-semiconductors connection. They are characterised by a rectifying mechanism, (i.e. a total resistance which depends on the polarity of the applied voltage) arising from the presence of the potential barrier caused by stable space charge at the interface of the metal-semiconductor contact, and the current transport for such contacts are characterised by thermionic as well as field emission [149].

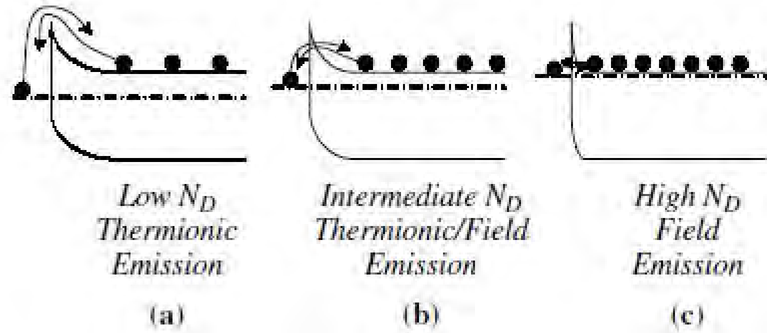

Fig. 4.3: Depletion-type contacts to n-type substrates with increasing doping concentrations. The electron flow is schematically indicated by the electrons and their arrows [151].

The barrier height in reality is shown to depend weakly on the doping concentration of a the semiconductor, since the surface-state density which brings about Schottky barrier is mainly influenced by doping [151, 153]. Fig. 4.3 illustrates the role of the doping level of semiconductors on the conduction mechanisms for a metal-n-type semiconductor contact for example [151]. For lightly-doped semiconductors Fig. 4.3(a), the current flows as a result of thermionic emission, with electrons thermally excited over the barrier. In the intermediate doping range Fig. 4.3(b), thermionic-field emission (TFE) dominates with carriers thermally excited to an energy where the barrier is sufficiently narrow for tunneling to take place [151]. For high doping densities Fig. 4.3(c), the barrier is sufficiently narrow at or near the bottom of the conduction band for the electrons to tunnel directly, known as field emission (FE) [151]. A more detail explanation of the transport process will be discussed in section 4.3, and a more general discussion of the Schottky barrier process can be found in [149] and [152].

University of Cape Town

4.1.2 Interface states

The Schottky-Mott relation relates the potential barrier ϕ_{BH} at a metal-semiconductor junction with the metal work function ϕ_M and the semiconductor electron affinity χ_S as shown in equation 4.1 which predicts the barrier height in the absence of interface states [150]. Fig. 4.4 shows the junction for a metal-semiconductor interface, assuming a large flat surface of metal and semiconductor place parallel to each other and separated by a small gap δ, filled by vacuum or a dielectric layer. The quantity $q\phi_0$ above E_V, at the semiconductor surface is called the neutral level above which the states are of acceptor type (neutral when empty, negatively charged when full) and below which the states are of donor type (neutral when full of electrons, positively charged when empty) [145].

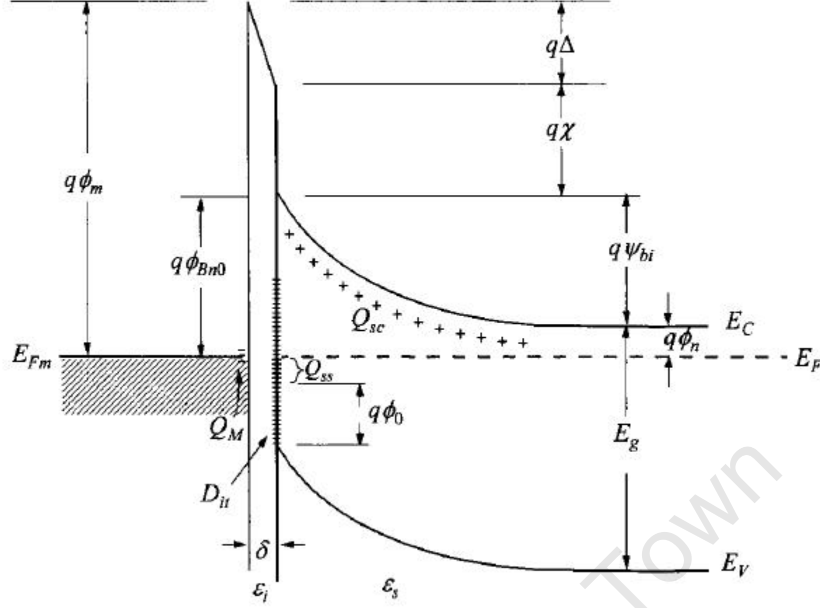

Fig. 4.4: Band diagram of a semiconductor with surface states held at small distance from the metal surface with band bending [145]

University of Cape Town

The barrier height ϕ_{Bn0} of the metal-semiconductor contact, is the barrier that must be surmounted by electrons flowing from the metal into the semiconductor [145]. Assuming an interfacial layer with a thickness of a few angstroms and therefore essentially transparent to electrons, and a semiconductor with acceptor interface traps whose density is D_{it} states/cm^{2}eV, and constant over the energy range from $q\phi_0 + E_V$, to the Fermi level. The interface-trap charge density on the semiconductor Q_{ss}, is therefore negative and is given by [145],

$$Q_{ss} = -qD_{it}(E_g - q\phi_{B0} - q\phi_{Bn0}), \tag{4.3}$$

The space charge that forms in the depletion layer of the semiconductor at thermal equilibrium is given as [145]

$$Q_{sc} = qN_D W_D = \sqrt{2q\varepsilon_s N_D \left(\phi_{Bn0} - \phi_n - \frac{kT}{q}\right)}. \tag{4.4}$$

In the absence of any space-charge effects in the interfacial layer, an exactly equal but opposite charge, $Q_M (C/cm^2)$, develops on the metal surface. For thin interfacial layers the total equivalent surface charge density on the semiconductor surface is given by the sum of

equation 4.3 and 4.4

$$Q_M = -\left(Q_{ss} + Q_{sc}\right). \tag{4.5}$$

The potential ΔV across the interfacial layer due to the surface charges on the metal and semiconductor can be derived from Gauss law and is given by [145]

$$\Delta V = \frac{Q_M \delta}{\epsilon_i \epsilon_o}, \tag{4.6}$$

and the resulting electric field near the interface is given by,

$$E = \frac{Q_M}{\epsilon_i \epsilon_o}. \tag{4.7}$$

where ϵ_i is the permittivity of the interfacial layer and δ its thickness.

For a moderately doped semiconductor, this field is of the order of 10^4 to $10^5 V/cm$ which results in a potential change of about $1V$ in $50nm$ or longer interface layer. This field is due to the presence of a balanced charge of equal magnitude but of opposite sign on the surface of the metal as mentioned earlier [150]. With a filled interfacial layer, the resulting potential and hence the electric field will depend on the dielectric constant of the interface material. What this entails is that for electric field to varnish in these space, is that an external bias V_{ext} of magnitude given by equation 4.8 must be applied to the interface [150],

$$V_{ext} = \phi_m - \left(\chi - \psi_{bi} - \phi_n\right). \tag{4.8}$$

In equation 4.8, ψ_{bi} is the built in voltage due to band bending and ϕ_n is the conduction band minimum with respect to the Fermi-level, determined by charge neutrality condition. This implies that the value of the Schottky Barrier Height (SBH) does not depend on the presence of surface states at the junction, but on the distribution of charges at the interface for which the presence of an interfacial layer plays a role [150]. A number of models have been developed to explain the contribution of interface state at the junction of the metal-semiconductor and how this affect the eventual transport of carriers, for more discussion please see the reference [150].

University of Cape Town

4.2 Charge transport in a nanoparticulate semiconductor network

Fig. 4.5 illustrates the connection of metallic electrodes to (a) bulk and (b) a single nanoparticle to which an external voltage is applied [154]. Charge transport through bulk semiconductors connected to the outer electrodes is attributed to the motion of delocalized electrons [154]. The current is usually continuous and typically obeys Ohm's law as shown in Fig. 4.5(a). However, for a nanoparticle separated as an island by poorly permeable tunneling barriers from two outer electrodes as shown in Fig. 4.5(b), the number of electrons in the particle is always an integer and an electron can only enter or leave the nanoparticle as an entity when external voltage is applied.

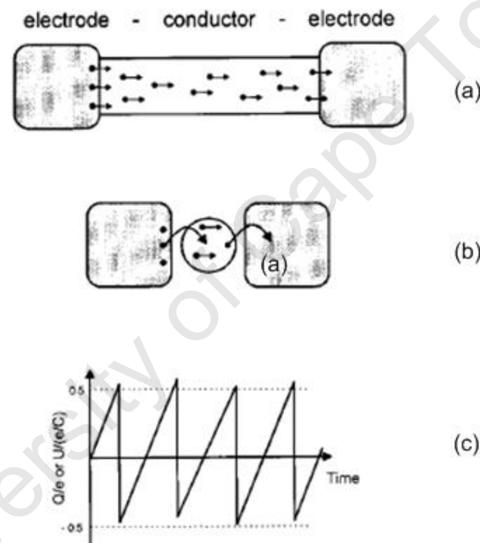

University of Cape Town

Fig. 4.5: Transport of charge carrier for (a) bulk conductor connected by two metallic electrodes and (b) a nanoparticle between two electrodes and E_C is determined by the size of the particle R and its spatial distance to the electrodes. (c) Time development of the junction charge imposed by a constant current source. Taking from [154]

If a nanoparticle with very small self capacitance C_0 is charged by only one excess electron, its electric potential will rise to prevent further charging. To add an extra electron to the island, the applied potential energy E_c should be significantly higher than the columbic blockage potential expressed as [154],

$$E_c = \frac{q^2}{2C} \approx \frac{q^2}{8\pi\epsilon_o\epsilon_r R}. \tag{4.9}$$

Where C is the effective capacitance of the island, determined by the size of the particle R,

and its spatial distance to its neighbors or electrodes. ϵ_o is the permittivity of vacuum, and ϵ_r is the dielectric constant of the nanoparticle surroundings [155].

When the voltage across the nanoparticle is increased, the charge q on the junction will increase as long as the total charge $|Q| < e/2$. The junction is in the Coulomb blockage state and there is no flow of current [154]. At $|Q| > e/2$ tunneling will happen. If the junction is maintained at this bias, an oscillation of the current across the junction in a sawtooth-like manner with the fundamental frequency $f = I/e$ as shown in Fig. 4.5(c) will result [154]. Such single electron levels can be adapted to create, for example, switches, transistors, or digital electronic circuits in general where the presence or absence of single electrons at a certain time and place provides the digital information.

In a special case where nanoparticles or their clusters are surrounding by a dielectric ligand shell, as shown in Fig. 4.6, then an electron in a nanoparticle from cluster 1 entering the barrier presented by the dielectric into cluster 2 for example, will have certain transmission probability T, and reflection probability R, depending exponentially on the energy gap. This energy gap is defined by the highest occupied molecular orbital (HOMO) and the lowest unoccupied molecular orbital (LUMO) of the dielectric shell and the length L of the barrier [154]. The transmission probability and hence electrical transport is sensitive towards variation of interparticle separation distance and can be represented as [154],

$$T \sim q^{-2\sqrt{mE_g}L/\hbar} \tag{4.10}$$

A general description of transport for such conductor/semiconductor nanocomposites in 2 or 3 dimensions can be achieved in the framework of three-phase percolation models. In these models, three phases are distinguished, namely the conductor phase, the insulator phase, and the regions close to the interfaces. The overall conductivity of this form of nanocomposite is usually determined by the percolation behavior of the interfacial regions [156]. Many important properties of polymer-nanoparticle composites usually change in proximity to the percolation transition that occurs when a continuous path of touching or nearly touching nanoparticles is established from one side of the film to the other [157]. As the relative amount of particles compared to the dielectric medium increases, the dielectric thickness separating the clusters reduces, thus increasing the transmission probability of electron from one cluster to another. When the particle concentration reaches the percolation threshold, conduction switches from one dominated by tunneling to that due to the touching particles.

University of Cape Town

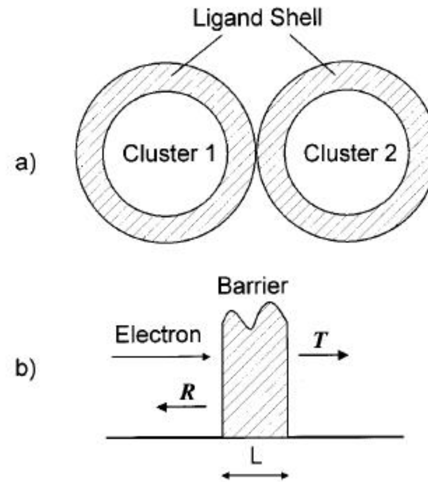

Fig. 4.6: (a) Two embedded clusters of nanoparticles separated by a junction, where the thickness of the dielectric shell determines the length of the insulating barrier. (b) An electron entering the barrier of length L from the left hand space. Barrier height and length determine the transmission probability T and the reflection probability R, where $T = 1 - R$. Taking from [154]

University of Cape Town

Various mechanism have been employed to describe the conduction process of nanocomposites and dielectrics in general. The important ones are variable hopping conductance, space charge limited current, Poole-Frenkel/Schottky-Richardson and the Fowler-Nordheim conduction process. These different processes shall be discussed in detail in subsequent sections. However, because of the role played by interfaces, especially at the metal-semiconductor or metal-nanocomposite junction as the case may be, the next section focuses on conduction processes that may result from the natures of the interface of a metal-semiconductor junction for example.

4.3 Current transport process across a metal semiconductor interface

The current transport mechanism across a metal-semiconductor contact has been associated to one due to majority carrier rather than to minority carrier transport found in a PN junction [145]. Five main processes of charge carrier transport have been identified for metal semiconductor metal systems under forward bias as shown in Fig. 4.7 [145]. For an n-type semiconductor-metal contact for example, the following processes may occur:

1. Charge carriers transport may either be through emission from the semiconductor over the potential barrier $q\phi_{BN}$ presented at the metal semiconductor interface, represented

by the arrow of process 1 in Fig. 4.7

2. The transport process may be due to quantum mechanical tunneling through the barrier from the semiconductor to the metal. This process is pronounced for heavily doped semiconductor and it is responsible for ohmic conduction at a metal semiconductor interface [151, 158]. This is represented by the arrow of process 2.

3. The third type of transport that may occur is recombination in the space-charge region created at the metal semiconductor junction. This is similar to the recombination in a PN junction, represented by the arrow of process 3.

4. Due to a possible electron density gradient at the interface of a metal-semiconductor junction, diffusion of electrons in the depletion region may occur. This is represented by the arrow of process 4.

5. The fifth is one of hole injection from the metal into the semiconductor. Represented by the arrow of process 5.

However, when the interface is formed with a composite of semiconductor and polymeric binder, one would expect the transport mechanism to be a mixture of the above mention processes plus the well know hopping transport in polymer blend films with metallic electrodes [159]. The following subsections highlight some of the common transport models that are widely applied to describe charge carrier transport through a metal-semiconductor/dielectric-metal interface structures.

University of Cape Town

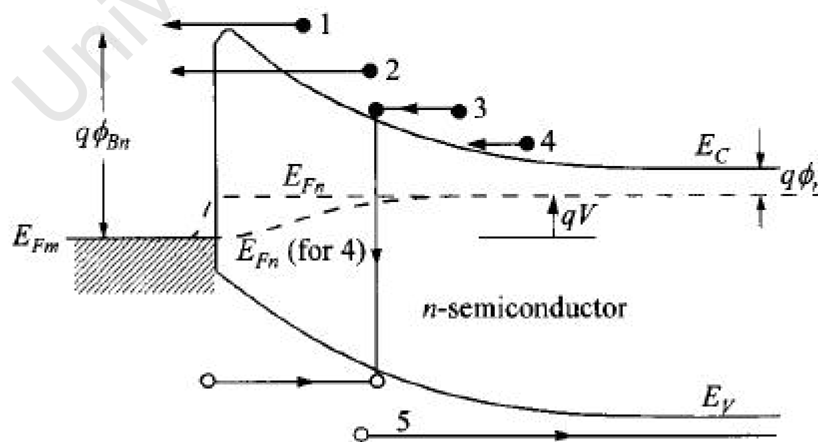

Fig. 4.7: Five basic transport processes under forward bias of a metal semiconductor contact. (1) Thermionic emission. (2) Tunneling. (3) Recombination. (4) Diffusion of electrons. (5) Diffusion of holes. taken from [145].

4.3.1 Thermionic emission theory.

Thermionic emission (TE) in solids is the process where charge carriers (electrons) from a surface are driven over a barrier by acquiring thermal energies larger than the confining barrier or electrostatic forces restraining the charge carriers. The current density $J_{S \rightarrow M}$ from semiconductor to metal is due to the density of carriers with energies sufficient to overcome the potential barrier created at the metal semiconductor interface, and can be represented as [145]

$$J_{S \rightarrow M} = \int_{E_f + q\phi_{B0}}^{\infty} q v_x \partial n, \tag{4.11}$$

where $E_f + q\phi_{B0}$ is the minimum energy required for thermionic emission into the metal from the semiconductor and v_x is the carrier velocity in the direction of the transport [149]. The electron density ∂n is given by [145]

$$\partial n = N(E) F(E) \partial E, \tag{4.12}$$

where $N(E)$ and $F(E)$ are the density of state and distribution function respectively.

When a voltage is applied across the metal semiconductor contact, the current density $J_{S \rightarrow M}$ can be obtained from solving equation 4.11 to give

$$J_{S \rightarrow M} = A^* T^2 exp\left(\frac{-q\phi_B}{K_B T}\right) exp\left(\frac{qV}{K_B T}\right), \tag{4.13}$$

where q, ϕ_B, V, K_B and T have there usual meaning, and

$$A^* = \frac{4\pi q m^* K_B^2}{h^3}, \tag{4.14}$$

is the Richardson constant for thermionic emission, which for free electrons or N type silicon $A^* = 120 A/cm^2 K^2$ (For detail derivation of equation 4.13 and 4.14 see [149]).

The implication of equation 4.13 is that the barrier height for electrons moving from the metal to the semiconductor is unaffected by the applied voltage, and is therefore proportional to the current flowing from the semiconductor to the metal with no applied voltage (i.e. when

University of Cape Town

$V = 0$) given by

$$J_{V=0} = -A^{*}T^{2}exp\left(\frac{-q\phi_{B}}{K_{B}T}\right). \tag{4.15}$$

This is called the saturation current [160].

4.3.2 Field emission/tunneling current theory.

Generally for a heavily doped semiconductor or for operation at low temperatures, the depletion region is so narrow that the electrons can tunnel through the barrier near the top, where the barrier is thin enough. Such process is termed, Thermionic Field Emission (TFE). In other instances, for degenerate semiconductor systems, electrons can tunnel through the barrier near the fermi level, in which case the tunneling current will be dominant. Such a mechanism is called Field Emission (FE). This is illustrated in Fig. 4.8 for a Schottky barrier junction formed by a metallic contact to an n-type degenerate semiconductor under forward and reverse bias operation [160].

The relative contributions of these components, depend on both temperature and doping level. A rough criterion for determining which of the emission type dominates in a transport, is to compare the thermal energy kT to E_{oo}, where E_{oo} is defined as [145, 151, 150]

$$E_{oo} \equiv \frac{q\hbar}{2}\sqrt{\frac{N}{m^{*}\varepsilon_{s}}}. \tag{4.16}$$

Three main deductions can be made from this comparison. First, when $k_{B}T >> E_{oo}$ TE dominates and the original Schottky-barrier behavior prevails without tunneling. Secondly, when $k_{B}T << E_{oo}$, FE (or tunneling) dominates. And lastly, when $k_{B}T = E_{oo}$, TFE which is a combination of TE and FE is the main mechanism [150, 145].

4.3.3 Diffusion theory.

The diffusion theory for minority carriers near the junction of a metal-semiconductor assumes that the depletion layer formed at the metal semiconductor interface is large compared to the mean free path of the carriers [152]. It also assumes that the current in the depletion region depends on the local field and concentration gradient [145]. The current density under

University of Cape Town

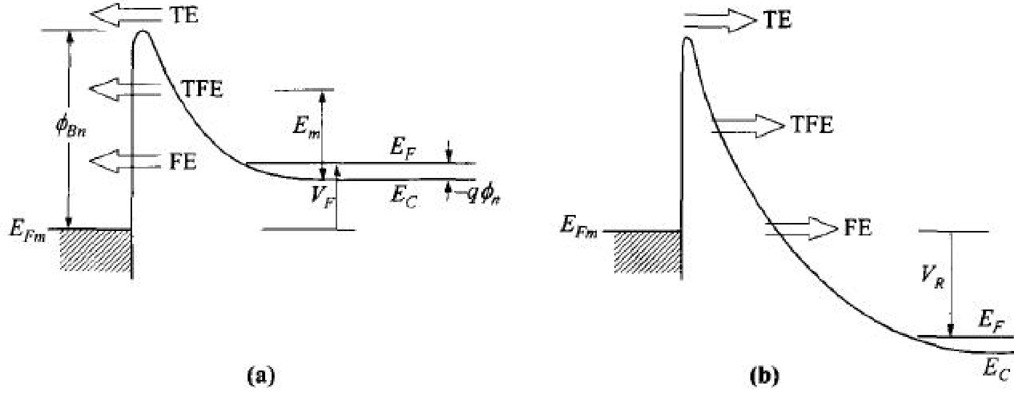

Fig. 4.8: Energy band diagram showing different tunneling current type under (a) forward bias and (b) reverse bias of a metal-n-type degenerate semiconductor. Taken from[145].

University of Cape Town

this condition can be expressed as

$$J_n = q\left(n\left(x\right)\mu E + D_n\frac{\partial n}{\partial x}\right), \tag{4.17}$$

where μ is the mobility and D_n is the diffusion constant for the carrier. In the presence of a Schottky barrier, equation 4.17 is solved to yield a current which depends exponentially on the applied voltage V, and the barrier height ϕ_B,

$$J_n = \left(\frac{q^2 D_n N_c}{KT}\left[\frac{q(V_{bi}-V)2N_D}{\epsilon_s}\right]^{1/2}\right) exp\left(\frac{-q\phi_B}{K_BT}\right) exp\left(\frac{qV}{K_BT}-1\right), \tag{4.18}$$

$$= J_{SD} exp\left(\frac{qV}{K_BT}-1\right), \tag{4.19}$$

where V_{bi} is the built in potential and all other symbols have there usual meaning. One important distinction between the saturation current density for thermionic emission transport and that due to diffusion, is that the saturation current density for thermionic emission depends largely on temperature, whereas the saturation diffusion current is less sensitive to temperature but varies with the applied voltage across the barrier. The other difference to thermionic and tunneling current is that current is due to the non equilibrium distribution of free carriers in the depletion/space charge region.

4.3.4 Space charge-limited current (SCLC) theory.

Electronic properties of semiconductor materials are strongly influenced by the presence of carrier trapping centres. The space charge limited current model has been used to explain the electrical properties of some semiconductor and insulator materials [161, 162, 163, 164, 165, 166], and could possibly be employed for the analysis of a hybrid system formed by embedding semiconductor particles in a dielectric matrix.

The SCLC results from carrier injection into a semiconductor or insulator, as the case may be, from a metallic contact. SCLC is due to the presence of a disordered localized state distribution within the range of the energy gap, and may be consider as trapping levels similar to localized state caused by impurity and dislocations [167]. The presence of these traps levels leads to reduction of the conduction current, as these traps remove most of the free carrier from the conduction stream. Even injected charges may be trapped and immobilized.

For a trap free state, the current is proportional to the square of the voltage. After an initial current flow, positive and negative space charge builds up near the metal-insulator and semiconductor insulator interface, bringing about a distortion in the potential distribution at the interface, resulting in current with a power law dependency on the applied voltage, $I \propto V^m$[161]. When the applied voltage is removed, a large internal field remains, which causes some but not all charges to flow back to their equilibrium position, resulting in the $I-V$ characteristic showing hysteresis [149].

For SCLC in the presence of discrete charge trapping, the charge transport mechanisms can be represented as

$$J = \frac{9}{8}\epsilon\mu\theta\frac{V^2}{d^3}, \tag{4.20}$$

where ϵ is the dielectric constant of the materials, and μ is the mobility of charge carrier. d is the distance between electrodes and θ is the ratio of the free carrier density P_0 to the trapped carrier density P_t, given by

$$\theta = \frac{P_0}{P_t} = \frac{N_{fc}}{N_t} exp\left(\frac{-E_t}{K_B T}\right), \tag{4.21}$$

where N_{fc} is the effective density of free charge carrier in the valence band, N_t is the trapped carrier density and E_t is the energy of trap level.

University of Cape Town

Experimentally, θ can be determined from the ratio of the current at the beginning I_1, and at the end of the rise I_2, of the square law region [168]. Thus

$$\frac{I_1}{I_2} = \theta = \frac{N_{fc}}{N_t}. \tag{4.22}$$

When traps are present, the Trap-Charge-Limited-Current (TCLC) density becomes pronounced. With an exponential distribution of traps in the band gap of the materials, the current is given by

$$J = q\mu N_{fc}\left(\frac{\epsilon\epsilon_0}{qN_t}\right)^l \frac{V^{l+1}}{d^{2l+1}}, \tag{4.23}$$

where ϵ_0 is the permittivity of free space,
and d is the separation distance of the contacts,
N_{fc} is the effective density of carriers in the valence band and l is a parameter given by

$$l = \frac{T_t}{T}, \tag{4.24}$$

where T_t is a characteristics temperature and the density of trap state is given by,

$$N_t = P_{oE}K_BT_t, \tag{4.25}$$

where P_{oE} is the carrier density per unit energy at the valency band, and the exponential trapping distribution give by,

$$P(E) = P_{oE}exp\left(\frac{-E}{K_BT}\right). \tag{4.26}$$

For higher field there may be a sharp rise in current with a small change in voltage. This rise corresponds to complete filling of the traps N_t. The total trap density can be related to the value of the trap filling voltage V_{tr} by the following [164]

$$N_t = \frac{2\epsilon}{ed^2}V_{tr}. \tag{4.27}$$

Using Equation 4.23 and 4.25 the value for N_t and P_{0E} can be estimated. The equilibrium concentration of charge carriers in the valence band can also be estimated from the knowledge

University of Cape Town

of V_{tr} given by

$$N_{fc} = \left(\frac{\epsilon \epsilon_0 \theta}{q d^2} \right) V_{tr}. \tag{4.28}$$

University of Cape Town

4.4 Experimental procedure

4.4.1 Materials and sample preparation

To investigate the charge carrier transport through silicon nanocomposites based on inclusion of milled P type and metallurgical silicon powder into linseed oil and acrylic medium, a metal-nanocomposite-metal structure was formed. To serve as substrate, a commercially available perspex sheet, cut into size of $50mm \times 50mm \times 5mm$ was used. The surface of the plastic was cleaned with ethanol before printing. A transfer printing method was used to print a conducting silver paste (5000 silver conductor) from Du Pont [169] on to the surface of the plastic. This method which utilises a rubber pad, for picking up a pattern engraved on a metallic cliche will be discussed in the next chapter on device fabrication.

Fig. 4.9 shows a schematic of the printed metallic electrodes on plastic substrate. The printed silver structures were allowed to cure in open air overnight and then heat treated in an oven set at 120^oC for 30 minutes as recommended by Du Pont. This ensure a resistivity of about $1.5 \times 10^{-5}\Omega cm$ which is negligible when compared with the resistivity of the nanocomposites used for this experiment. The structure consist of two silver electrodes separated by a distance $d = 0.3mm$. The electrodes have a width of $5mm$ and are $\approx 70\mu m$ thick after curing.

University of Cape Town

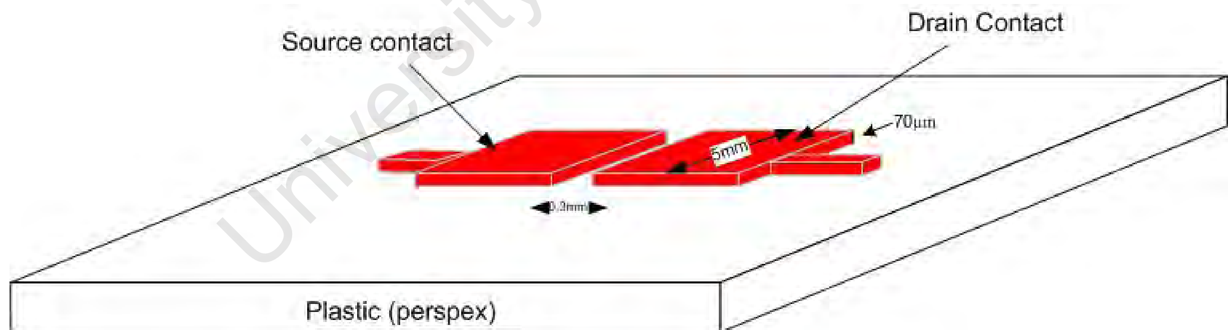

Fig. 4.9: The transfer printed silver electrode on plastic. The structure parameter are $W = 5mm, L = 0.3mm$ and thickness $70\mu m$.

Following the procedure described in chapter 3, silicon powder produced from P-type wafers, of resistivity $14 - 22\Omega cm$, and from metallurgical silicon milled for 5 hours were dispersed separately in linseed oil and acrylic medium to form nanocomposite inks, with varying proportion of the fillers in the separate binders, as shown for the P powder in table 4.1. Printing of these inks onto the already cured silver strips was carried out using a stencil and doctor blade technique described earlier in chapter 3. Fig. 4.10 illustrates the printing of the

nanocomposite inks over the channel created by the metallic electrode, and also spreading over a large area of the electrode to ensure electrical connection with a glass rod. The masking tape used for the stencil is of thickness $\cong 180\mu m$, and the resulting nanocomposite film thickness after shrinkage on curing was estimated to be $\cong 140\mu m$.

Table 4.1: Nanocomposite ink formulation for P type powder in linseed and acrylic, with ink label and the corresponding composition of nc-Si:binder ratio and also type of solvent used for wetness purpose.

nc-Si	Ink type	Binder	nc-Si:Binder ratio(wt.%)	Solvent
P	PLIN-10-01	Linseed oil	10 : 90	Lacquer thinner
P	PLIN-30-01	Linseed oil	30 : 70	Lacquer thinner
P	PLIN-50-01	Linseed oil	50 : 50	Lacquer thinner
P	PLIN-60-01	Linseed oil	60 : 40	Lacquer thinner
P	PLIN-70-01	Linseed oil	70 : 30	Lacquer thinner
P	PLIN-80-01	Linseed oil	80 : 20	Lacquer thinner
P	PLIN-90-01	Linseed oil	90 : 10	Lacquer thinner
P	PACR-10-01	Acrylic paste	10 : 90	Distilled Water
P	PACR-30-01	Acrylic paste	30 : 70	Distilled Water
P	PACR-50-01	Acrylic paste	50 : 50	Distilled Water
P	PACR-60-01	Acrylic paste	60 : 40	Distilled Water
P	PACR-70-01	Acrylic paste	70 : 30	Distilled Water
P	PACR-80-01	Acrylic paste	80 : 20	Distilled Water
P	PACR-90-01	Acrylic paste	90 : 10	Distilled Water

University of Cape Town

4.4.2 Forward and reverse I-V measurement

The experimental setup used for the electrical characterization of the samples consist of the Keithley 4200 SCS complete $I-V$ characterisation setup, with current and voltage resolution of $1pA$ and $2\mu V$ respectively. This instrument was used with an in-house constructed probe station, which consists of a sample platform and three probes enclosed in a double walled box made from aluminum sheet, with the walls electrically isolated from each other with expanded polystyrene as shown in Fig. 4.11. This is to ensure that the effect of electromagnetic noise from near by electrical systems is minimized.

The polystyrene also acts as a heat insulator for temperature dependent measurement using an enclosed heating system. This system consists of a wire wound heater, controlled by a microprocessor. The controller system is fitted with an LM34 feed back temperature sensor, which is accurate to $\pm 1^0 C$ of the set point. The heater control uses a digital implementation of a proportional integral derivative (PID) scheme, programmed into the microprocessor for modulating the pulse width of the DC current through the heater. The noise from the heater

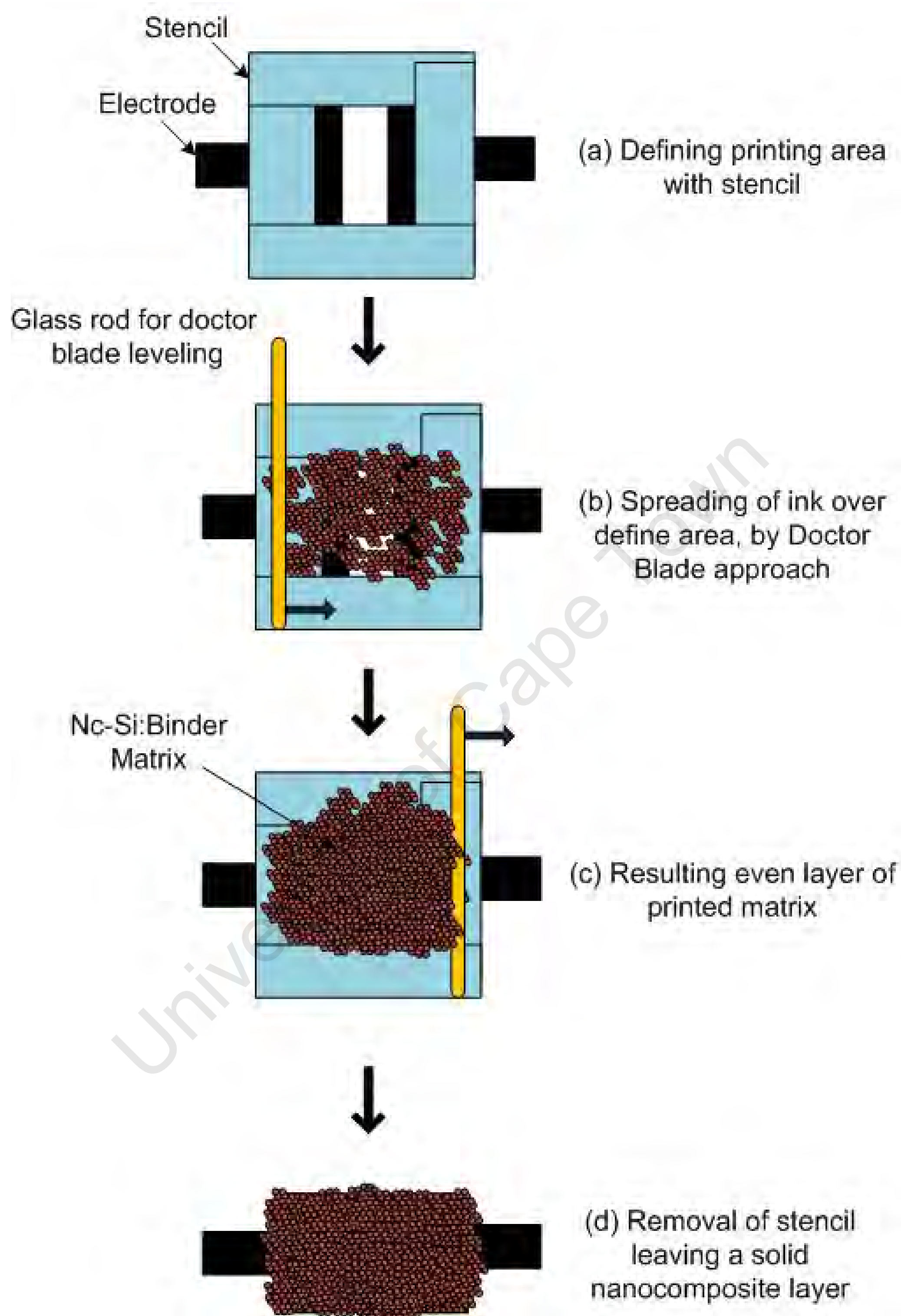

University of Cape Town

Fig. 4.10: Stencil printing a silicon nanocomposite structures on pre-printed silver electrodes on plastic substrate

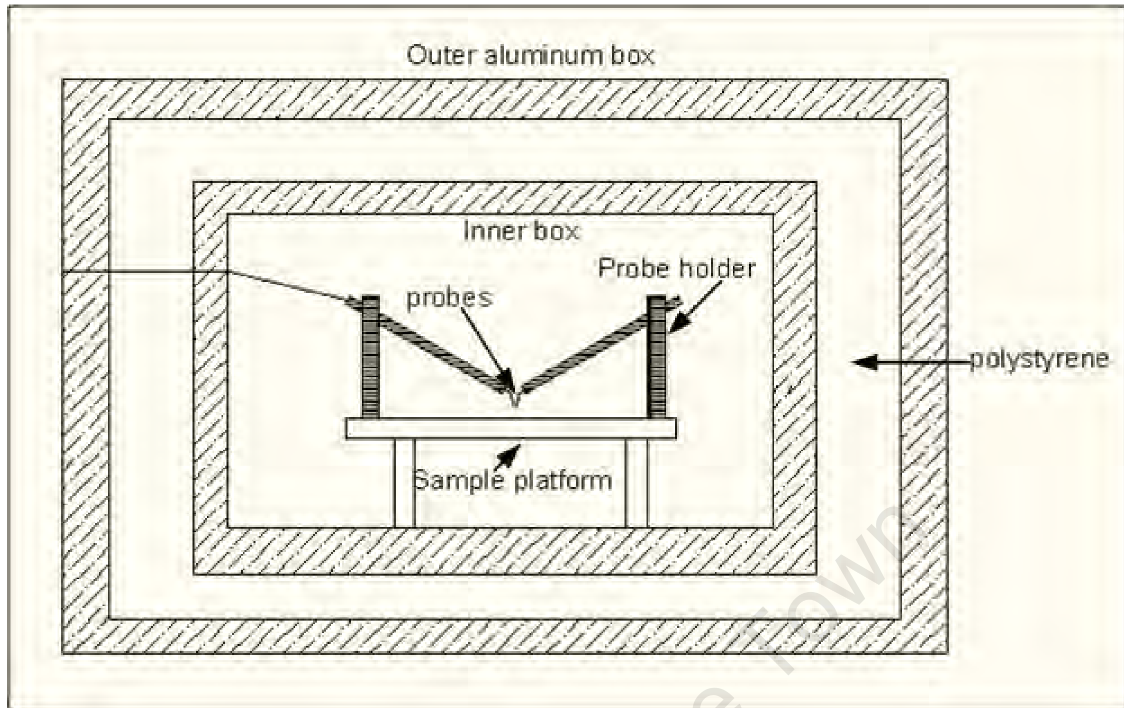

Fig. 4.11: Double walled box probe station for electrical measurement.

University of Cape Town

and other external electrical system was found to be negligible. The enclosed box also serves as a shield to any source of light that may result in photo induced conduction.

The Keithley system was programmed to sweep the bias voltage across the electrodes of the metal-nanocomposite-metal structures from $-200V$ to $200V$ in a dual sweep mode, simultaneously logging current measurement with voltage on a spread sheet. A hold time of 60 seconds and sweep delay of 1 second was set to allow for current settling after each sweep. A filter factor of 5 was used, this features allows for taking and averaging over 5 successive current measurement for a given voltage step. $I-V$ characteristics was carried out at 295K to 363K for the PLIN samples and then at 295K on all the samples. The results of the different $I-V$ measurements were later analysed with Origin Software.

4.5 Results and Discussion

4.5.1 Assumptions for the determination of carrier transport type.

Fig. 4.12 illustrates the metal-nanocomposite-metal structures on plastic substrate used for these experiments. The procedure for determining the charge carrier transport in the different nanocomposite structure, assumes that the flow of positive current due to application of a potential difference across the structure is lateral, and current flow through the area presented by the wall of the electrode only, as illustrated in Fig. 4.12(a). The area for current flow is $3.5 \times 10^{-7} m^2$, calculated from the average thickness of the electrode $t = 70 \mu m$ and the width of the electrode $W = 5mm$.

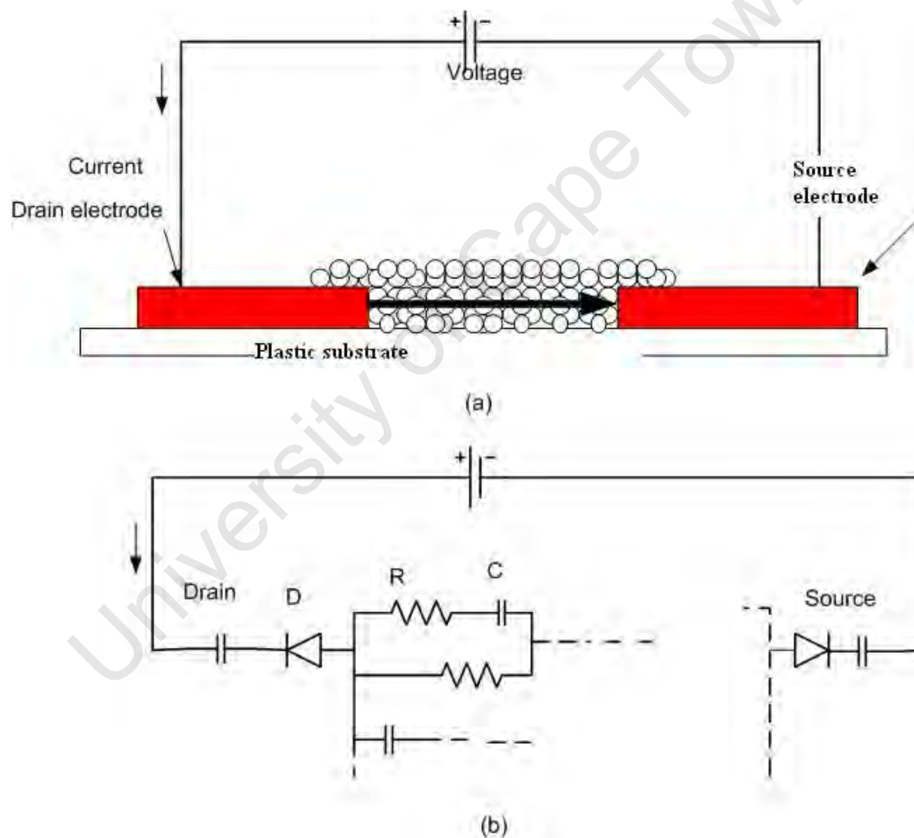

University of Cape Town

Fig. 4.12: (a) Schematic diagram of the test structure (b) electrical model of the nanocomposites structure under electrical bias

A simple illustrative model that can describe the structure of the metal-nanocomposite-metal structure is shown in Fig. 4.12(b). This assumes a perfectly symmetric back-to-back diode configuration, with a random connection of resistors and capacitors in between the two diodes at the drain and source electrodes. The back-to-back diode configuration is assumed

to result from the contact between the source and drain electrodes and the nanoparticles, while the resistors model the linear resistance of the nanoparticles measured from one end to the other, and the capacitors result from the presence of an interfacial layer between a pair of nanoparticles for example.

The forward current from the drain to source electrode will be hindered by: (1) a barrier at the contact of the drain to the silicon particles; (2) by insulation resulting from an interfacial layer at the boundary of the drain/nanocomposite; (3) the impedance resulting from the random distribution of resistors and capacitors; and finally at the source end, (4) the barrier presented by the contact of the source electrode to the nanocomposite under forward bias and the possible insulation layer at the source electrode nanocomposite interface. A complex combination of charge transport processes may result from a real nanocomposite structure such as presented in this work. As such, the analysis presented in the following sections will follow a systematic study of all possible conduction mechanism that may predominate or coexist. First, the assumption that a particular charge carrier transport process dominates will be made, and deduction will be based on how well the test of the particular transport model fits the experimental $I-V$ characteristics. Particularly, the effect of varying the concentration of the particle on $I-V$ characteristics will be focussed on.

4.5.2 Temperature dependence of the forward I-V characteristics

Temperature dependent $I-V$ characteristics measurement of a metal-semiconductor (MS) contact is an important method for obtaining information about the different conduction mechanism that could result due to the MS contact [170, 171, 172]. The thermionic emission theory (TE) describes the effect of temperature on important Schottky contact parameters such as Schottky Barrier Height (SBH) and the ideality factor. For an ideal Schottky contact, the $I-V$ characteristics should have a positive temperature dependence, since the current transport across the metal-semiconductor interface is a temperature activated process [171].

The presence of series resistance R_s in a Schottky contact and a thin insulator layer at the MS interface are important parameters that affect the behaviour of MS Schottky contacts. Usually at low bias voltages, the forward current has an exponential dependence on the voltage but deviates due to the effect of device parameters, such as the series resistance when the applied voltage is sufficiently large [173, 174].

Figure 4.13 shows the temperature dependent, forward and reversed bias dark I-V plots for the PLIN based nanocomposites with particle loading of 30, 50, 70 and 90 wt.% as an

University of Cape Town

example, for temperature in the range 295K to 353K in step of 10K (see the Appendix Fig. A.1 for the 10, 60 and 80 wt.% plots). From the plots, three basic features can be identified:

- Samples PLIN-10-01 and PLIN-30-01 show a positive dependence of the Source-Drain current on temperature for the entire applied external voltage range, while samples with particle loading above 50 wt.% show a negative dependence of the source-drain current on temperature.
- The $I - V$ characteristics for the samples PLIN-10-01 and PLIN-30-01 are fairly linear for both positive and negative voltages, with two different slopes, while the $I - V$ characteristics of the samples with higher particle loading show a clear nonlinear behaviour.
- The $I - V$ characteristics for forward as well as reverse bias of the structures are fairly symmetric for all the samples with high particle loading. This is to be expected because the test structure themselves are symmetrical with similar contacts at each side.

A repeat of the experiment for the another pair of samples prepared from the same inks, namely samples PLIN-10-02 to PLIN-90-02, shows the same characteristic $I - V$ behaviour, indicating that the features are not just random but apply in general to this category of structures.

To examine the temperature behaviour closely, an Arrhenius plot of current on a logarithmic scale and temperature on a reciprocal scale was plotted for the different samples. Fig. 4.14 shows the Arrhenius plot at a fixed voltage of 150V for the low particle loading (10 and 30 wt.%) and higher particle loading (50 and 90 wt.%) samples. The lower concentration composites exhibited a positive current dependence on temperature, while the composites with particle loading above 50 show a negative dependence of the current on temperature. The 50 wt.% composite in particularly, exhibited both behaviours, with the negative behaviour being much more pronounced. A possible interpretation of the temperature dependent behaviour as seen in these composites, can be derived from decomposing the thermionic emission model, given as [145]

$$J_{S \to M} = A^* T^2 \exp\left(\frac{-q\phi_B}{K_B T}\right) \left[\exp\left(\frac{qV}{nK_B T}\right) - 1\right] \tag{4.29}$$

into a form from which the Arrhenius plot is derived. Assuming the exponential in V is large compared to unity,

$$\ln J = \ln A^* + 2 \ln T - \frac{\phi}{K_B T} + \frac{qV}{nK_B T}. \tag{4.30}$$

At low concentration the energy of the carriers is much lower than the barrier presented

University of Cape Town

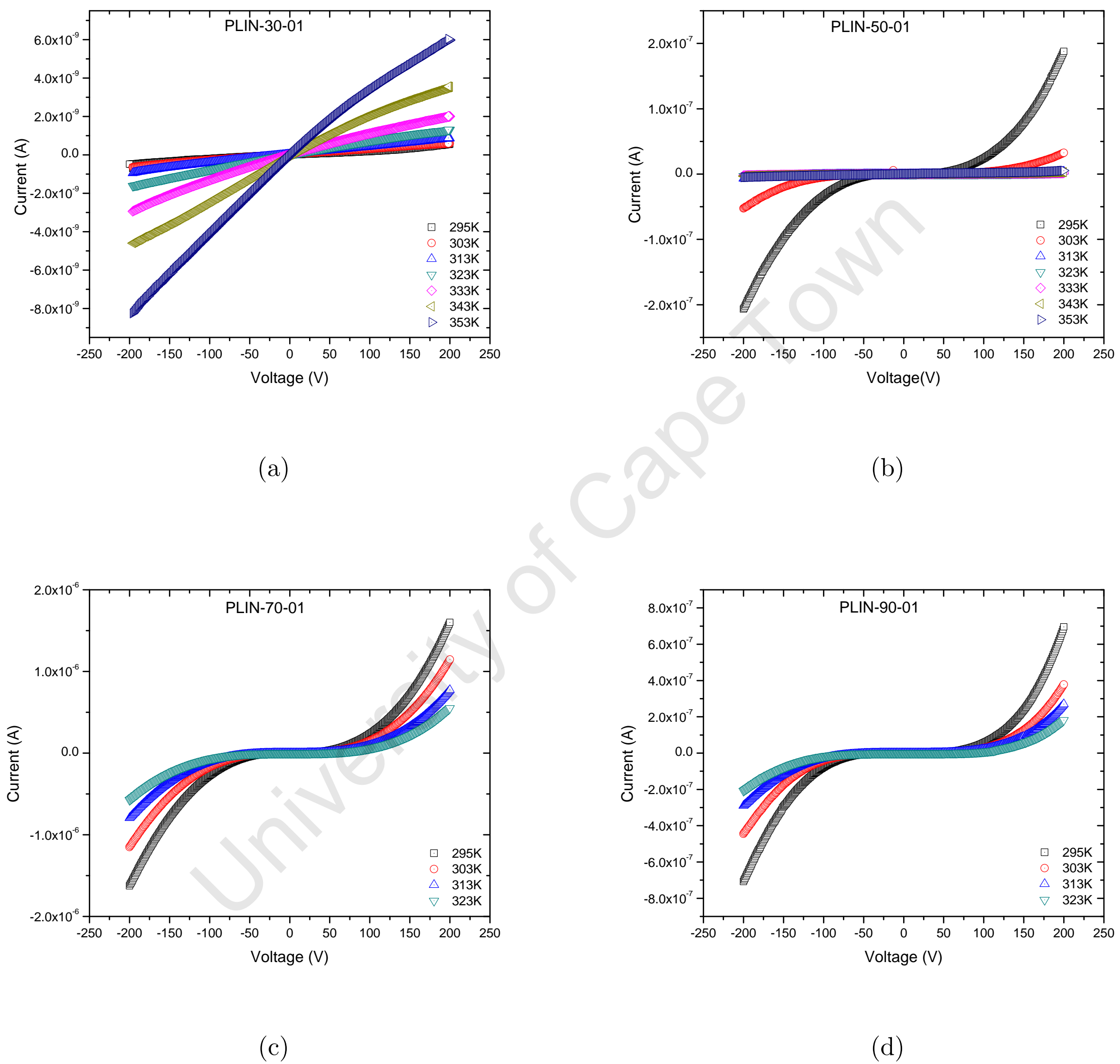

University of Cape Town

Fig. 4.13: Temperature dependent forward and reverse bias I-V characteristics for samples (a)PLIN-30-01, (b)PLIN-50-01, (c) PLIN-70-01, (d) PLIN-90-01 in the temperature range specified on each plot.

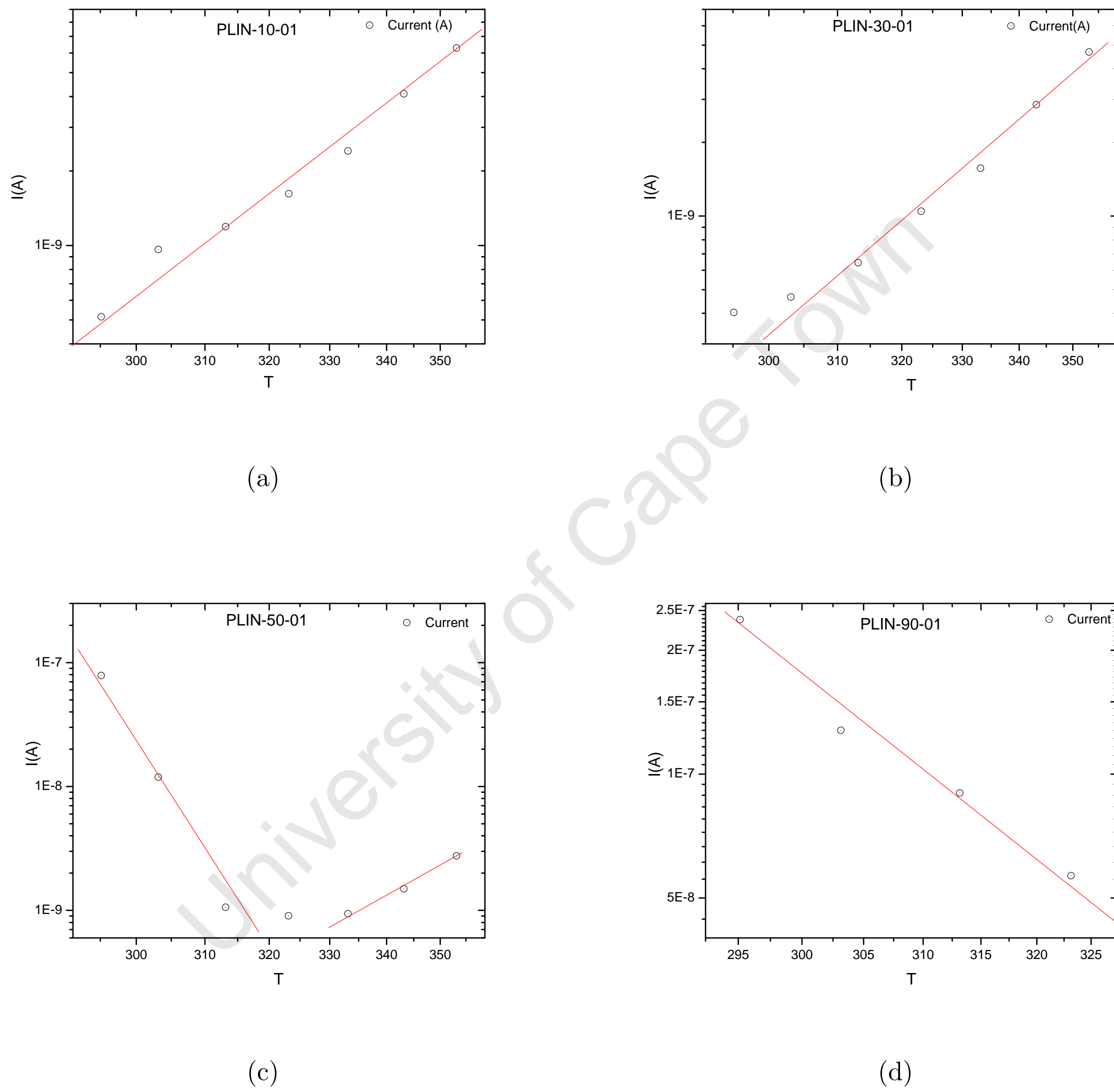

University of Cape Town

Fig. 4.14: Arrhenius plot of current on a logarithmic scale vs. temperature on a reciprocal scale for (a)PLIN-10-01, (b)PLIN-30-01, (c) PLIN-50-01 and (d) PLIN-90-01 showing a positive temperature dependence of current for particle loading 10 and 30 while for particle loading 50 and above shows negative dependence.

at the interface of the metal nanocomposite structure ($qV/n \ll \phi$). As the temperature increases the carriers have sufficient thermal energy to overcome any thermally activated barrier. At higher concentrations the carriers energy is close to or above the barrier height ($qV/n \gg \phi$), and as such current injection through the reverse biased junction is not due to thermal activation in this case. The nanocomposite with 50wt.% concentration appears as the midpoint between the positive and negative temperature activated process as it exhibits both behaviour.

The obvious change from fairly linear $I - V$ characteristics at 10 and 30 wt.% to nonlinear behaviour at particle loading above 30 wt.% can be associated with a change in the nature of transport at certain critical filler concentration $c \approx 50wt.\%$ from transport dominated by the properties of the matrix to that due predominantly to the Si nanoparticles [18].

Due to this opposite behaviour of the dependence of the I-V characteristic at low and at high concentrations, it is difficult to compare the different samples based on temperature. However since the samples must all operate at room temperature, the following sections will limit the study of the $I - V$ characteristics of the nanocomposites and determination of the charge transport to 295K, the ambient temperature in the measurement box. In many of the sections, basic charge transport theories particular to how it applies to the nanocomposites under discussion in this study will be introduced or restated for emphasis.

University of Cape Town

4.5.3 Characteristic I-V behaviour at 295K

Fig. 4.15 shows the characteristic forward and reverse $I - V$ behaviour at 295K for seven different particle loadings of the P type and metallurgical silicon powders, in linseed oil and acrylic medium.

Considering the linseed oil based nanocomposites, Fig. 4.15(a) and (b), five basic features can be deduced:

- The $I - V$ characteristics for 10 and 30 wt.% silicon composites are fairly linear, with a relatively low current compared to particle loadings above 30 wt.%, which exhibit a characteristic nonlinear behaviour at higher voltages. A comparison of the $I - V$ characteristics for samples PLIN-xx-01 and MLIN-xx-01 with their respective pairs PLIN-xx-02 with MLIN-xx-02(see Appendix Fig. A.2), shows a close similarity for each type, suggesting a fair reproducibility of the $I - V$ behaviour.
- There is an increase in conductivity of the nanocomposite with increasing particle loading up to a maximum around $70 - 80wt.\%$. For particle loading above this, the conductivity reduces to a lower value as shown in the inset for current at 150V.
- As discussed above, the curves are symmetrical in both current directions.
- The maximum measured current for a given voltage is higher for the PLIN system than the MLIN system.
- Both systems exhibit some hysteresis, as the decreasing (-200 to 200 V in step of 1V) $I - V$ characteristics do not follow the same path as the increasing (200 to - 200V in step of -1V).

University of Cape Town

A similar consideration of the acrylic based nanocomposites, shows that:

- there is an optimal ratio of approximately $30wt.\%$ silicon powder in acrylic for which the conductance is maximum.
- Similar to the linseed oil based nanocomposites, the acrylic based nanocomposites exhibit hysteresis in the $I - V$ behaviour.

From the above observations, it is tempting to discuss the characteristics in terms of percolation. Using percolation conditions, for a particle concentration P above a critical concen-

tration P_c, the conductivity scales in the vicinity of P_c as [18]

$$\sigma = \sigma_o \left(P - P_c \right)^{\gamma}, \tag{4.31}$$

for values of $P > P_c$, where γ is the conductivity exponent which is independent of geometry of the system. Assuming the different binders, linseed oil and acrylic medium, to be perfect insulators, then the conduction part is formed by the network of Si clusters. For this system however, the conductivity is observed to reach a maximum at $70 - 80wt.\%$ in the case of linseed oil, and around $30wt.\%$ in case of the acrylic based systems, after which a further increase in concentration results in a reduction in conductivity. This suggests a conductivity type deviating from that predicted by percolation theory, due to some other factors. For example, for 10 and 30 wt.% nc-Si in linseed oil the $I-V$ characteristic is fairly linear. At this filler to binder ratio, the fillers (nc-Si) and the different clusters may be isolated from each other and from the electrodes by interface layers due to the binder as seen earlier in the SEM micrographs of the composites in chapter 3. From 50 wt.% however, the nonlinear behaviour of the $I - V$ characteristics suggests a switch of conductivity to one predominantly due to coupling of the Si clusters. Thus the critical concentration P_c for the linseed based system is approximately $50wt.\%$. The reduction in conductivity above $80wt.\%$ may be associated to reduction in the binding strength of the Si clusters to each other and to the metallic electrodes due to the reduced binder proportion. In the case of the acrylic based system, optimum conductivity is reached at $30wt.\%$ and further increase in concentration results in loss of strength in binding the clusters together, and thus reduction in conductance.

The reason for the improved performance of the P type Si over the metallurgical type Si may be associated with the initial resistivity of the bulk silicon in both cases. Also the improved performance of the linseed oil based composite over the acrylic composite may be attributed to the binding strength of the linseed oil over the acrylic binder resulting in a closed knitted network of its clusters relative to the open network of clusters in the acrylic composite as observed in chapter 3. The following sections will test the effect of particle loading on the charge carrier transport of the nanocomposites against different models starting with a thermionic emission model.

University of Cape Town

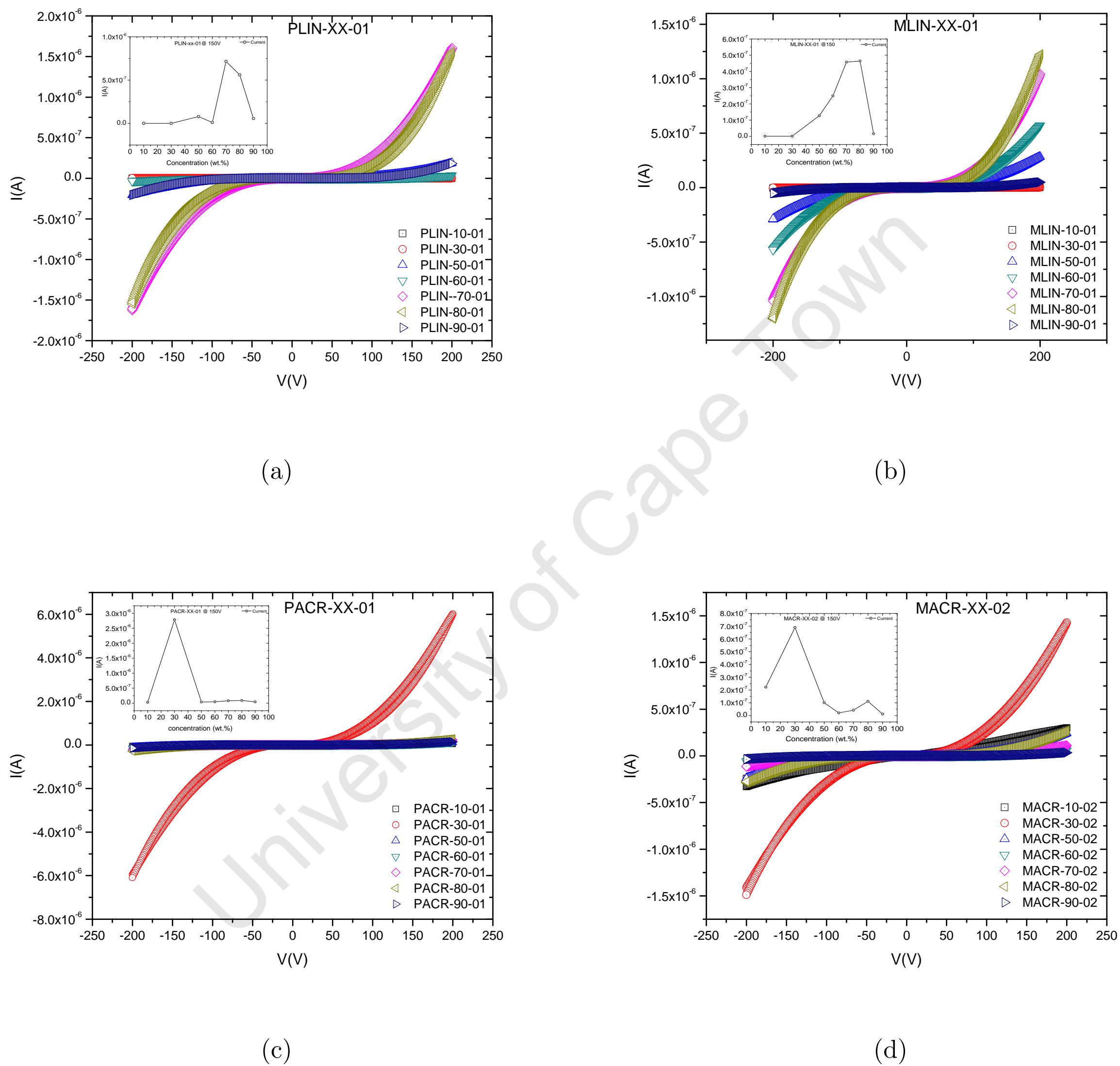

University of Cape Town

Fig. 4.15: Forward and reverse bias $I-V$ characteristics for (a) PLIN-xx-01 (b) MLIN-xx-01 (c) PACR-xx-01 and (d) MACR-xx-01, where xx stands for 10, 30, 50, 60, 70, 80 and 90 wt.% of the silicon powder. The inset shows the current at 150V as a function of particle loading.

4.5.4 Contribution of charge carrier transport due to thermionic emission (TE)

The main purpose of an $I-V$ measurement for a typical metal semiconductor structure is to determine the Schottky barrier height which often reveals the nature of the interface [150]. One of the important parameters that can be extracted from such $I-V$ measurement is the ideality factor n, which seemingly reveals how well a transport mechanism type matches thermionic emission at the interface [150].

Assuming a homogeneous Schottky barrier with carrier transport dominated by thermionic emission, analysis of the experimental forward bias $I-V$ characteristics can in principle be based on the thermionic emission theory model for which the current is [150]

$$I = I_o \left\{ \exp\left(\frac{q\,(V - IR_s)}{nK_BT} \right) - 1 \right\}, \tag{4.32}$$

where I_o is the saturation current given by [150],

$$I_o = AA^*T^2 \exp\left(-\frac{\phi_B}{K_BT} \right). \tag{4.33}$$

A is the area covered by the contact between the metal and nanocomposite, A^* is the Richardson constant [150], T is the absolute temperature, ϕ_B is the Schottky barrier height and K_B is the Boltzmann constant. The magnitude of I_o is usually independent of the applied potential, and can be derived experimentally from the intercept of a straight line of a semilog forward $I-V$ plot at $V = 0$ assuming $|IR_s| \ll |K_BT/q|$. The ideality factor n can likewise be derived from the inverse of the slope of the semi-logarithmic $I-V$ plot, and is expressed mathematically as [150]

$$n = \frac{q}{K_BT} \left(\frac{\partial\,(\ln I)}{\partial V} \right)^{-1}. \tag{4.34}$$

In equation 4.32, R_s is the series resistance from a combination of the bulk nanocomposite resistivity and the contact resistance at the metal nanocomposite interface. Usually the forward $I-V$ characteristics for an ideal Schottky contact are linear on a semi-logarithmic scale at low voltages, but deviate from linearity due to combined effect of series resistance, interface states, and large applied voltage bias. The series resistance R_s is then apparent in the non linear region of the semi-logarithmic $I-V$ characteristic at high applied voltages

University of Cape Town

[175].

The direct extraction of experimental values of the barrier height ϕ_B, ideality factor n, the saturation current I_0 and the series resistance R_s for the metal-nanocomposite structures used in this experiment, were determined from the forward semilog I-V characteristics at room temperature (295K) for the selected samples specified above, following procedure as discussed in [151, 172, 176, 171, 177]. Fig. 4.16 shows the semi-logarithmic $I-V$ plot for sample PLIN-10-01 and the application of the above method for the extraction of the parameters ϕ_B, n, I_0 and R_s as an example.

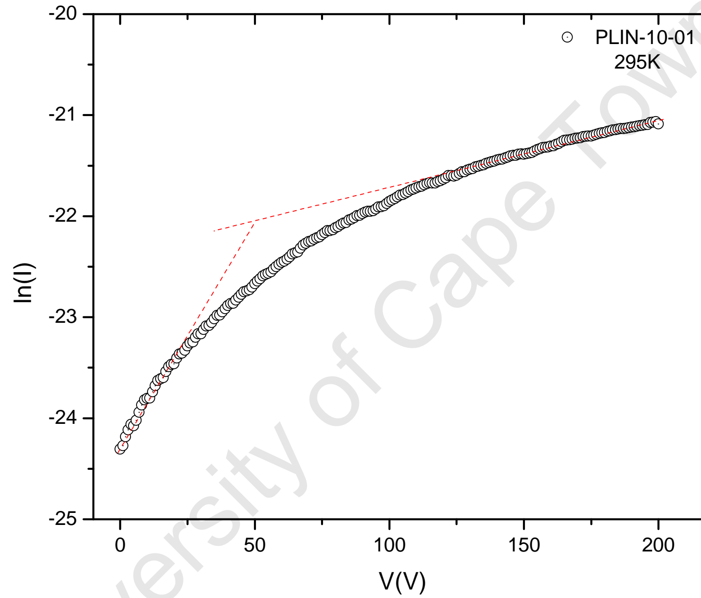

University of Cape Town

Fig. 4.16: Graph of $ln(I)-V$ for PLIN-10-01 used for direct extraction of thermionic emission (TE) parameters at (295K).

The ideality factor n was calculated from the slope of a best line of fit for the linear region at low bias voltage, using equation 4.34, to be $n = 928 \pm 24$. This high value reflects the departure of the transport from an ideal thermionic emission process, for which $n = 1$, suggesting that TE may not be a dominant charge carrier transport process in this particular device. The saturation current I_0 was derived from the intercept of the same line of fit at $V = 0$, as $I_0 = 2.92 \pm 0.04 \times 10^{-11} A$, from which the value of the Barrier Height (BH) was derived as $\phi_B = 0.85eV$. The series resistance was calculated from the slope at the high voltage region $120V < V \leq 200V$, where the effect of series resistance is pronounced, as $R_s = 2.74 \times 10^{11}\Omega$.

When the series resistance is significantly high, as in the case above, it is not always possible to discern a linear region in the semi-logarithmic $I-V$ plot. As such various schemes have been proposed which greatly facilitate the analysis of $I-V$ characteristics by using the low bias portion of the $I-V$ curves [150]. One of such is the method proposed by Cheung and Cheung [178] for extracting the series resistance R_s for ideality factor $n > 1$. This method was employed for the analysis of the $I-V$ characteristics of the selected samples for comparison. In this method, a plot of $dV/dln(I)$ vs I from equation 4.32 will yield a slope equal to the series resistance R_s, and the intercept on the y axis is proportional to the ideality factor n. Fig. 4.17 shows the application of this method to the $I-V$ characteristics of sample PLIN-10-01 at 295K. This method yields a lower ideality factor of $n = 615 \pm 54$ but a comparable series resistance of $2.2 \pm 0.1 \times 10^{11}\Omega$.

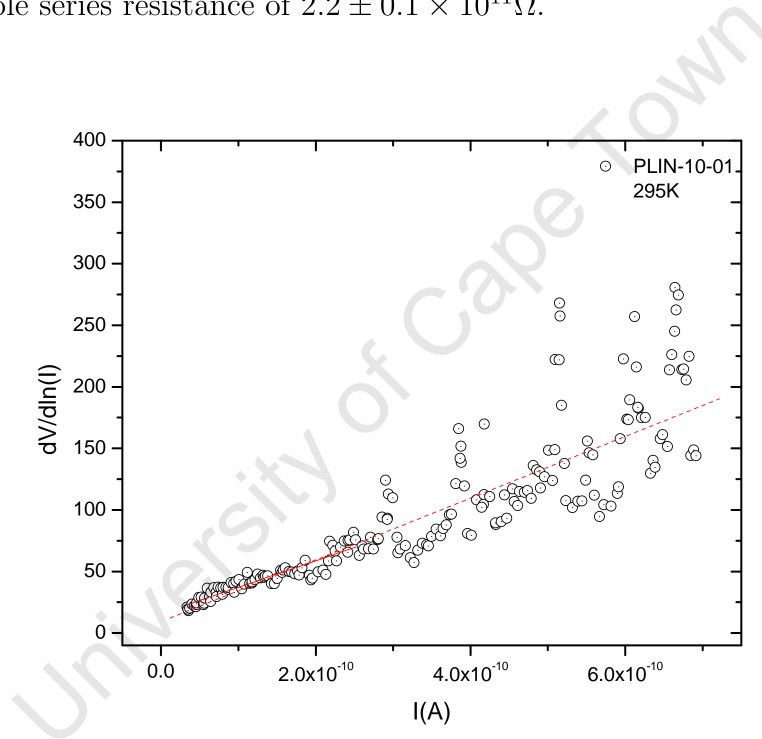

University of Cape Town

Fig. 4.17: Graph of $dV/dln(I)$ vs I demonstrating the Cheung and Cheung [178] method for extraction of series resistance and ideality factor on sample PLIN-10-01 at 295K.

The ideality factor derived from the above plot is then used in the extension [179],

$$H(I) = V - n\frac{KT}{q}\ln\left(\frac{I}{AA^{*}T^{2}}\right), \tag{4.35}$$

where $A^{*} = 32A/cm^{2}/K^{2}$, the Richardson constant theoretically calculated from the TE model for P type silicon was used [180]. Cheung and Cheung [179] showed that equation

4.35 can also be expressed as

$$H(I) = IR_s + n\phi_B. \tag{4.36}$$

A plot of the function $H(I)$ vs I will yield a straight line with a slope equal to the series resistance and the intercept is a product of the ideality factor and the barrier height. Fig. 4.18 shows the application of this method for the extraction of the barrier height and series resistance of the sample PLIN-10-01 at 295K. This method yields a barrier height $\phi_B = 0.84 \pm 0.07eV$ and a series resistance of $2.15 \times 10^{11}\Omega$. These values are comparable with the barrier height and series resistance values obtained from the direct method discussed above, showing that the direct methods may be employed as a satisfactory methods for extraction of Schottky barrier parameters for this work.

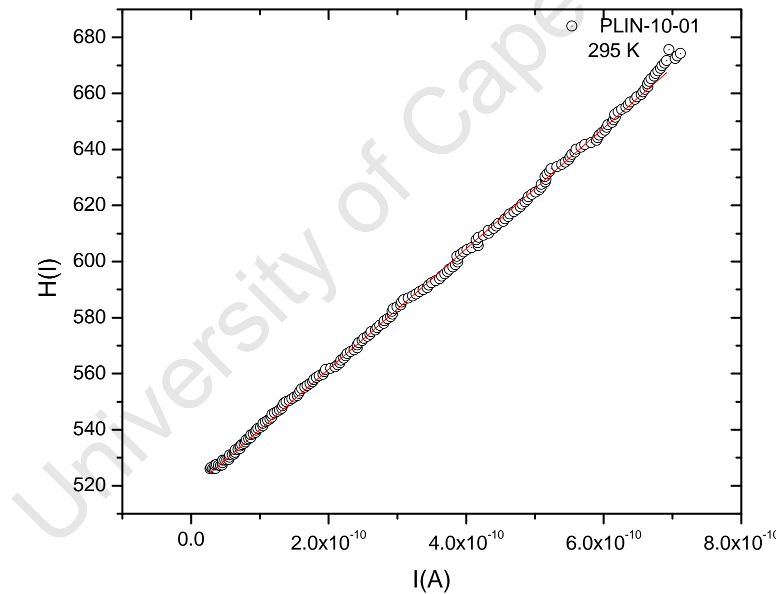

Fig. 4.18: Graph of $H(I)$ vs I for the extraction of the barrier height and series resistance for sample PLIN-10-01 at 295K.

University of Cape Town

The direct extraction method was chosen for the analysis of all the other nanocomposite samples for the purpose of extraction of the TE parameters at temperature 295K. The values of the different parameters obtained from the analysis on $I-V$ characteristics for the different samples are shown in the Appendix A.1

Fig. 4.19 shows the effect of particle loading on the derived ideality factors (n), Schottky

barrier heights (ϕ_B) and the series resistances (R_s). From Fig. 4.19(a), the plot of the derived ideality factor with concentration, one can observe an effect which depends on the binding medium, with the linseed oil based nanocomposites exhibiting a sharp drop in ideality factor from 30 to 50 wt.% particle loading and reaching a minimum at 70 wt.% for MLIN and 80 wt.% for the PLIN. The acrylic based nanocomposite on the other hand, shows relatively smaller ideality factor values with a sharp drop between 10 and 30wt.% particle loading in both PACR and MACR nanocomposites. From Figs. 4.19(c) and 4.19(d) the plot of variation of the derived series resistances with particle loading in the linseed based and acrylic based nanocomposite respectively, a trend similar to that observed for the variation of the ideality factor with particle loading was observed. In the linseed oil based composite as shown in Fig. 4.19(c) for example, the resistances drops sharply to a relatively low value when the particle loading reaches 50 wt.%, reducing further to a minimum at about 70 - 80 wt.%, corresponding to the minimum in the derive ideality factor shown earlier. Similarly, the resistance in the acrylic based nanocomposite exhibited a lower series resistance and a minimum resistance at about 30 wt.% particle loading.

University of Cape Town

From these observation there is a clear indication that the powder type does not have a significant effect on the TE parameters. However, the type of binder in which the filler is embedded has a direct effect on the conduction properties. The governing charge transport process is due to the nanoparticles when concentration reaches 50 wt.% and beyond in the case of the linseed based nanocomposites, due to their marked change in resistance value at this particle loading. In the case of the acrylic medium, this marked change in series resistance value is observed at about 30 wt.%. There appears to be a possible correlation between the ideality factor, a measure of the departure of the transport process from thermionic emission and the derived series resistance. As the series resistance reduces, the closer the transport process is to thermionic emission, and thus the high ideality factors reported earlier may in fact be due to the presence of very high series resistances [150].

The derived SBH as shown in Fig. 4.19(b), for the linseed based nanocomposites shows a systematic dependence on concentration with a minimum SBH at about 70 and 80 wt.% for MLIN and PLIN respectively. The values of the derived SBH vary between $0.83 - 0.88eV$ for PLIN and $0.84 - 0.92eV$ for MLIN. These values are close to $0.87eV$, the theoretical SBH of silver to a moderately doped P type silicon wafer [181]. Similarly, the derived SBH of the acrylic based nanocomposites increases fairly systematically with increase in concentration, also lie close to the theoretical value of $0.87eV$.

From the foregoing, it is reasonable to suggest that the contribution of thermionic emission

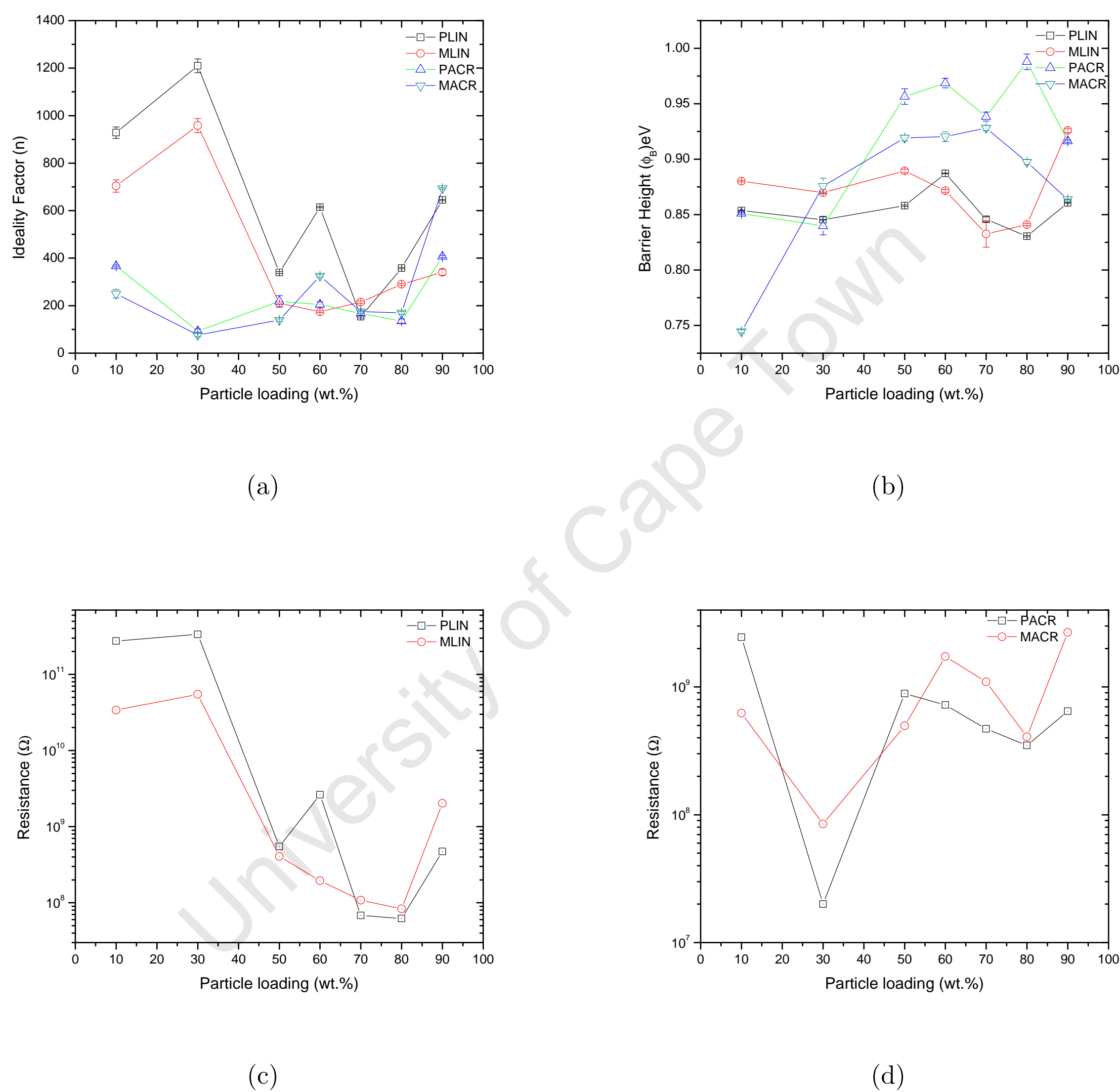

University of Cape Town

Fig. 4.19: The effect of particle loading on the derived (a) ideality factors (n), (b) Schottky barrier heights (ϕ_B) (c) the series resistances (R_s) for the linseed based nanocomposites and (d) the series resistances (R_s) for the acrylic based nanocomposites.

process to the overall transport process in this system is small but depends largely on the concentration of Si nanoparticles dispersed in the binder and on the binding strength of the binder. A linseed oil based nanocomposite matrix shows similarity to the TE process at concentration of about $70-80wt.\%$, and the acrylic based matrix at about $30wt.\%$. It is not clear from this analysis if one type of silicon nanoparticle performs better than the other, but it is clear that the acrylic based matrix has an overall better performance in terms of contribution from the derived series resistances. The closeness of the derived SBH to the theoretical SBH of silver to a moderately doped P type silicon wafer suggest holes as the possible carrier type in all the nanocomposites. With this in mind, it is therefore necessary to determine the contribution from the other transport mechanism by testing the $I-V$ characteristics of the different samples with the other models suggested above.

University of Cape Town

4.5.5 Contribution of thermionic field emission (TFE) to charge carrier transport in silicon nanocomposites

When the current transport is controlled by TFE or tunneling, the relationship between the current and voltage can be expressed in the low voltage region as [164, 170, 172]

$$I = I_0 \exp\left(\frac{qV}{E_0}\right), \tag{4.37}$$

with

$$n = \frac{E_0}{K_B T} = \frac{E_{00}}{K_B T} \coth\left(\frac{E_{00}}{K_B T}\right). \tag{4.38}$$

E_{00} is the characteristic tunneling energy that is related to the tunneling effect transmission coefficient given as [149],

$$T(\eta) \sim \exp\left(\frac{-\phi_B}{E_{00}}\right), \tag{4.39}$$

and

$$E_{00} = \frac{h}{4\pi}\left(\frac{N_D}{m^* \varepsilon_s}\right)^{\frac{1}{2}}, \tag{4.40}$$

where N_D is the total carrier density, m^* is the effective mass of the carrier, $\varepsilon_s = 11.0\varepsilon_0$ for silicon and $h = 6.626 \times 10^{-34} Js$.

Fig. 4.20 shows a plot of the calculated characteristic tunneling energy using the ideality factor values from section 4.5.4, versus particle loading for the different nanocomposites. As seen in the plot, the calculated tunneling energies are higher for the linseed oil based ink compare to the acrylic based ink at low particle loading, with a maximum of about $E_{00} = 30.73 \pm 0.72 eV$ and $E_{00} = 24.36 \pm 0.74 eV$ for PLIN and MLIN respectively at $30 wt.\%$, compared with the minimum values of $E_{00} = 2.36 \pm 0.24 eV$ and $E_{00} = 1.95 \pm 0.20 eV$ for PACR and MACR respectively with same particle loading. As the concentration of nc-Si powder increases beyond $60 wt.\%$, the characteristic tunneling energy may be reasonably said to become independent of the particle and binder type, as the tunneling energy for all the nanocomposites fall approximately at about the same values.

The characteristic tunneling energy E_{00} for the different inks obviously should have their respective minimum at concentration values corresponding to their minimum calculated ide-

University of Cape Town

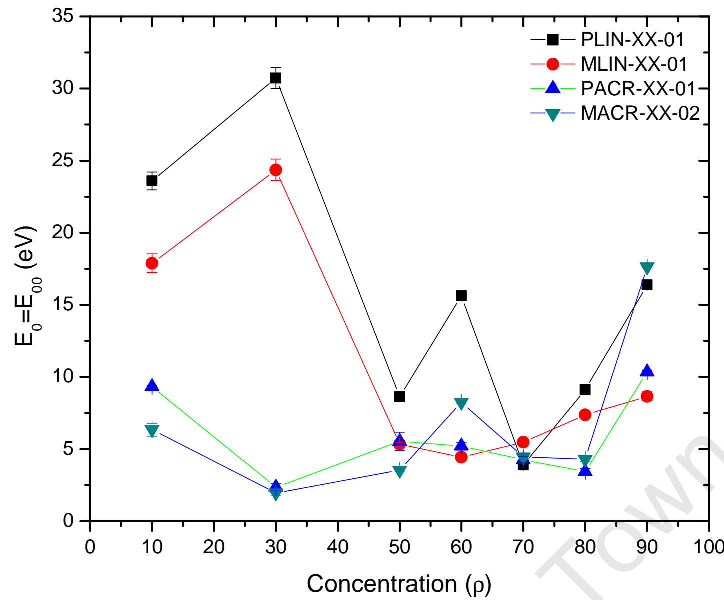

Fig. 4.20: Plots of theoretical calculated tunneling energy E_{00} dependence on particle loading (concentration) for the different nanocomposite.

University of Cape Town

ality factors, since $n \propto E_{00}$. The obtained value of the characteristic tunneling energy E_{00} is a property of the nanocomposite matrix and is an indicator of how efficient thermally activated tunneling is in this model [150]. As explained in a review by Tung [150], E_0 can be thought of as the amount of band bending for a semiconductor that would yield a tunneling probability of $\approx 37\%$ at the base of the barrier.

To determine whether thermionic field emission (TFE) or field emission (FE) will predominate in a giving transport process, the obtained value of E_{00} is compared with K_BT. When $K_BT \gg E_{00}$ for a given temperature, then TFE process will dominate. On the other hand, field emission (FE) process will dominate if $E_{00} > K_BT$ [150]. In this case, for all concentrations and type of nanocomposite system considered, $E_{00} \gg K_BT$. This is suggestive of a process where the contribution to current transport is due to FE or tunneling [150, 145], and contributions from thermally activated process like TFE and TE are insignificant.

4.5.6 Contribution of field emission (FE) to carrier transport

A simple model to describe tunneling in a metal-nanocomposite matrix can be illustrated with current of electrons encountering a finite potential barrier of height ϕ_B at the metal

nanocomposite interface. Even when the energy of the carrier is lower than the barrier height, its wave function does not vanish at the interface, but falls off exponentially into the barrier [182]. There exists a finite probability that electrons from the metal electrode can travel a short distance into the nanocomposite, and the overlap of the wave function gives rise to a non resonant tunneling current density.

The simplest model used to describe an $I - V$ characteristic dominated by direct tunneling through a barrier is represented by Simmon's approximation [183, 184]

$$\begin{aligned} J_{DT} = \tfrac{q}{4\pi^2 \hbar d^2} \Big\{ \left(\phi - \tfrac{qV}{2}\right) \exp\left(-\tfrac{2d\sqrt{2m_e}}{\hbar}\sqrt{\phi - \tfrac{qV}{2}}\right) \\ - \left(\phi + \tfrac{qV}{2}\right) \exp\left(-\tfrac{2d\sqrt{2m_e}}{\hbar}\sqrt{\phi + \tfrac{qV}{2}}\right) \Big\}, \end{aligned} \tag{4.41}$$

where m_e is the electron mass, $\hbar = h/2\pi$ is Planck constant, d is the tunneling barrier width, and α is a unitless adjustable parameter that is introduced to modify the simple rectangular barrier model or to account for an effective mass ($m^* = \alpha^2 m$) [184].

In the region of low applied voltage such that $qV \ll \phi$ the direct tunneling current can be represented as

$$J_{DT} = \frac{\gamma\sqrt{\phi}}{d} \exp\left(-Ad\sqrt{\phi},\right) V \tag{4.42}$$

where

$$\gamma = \frac{q\sqrt{2m^*}}{4\beta^2\pi^2\hbar^2}, \tag{4.43}$$

and $A = 2\beta\sqrt{2m^*/\hbar^2}$, m^* is the effective mass of the electron in the Matrix, $\hbar$ is the plank's constant and β is a constant having a value $\beta \cong 1$. ϕ is the average barrier height and d is the barrier width. From equation 4.42, in the case of $qV \ll \phi$, the current density J should be proportional to the applied bias voltage V and independent of temperature.

For intermediate voltages $qV < {}^{\phi}\!/_{2}$ Equation 4.42 reduces to

$$J_{DT} = \frac{\gamma\sqrt{\phi}}{d} \exp\left(-Ad\sqrt{\phi}\right) \left(V + \sigma V^3\right), \tag{4.44}$$

where

$$\sigma = \frac{(Aq)}{96\phi d^2} - \frac{Aq^2}{32d\phi^{3/2}}. \tag{4.45}$$

University of Cape Town

Finally for the case $qV > \phi$ equation 4.42 reduces to the Fowler-Nordheim form,

$$J_{FN} = AE^2 \exp\left(-\frac{B}{E}\right), \tag{4.46}$$

where $E = V/L$ is the electric field across the matrix of length L, and B and C are given by

$$A = \frac{q^3}{16\pi^2\hbar m^*\phi}, \tag{4.47}$$

and

$$B = \frac{4\sqrt{2m^*}}{3q\hbar}\phi^{3/2}. \tag{4.48}$$

If the current is dominated by Fowler-Nordheim tunneling, then a plot of $ln(J/E^2)$ vs $1/E$ should yield a straight line. The intercept with the y axis and the slope would yield the values of A and B respectively. Once the values of A and B are known, the value of m^* and ϕ can be estimated from equation 4.46. This plot will exhibit a logarithmic growth in the low bias regime, i.e. where $qV < \phi$, and as the applied bias increases there is a change from logarithmic growth to linear decay. The applied bias necessary to effect this change is the transition voltage (V_{trans}), which is related to the barrier height [183, 185].

Fig. 4.21 shows Fowler-Nordheim plots of $ln(J/E^2)$ vs $1/E$ for the different nanocomposite samples. From Fig. 4.21(a), the PLIN nanocomposites are observed to have a positive slope for concentration 10 and 30 wt.% particle loading, and above this particle loading, from 50 wt.% upward, the characteristics shows a change from positive slope at high $1/E$ to linear decay at low $1/E$, with a clear transition point, which depends on the concentration. A similar trend was observed with the MACR based nanocomposites shown in 4.21(d), for which the 10 wt.% particle loading shows a positive slope, and all the other nanocomposites with particle loading above 10 wt.% starting with 30 wt.% exhibit a change from logarithmic growth at low field to linear decay at higher field, with transition point similarly dependent on concentration.

On the other hand, the MLIN and the PACR based nanocomposites, shown in Fig. 4.21(b) and 4.21(c), show the characteristic change from logarithmic growth at low field to linear decay at higher field with the transition point again depending on concentration for all concentrations of particles. One other observation from the Fowler-Nordheim plot is that $ln(J/E^2)$ at the transition point is maximum for the concentration where the samples exhibit maximum conductance.

University of Cape Town

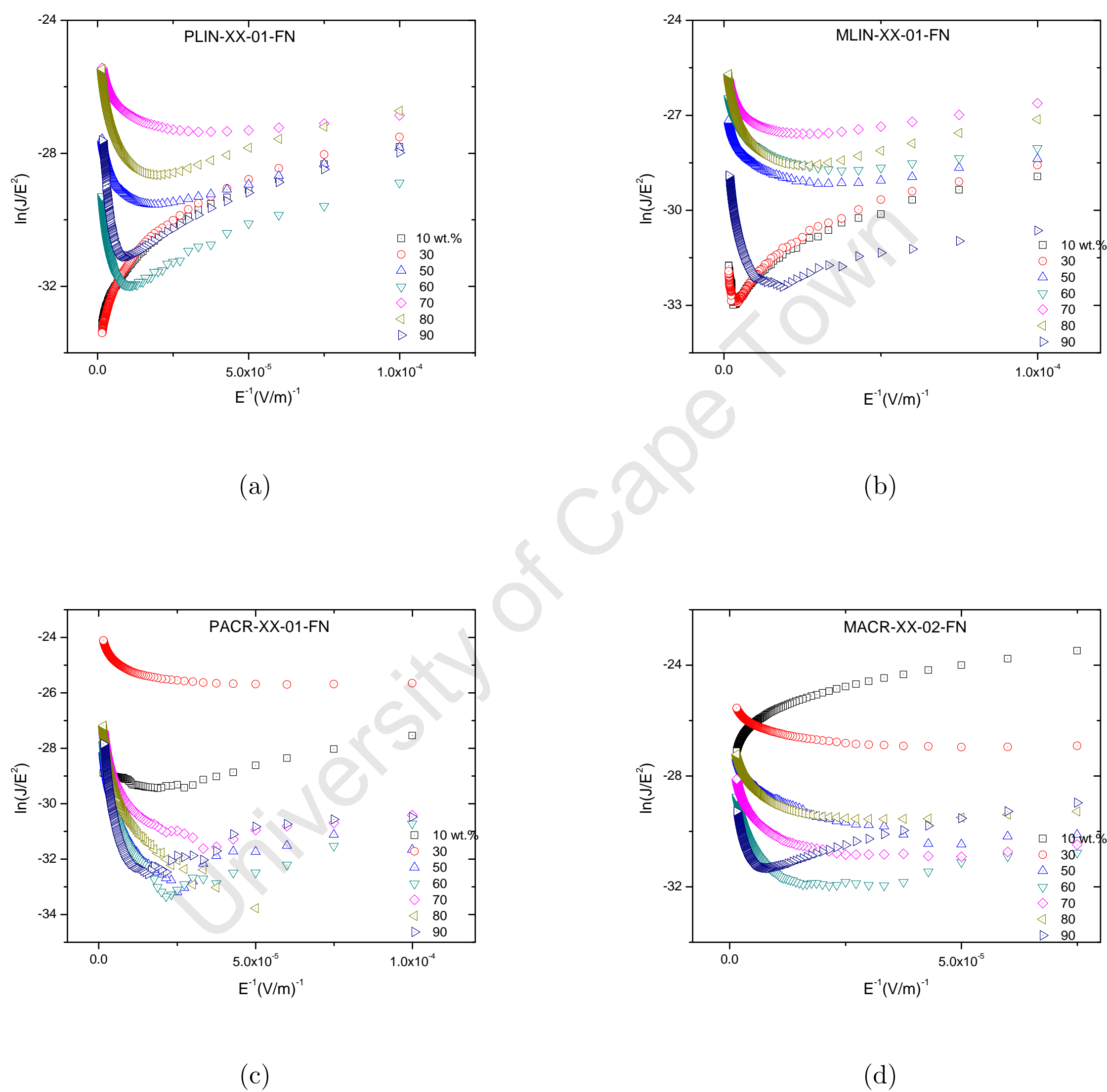

University of Cape Town

Fig. 4.21: Plots of $ln(J/E^2)$ vs. E^{-1} for (a) PLIN-xx-01 (b) MLIN-xx-01 (c) PACR-xx-01 and (d) MACR-xx-02.

The above observations can be interpreted as follows: At the junction of the metal and nanocomposite, there may arise interfacial region which impedes the flow of current from the metal into the bulk nanocomposite. When a potential difference is applied across this junction, ideally a potential gradient of constant slope is created. Fig. 4.22 shows the schematic of a potential which decays from the metal to the nanocomposite, for example, with a finite barrier height at the metal insulator interface. The flow of electrons from the metal to the nanocomposite could be through tunneling either directly from the conduction band of the metal to the conduction band of the silicon, or they can first emerge in the insulator LUMO levels and then hop to the Si in the matrix [186].

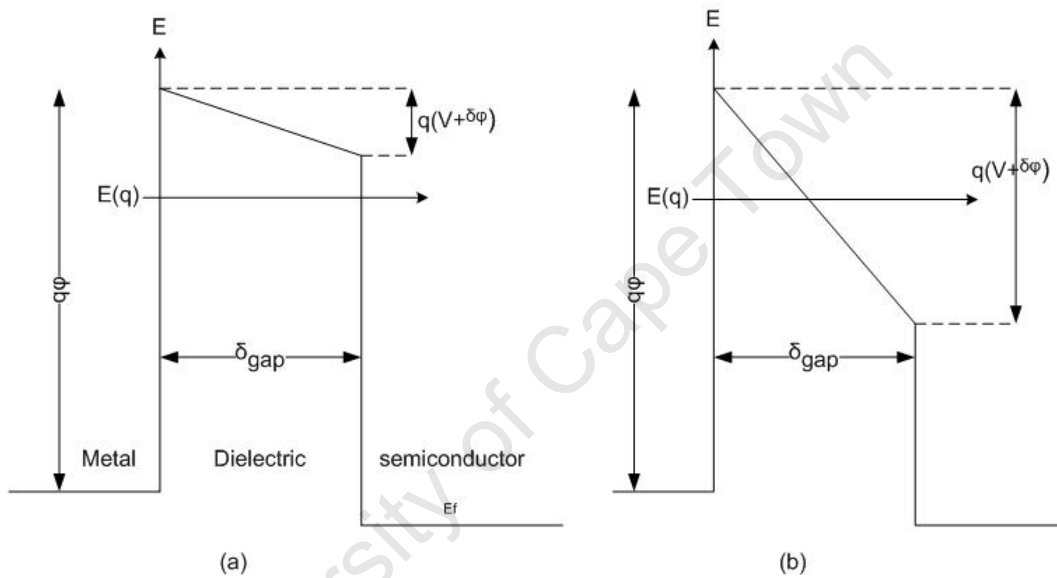

Fig. 4.22: Energy barrier of a typical Metal/Semiconductor structure with interfacial dielectric layer showing (a) Direct tunneling and (b) the FOWLER-NORDHEIM tunneling regime,(adapted from [187]).

University of Cape Town

At relatively low field, when $qV < \phi$, the electron can only tunnel through the entire barrier width posed by the interfacial dielectric layer as depicted in figure 4.22(a). At high field a potential gradient appears, thus resulting in an effective barrier width lower than that posed at low field. Hence, the electron can easily tunnel through at the edge of the potential barrier. The transition from direct tunneling to field emission occurs at a voltage V_{trans}, required to change the shape of the barrier from trapezoidal to triangular.

Figure 4.23 shows a typical Fowler-Nordheim plot $ln(J/E^2)$ vs. E^{-1} for PLIN-50-01 with the dashed line indicating the transition voltage required for the change from logarithmic growth at low field indicating direct tunneling (positive slope region), to linear decay region at higher field (negative slope region) indicative of field emission, with an estimated transition point at $16.05eV$. The effective barrier height can be determine by equating the intercept and

slope of the FN plot to equations 4.47 and 4.48 respectively [188, 186].

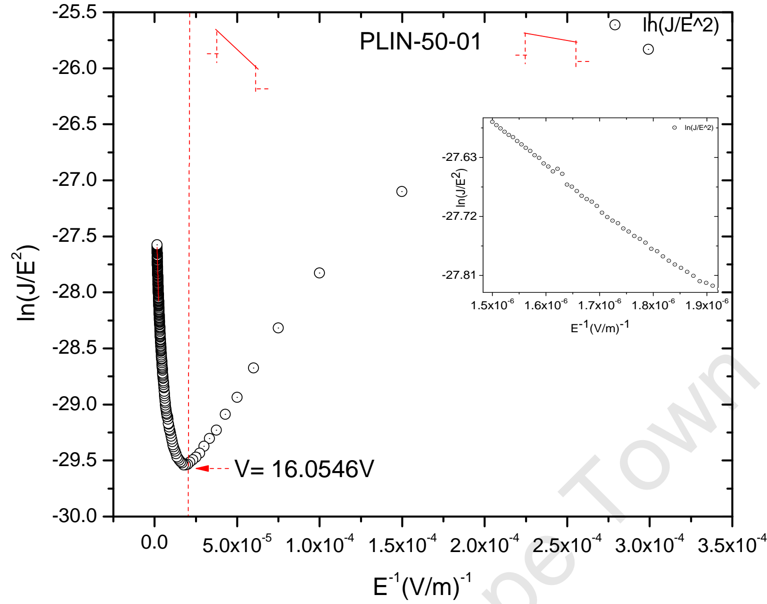

Fig. 4.23: Typical Fowler-Nordheim $ln(J/E^2)$ vs. E^{-1} for PLIN-50-01 showing characteristics change from logarithmic growth at low field to linear decay at higher field with an estimated transition point at $16.05eV$. The inset show the linear region at high field.

Application of equations 4.47 and 4.48 for the simultaneous determination of the effective barrier height and effective mass of carriers in the nanocomposites does not yield physical values. However, assuming the carriers in the nanocomposite are free electrons, i.e. $(m^* = m_o)$, from equation 4.48 which relates the slope with the potential barrier, values of the barrier height for the different nanocomposites was derived (see table A.3). This was considered preferable to using equation 4.47 for the intercept, because it is less affected by any offset in the voltage value. Figure 4.24 show the estimated transition voltage and the estimated barrier height respectively derived from the different slope value for samples exhibiting transitional region or negative slopes.

From the plots, V_{trans} and ϕ_{FN} are observed to have similar dependence on particle loading or concentration of the fillers in the nanocomposite. For the linseed oil based nanocomposites for example, comparing 4.24(a) and 4.24(b) for PLIN and MLIN respectively, the value of V_{trans} has a minimum at 70 wt.% and 60 wt.% for PLIN and MLIN inks respectively, while the value of ϕ_{FN} is minimum at 70 wt.% in both cases. Beyond this concentration the value of V_{trans} and ϕ_{FN} is observed to increase with increase in particle loading.

University of Cape Town

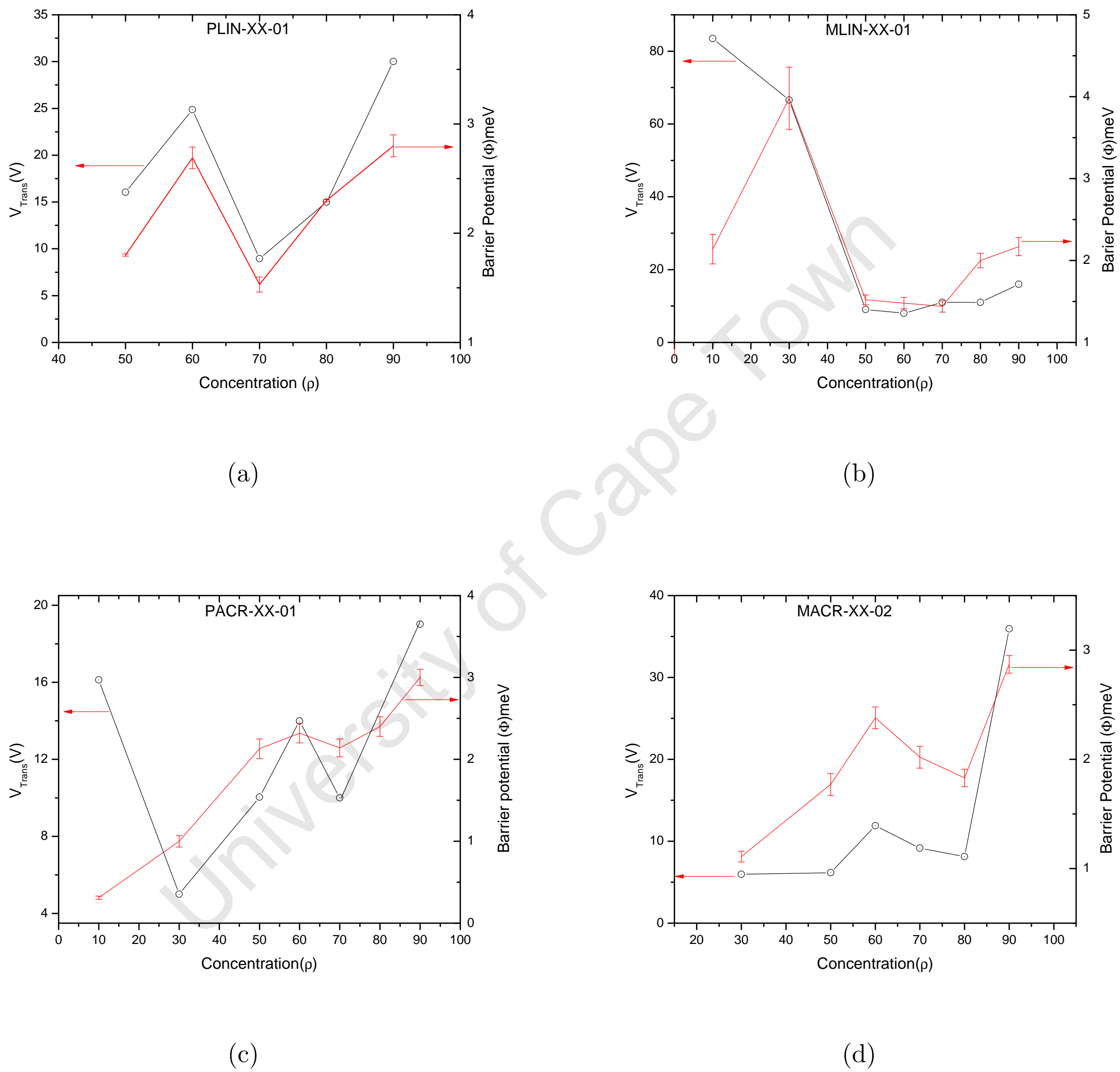

University of Cape Town

Fig. 4.24: Showing variation of estimated value of V_{trans} and Barrier Potentials derived from the negative slopes of plots of $ln(J/E^2)$ vs. E^{-1} for (a) PLIN-XX-01 (b) MLIN-XX-01 (c) PACR-XX-01 and (d) MACR-XX-02

In the case of the MLIN inks, the estimated value of V_{trans} for 10 wt.% and 30 wt.% are 83.48V and 66.60V respectively. These are high point compared to the value of V_{trans} for concentration of 50 wt.% and higher as shown in figure 4.24(b). The deduction one could reasonably make from the above is that, at relatively low concentration namely (10 and 30 wt.% Linseed nanocomposites) for PLIN and MLIN, the transport is dominated by direct tunneling. For concentration of 50 wt.% nc-Si and above as observed for both PLIN and MLIN, there is a change from direct tunneling to field emission at relatively lower applied voltages and barrier height, with the minimum $V_{trans} = 8.95V$, $\phi_{FN} = 1.53meV$ for PLIN at 70 wt.% and $V_{trans} = 8.00V$, $\phi_{FN} = 1.48meV$ for MLIN at 60 wt.%. The only significant difference is in the 90 wt.% inks where V_{trans} for PLIN is almost twice that for MLIN.

The charge injection in this model, to a large extent seems to depend on the concentration of the particles in the binder rather than the type of particle, as earlier observed in the thermionic emission model. A similar, deduction can be made when the PACR, 4.24(c) and MACR, 4.24(d) nanocomposite systems are compared. In this case however the minimum value of V_{trans} is seen at concentration of 30 wt.% for both PACR ($V_{trans} = 5.00V$) and MACR ($V_{trans} = 5.96V$), while the minimum ϕ_{FN} is at 10 wt.% and 30 wt.% for PACR ($\phi_{FN} = 1.00meV$) and MACR ($\phi_{FN} = 1.11meV$) respectively.

The variation of the estimated V_{trans} and derived ϕ_{FN} with concentration can be seen to have a reasonable correlation with the observed pattern of the variation of series resistance with concentration, as shown earlier in section 4.5.4. From the analysis above, it is reasonable to suggest that for all nanocomposite system considered, the contribution of direct tunneling is pronounced at low voltages, and field emission at high voltages. The transition voltage from direct tunneling to field emission is strongly dependent on the particle loading or concentration of nc-Si particle in a given binder, optimum at about 70 wt.% in the linseed oil based ink and about 30 wt.% in the acrylic based ink.

University of Cape Town

4.5.7 Contribution resulting from lowering of the columbic potential barrier by the external electric field: Richardson-Schottky and Poole-Frenkel emission process

Due to the assumed dielectric nature of the interface as well as the bulk silicon nanocomposites resulting from the fabricated metal-nanocomposite-metal structure, a possible electric field effect in the dielectric matrix may arise. Two basic mechanisms, namely a barrier-limiting process in the interface of the metal contact to an interfacial insulator, and a bulk-limiting current through the matrix structure may coexist [189].

Thermally assisted conduction of charged carriers over a lowered columbic potential due to applied electric field is a notable feature in systems with dielectrics. The conduction could either be a transition over the barrier presented by the dielectric, i.e Richardson-Schottky (RS) type conduction, or by a combination of charge carrier release due to ionization of impurity centres in the dielectric, under the effect of an external electric field [190] and by thermal emission of carrier from randomly distributed traps to the conduction band (as a result of lowering of the columbic potential barrier by the external electric field), i.e. The Poole-Frenkel (PF) effect [191]. For the RS type conduction mechanism, the dependence of the current density J, on the internal field E in the dielectric, arising from the externally applied voltage is given by [192, 190, 193]

$$J = A^{*}T^{2}\exp\left\{\frac{q\left(\beta_{RS}E_{dielectric}^{1/2} - \phi_{RS}\right)}{K_{B}T}\right\}, \tag{4.49}$$

where $A^{*} = 1.2 \times 10^{6} A/m^{2}K^{2}$ is the Richardson constant ($A^{*} = 3.2 \times 10^{5} A/m^{2}K^{2}$ for hole transport), q the electronic charge, $\beta_{RS} = \left(q/(4\pi\varepsilon\varepsilon_{0})\right)^{1/2}$ is the field lowering coefficient or the Richardson-Schottky parameter, which is related to the dielectric constant ε of the insulator, and ϕ_{RS} is the barrier height at the metal-dielectric interface at zero field.

Equation 4.49 also holds for the PF conduction mechanism. In this case however the barrier ϕ_{PF} is a measure of the depth of a potential well, as oppose to the height of a step in the RS model. The Poole-Frenkel parameter is related to the Richardson-Schottky parameter by [190]

$$\beta_{PF} = 2\beta_{RS}. \tag{4.50}$$

The implication of field assisted thermal ionization in the Poole-Frenkel effect is to lower the

University of Cape Town

ionization potential E_g of atoms in a solid by an amount equal to β_{PF}. This results in a field dependent conductivity given by [194]

$$\sigma = \sigma_0 \exp\left(\frac{\beta_{PF} E^{\frac{1}{2}}}{2K_B T}\right), \tag{4.51}$$

where σ_0 is the low field conductivity given as

$$\sigma_0 = q\mu N \exp\left(\frac{-E_g}{2K_B T}\right). \tag{4.52}$$

Equation 4.51 may be represented in terms of current density as

$$J = J_0 \exp\left(\frac{\beta_{PF} E^{\frac{1}{2}}}{2K_B T}\right), \tag{4.53}$$

where $J_0 = \sigma_0 E$ is the low field current density and μ is the carrier mobility [194].

From equation 4.49 a plot of $ln(J)$ vs. $E^{1/2}$ at a constant temperature for predominantly RS or PF conduction mechanism will result in a straight line with slope equal to $q\beta_{RS}/K_B T$ from which β_{RS} can be deduced and the intercept to the y axis gives $C = \ln(AT^2) - q\phi_{RS}/K_B T$ or $C = \ln(AT^2) - q\phi_{PF}/K_B T$ as the case may be, from which either ϕ_{RS} or ϕ_{PF} is obtained.

Fig. 4.25 shows a plot of $ln(J)$ vs. $E^{1/2}$ for the four nanocomposite systems considered in this experiment, assuming that the internal electric field $E = V/L$, where V is the external applied potential and L is the electrode separation over the composite. In all the systems, three field regions can be defined, for which the plot $ln(J)$ vs. $E^{1/2}$ has an approximate linear relationship. These regions are classified as (a) low field $0 < E^{1/2} <\approx 270(V/m)^{1/2}$, (b) medium field $270 < E^{1/2} <\approx 550(V/m)^{1/2}$ and (c) high field $550 < E^{1/2}(V/m)^{1/2}$.

By considering the medium and high field regions in Fig. 4.25, where the effect of electric field on the transport is expected to be pronounced, it is clear that $ln(J)$ changes linearly with $E^{1/2}$ to a reasonable degree. In fact, the behaviour shown in Fig. 4.25 cannot be explained with a constant $\beta_{RS/PF}$ in the different regions, but it is an electric field dependent parameter. As explained in [195], the spontaneous value of $\beta_{RS/PF}$ can be extracted from the slope of the tangent to the curve at a specific value of E given by

$$\frac{\delta(\ln(J))}{\delta E^{1/2}} = \frac{q\beta}{KT}, \tag{4.54}$$

University of Cape Town

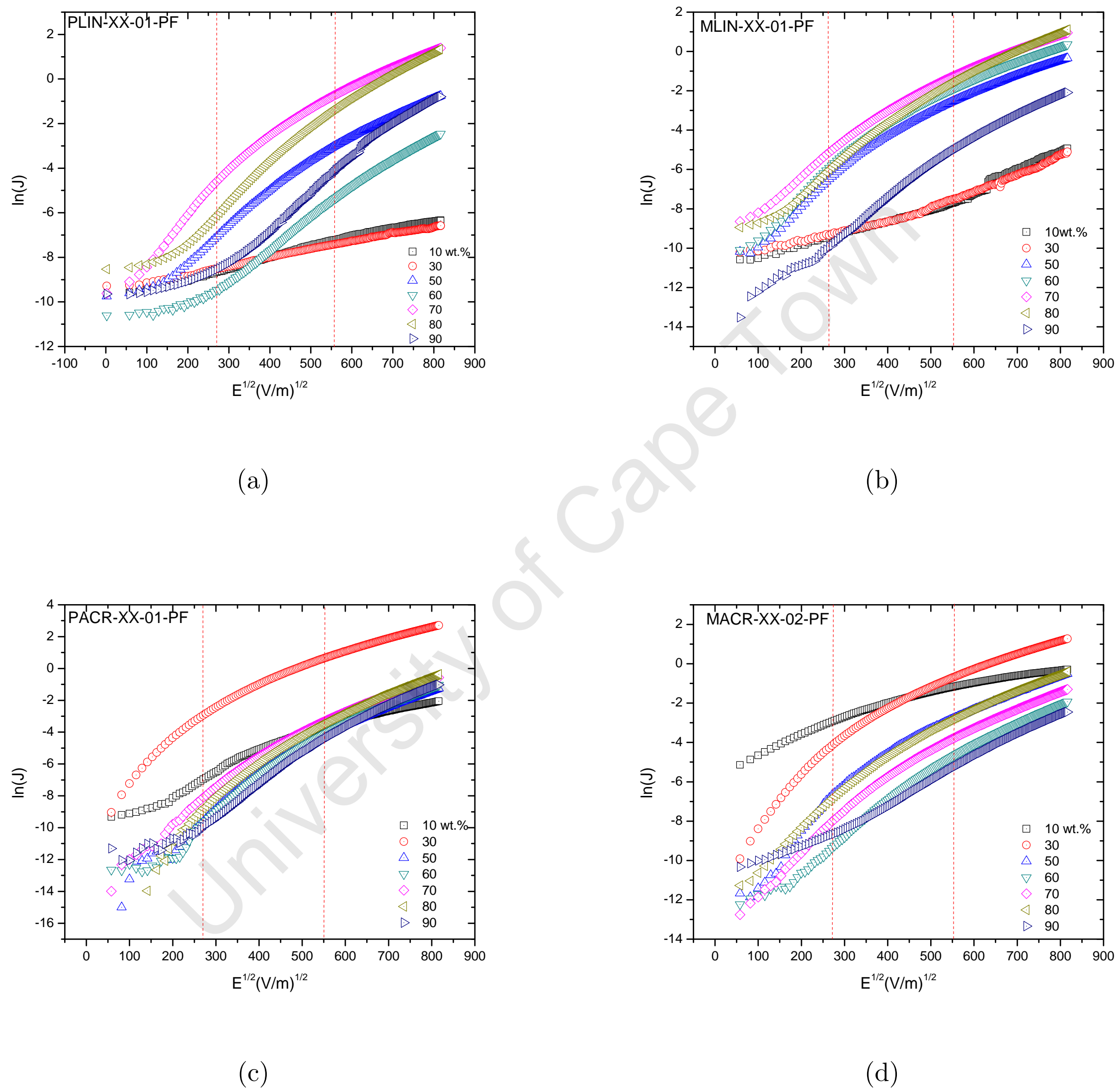

University of Cape Town

Fig. 4.25: Typical Poole-Frenkel plots of $ln(J)$ vs. $E^{0.5}$ for (a) PLIN-xx-01 (b) MLIN-xx-01 (c) PACR-xx-01 and (d) MACR-xx-02.

where the variation of $\beta_{RS/PF}$ with E is given by [195]

$$\beta_{RS/PF} = \beta_o E^{-\alpha}, \tag{4.55}$$

with β_o and α constants for a given temperature.

The transport in these regions may therefore be associated either with Poole-Frenkel or Richardson-Schottky conduction mechanism. Using equation 4.49, values for β_{RS} or β_{PF} and ϕ_{RS} or ϕ_{RF} as the case may be, where separately derived, from the slope and intercept of a linear fit on plots of $ln(J)$ versus $E^{1/2}$ at the medium as well as the high field regions for all the nanocomposites (see Appendix A.4). Using the value of the derived β_{RS} or β_{PF} the dielectric constant of each nanocomposite was also estimated from

$$\beta_{RS/PF} = \left(\frac{q}{4\pi\varepsilon\varepsilon_o}\right)^{\frac{1}{2}}. \tag{4.56}$$

To determine how the derived field lowering coefficient $\beta_{RS/PF}$ and the barrier height/trap potential $\phi_{RS/PF}$ values shown in Appendix A.4 vary with the concentration of the filler in nanocomposites, a plot of $\beta_{RS/PF}$ and $\phi_{RS/PF}$ vs. concentration for the nanocomposites in the higher and medium field region was carried out. Fig. 4.26(a) to Fig. 4.26(b) shows how the derived field lowering coefficient $\beta_{RS/PF}$, varies with the concentration of filler in the nanocomposites in the higher and medium field regions respectively. In both regions, the field lowering coefficient appears to increase to some degree with increasing concentration. Since the barrier lowering factor $\beta_{RS/PF}$ is related to the dielectric constant of the nanocomposite, it is reasonable to suggest that the value of $\beta_{RS/PF}$ is defined by a combined dielectric constant of silicon and the polymeric binders, and may vary considerably with the proportion of particles in the matrix.

The derived values of dielectric constants for the nanocomposites using equation 4.56, yielded very small values compared to the theoretical dielectric constant values for silicon (11.7-12.9) or linseed oil /Acrylic (3.2-3.5/2.1-3.9). Gaffar et al [195] stated that, in many of the reported experiments where $\beta_{RS/PF}$ is derived, it often turns out to be dependent on sample thickness which precludes the simple interpretation given to it by the model from which the equations used were derived. The derived dielectric constants were often found to be inconsistent with the corresponding experimental values measured by other means [195].

The dependence of the derived barrier height/trap potential $\phi_{RS/PF}$ on concentration for the high field regions as shown in Fig. 4.26(c), and the low field regions shown in Fig. 4.26(d),

University of Cape Town

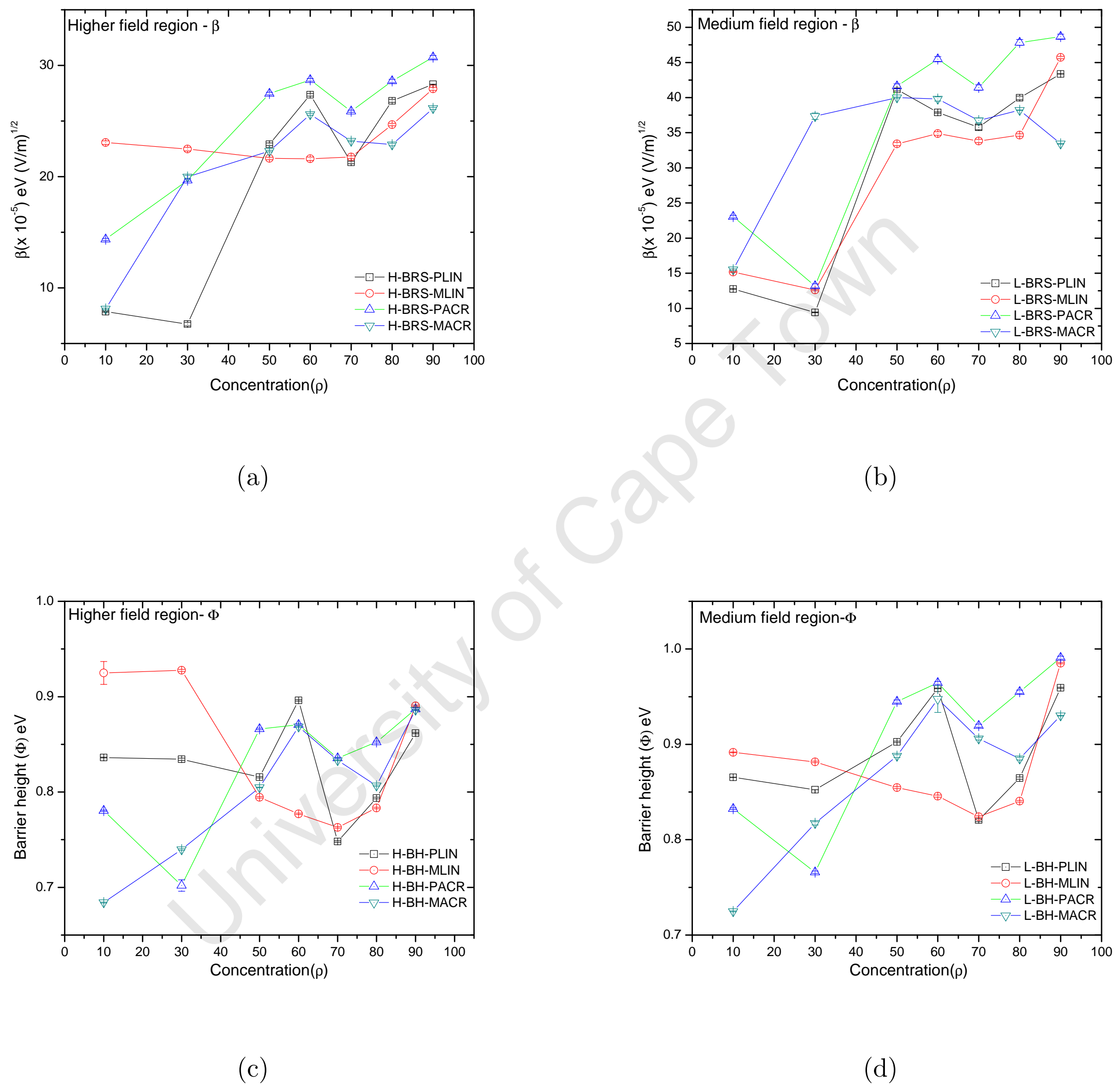

University of Cape Town

Fig. 4.26: Plots of dependence of (a) $\beta_{RS/PF}$ derived from the high field region (b)$\beta_{RS/PF}$ derived from the medium field region (c) $\phi_{RS/PF}$ derived from the high field region (d) $\beta_{RS/PF}$ derived from the medium field region on concentration of fillers in the four different nanocomposite systems.

reveals a clear dependency on concentration of filler and type matrix. The acrylic based nanocomposites for example PACR, has minimum $\phi_{RS/PF} = 0.70/0.77eV$ at 30 wt.% for high and medium field regions respectively while MACR has minimum barrier height/trap potential $\phi_{RS/PF} = 0.68/0.73eV$ for high and medium field regions respectively at 10 wt.%. These concentrations are about the concentration for which the Acrylic samples exhibit relatively low series resistances and hence best conductance.

Similarly, the linseed oil based nanocomposites namely PLIN and MLIN, exhibit minimum values of $\phi_{RS/PF} = 0.75/0.82eV$ and $\phi_{RS/PF} = 0.76/0.82eV$ respectively at their common minimum of 70 wt.%, again corresponding to the concentration at which these nanocomposite exhibits relatively low series resistances. These values of $\phi_{RS/PF}$ are the energies required to transfer electrons from the trap level to the conduction band in case of the Poole-Frenkel process [196] or to surmount a barrier potential in the case of the Richardson-Schoottky process.

The distinction between the Schottky-Richardson transport process and Poole-Frenkel process cannot be established in this case, because the experiment was carried out at 295K only. From the above, however, it is evident that there is a major contribution of this type of conduction mechanism to the overall transport in the nanocomposite systems.

University of Cape Town

4.5.8 Evaluation of the contribution from space charge limited current (SCLC) to the overall transport

In a typical metal-semiconductor-metal system, charges injected from one electrode travels through the bulk and then emerges at the second electrode. If the rate at which charges are injected is equal to the rate of motion, then charges do not accumulate. If the mobility through the bulk is low, which is the case for many dielectric systems, then charges are likely to accumulate at the interface and in the bulk. The electric field due to the accumulated charges will influence the conduction process [197].

The $I-V$ characteristics of printed thin film of silicon nanoparticles dispersed in a polymer binder as described by Ando et al. [18], exhibits varistor-like characteristics, where $I \propto V^m$. Such a power law relationship $I \propto V^m$ for which ($m > 2$), describes a conduction mechanism influenced by an exponential distribution of traps [164]. To determine the contribution of the space charge limited current (SCLC) conduction mechanism to the overall charge carrier transport, a plot of $ln(I)$ vs. $ln(V)$ was carried out from the $I-V$ characteristics for all the nanocomposite samples used for the experiment.

Fig. 4.27 shows the concentration dependent plot of $ln(I)$ vs. $ln(V)$ for the four different nanocomposites. From their plots, it is clear that there exists a power law dependance of I on V in the higher voltage regions for all the nanocomposites. The form and concentration dependence of the plots appears to depend on the matrix type rather than the type of particles, as seen by the similarity of $ln(I)$ vs. $ln(V)$ plots for PLIN Fig. 4.27(a) and MLIN Fig. 4.27(b). Similar correspondence can be seen between the acrylic based structures PACR Fig. 4.27(c) and MACR Fig. 4.27(d).

For the linseed oil based nanocomposite systems, the plot of $ln(I)$ vs. $ln(V)$, as exemplified for sample PLIN-10-01 in Fig. 4.28 plot yields three basic power law regions, A for low bias, typically for $V < 15V$, B for intermediate voltage bias $15 < V < 45V$ and C in the region $45 < V$ for high voltages. The power law exponent values, $m_A = 0.20$, $m_B = 0.68$ and $m_C = 1.15$, were derived from linear fits to the three regions identified . A similar approach was used to derive the power law exponent for all the other concentrations (30 to 90 wt.%). In the case of the acrylic based system however, the three regions were not observed for all concentrations, with the first and second regions merged in some of the samples. In sample PACR-80-01, in particular, only one region appears to exist.

Figure 4.29 shows how the three power law exponents vary with the concentration of particles in each matrix (binder) system. From the plot, the different nanocomposites exhibited slope

University of Cape Town

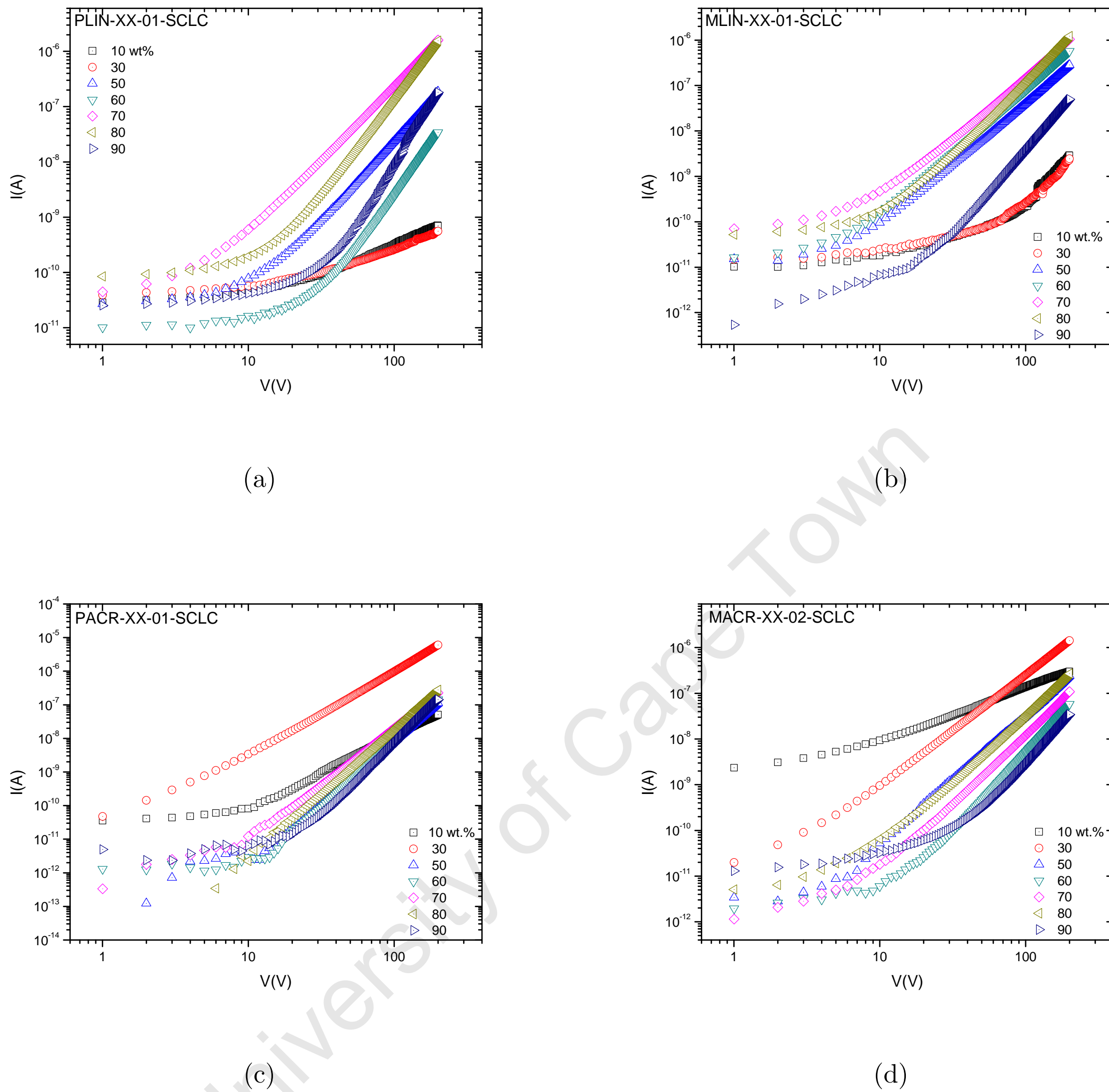

University of Cape Town

Fig. 4.27: Showing plot of $ln(I)$ vs. $ln(V)$ for (a) PLIN-XX-01 (b) MLIN-XX-01 (c) PACR-XX-01 and (d) MLIN-XX-02.For which three or two main regions demarcated by the broken line can be identify.

values in the three field regions which increase with concentration. The region A, has slope values $m_A < 1$ for all the nanocomposites considered, and describes the path of the $I - V$ characteristics where the applied bias is lower than the potential barrier presented by the space charge region, so no appreciable current is able to flow until the applied bias balances the potential drop, as expressed in equation 4.6. Current transport in this voltage range can only be due to some form of tunneling or thermionic emission as described above.

For region B, the slope m_B is seen to increase from values of about 1 to above 2 for all the nanocomposite structures (except for the drop in the value of m_B at 50 and 60 wt.% for

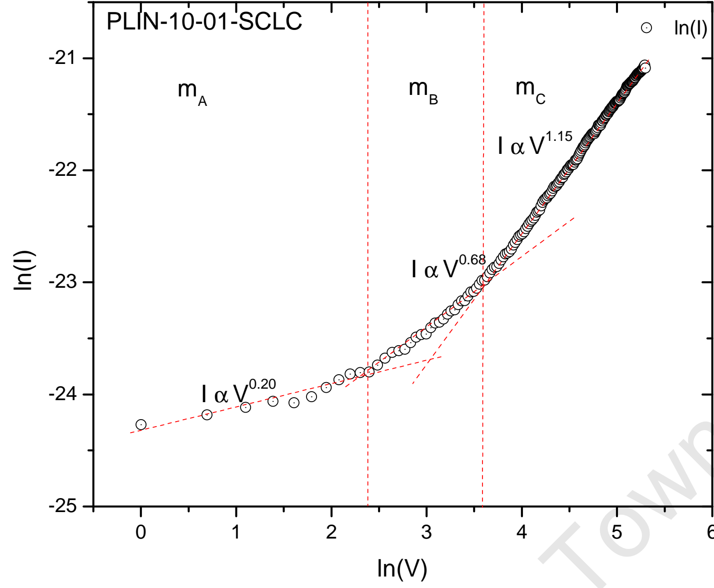

Fig. 4.28: Plot of $ln(I)$ vs. $ln(V)$ for sample PLIN-10-01, showing three different slope regions demarcated by the broken lines with slope values m_A, m_B and m_C calculated from the best line of fit to the three different linear regions

University of Cape Town

the PACR composite). This region where the slope of the $ln(I) - ln(V)$ plots is approximately equal to unity, represents when the applied external potential is just greater than the potential barrier ($qV > \phi$) presented at the interface and the bulk material. The $I - V$ characteristics in this region may be approximately represented by an Ohmic conductance process, with the current transport described with [194]

$$J = qP_o\mu\frac{V}{d}. \tag{4.57}$$

In equation 4.57, assuming holes as the single charge carriers, q is the electronic charge, μ is the carrier mobility and V is the applied voltage. With the electrode spacing for the structures $d = 0.3 \times 10^{-3}m$. P_o is the concentration of free carriers given by,

$$P_o = N_v exp\left(\frac{-E_F}{KT}\right) \tag{4.58}$$

where E_F is the position of the Fermi level above the valency band edge and N_v is the density of states in the valency band.

At relatively high fields, the value of the slope approaches $m = 2$ at lower particle concen-

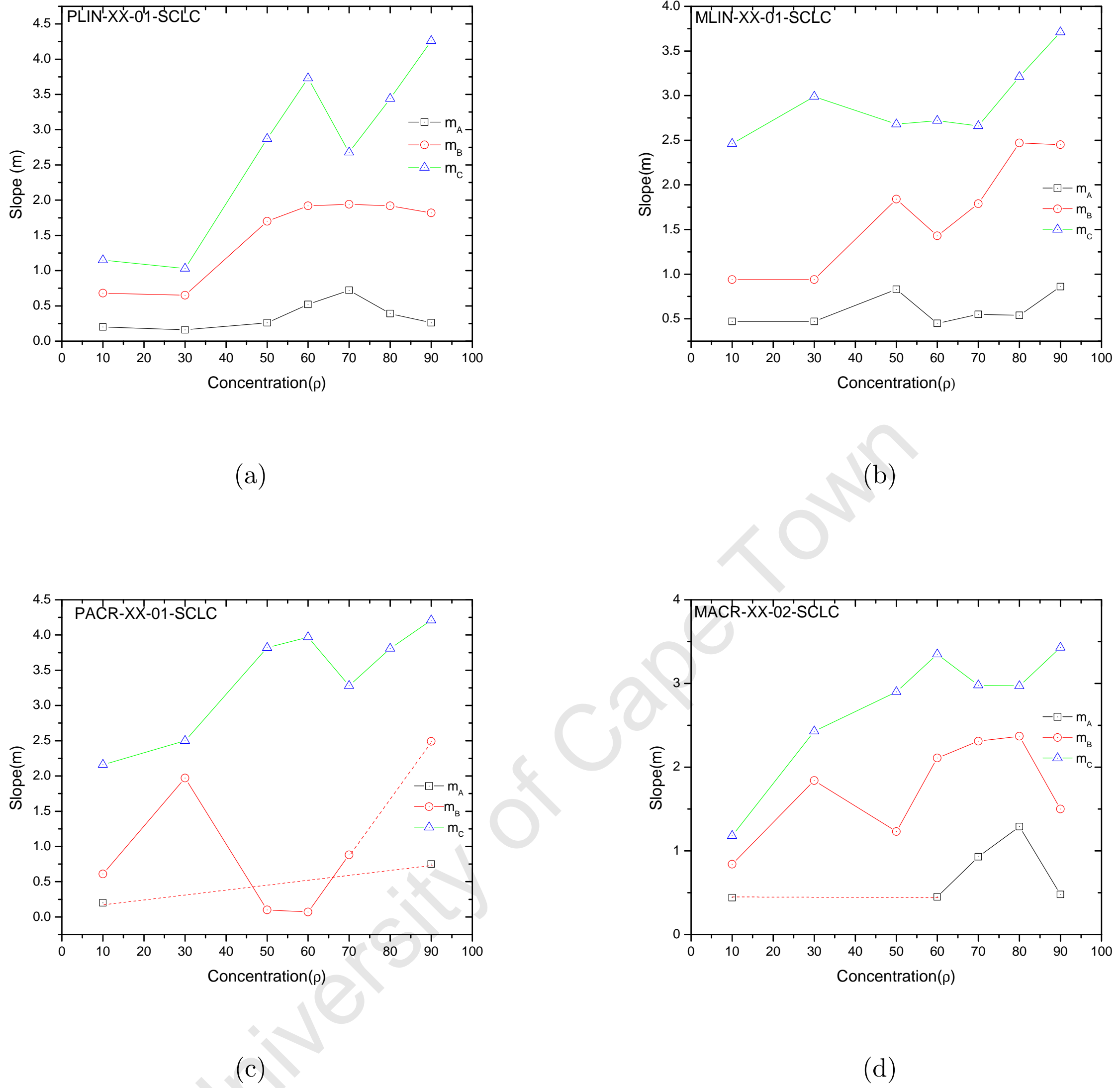

University of Cape Town

Fig. 4.29: Plots of variation of the three slope region with concentrations for (a) PLIN-XX-01 (b) MLIN-XX-01 (c) PACR-XX-01 and (d) MLIN-XX-02. The broken lines are used over the merged regions.

tration, and increases beyond 2 with increasing particle concentration for all the composites. For regions where m is about 2, SCLC charge transport can be assumed to be the dominant conduction process [197]. For such systems, the current density for trap level controlled conductance can be expressed by equation 4.20 repeated here as [194]

$$J = \left(\frac{9}{8}\right) \varepsilon\varepsilon_o \mu\theta \left(\frac{V^2}{d^3}\right), \tag{4.59}$$

where θ is the ratio of the concentration of free carriers to the trap carrier density, and all

the other different symbols are as previously defined.

The increase in current with voltage for which the power law exceeds 2, is attributed to the effect of trap filling, when the external applied voltage reaches V_{tr}, a voltage for which charge injected from the contact into the nanocomposites for example is sufficient to fill all the traps presented at the interface or within the bulk, and charge carrier transport becomes trap filled limited. This voltage V_{tr} signals a transition from Ohmic to the square law conductance, and is related to the equilibrium concentration of free carriers, repeated here again for convenience as

$$P_o = \left[\frac{\varepsilon\varepsilon_o\theta}{qd^2}\right] V_{tr}. \tag{4.60}$$

University of Cape Town

From figures 4.27 and 4.29 (and Appendix A.5) it is clear that SCLC conduction starts at the intermediate voltage level and becomes the dominant effect at high voltages. The following deductions about the contribution of SCLC to the overall charge transport in the high field or voltages regions can be summarised.

- In the PLIN systems, contribution from SCLC was not observed for external applied voltages up to 200V for the 10 to 30 wt.% nc-Si in linseed oil. However for a concentration 50 wt.% and above, SCLC contributions ($m \approx 2$) were observed at relatively small applied voltages, while the transport is dominated by trap filled limited current (TFLC) ($m > 2$) from voltages above V_{tr} which is observed to depend on the concentration.
- For the MLIN system, contributions from SCLC, and thereafter dominated by TFLC, was observed for all concentration as $m > 2$ in the high voltage region for all cases.
- The PACR system also exhibited significant contributions from TFLC as $m > 2$ for all concentrations with typical V_{tr} values lower than in the PLIN and MLIN systems.
- The MACR system also shows a similar contribution from TFLC current at relatively higher voltages for all concentrations except for 10wt.% where the characteristics did not exhibit characteristics typical of SCLC even up to maximum voltage of 200V.

From the above observations it is reasonable to suggest that contribution from SCLC and TFLC is significant in the overall charge carrier transport of the nanocomposites considered in this work. The results also show a dependence of the TFLC on concentration of particles at high voltages.

4.5.9 Contribution from hopping conduction to charge carrier transport in silicon nanocomposites.

Conduction in insulators, nanocomposites or dielectric systems in general, has been shown to include contributions from temperature dependent hopping mechanism [198, 199, 200]. For systems with marked temperature dependent charge transport, three basic models: (a) nearest neighbour hopping; (b) Mott's variable range hopping and (c) Efros-Shklovskii's variable range hopping mechanism can be employed to interpret the $I - V$ characteristics [201].

For a composite system in which the donor sites (in this case silicon nanoparticles) are randomly distributed in an insulating matrix, nearest neighbour hopping usually involves charge carrier hopping from an occupied donors to the nearest empty donor site. This is a process characterised by a temperature dependence of resistivity, given by [201]

$$\rho = \rho_0 \exp\left(\frac{E_A}{K_B T}\right), \tag{4.61}$$

University of Cape Town

where ρ_0 is a constant, T is the absolute temperature, and E_A is the activation energy. In the Mott variable range hopping model, the temperature dependence of resistivity is given by [200]

$$\rho = \rho_0 \exp\left(\frac{T_0}{T}\right)^v, \tag{4.62}$$

where $v = 1/(d+1)$ and d is the dimensionality of the system: T_0 is a characteristic temperature, related to the density of states at the Fermi level, given by Mott's activation energy

$$KT_0 = \left(\frac{\alpha}{N(E_F)\xi^3}\right). \tag{4.63}$$

α is the coefficient of decay in the localized state, which is equal to 18 for 3D systems, $N(E_F)$ is the density of states and ξ is the localization length. The Efros-Shklovskii variable range hopping mechanism is similar to the Mott model, and the resistivity is given by [201]

$$\rho = \rho_0 \exp\left(\frac{T_0}{T}\right)^{\frac{1}{2}}. \tag{4.64}$$

In this case, the temperature dependence of the resistivity is caused by coulomb interactions

and is expressed as [201]

$$K_B T_0 = \left(\frac{\beta_D q^2}{4\pi\varepsilon_0 \varepsilon \xi} \right) \tag{4.65}$$

where β_D is a coefficient which depend on the dimensionality of the system and ε_0 and ε are the permittivity of free space and the dielectric constant of the material respectively.

Fig. 4.30 shows semi-logarithmic plots of the dependence of conductance (σ), versus the absolute temperature (T), on particle concentration for the PLIN nanocomposite for which some temperature dependent $I - V$ characteristics were measured.

From the plots of Fig. 4.30(a) and Fig. 4.30(b) for the 10 and 30 wt.% nanocomposites, one can see a clear positive linear dependence of $log(\sigma)$ on the absolute temperature T. For the three field regions considered, 10V, 50V and 150V, representing the low, medium and high field regions respectively, the derived slopes, and hence the estimated values of the activation energy using equation 4.61, all lie in a close range $3.5 - 4.5meV$ for the two samples.

For particle concentration 50 wt.% and above as shown for 50 and 90 wt.% in Fig. 4.30(c) and Fig. 4.30(d) respectively, the plots of $log(\sigma)$ vs. T gives a negative correlation. A similar trend was observed in the Arrhenius plots for these particular concentrations in section 4.5.2.

While hopping mechanism may contribute significantly to the overall carrier transport of the nanocomposites in the low particle concentration, the behaviour at concentrations above 50 wt.% is clearly due to other processes as it does not satisfy the hopping models. The observed decreases in conductance at higher concentration with increasing temperature may reasonable suggest a conduction limited by scattering, as injected carriers traverse the medium when the nanocomposite reaches the percolation threshold.

From the plot of Fig. 4.30(c) it is reasonable to suggest that the concentration 50 wt.%, is the transition point between the hopping conduction at low concentration and the possible scattering limited conductance at high concentrations, as it posses both positive and negative temperature dependent conductance with a turning point which depends on the field.

However, since hopping conduction has a field dependent property, which relates the current density with applied potential $J \propto V$. This implies that a system with hopping conduction should exhibit a linear $I - V$ characteristics. From the $I - V$ plots of the systems shown in Fig. 4.15, one could reasonably suggest that the contribution due to hopping is limited to ranges of applied voltages where direct tunneling is predominant, or to composites with lower concentrations.

University of Cape Town

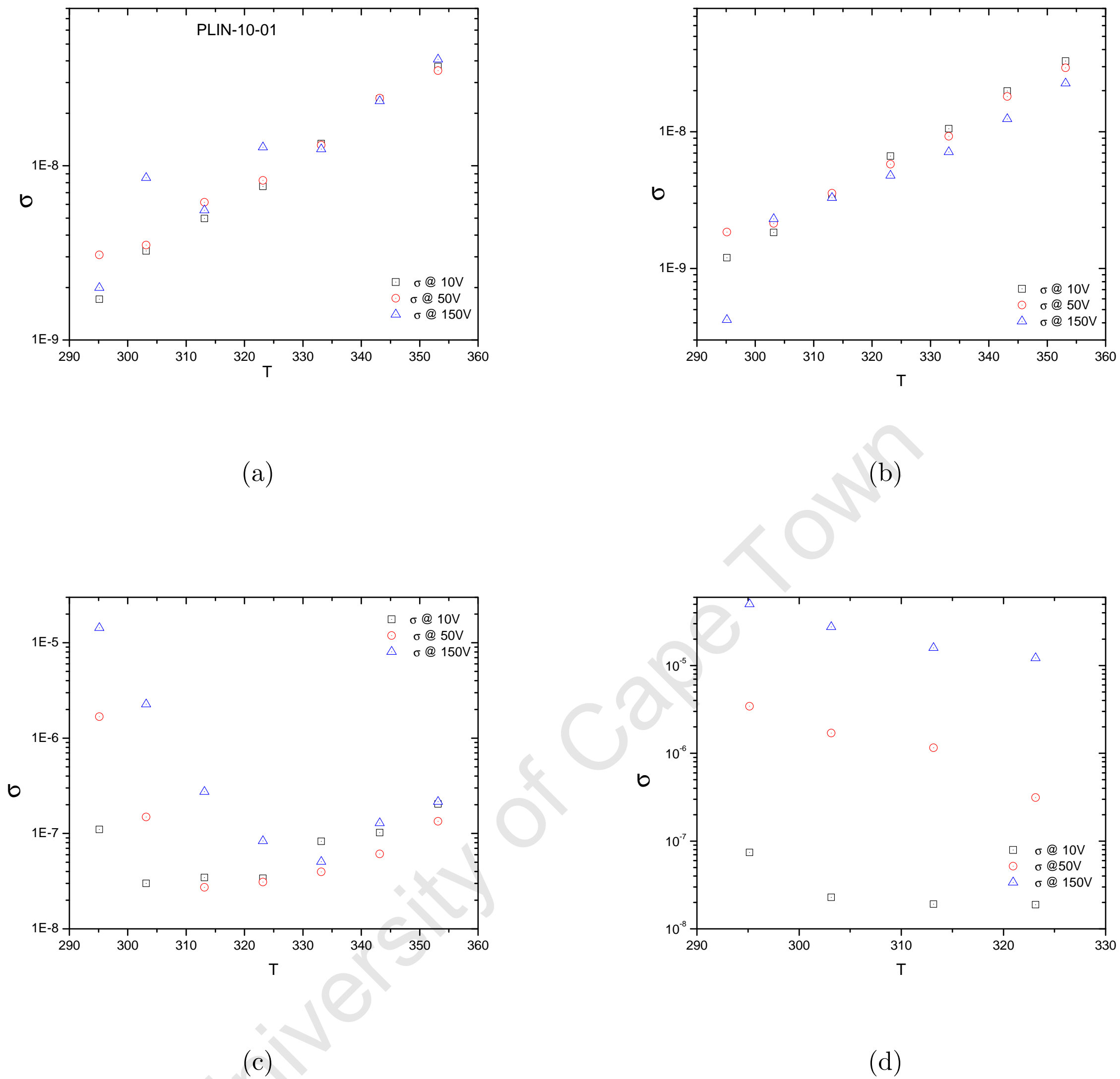

University of Cape Town

Fig. 4.30: A semi-logarithmic plots of the dependence of conductance σ versus the absolute temperature T on particle concentration for the PLIN nanocomposite (a) PLIN-10-01 (b) PLIN-30-01 (c) PLIN-50-01 and (d) PLIN-90-01.

4.6 Summary of carrier transport mechanism

The test of different transport models generally applied to study metal-semiconductors and insulator/dielectric systems on the forward $I - V$ characteristics of these nanocomposites reveals that the carrier injection and transport is determined by two main factors: (1) the concentration of particles constituting the composite, and (2) the level of external bias voltage on the structure.

The nanocomposite systems have a percolation threshold of 70wt.% and 30wt.% for the linseed oil and acrylic based composites respectively. These concentration values give optimum conductance across the structure. Below the percolation threshold, transport is mainly limited by the matrix or insulating binding medium. Direct tunneling and field emission (FE) are major contributors to the transport at low field, while thermally activated processes, such as hopping and thermionic emission are the major contribution to the transport process at higher field. Above the percolation threshold, charge transport is through the network of silicon nanoparticles and injection of carriers through the barrier at the interface of the metal nanocomposite structure becomes pronounced. This injection of carriers at high field may be via TFE or FE.

At higher concentrations, the Poole-Frenkel and Richardson-Schottky conduction mechanisms, resulting from barrier limiting process in the interface of the metal contact to an interfacial insulator, and a bulk limiting current through the matrix structure coexist. Charge transport is by a combination of charge carrier release due to ionization of impurity centres in the dielectric and thermally assisted conduction of charged carriers over a lowered columbic potential due to the applied electric field, or it may result from thermal emission of carrier from randomly distributed traps to the conduction band. A similarly pronounced contribution due to the accumulation of charges at the interface and by an exponential distribution of traps in the bulk resulting in a power law relationship$I \propto V^m$ is pronounced at concentrations above threshold. The observed transport mechanism is dominated by space charge limited current conduction at medium applied field where ($m > 2$) and by trap filled limited conduction at high voltages.

University of Cape Town

5. Devices application of silicon nanocomposites

The electronics industry has up until recently been concern with the further realization of Moor's hypothesis, which states that the number of transistors on a single chip (of the same size) should subsequently double about every two years. Through advances in photolithography, and more recently X-ray and electron beam lithography, transistor density and integration have increased tremendously[202]. However the continuous downscaling of devices is reaching it's limit. As the channel length of transistor now approach values comparable to the wavelength of light, the use of conventional photolithography is simply physically incapable of a continuous feature size reduction. Excessive heat generation, cross talking between transistors, low yield and the high cost of technology required to carry out such nano-fabrication are some of the hurdles toward further level of processor miniaturisation and integration.

In view of the limitation of photolithography, printed electronics, that defines the printing of electronics on common media such as paper, plastic, and textiles using standard printing processes is emerging as a force to be reckoned with for mass produced electronics device technology [203]. However the future of this emerging industry will dependent largely on high-performance semiconductor inks [204].

At present organic inks made from conductive polymers, plastics, or small molecules present serious mobility, stability and cost challenges. As a result, many researches are directed toward improving these important characteristics, either by the formulation of new organic semiconductors or from a hybrid of organic/inorganic composites materials. Nanocrystalline silicon had received great focus as a good candidate for an hybrid organic/inorganic composites because of the interesting features silicon exhibits as its size reduces to the nanometre range. As such several companies are developing silicon inks based on nanocrystalline silicon or on other silicon compounds [204].

University of Cape Town

5.1 Hybrid organic-inorganic materials for printed electronics devices

Hybrid materials are potentially very attractive for their electrical properties which result from a combination of properties of both organic and inorganic materials within a single molecular-scale composite [205]. Inorganic solids like silicon are bound by strong covalent bonding, compared to the weak van der Waals attraction in the organic solid state. Thus combining within a material the desirable electrical properties of an inorganic component with the ease of processing common to organic materials provides unique opportunities with respect to the individual components [205].

Inclusion of such silicon nanoparticles in polymeric binders to form an active nanocomposite inks is aimed at achieving this purpose. These inks may be adapted for printed electronics through various processes such as screen printing, ink jet printing and transfer printing. Although the level of resolution and registration required by complex electronics is unattainable by this process, the ease of applying the process for large area, flexible substrates, offers overall cost effective solutions in areas like photovoltaics [204]. A possible application of printable electronics, is in the area of transistor array on flexible substrates. This application is very cheap because it does not involve expensive vacuum equipment, multiple photolithographic patterning steps and high-temperature processing [206].

University of Cape Town

This part of the research presents a procedure for the production of an all printed transistor on a cheap plastic substrate, applying the silicon nanocomposites developed and characterised earlier, with respect to determining the dominant charge transport in chapter 4, as the active material in a metal insulator field effect transistor. The steps which include printing of metallic electrodes for electrical connections, printing of a dielectric insulator as well as the silicon nanocomposites will be explained. The device performance was evaluated by conducting measurements of the $I-V$ characteristics including measurement of the output and transfer characteristics in order to determine the transconductance and carrier mobility. The stability of the devices under electrical stress is also discussed.

5.2 Review of nanocrystalline silicon based transistors

Nanocrystalline silicon (nc-Si), was first reported in 1968, and has raised a great deal of interest because of its superior properties over amorphous and organic semiconductors, with

regard to its application in photoelectronic and microelectronic devices [207]. Research efforts in nanoelectronics have been directed at studying electron transport in laterally-defined nanometre-scale structures in the hope that phenomena might be discovered that could form the basis for novel electronic devices [208]. This has resulted in a variety of novel nanometer-scale devices, such as those based on interference phenomena, conductance quantization, and Coulomb blockade effects [208, 209, 210]. Two main transistor devices that are based on this approach include: single electron transistors (SETs), which exploit the quantum effect of tunneling to control and measure the movement of single electrons [211, 212]; and resonant tunneling transistors (RTTs), which requires a band-edge discontinuity to form a quantum well [213].

Nanocrystalline silicon has been used as the active layer in conventional thin-film transistor structures, because of its high mobility and stability features as mentioned earlier. As a result many methods have been developed for the deposition of nc-Si. Traditionally nc-Si is deposited via chemical vapour deposition techniques. Commonly used methods include, hot wire chemical vapour deposition (HWCVD) and plasma enhanced chemical vapour deposition (PECVD). Typical CVD methods involve the deposition of the nc-Si:H layer from silane gas at temperatures above 1000^0C onto glass or silicon substrates [214].

Attempt at low temperature deposition of nanocrystalline silicon thin films, suitable for flexible and inexpensive substrate, often results in amorphous silicon (a-Si:H). In many cases the resulting amorphous silicon is recrystallized to form nc-Si [214] through other processes like rapid thermal annealling, laser-induced crystallisation [215] or pulse thermal processing (PTP) utilizing high-density infrared plasma arc lamps [216]. However it has been demonstrated that(HWCVD) can be adapted to allow device-quality material deposition of both hydrogenated amorphous (a-Si:H) and nanocrystalline (nc-Si:H) silicon thin films at substrate temperatures below 300^0C [217].

Field-effect transistors based on nanocrystalline silicon can provide a common, inexpensive method of driving individual pixels in LCD and OLED displays and also for integrating switching elements and peripheral drivers in high-performance large-area active matrix displays. Necessary conditions for achieving high frame rates in high-resolution displays include increased drain currents resulting from high mobility [218, 219]. Thin-Film transistors (TFTs) based on nanocrystalline silicon (nc-Si) are candidates for such applications because of their high electron mobilities of up to $150cmV^{-1}s^{-1}$ and hole mobilities up to $1cmV^{-1}s^{-1}$, which are much more higher than amorphous silicon [220]. Apart from this nanocrystalline silicon is more stable as it does not suffer from degradation under bias stress and under

University of Cape Town

illumination common to amorphous silicon and organic semiconductors [221, 222].

5.3 Thick-film deposition and patterning

In order to fabricate electronic devices and connecting circuits, patterning of the semiconducting films is necessary to define the active area of the device [205]. Since the aim is the combination of organic or hybrid nanocomposites with low-cost and flexible substrates, this implies that similarly low-cost and low-temperature patterning processes must be developed [205]. Conventional processes like photolithography, etching, or focused-beam (e.g., ebeam,ion-beam, laser-beam) techniques for patterning inorganic thin films are generally not suitable for hybrid thick films [205]. In general many of the present methods applied for patterning conventional thick film circuit employ printing techniques. The following subsections will discuss in general the different printing methods and their applications for thick film electronics patterning, with particular emphasis on the transfer printing technique.

5.3.1 Printed electronics

Printing is an age old means for producing and reproducing text and images, typically with ink on paper using a printing press [223]. Because of its efficiency in producing text and images, over time people have come up with ways of adapting printing for printed electronics [224]. Initially application was limited to printing of interconnections on a printed circuit board, and the printing of thick film passive devices like resistors and capacitors. However the desire to produce active devices and interconnections between them together in a single printing process is the reason for the new trend of printed electronics [225].

Printing of passive devices, like capacitors for example, may be realized by a simple printing sequence of conductor ink and insulator ink, followed by another conductor ink. Although active devices such as light emitting diodes (LED) based on organic semiconductors may be produced using a similar process, in general the printing of active semiconductor material, either as solution or colloid of organic and inorganic components, may require further adaptation of the printing process. Since printed electronics is compatible with flexible substrates, microelectronic devices can in principle be produced using or adapting the several well know printing process, without an expensive clean room setup [226]. Many of the printing process considered as candidate for printed electronics include: Offset lithography, flexography, gravure, ink jet, screen printing and pad printing [223].

University of Cape Town

- Flexography is classified as a direct printing method where flexible elastomeric printing plates with a slightly raised image are inked, and the image is then transferred onto a substrate. This is achieved by creating a positive mirrored master of the required image as a 3D relief in a rubber or polymeric material [227]. The method of printing is such that an amount of ink is deposited upon the surface of the printing plate (or cylinder) using an engraved anilox roll whose texture holds a specific amount of ink. The print surface then rotates, contacting the print material which transfers the ink [228]. An all-polymer field effect transistor in which the source and drain electrodes are printed by using flexographic printing has been reported by Makela et. al.[229]. Since flexography can be used with a wide range of water and oil based inks, flexography printing looks promising for the printing of organic and inorganic semiconductor inks.

- Gravure printing is another type of direct printing process which may be adapted for printed electronics. In this technique the recessed printing image is formed by a raster of small cups which has been chemically etched or engraved on a metallic surface of a printing cylinder. During printing the cups are filled with inks while the excess inks are removed with a doctor blade. A defined amount of ink from inside the cup is then transferred onto a flexible substrate when brought into direct contact with the printing cylinder [230]. Many researchers have demonstrated that gravure technique can be used for electronic device printing. Puetz [230] for example used direct gravure, for printing a UV-curable indium tin oxide (ITO) nanoparticle patterns on polyethylene terephthalate and polyethylene naphthalate foils. A review of other applications for printed electronics can be found in [231, 232].

- Ink Jet printing is a direct non-contact printing method that operates by propelling variable-sized droplets of liquid onto the substrate [233]. This method holds a greater promise as a means of device integration offering targeted film deposition. Application of inkjet for the printing of conducting electrodes to different electronic devices has been demonstrated by many workers. Similarly, application of high-resolution inkjet printing of all-polymer transistor circuits has been reported [234, 235].

- Screen printing is probably the oldest method of printing. It is essentially a stencil process in which the printing ink is forced through open area of a mesh reinforced stencil resulting in a sharp-edged print on the surface of the substrate [236, 225]. Screen printing, has a great promise in the fabrication of electronic devices because of the great adaptability of the fabrication process. A major application of screen printing for printed electronics, is with the development of thin but highly efficient crystalline silicon solar cells [237, 238]. Screen printing of FETs had also been demonstrated for

University of Cape Town

organic semiconductor and with little effort screen printing can easily be adapted for printing inorganic-organic semiconductor inks the active part of a transistor structure [239].

- Pad printing is a type of offset gravure printing where an image from the printing plate is transferred onto a substrate using an elastomer pad. It is an indirect process which allows printing on otherwise impossible regions of a desired substrate of any shape [240]. Pad printing as been described as an efficient method for patterning the electrodes of an OFET, with dimensions of about $20\mu m$ achievable [241]. For the purpose of this research, a commercially available pad printer was adapted for printing the metallic electrode structures of a MISFET. For this reason the principle of operation of this technique is described in detail below.

5.3.2 Principle of pad printing

The main components of a pad printing process, as described in [242], and shown in Fig. 5.1 include: the printing plate, ink, silicon rubber printing pad, a Doctor blade, and an assembly of these components either for an automated or manual process.

- **Printing Plate:** The printing plate (cliche) is generally steel or a nylon photopolymer material which carries the desired image or structures to be printed. The image are normally created on the printing plates by chemical etching. Its function is to hold inks in the etched cavity for later pickup by the pad. To achieve optimum printing with the pad printer, certain recommendations on the design of the plates must be considered. For example, the desired image should be at a distance of at least 25 mm from the outer edge, and centered on the plate. And if long or fine lines are desired, the image must be at an angle of $\approx 5^o - 15^o$ to the blade track as recommended in [243]. This is to prevent the doctor blade from dipping too low and scooping out too much ink. For optimal printing an etching depth of $25\mu m$ is recommended [243].

- **Inks:** The most important component in the pad printing process is the ink. Its properties such as easy workability, long pot life in wells/cups, ease of cleaning, and best possible adhesion to all objects and material without need of pre-treatment or subsequent treatment, determine to a large extent the final print quality [242, 243]. Pad printing inks consist of binders, solvents and pigments. The evaporation of the solvent from the ink is the main mechanism that enables the process to operate. Inks used for Pad printing are therefore often categorised based on their drying behaviour:

University of Cape Town

- physically drying inks;
- chemically curing inks;
- heat curing inks;
- UV curing inks.

While each ink type has its advantages and application area, the type of ink base chosen for a print process will depend on one or all of the properties mentioned above. Inks for printing of electronic devices must be tuned to fulfil the printability requirements while conserving the electrical features desired of the final print.

- **Pad:** The purpose of the pad is to receive the image from the cliche, transfer the ink film to the substrate, and deposit it there. The important requirement for a pad is that it must be constructed so that it is capable of being bent or flexed or twisted without breaking, and must guarantee transfer of the image without smudges or blurring [243]. Printing pads are made of materials such as silicone rubber in a wide array of shapes, hardnesses and qualities. Pad properties such as size, shape, and hardness affect printability in many ways, and the choice of a pad will depend on the size of the area the print should cover and the definition of the final print. A hard pad for example is suitable for reproducing print well, and has a greater life expectancy due to its physical stability. However it will not be suitable for printing on fragile or delicate substrate. Similarly for reproducing corners at an exact angle a soft pad is required [243].

- **Doctor Blade**: This is a metal strip used to wipe out excess ink off the image areas on the printing plate, leaving ink inside the etched areas of the plate. In most cases it is made from mild steel to enable slight bending as the blade sweeps over the printing plate.

A pad printing cycle involves six main steps as shown in Fig. 5.2 below. In the starting position the printing ink is used to flood the image area on the printing plate, covering the image and filling it with ink. The doctor blade is now moved across the surface of the printing plate, removing all excess ink and exposing the etched image, which is filled with ink. The top layer of ink becomes tacky as soon as it is exposed to the air, enabling it to adhere to the transfer pad and later to the substrate.

The transfer pad then comes over the image and presses down onto the printing plate momentarily. As the pad is compressed, it pushes air outward and causes the ink to lift from

University of Cape Town

the etched artwork area onto the pad. As the transfer pad lifts away, the tacky ink film inside the etched artwork area is picked up on the pad. A small amount of ink remains in the printing plate. The transfer pad then moves away to the desired position on the substrate and compresses down onto the substrate, transferring the ink layer picked up from the printing plate to the substrate surface. Then, it lifts off the substrate, returning to the initial position, which completes one print cycle. This process may be repeated depending on the desired print thickness. Often for fast drying inks, in most cases a one cycle print is sufficient to give a good imprint [240, 242].

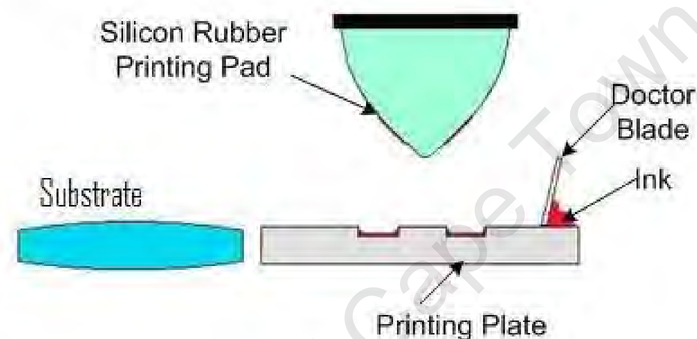

Fig. 5.1: The basic components of a pad printing process [242, 244].

University of Cape Town

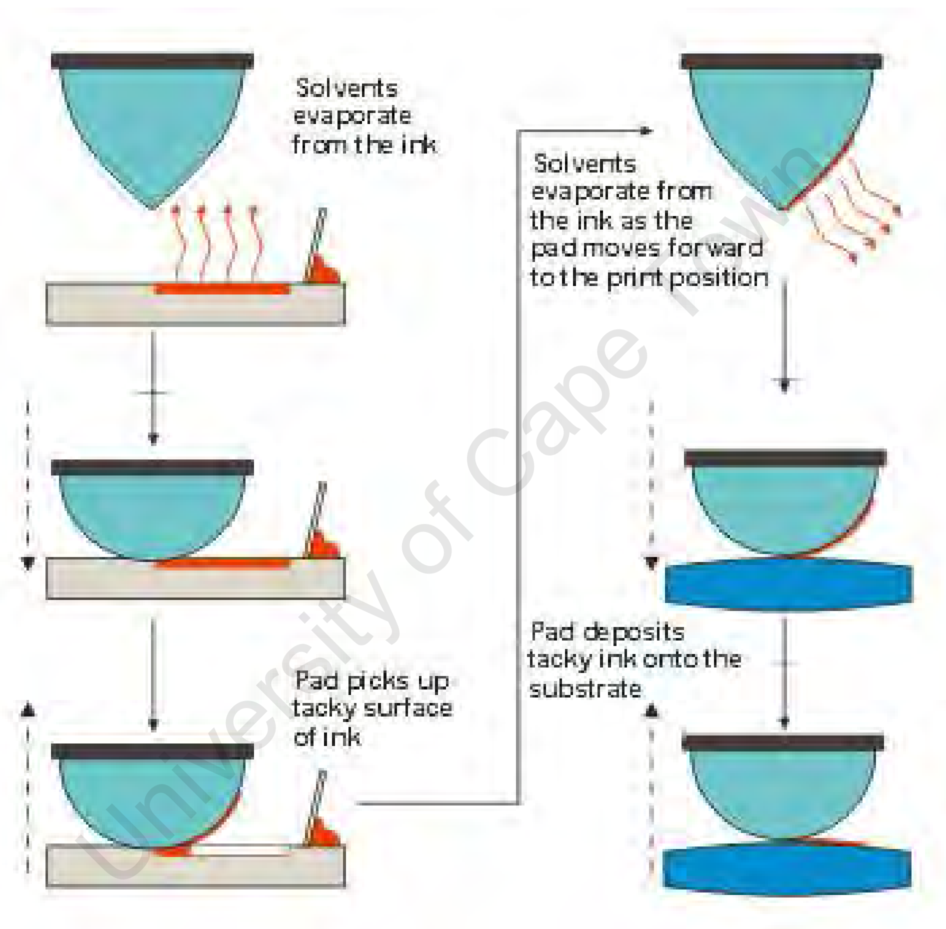

University of Cape Town

Fig. 5.2: The six stages of a typical printing cycle of in a pad printing process [242].

5.4 Transistor structure

Printing of semiconductor devices like transistors, in most cases employs structures similar to those used in thin film electronics. A typical thin film transistor (TFT) structure follows a consecutive deposition of the gate, source and drain electrodes, and also the insulator and channel materials [222]. Four basic structures, classified by the deposition order of the structural components, as shown in figure 5.3, have been adopted in TFT fabrication [205].

In the staggered structure the source and drain electrode are the first to be deposited on the chosen substrate. This is then followed by the active semiconductor layer, the gate dielectric and then the gate electrode in that order. If this process is inverted, such that the gate electrode is the first to be deposited, and the other components deposited in the reversed order of the described staggered structure, then an inverted staggered structure is formed. In both structures the gate and the source-drain electrode are on opposite sides of the active semiconductor material and the gate dielectric [205]. In the case of the coplanar structure, the three electrodes are on the same side of the active semiconductor material, with the gate dielectric material separating the gate electrode from the source-drain electrode. If the semiconductor layer is the first to be deposited, then the device is simply refereed to as coplanar. On the other hand, if the semiconductor is deposited last, then it is referred to as inverted coplanar. TFT structures are further referred as top-gate or bottom-gate structures depending on the position of the gate electrode in the structure [245].

While the choice of a particular structure may be determined by ease and convenience of the fabrication process, the performance of a TFT has been observed in many cases to be dependent on the position of the active semiconductor layer in the assembly [246][179]. For applications requiring the printing of semiconductor inks on flexible substrates, inverted coplanar structures may be the preferred choice of structure, mainly because of their simplicity, but also because the semiconductor ink is printed at the last stage, preventing interaction that may result in contamination from the print of wet components of the electrode or dielectric.

University of Cape Town

5.5 Basic TFT operation

The basic function of a field-effect transistor is to modulate the current flowing in a conducting channel between the source and drain electrodes by means of a variable voltage applied at a third electrode [205]. The important parameters of TFTs in general are the channel width,

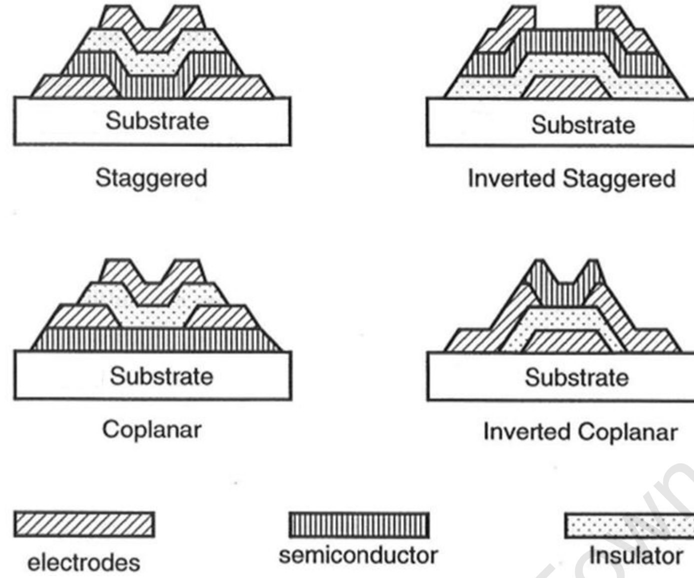

Fig. 5.3: Four types of commonly used TFT structures. Taking from [245]

University of Cape Town

W, the channel length, L, and the capacitance C_{ox} per unit area of the insulator layer of thickness d [205]. To describe the current voltage characteristics, we consider a long channel (low electric field) enhancement type FET as shown in Fig. 5.4. This structure generally operates in a normally on mode, and current through the channel is either depleted by the application of a positive gate potential, or enhanced by application of a negative voltage in case of a P channel device. The reverse is true for an N channel device.

Generally the current voltage behaviour of such a TFT is modeled using the conventional gradual channel approximation in which a uniform potential drop along the channel is assumed [247]. Under such idealized conditions, the channel charge density $Q_n(y)$, at any y-position is given by [247],

$$Q_n(y) = -C_{ox}\left([V_{gs} - V_T] - V(y)\right), \tag{5.1}$$

where the quantity $V_{gs} - V_T$ is the effective voltage applied to the gate, $V(y)$ is the potential at position y in the channel. C_{ox} is the channel capacitance per unit area , given as

$$C_{ox} = \frac{\epsilon_{ox}}{d}, \tag{5.2}$$

where ϵ_{ox} and d are the dielectric constant and thickness of the insulator layer respectively.

The current voltage characteristic curve for insulated gate field effect transistor in general is

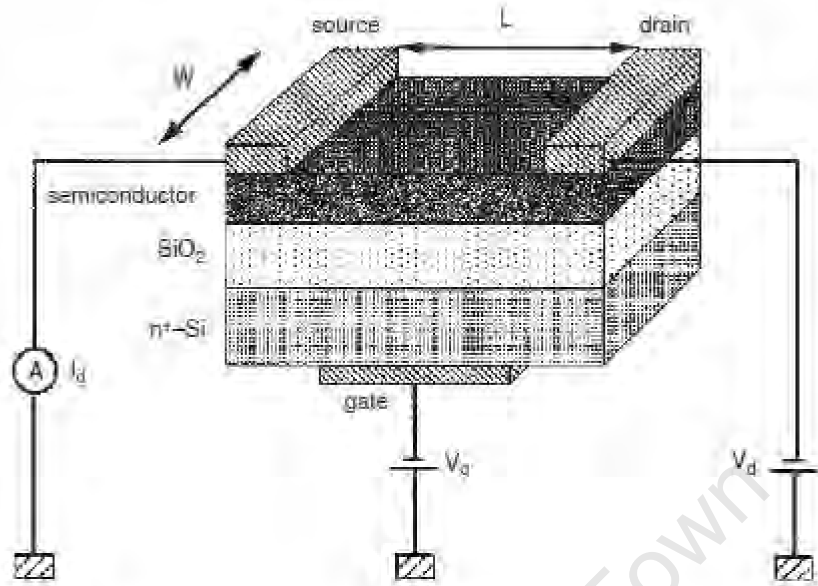

Fig. 5.4: Schematic diagram of a typical field-effect transistor. W and L are the channel length and width, respectively and having and an oxide layer as insulator (MOSFET)[205].

University of Cape Town

divided into the cut-off, linear and saturation regions. In the cut-off region, where $V_{gs} < V_T$, where V_T is the threshold voltage, the transistor effectively passes no current and remains in an off-state irrespective of the drain source voltage V_{ds} applied across the channel. When the applied drain source voltage V_{ds} is positive but less than the effective voltage applied to the gate electrode the behavior is ohmic, and this region is described as the linear operating region. However as V_{ds} increases beyond the effective gate voltage the channel is pinched off, and as a result the transistor current reaches saturation. Further increase in V_{ds} does not increase the drain current any further. The two important operating regions namely, the linear and saturation regions, of a typical TFT are described in detail in the following subsections.

5.5.1 Linear region

The current flowing in the FET channel for a given drain source potential can be represented as

$$I_D = -WQ_n(y)v(y), \tag{5.3}$$

where W is the width of the transistor structure and $v(y)$ is the velocity of the charges in the channel. Equation 5.3 can be expressed in terms of the electric field as

$$I_D = -WQ_n(y)\mu_n E. \tag{5.4}$$

Using equation 5.1, a generalize expression for the drain current in the transistor can be represented as

$$I_D = \mu_n C_{ox}\frac{W}{L}\left[\left(V_{gs} - V_T\right)V_{ds} - \frac{V_{ds}^2}{2}.\right] \tag{5.5}$$

For small V_{ds} value the quadratic term becomes small, and the $I - V$ characteristic is linear in V_{ds} and may be represented by

$$I_D = \mu_n C_{ox}\frac{W}{L}\left[\left(V_{gs} - V_T\right)V_{ds}\right]. \tag{5.6}$$

5.5.2 Saturation region

When $V_{gs} > V_T$ and $V_{ds} > (V_{gs} - V_T)$ are high enough such that the channel is pinched off, to indicate the lack of channel region near the drain. The drain current is now weakly dependent upon drain voltage V_{ds}, and controlled primarily by the gate-source voltage. This characteristic can be modeled very approximately using equation 5.5, which is re-written for saturation with V_{ds} been replaced by V_{d-sat} as [247, 248]

$$I_D = \mu_n C_{ox}\frac{W}{L}\left[\left(V_{gs} - V_T\right)V_{d-sat} - \frac{V_{d-sat}^2}{2}\right], \tag{5.7}$$

which simplifies to

$$I_D = \mu_n C_{ox}\frac{W}{2L}(V_{gs} - V_T)^2. \tag{5.8}$$

5.5.3 Determination of device parameters

The transfer and output characteristics of a TFT, usually derived from $I - V$ characteristics with variation of gate voltage and fixed drain source voltage, and variation of the drain source voltage with different gate voltages respectively, are important measurements used to determines the field effect mobility, threshold voltages, and on/off ratio of a field effect transistor. The technique for the extraction of the mobility from a transfer curve measurement assumes a majority carrier transport and usually derived from either the saturation or

University of Cape Town

linear region of the transfer characteristic. Extraction of mobility in the saturation region, assumes approximately a relation between the drain current I_{DS}, the gate voltage V_{GS} and threshold voltage V_T according to equation 5.8.

By plotting $I_{DS}^{1/2}$ vs. V_{GS}, i.e. transfer characteristics in the saturation region for which $(V_{GS} > V_T)$, the value of the field effect mobility and the threshold voltage can be derived from the slope and intercept of the plot respectively as illustrated in Fig. 5.5 for an a-Si:H TFT discussed in [205].

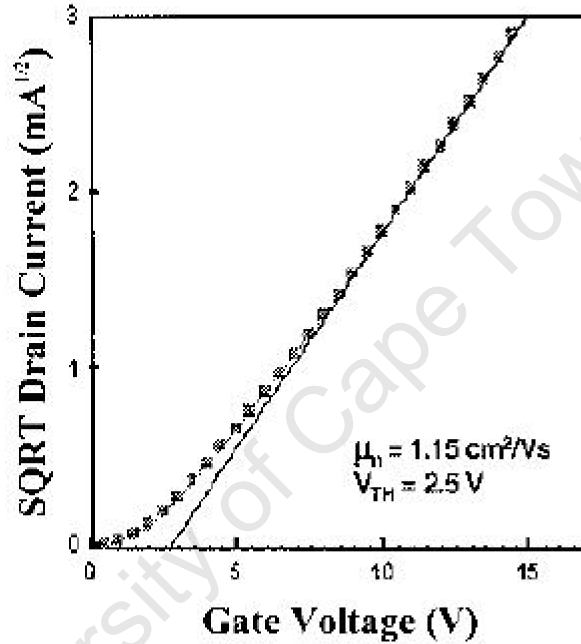

University of Cape Town

Fig. 5.5: A typical transfer Plot of square root of drain current as a function of gate voltage for an a-Si:H TFT to obtain the field-effect mobility in the saturated region [205].

In the linear region, equation 5.7 applies for $V_{DS} << (V_{GS} - V_T)$ approximately as

$$I_{DS} \approx \frac{W}{L} C_i \mu \left(V_{GS} - V_T\right) V_{DS}. \tag{5.9}$$

Hence a slope of the plot of I_{DS} vs. V_{GS} taken at a constant V_{DS} in the linear regime is related to the mobility, such that

$$\mu = \frac{\partial I_{DS}}{\partial V_{GS}} \frac{L}{W C_i V_{DS}}. \tag{5.10}$$

The capacitance C_i is derived from dielectric measurement typically performed using a parallel plate capacitance measurement method, where the complex impedance is measured at

a specified frequency, typically about $50Hz$ [249].

The on/off ratio is generally obtained from the ratio of the maximum drain current to the minimum drain current values obtained in a transfer characteristic measurement, and may be different for different V_{ds} values [249]. Other parameters of interest include the subthreshold swing, defined as the voltage required to increase the drain current by a factor of 10. This is given by the maximum slope on a $log(I_d)$ vs. V_{gs} curve in the subthreshold regime [249].

5.5.4 MISFET's with non ohmic source and drain contacts

In a conventional CMOS FET the source and drain regions are heavily doped to ensure ohmic contact. In thin film and printed electronics however, FET's are usually fabricated on inexpensive and transparent substrates which cannot pass through high temperature processes. Hence the source and drain contact formation by ion implantation and subsequent thermal annealing employed in conventional process becomes difficult to achieve in such FET's [250]. Direct metallic source and drain contacts combined with a metallic gate can be easily fabricated using simple low temperature processes with a low manufacturing cost. Direct metallic contact to the semiconductor channel of the FET will result in a number of interface structures which ultimately determine the transport of carriers at the interface and within the channel. In the most common case the contacts between the metal and the semiconductor will be a Schottky contact, and transistors with such contacts are referred to as Schottky barrier Source/Drain Transistors (SSDT).

Such a SSDT using $CoSi_2/Si$ Schottky contact at both source and drain has been reported by Zhao et. al. [251], and was found to operate in both inversion and accumulation modes. Due to the high Schottky barrier heights of such interface, working voltage are usually very high. Such transistor operation is achieved by the modulation of the transmission coefficient of carrier through the Schottky barrier height[252]. Where the active material is a nanocomposite of semiconductor particles in a polymeric binder, interface states at the junction of the metal-semiconductor matrix may arise as discussed in chapter 4. This has been shown to give rise to a number of carrier transport characteristics. The operation of such system in a transistor structure would therefore be one of modulation of the different probability of the different transport phenomenon present in the structure due to application of external voltages on the source and drain electrodes.

University of Cape Town

5.6 Experimental Method

The goal of this section is to present a simple technique for producing functional transistors. The experimental method used to achieve this goal can be divided into two main stages. The first involves the printing of the inverted coplanar TFT structures using a metallic and dielectric pastes, and the second stage is the printing of semiconductor nanocomposite (similar to those developed for the transport analysis in chapter 4) over the channel created by the source and drain electrodes.

5.6.1 Fabrication of Transistor structures

The inverted coplanar TFT structures is the choice structure for this experiment, two types a nonconventional and conventional inverted coplanar TFT structures were used. The first is a printed structure fabricated on a plastic substrate, while the second consists of an oxide dielectric and vacuum deposited gold source and drain contacts on a silicon wafer donated by Konarka [253]. This choice is influenced mainly by the ease of fabrication, allowing for the passive structures namely the gate electrode, gate dielectric and the source-drain contacts to be fabricated first and finally the nanocomposite overlay on the finished structure. Attempts to produce the other three types of TFT structures, where the active layer is placed between at least one of the passive components did not yield a physically good transistor, due to a chemical reaction of the solvent in the initial passive components composition with the nanocomposite structure. The other main reason is the availability of a ready made standard inverted coplanar TFT structures. The two types of structure are described in detail below.

- **Printed Transistor Structure:** The printed transistor structure consists of a plastic substrate with the metallic gate, source and drain electrodes and a polymeric gate dielectric. The material used for the metallic electrodes was the DuPont 5000 silver paste [169]. Printing of this silver paste was carried out using the pad printing process on perspex substrates, cut into sizes of $50 \times 50 \times 5mm$. Figure 5.6 shows a photograph of a finished printed transistor structure awaiting the printing of the semiconductor ink over the channel area. First a printed **"T"** shaped gate electrode was printed on the plastic substrate using the six step procedure for pad printing described earlier. The width of the line section was measured as $0.32mm$, which is just $0.02mm$ off the size on the template, showing how accurately the pad printing process can reproduce the image. The printed gate electrode was then placed in an oven set at 100°C to cure overnight.

University of Cape Town

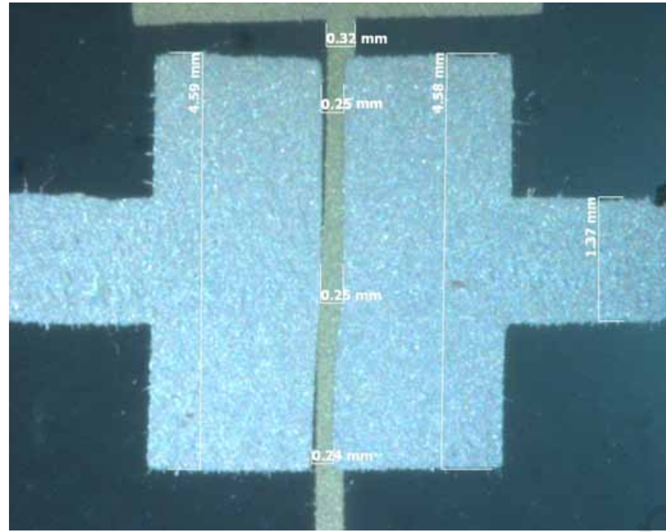

Fig. 5.6: Showing the complete transistor structure. The gate is overlaid with the a dielectric and then the source and drain contacts

University of Cape Town

The next step was deposition of the DuPont 8013 dielectric layer over the gate. Using a stencil, formed from adhesive tape, an open area over the printed gate electrode was defined. The gate dielectric was then spin coated over the defined area using a home built spin coater. The spinning speed was not measured as there is no installed speed monitor on the spin coater. However the spinner was run at a reasonable constant speed achieved by applying $8V$ DC to the spinning motor. This ensured spreading out of the dielectric paste. The rotation was maintained for 5 minutes, long enough to ensure a relatively thin translucent layer of the dielectric over the gate electrode. The spun dielectric paste over the gate electrode was then cured in a light box described in [254] which is fitted with a $400W$ light bulb acting as source of UV for 48 hours period.

After curing the dielectric layer appears as a solid translucent layer over the gate electrode. Using same procedure as for the gate electrode, the source and drain contacts were then printed over the dielectric layer ensuring that the $0.3mm$ channel gap between the source and drain contact centers over the bottom gate **"T"** line. The finished structure was then placed in an oven set at 100^oC to cure overnight.

- **Konarka Transistor Structure:** These transistor structures are shown diagrammatically in Fig. 5.7. The structures are fabricated on a highly n-doped ($n \approx 3\times10^{17}cm^{-3}$) silicon wafer, serving as the gate electrode with a thermally grown gate oxide of $230 \pm 10nm$ SiO_2. The drain and source are from gold placed over the gate oxide structure using a lift-off technique. The thickness of the deposited gold was $50nm$.

Each substrate of area $15 \times 15mm^2$ consist of 16 transistor structures as seen in Fig. 5.7(a). A magnified image of a structure is shown in Fig. 5.7(b). The structures all have a channel width $W = 10mm$ and channel lengths $L = 2.5\mu m$, $L = 5\mu m$, $L = 10\mu m$ and $L = 20\mu m$ in groups of four. The contact pad area is $0.5 \times 0.5mm^2$. To ensure good and rugged contact needed for electrical connections during characterizing, a small amount of 5000 series silver paste was painted on each pad.

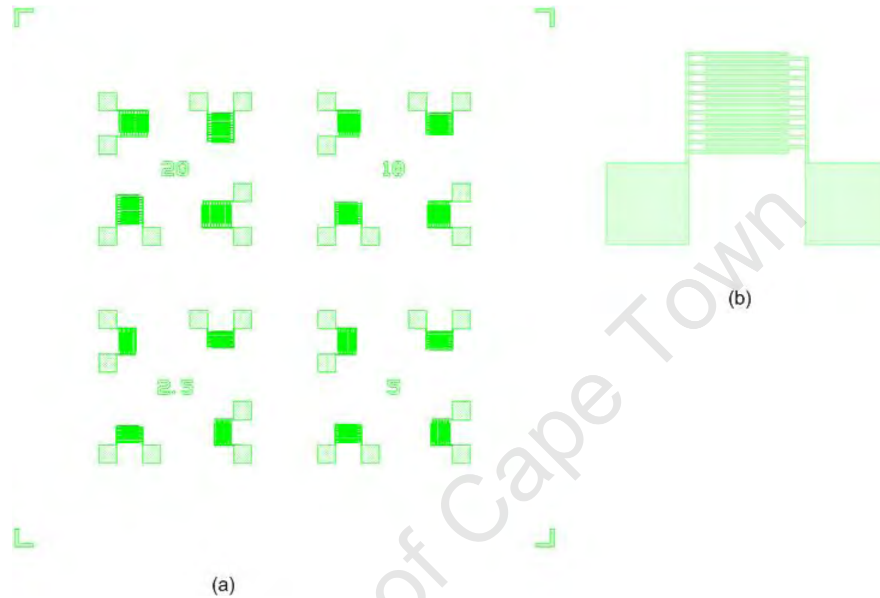

University of Cape Town

Fig. 5.7: (a) Schematic of the standard TFT structures donated by Konarka [253], having 16 TFT with channel width $W = 10mm$ divided into 4 types based on channel lengths $L = 2.5\mu m$, $L = 5\mu m$, $L = 10\mu m$ and $L = 20\mu m$ respectively. (b) A magnified image of one of the TFT structure.

5.6.2 Deposition of active nanocomposite layer and transistor characterisation

The active layer in the transistor structure consisted of nanocomposites formed by inclusion of P and N type silicon powders in either linseed oil or acrylic binding medium. Deposition of the nanocomposite over the channel defined by the source and drain electrode was perform by (1) drop casting or (2) stencil printing as described in chapter 4. Since the experimental procedure for each of the three transistor type is different, the analysis for each of the transistor type will be preceded by a short descriptions of the nanocomposite used, how it was deposited and the electrical characterisation of the transistor using the Keithley 4200 SCS complete $I - V$ semiconductor characterization system described earlier in chapter 4.

5.7 Results and discussion

The performance of a FET may be may be characterised by several parameters such as the field-effect mobility, on/off ratio, and threshold voltage V_T as discussed above. In general, the minimum parameters required to evaluate a transistor performance as stipulated in the IEEE standard for organic transistors [249] should also include the physical dimensions of the transistor structures. In the following subsections, analysis and parameter extraction for the three types of transistor and the composition of the active layer will be presented.

5.7.1 All printed thick film nanocomposite transistor on plastic substrate

Table 5.1 and 5.2 show the PLIN and PACR nanocomposite compositions and the physical parameters of the fabricated transistors respectively. The active layer was formed by drop casting the respective nanocomposite ink over the channel created by the source and drain electrode with channel width ($W = 300\mu m$) and length ($L = 1mm$), shown diagrammatically in Fig. 5.8. The capacitance between the gate and drain-source contact, overlaid by the different cured nanocomposite was measured directly, with Peak Electronic atlas LRC meter running at 200KHz, as $\approx 2pF$ in both case.

University of Cape Town

Table 5.1: Table showing Ink formulation for first transistors

Silicon P+$(2-5\Omega cm)$(g)	Binder (g)	solvent	Si wt.% in binder	Tag
0.25	0.08	distilled H_2O	76	PACR-01
0.25	0.10	Lacquer thinner	71	PLIN-01

Table 5.2: Transistors structure parameters

Structure	Gate length	Gate width	Insulator type	Capacitance
Bottom gate	$300\mu m$	$1mm$	DuPont 8013	$\approx 2pF$

Fig. 5.9(a) shows the output characteristics for one of the acrylic based transistors (PACR-01), for measurement carried out after about 24 hours fabrication, at a temperature of 295K. The drain source voltage V_{ds} was taken from $0 - 150V$ in step of $1V$, for a positive gate potential between $0 - 100V$ in step of $20V$.

As seen from the plot, when positive potential is applied to the gate electrode, the transistor become relatively less conductive. Such characteristics are typical of a normally on depletion mode transistor. This suggests holes as the dominant carriers for conduction within the

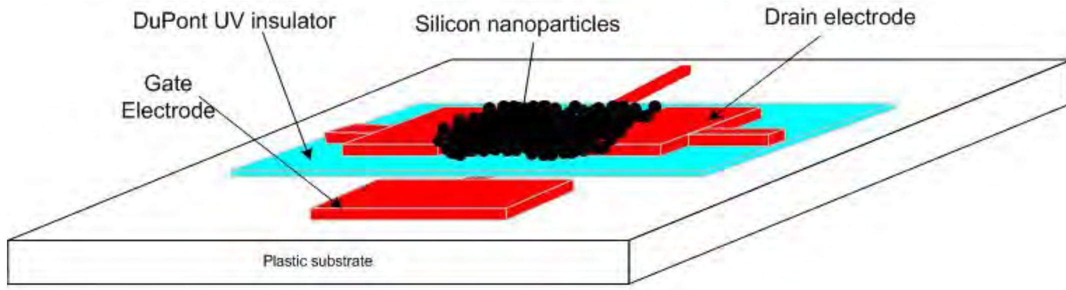

Fig. 5.8: Illustrating the complete transistor structure formed with gate electrode separated from the source and drain electrodes by a thin polymeric dielectric and then with a drop casted silicon nanocomposites filling the channel region

channel. As the source drain potential V_{ds} is increased from $0 - 150V$, a steep increase in current I_{DS}, without current saturation was observed. This behaviour is associated with transistors having non-ohmic drain source contacts [255].

The gate leakage current shown on the same graph, is very small relative to the drain current and remains roughly constant over the entire gate voltage sweep. The transfer characteristics of the transistor were taken at three different V_{ds} values as shown in figure 5.9(b) to 5.9(d) assuming these regions are all within the linear operation regime. The calculated field effect mobilities and transconductance derived from equation 5.10, and the approximate I_{ON}/I_{OFF} was calculated by dividing the maximum current with the minimum recorded current value in the transfer characteristic plot. The different parameter values are displayed in table 5.3 for the three different transfer characteristic V_{ds} values.

Table 5.3: Table showing three main parameters derived from the transfer characteristics of PACR-01 at three different V_{ds} voltages

Vds (V)	Transconductance(A/V)	Mobility (μ) $cm^2V^{-1}s^{-1}$	I_{ON}/I_{OFF}
20	9.06E-13	2.64E-05	1.04
40	2.90E-12	3.26E-05	1.04
60	2.05E-12	1.54E-05	1.04

A re-measurement of the output and the transfer characteristics of the same transistor PACR-01, was carried out approximately 72 hours from fabrication, this time however, the applied gate voltages was higher. Fig. 5.10(a) and Fig. 5.10(b) show the output and transfer characteristics recorded for this device. From the transfer characteristics plot, the transconductance derived from the slope of the approximately linear region is $2.65 \pm 0.05 \times 10^{-12}S$. The calculated hole mobility is $2.38 \pm 0.01 \times 10^{-5}cm^2V^{-1}s^{-1}$, and the estimated I_{ON}/I_{OFF} of 1.12. The mobility and I_{ON}/I_{OFF} values are close to those calculated earlier for a similar V_{DS} value, showing reproducibility in the behaviour of the transistor.

University of Cape Town

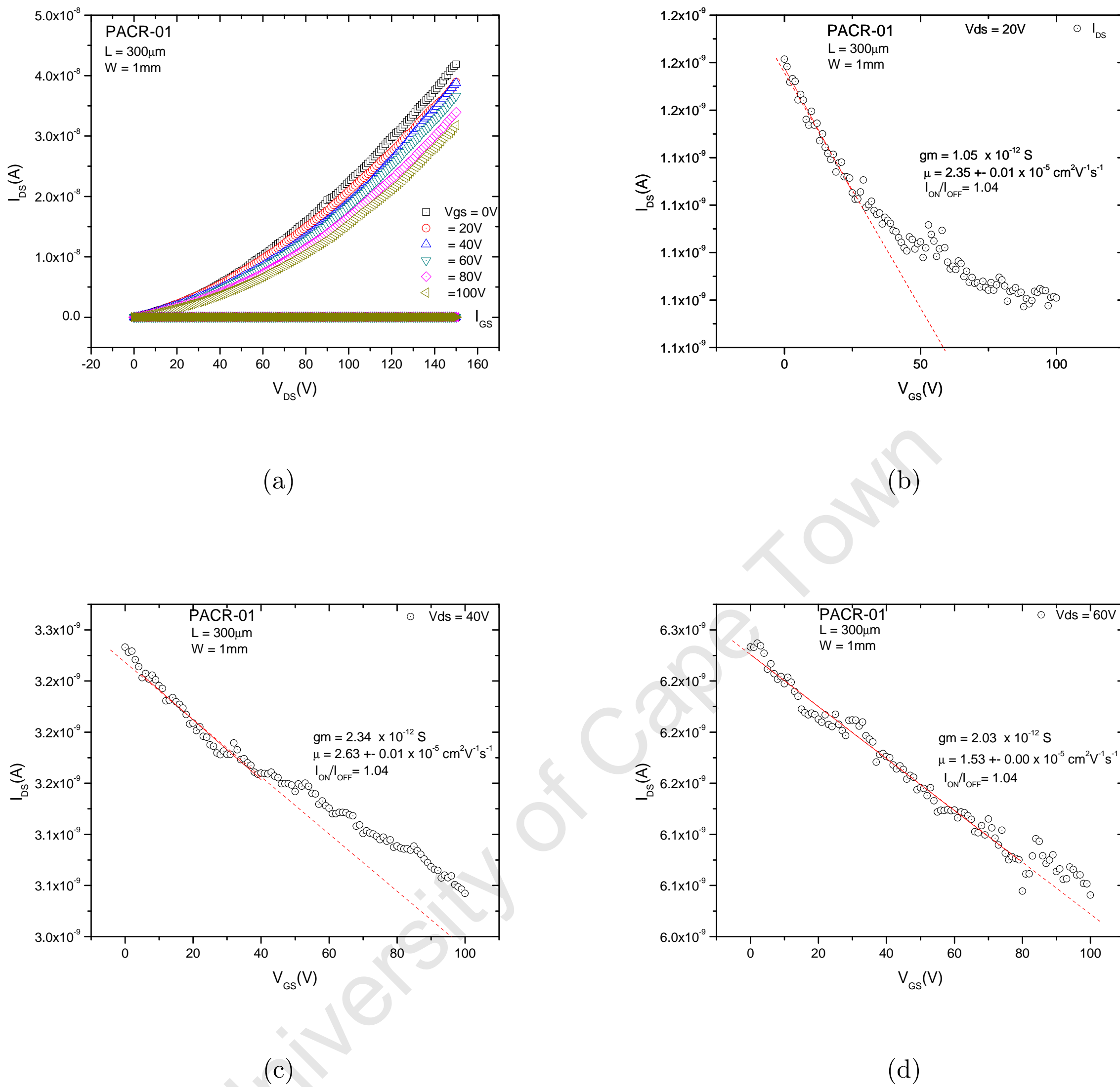

University of Cape Town

Fig. 5.9: (a) The output characteristic for PACR-01 transistor operating in normally on depletion mode and the transfer characteristic for (b) $V_{ds} = 20V$(c) $V_{ds} = 40V$ and (d) $V_{ds} = 60V$.

For the linseed oil based transistor PLIN-01, the output characteristics after 72 hours of fabrication, do not show a clear gate field effect but a systematic increase of the drain-source current I_{DS} with application of both positive and negative gate field as shown in Fig. 5.11. Firstly, the behaviour of the transistor is nonlinear, and no saturation of current even at higher voltages was observed. For voltages V_{DS} less than $100V$, the drain-source current I_{DS}, shows a sublinear behaviour (i.e. the power law dependence of the drain current on the applied V_{ds} is less than unity) [256, 257]. As discussed in chapter 4, such characteristics are due to built-in potential resulting from space charge at the interfaces and in the bulk

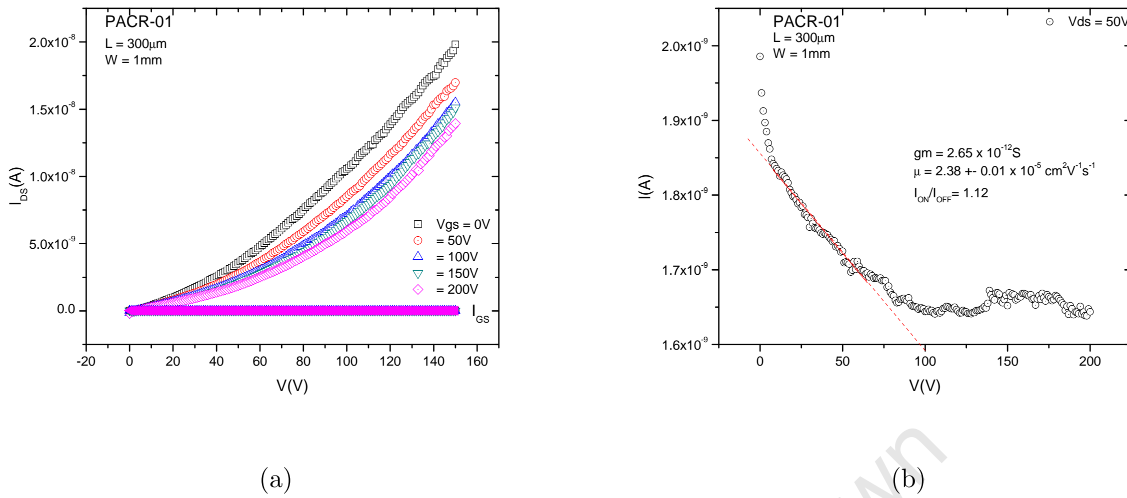

(a) (b)

Fig. 5.10: (a) the output characteristic for PACR-01 transistor operating in normally on depletion mode for relatively higher gate voltages and (b) the transfer characteristic for $V_{ds} = 50V$.

University of Cape Town

semiconductor matrix. Current transport in this regime is dominated by tunneling. As such the effect of applied gate voltage in this region will be insignificant.

For the region where $V_{DS} > 100V$, the drain-source current rises steeply with voltage increase, with no indication of current saturation. In this region the effect of applied gate voltage is relatively well pronounced, particularly for $(V_{DS} \approx 120V)$. These effects, though small, can reasonably suggest that the transistor behaves in a normally on, accumulation mode operation with negative gate voltages and in an inversion mode with positive applied gate voltage. Such a trend is typical of organic semiconductor transistors where the type of interface created at the metal semiconductor junction dictates the polarity of charge transport [258, 255]. In principle both electrons and holes charge carrier transport may occur, resulting in either n- or p-type conduction or ambipolar operation [258, 255].

Fig. 5.11(c) shows the transfer characteristics for a gate voltage swing from the positive to the negative half at the V_{DS} range where the modulation is presumed maximum. In this case the channel may have been induced with electrons as the dominant carrier since positive applied gate voltages result in a further increase in the drain current for source-drain voltage $V_{DS} = 120V$. The calculated electron mobility and on/off ratio are $7.81 \pm 0.14 \times 10^{-7} cm^2 V^{-1} s^{-1}$ and 1.16 respectively. While the on/off ratio is comparable to that of PACR-01 transistor calculated earlier, the mobility is far lower. The reason for this may be due to the difference in binder type, or the fact that p type conduction is more favoured than n type conduction in ambipolar devices [258].

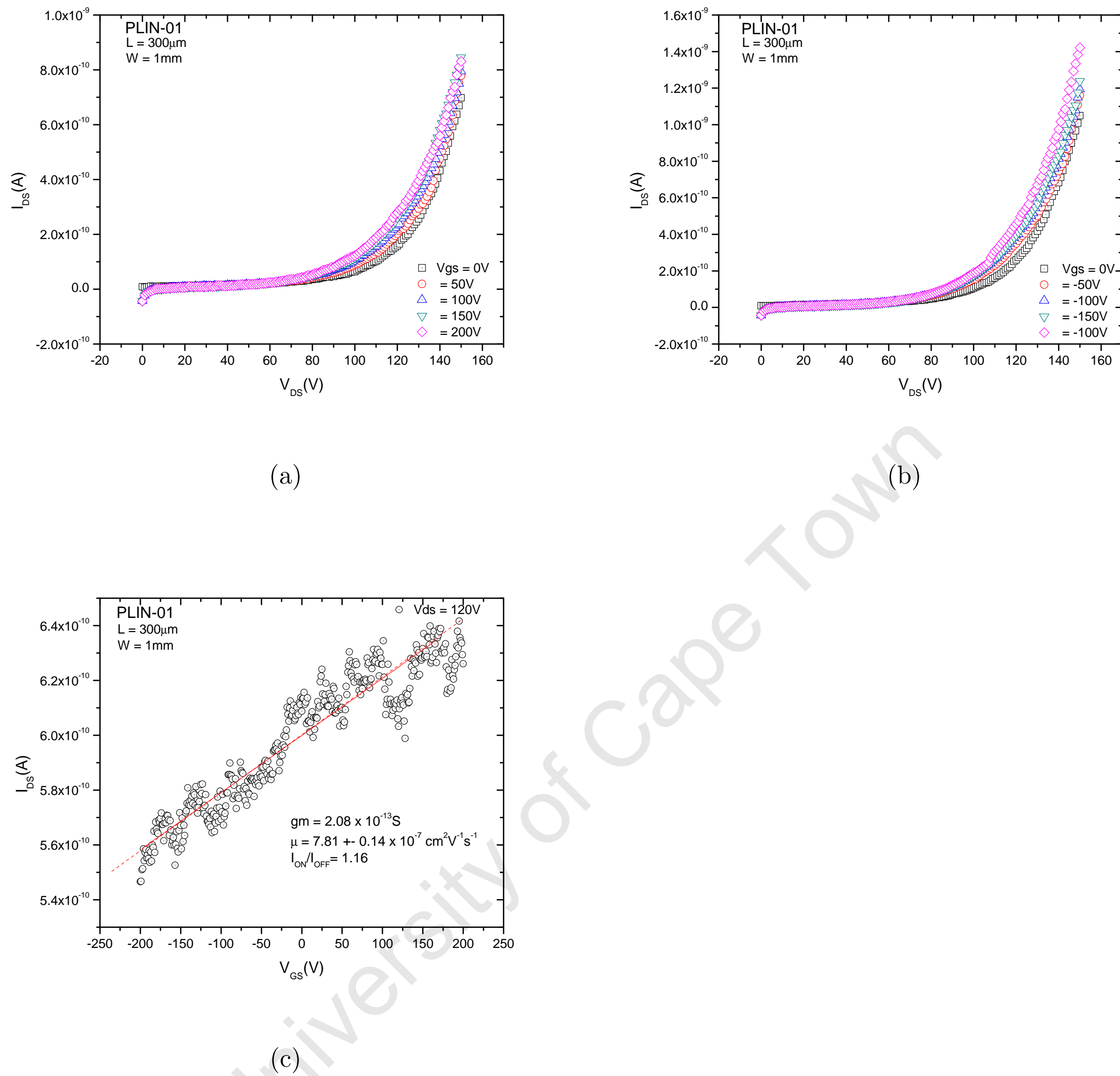

Fig. 5.11: Output characteristic for PLIN-01,(a) for positive applied gate voltages showing a normally on accumulation mode behaviour (b) for negative applied gate voltages showing still, a normally on accumulation mode behaviour and (c)Transfer characteristics for PLIN-01, showing a relatively small but definite enhancement of drain current for positive going gate voltage.

From the forgoing it is reasonable to suggest that the interface of the printed metallic contact and the two types of drop cast semiconductor nanocomposites plays a vital role in the charge transport in the transistor channel. The ambipolar behaviour seen for the PLIN-01 transistor may result from the nature of the interface as well as the nature of the semiconductor ink.

University of Cape Town

5.7.2 Thick film nanocomposite transistor formed on standard silicon wafer TFT structures

To compare and determine the characteristics of transistor made from the two main nanocomposites used above, the structure on standard silicon wafer TFT structures was employed for the experiment. The protective layer over the as received TFT structure was removed by dipping the wafer in acetone for 5 minutes, and the surface with the source-drain contacts was further rinsed with ethanol. Inks of P-type powder in linseed oil, in a ratio 70 : 30 wt.%, and in acrylic binder in the ratio 30 : 70 wt.% were produced using the procedure described in chapter 4. The nanocomposite ink was placed over the entire surface of the wafers covering the area defined by the source and drain electrodes using a pipette. The wafers were then held vertically on their edges to allow excess ink to flow off the surface for about 3 minutes. The resulting thick nanocomposite layer on the wafers surface was then allowed to cure overnight. For electrical characterisation, the base of the wafer was painted with silver paste to ensure a good gate contact. The transistors, labeled PLIN-02 and PACR-02, based on the nanocomposite type forming the active layer were then placed in an oven set at 100^oC for 30 minutes to ensure proper contact formation.

Fig. 5.12 shows the output characteristics for PLIN-02, with application of negative gate voltages (a) and then positive gate voltages (b) for one of the transistors with $L = 2.5\mu m$ and $W = 10mm$. The behaviour seen is similar to the characteristics observed for similar ink for the all printed transistor structures discussed earlier. However in this case the applied gate and drain voltages are far lower. Fig. 5.13 shows the output characteristics for transistor PACR-02 produced with a similar structure as PLIN-02. For the PACR-02 transistor, the gate bias is limited to $V_{GS} = \pm 20V$ as the gate oxide broke down for three similar structure at about $V_{GS} > 20V$. These plots reveal that the $I-V$ characteristics for both PLIN-02 and PACR-02 show nonlinear behaviours with a small but systematic effect of the application of gate voltages on the source-drain current. In the PLIN-02 as well as the PACR-02 transistor type, for applied source drain voltages $|V_{DS}| \leq 10V$ (region A) for example in Fig. 5.12(a), there is no appreciable change of the drain current with V_{DS} voltage change. For $|V_{DS}| \geq 10V$, however, the current rises steeply without reaching saturation as seen in region B and C, of the curve. The nonlinear characteristics of the $I - V$ in all cases, suggests either electric field barrier lowering (Poole-Frenkel transport) or enhanced thermal activation of carriers from coulombic traps (Richadson-Schottky transport), commonly seen in granular semiconductor systems [259].

The application of negative gate voltages does not show any gate effect at low V_{DS}. However,

University of Cape Town

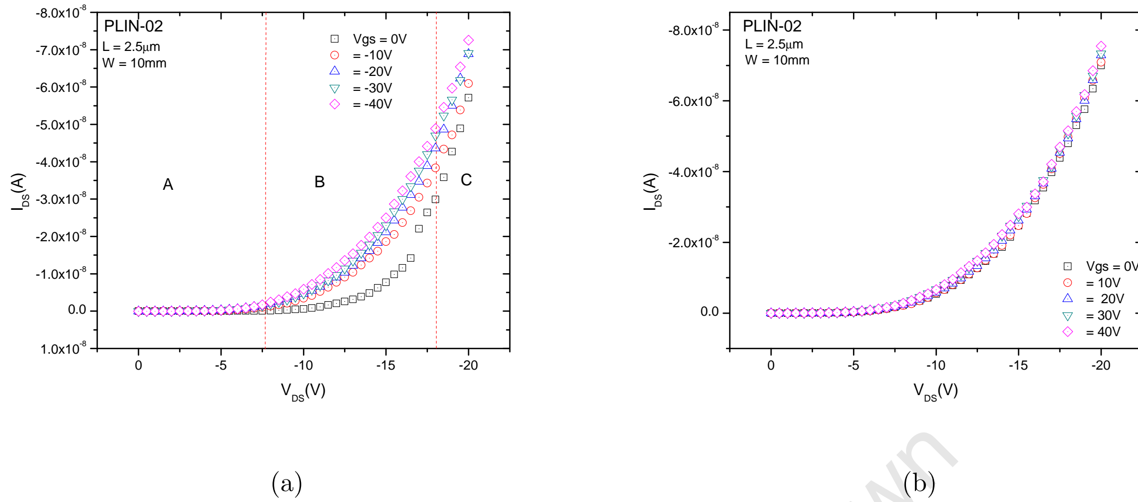

(a) (b)

Fig. 5.12: Output characteristic for (a) PLIN-02, with negative applied gate voltages showing three basic regions of operation in a normally on accumulation mode behaviour (b) PLIN-02, with positive applied gate voltages showing relatively small gate voltage effect.

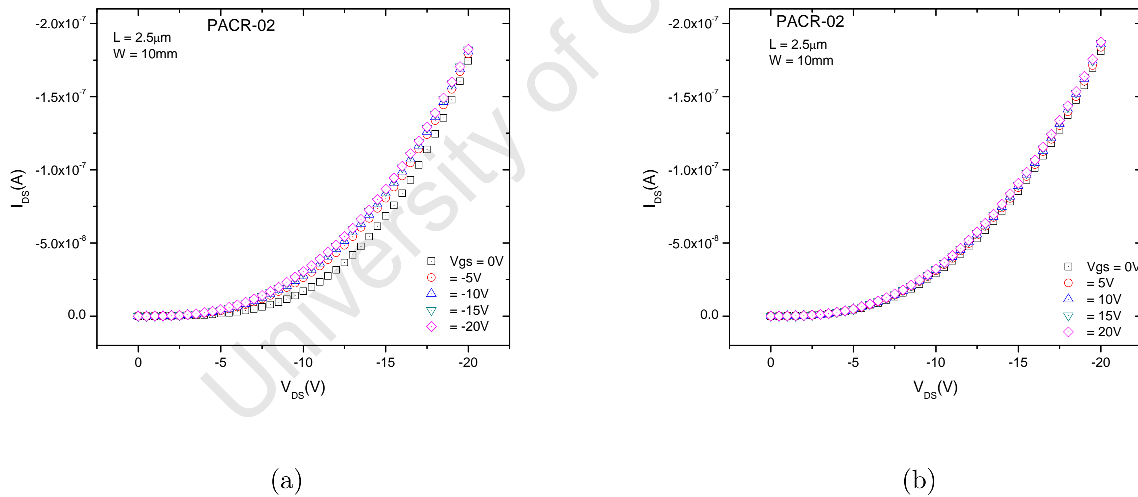

(a) (b)

Fig. 5.13: Output characteristic for(a) PACR-02, with negative applied gate voltages showing similar three regions of operation and enhancement of the channel current in a normally on accumulation mode behaviour (b) PACR-02, with positive applied gate voltages showing relatively small enhancement of the channel current in a normally on accumulation mode behaviour.

for $|V_{DS}| \geq 10V$ there is a relative enhancement of the drain current with the negative gate potential, which is less pronounced at even higher V_{DS} (region C in the graph). For positive applied gate voltages however, no clear or systematic effect on the drain current is seen.

University of Cape Town

Fig 5.14(a) and 5.14(b) shows a logarithmic plot of the output characteristics of the transistors. In this representation the curves have linear regions which indicates a power law dependence $I \propto V^n$. The dependence of the drain current on the source drain voltage (n), derived from the slope of the linear regions of the different $I - V$s, shows $n \geq 2$ in all cases with n generally higher for PLIN-02. Hence the carrier transport in both transistor types are consistent with Space Charge/Trap Filled Limited Current (SC/TFLC) transport discussed in chapter 4 [164].

Fig. 5.15(a) and 5.15(b) shows the effect of the applied gate voltages on the slope values n. From these plots it is seen that for both transistors, the slope reduces with increasing negative gate voltage. From these observation it is reasonable to suggest that the effect of negative gate applied voltage on the drain current is due to modulation of the space charge region and could result from field assisted release of the trapped carriers. However further study is necessary to verify this hypothesis.

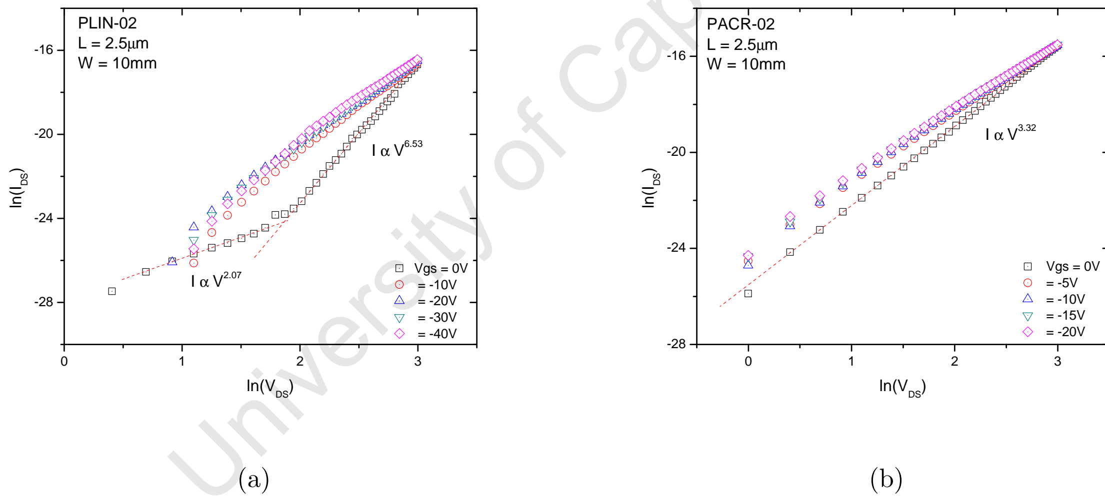

University of Cape Town

Fig. 5.14: Plot of $ln(I)$ vs. $ln(V)$ for the transistors (a) PLIN-02 and (b) PACR-02 indicating Space Charge/Trap Filled Limited Current conduction process as the major transport behaviour in the channel of the transistor.

To determine the field effect mobility for the two transistors, their transfer characteristics at $V_{DS} = -20V$ were measured. Fig. 5.16(a) and 5.16(b) shows the transfer characteristics respectively for negative to positive and positive to negative gate voltage swings, while Fig. 5.17(a) and 5.17(b) shows similar characteristics for PACR-02 transistor. The transfer behaviour shown by these two transistors is typical of an ambipolar transistors [258, 255] especially with transistor with non ohmic drain and source contacts [251]. For negative applied gate voltages the channel is induced with holes and the transistor acts in accumulation

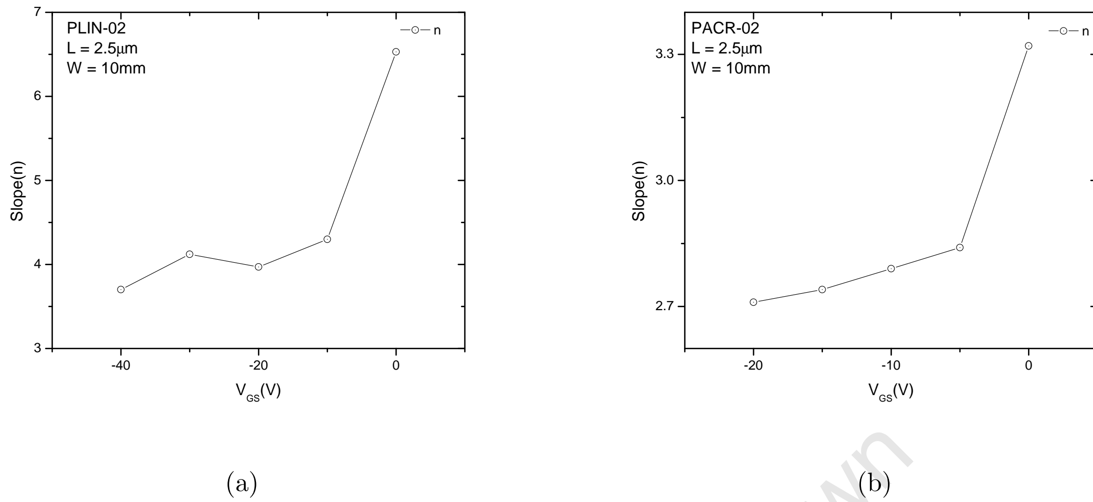

(a) (b)

Fig. 5.15: (a) Showing the variation of the estimated channel current dependence on applied source drain voltage n, for high channel field on the applied gate voltages for PLIN-02 and (b) PACR-02.

mode. For positive applied gate voltages an induced inversion of carriers favoring electron transport becomes dominant. The extracted electron and holes mobilities, I_{ON}/I_{OFF} and transconductance values are shown in table 5.4. The result shows a higher mobility value for PACR-02 than PLIN-02. Although with different ink composition ratios, this trend is similar to that observed for the printed TFT structures on plastic.

Table 5.4: Table showing the transconductance, holes/electron mobilities and the I_{ON}/I_{OFF} values derived from the transfer characteristics measurement on transistor PLIN-02 and PACR-02

Transistor type	gm	μ	I_{ON}/I_{OFF}	Carrier
PLIN-02	1.63 E-10	1.38E-07	1.11	holes
PLIN-02	2.06E-10	1.72E-07	1.09	electrons
PACR-02	3.57E-10	2.97E-07	1.04	holes
PACR-02	2.74E-10	2.28E-07	1.05	electrons

University of Cape Town

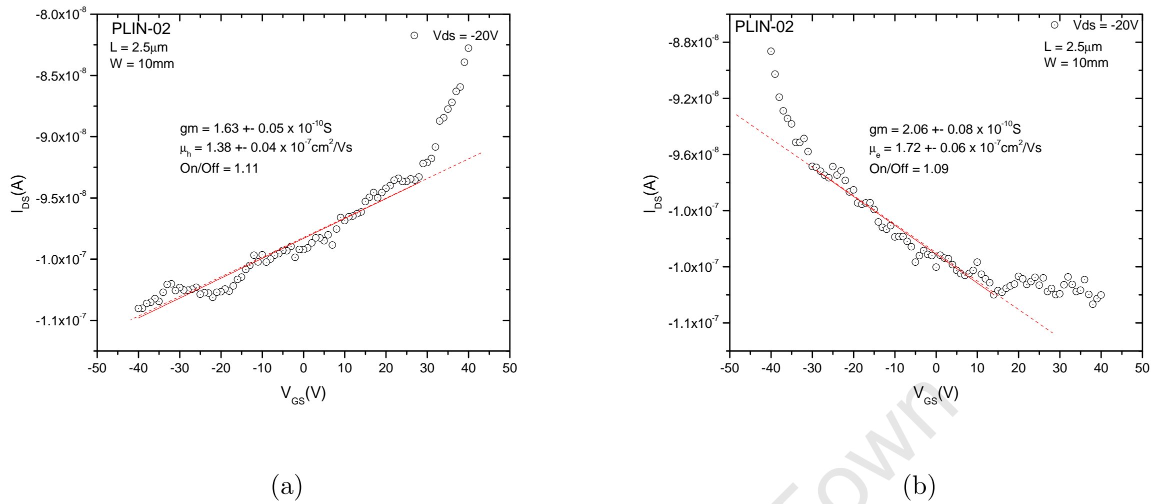

(a) (b)

Fig. 5.16: Transfer characteristics behaviour for (a) PLIN-02 with gate voltage swing from positive to negative indicating holes carrier enhancement. (b) PLIN-02 with gate voltage swing from negative to positive indicating electrons carrier transport enhancement. The slope shown value for all the plots gives the transconductance from which the field effect mobility and on/off ratios shown in the inset were derived.

University of Cape Town

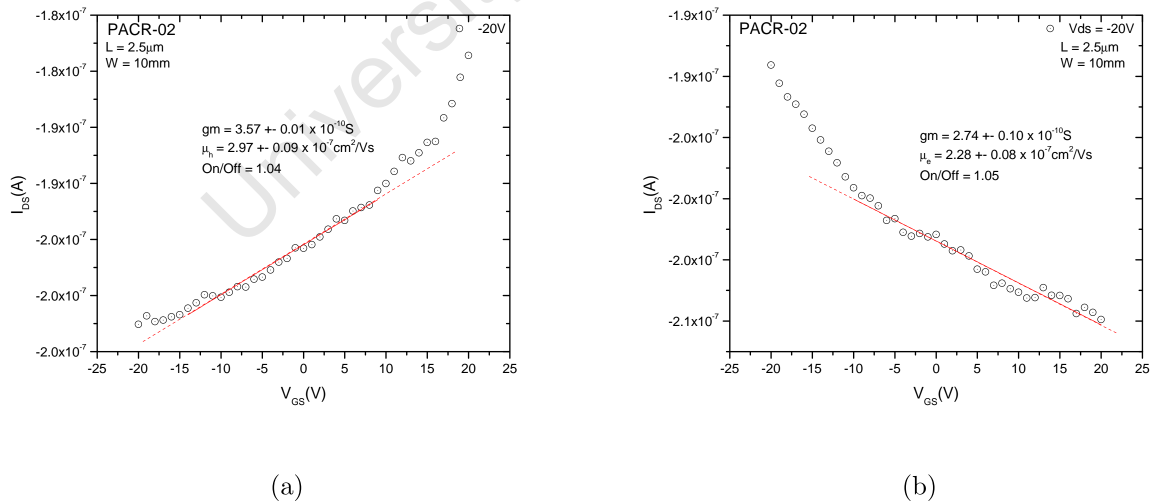

(a) (b)

Fig. 5.17: Transfer characteristics behaviour for (a) PACR-02 with gate voltage swing from positive to negative indicating holes carrier transport enhancement. (b) PACR-02 with gate voltage swing from negative to positive indicating electrons carrier transport enhancement. The slope shown value for all the plots gives the transconductance from which the field effect mobility and on/off ratios shown in the inset were derived.

6. Conclusions

In this study, a laboratory orbital pulverizer was used in a top-down production process to fabricate silicon nanoparticles. Morphological studies using scanning and transmission electron microscopy reveals that the powder consist of a wide range of size and shape. The most apparent are large faceted particles with sizes between $1\mu - 3\mu m$, and relatively smaller particles of sizes $40nm - 100nm$. The micrographs for the wafers milled for 1-5 hours, show that size reduction starts with cleavage of the crystal along preferred orientations, followed by a gradual attrition of the particle surface toward smaller particle sizes after about 2 hours of milling. Further milling after about 3 hours, only reduces the number of the large faceted particles. Similar observations were recorded from examination of milled metallurgical powder, except that the particles have a generally rounder shape, with no facets, than the ones from the wafer. Statistical determination of the dependence of the particle size, shape and size distribution on milling time carried out on the TEM images of the milled powders, reveals that the particle size distribution with milling time can be described by a log-normal function, with a median size decreasing with increasing milling time. A plot of the variation of the average particle size with milling time fits well with a first order exponential decay model, which was used to evaluate the effective particle size after very long milling time as about $120nm$ for the milled wafer.

Compositional study using energy dispersive X-ray (EDX) spectroscopy reveals that the level of the main contaminants, namely oxygen, iron and chromium remains fairly constant for the entire duration of the milling. Oxygen appears to be the main contaminant element, but may however be associated with the initial oxidation of the bulk material, rather than oxidation during the milling process. This reasoning is supported from the identification of oxide phases by Raman spectroscopy of the starting materials. Raman spectroscopy of the powder shows three prominent peaks, with one important one at $520cm^{-1}$ which can be associated with crystalline silicon. The effect of milling time on this peak was observed as a continuous shift toward lower wavenumber and a broadening of the FWHM from $23cm^{-1}$ to $26cm^{-1}$. These effects may be due to induced heavy plastic deformation which may have resulted in a refinement of the microstructure or distortion of the initial ordered lattice. However, Raman spectroscopy on all the milled P* powder shows that milling induced no amorphorisation, suggesting that the dominant effect is grain size reduction. Estimation and variation of crystallite size with milling using Scherrer's method from X-ray diffraction data confirms this. Structural analysis using electron diffraction as a compliment to the X-ray diffraction study reveals that particles in the milled powder are polycrystalline. The

University of Cape Town

above observations clearly show that the process of producing nanoparticles of silicon using this method has resulted in a structural change from a starting single crystalline wafer to polycrystalline nanoparticles.

Analysis of the SAXS data using Guinier's law reveals that the nanocomposites consist of particles with a broad distribution of sizes heterogeneities, i.e. a polydispersive system, confirming the observations of the morphological study. Analysis of the experimental data using Porod's law revealed that all the nanocomposite samples formed surface fractal aggregates with the exception of PLIN and MACR composites which show mass fractal behaviours.

The major contribution of this research is toward understanding the transport mechanism of charge carriers under electric field, and the dependence of the conduction process on variation of particle concentration of the composite in a metal-nanocomposite-metal structure. The main results and conclusion can be summarised as

- The conductance of the nanocomposite was observed to depend largely on the ratio of nc-Si:Binder used to form the composite. A critical concentration of about 70-80 wt.% nc-Si in the case of the linseed oil based structures and 30 wt.% for acrylic based structures was observed.

- Using a thermionic emission model for the Schottky barrier between the contact and the semiconductor nanocomposite, yields values for the diode ideality factors which are very high. This is associated with a series resistance in the range of 10^9 ohm. The values of the derived Schottky Barrier Height (SBH) however, vary between 0.83 and $0.92eV$ close to the theoretical SBH of $0.87eV$ between silver and moderately doped P type silicon. Arrhenius behaviour indicates a thermally activated process at low concentration, where the ideality factor is high. At high concentration n is lower and the forward bias diode term dominates. The computed tunneling energy E_{oo}, derived from the ideality factors for the different nanocomposite system, show $E_{00} \geq 100K_BT$, suggestive of a conduction process where thermal activation or field emission process is significant.

- For relatively low field, when the carrier energy $qV < \phi$, charge injection is dominated by direct tunneling. As the external applied bias increases there is a characteristic change from logarithmic growth at low field to linear decay at higher field in the Fowler-Nordheim (FN) characteristic plot, indicative of a switch to field emission at higher voltages. The characteristic transition voltage V_{trans} and the calculated barrier height have minimum values for structures with particle concentration with the highest

University of Cape Town

conductance. Thus the carrier transport is dominated by direct tunneling at low bias voltages while field assisted emission contributes significantly to the overall transport for high bias voltages.

- The presence of hysteresis in the forward as well as reversed biased $I-V$ characteristic and a non zero current at zero bias voltage, reveals a build up of space charges in the interfacial as well as the bulk matrix. At intermediate voltage regions $50 < V < 120V$, the current can be described in terms of space charge limited current (SCLC) conduction process. At relatively high voltage all structures with the exception of PLIN-10-01 and MACR-10-02 structures show a trap filled condition. The contribution of SCLC at intermediate voltage level and TFLC at high applied voltage bias is a significant contribution to the overall transport mechanism in this system.

In general the carrier transport mechanism for these nanocomposites depends largely on the concentration of the particles in the nanocomposite structure, and the electric field across the structure. At low concentrations the active nanocomposite layer is composed of sparsely dispersed silicon particles and smaller clusters with open gaps between the different clusters. Charge transport follows a thermally activated process and is determined mostly by the binder properties. At and above the percolation threshold the composites then consist of particles closely parked such that electrical conduction of free carriers is through the path created by the interconnection of cluster and due to tunneling through the thin wall of binder material forming the network. The effect of the particle properties such as the crystallinity, particle size and shape distribution as well as the dopant type and concentration in the starting material of the powder on carrier transport was not investigated. An extension of this research work will focus more closely on the contribution of such particle properties on carrier transport.

University of Cape Town

$I-V$ output and transfer characteristic measurements on insulated gate field effect transistors fabricated with the nanocomposite as the active layer reveal the following:

- The characteristic $I-V$ behaviours are nonlinear, with no saturation of current for the entire range of applied V_{ds} voltage. This characteristic has been suggested earlier to result from the nature of the interface at the metal nanocomposite junction resulting in field lowering of certain barrier height or field assisted thermal excitation of the carriers from columbic traps. Charge build up in the bulk composite resulting in SCLC and TFLC conductance process was also observed. The recorded modulation of drain current due to applied gate field is due to the modulation of certain probability that controls the different charge transport in the system.

- Further investigation reveals that the transistors function as ambipolar devices, with two different types of carriers type, electron and holes, and the dominance of either is determined by the sign and swing direction of the gate potential.

In conclusion, transistors with active nanocomposites made from inclusion of nanoparticles of silicon in linseed oil and acrylic medium respectively have ambipolar behaviours. The electronic properties of the active nanocomposite is such that transport is governed by other mechanisms different from drift, and the resulting field effect is due to modulation of the different transport probability rather than the drifting carrier. The mobilities in these transistors are still relatively low. As such further study of the transport with emphasis on the contact types and formation believed to play a major role in the transport is needed to improve the different transistor parameters.

University of Cape Town

References

[1] K.E. Gonsalves, S.P. Rangarajan, and J. Wang. *Handbook of Nanostructured Materials and nanotechnology. Synthesis and Processing*, volume 1. Academic Press, 2000. 1, 2.1.1, 2.1.3

[2] Philip Moriarty. Nanostructured materials. *Rep. Prog. Phys.*, 64:297–381, 2001. 1

[3] A. D. Yoffe. Semiconductor quantum dots and related systems: electronic, optical, luminescence and related properties of low dimensional systems. *Advances in Physics*, 50(1):1–208, 2001. 1, 2.1.2

[4] J. Christopher Love, Lara A. Estroff, Jennah K. Kriebel, Ralph G. Nuzzo, and George M. Whitesides. Self-assembled monolayers of thiolates on metals as a form of nanotechnology. *Chemical Reviews*, 105(4):1103–1169, 2005. 1

[5] S. Underwood and P. Mulvaney. Effect of the solution refractive index on the color of gold colloids. *Langmuir*, 10:3427–3430, 1994. 1

[6] J. Winter. Gold nanoparticle biosensors. presented at the Ohio State University, NSEC high school teachers workshop, accessed online 23-January 2009. `www.nsec.ohio-state.edu/teacher_workshop/Gold_Nanoparticles.pdf`. 1

[7] M. Marandi, N. Taghavinia, Z. Sedaghat, A. Iraji zad, and S. M. Mahdavi. Thermochemical growth of Mn doped CdS nanoparticles and study of luminescence evolution. *Nanotechnology*, 19:225705–09, 2008. 1

[8] F.E. Kruis, A. Goossens, and H. Fissan. Synthesis of semiconducting nanoparticles. *Journal of Aerosol Science*, 27:165–166, 1996. 1, 2

[9] Sebastien Nuttinck, Bertrand Parvais, Gilberto Curatola, and Abdelkarim Mercha. Double-gate finfets as a cmos technology downscaling option :an rf perspective. *IEEE Transcations on Electron Devices*, 54:279–283, 2007. 1

[10] Sebastien Nuttinck. Ultrathin-body SOI devices as a CMOS technology downscaling option: RF perspective. *IEEE Transcations on Electron Devices*, 53:1193–1199, 2006. 1

[11] Hei Wong and Hiroshi Iwaia. On the scaling issues and high replacement of ultrathin gate dielectrics for nanoscale mos transistors. *Microelectronic Engineering*, 83:1867–1904, 2006. 1

University of Cape Town

[12] C.C. Koch. Synthesis of nanostructured materials by mechanical milling: problems and opportunities. *Nanostructured Materials*, 9:13–22, 1997. 1

[13] Gavin Conibeer, Martin Green, Richard Corkish, Young Cho, Eun-Chel Cho, Chu-Wei Jiang, Thipwan Fangsuwannarak, Edwin Pink, Yidan Huang, Tom Puzzer, Thorsten Trupke, Bryce Richards, Avi Shalav, and Kuo-lung Lin. Silicon nanostructures for third generation photovoltaic solar cells. *Thin Solid Films*, 511-512:654–662, 2006. 1

[14] Martin A. Green and Gavin Conibeer. Nanostructured silicon-based tandem solar cells. Internet article, accessed online 15-February 2009. `http://gcep.stanford.edu/pdfs/i6W09tDtK-48PTmzHazOuw/2.2.6.Green_Conibeer_07.pdf`. 1, 4

[15] Wikipedia. Nanocomposite — wikipedia, the free encyclopedia. Internet article,accessed online 15-February 2009. `http://en.wikipedia.org/wiki/Nanocomposite`. 1

[16] T. Tanaka, G. C. Montanari, and R. Mulhaupt. Polymer nanocomposites as dielectrics and electrical insulation-perspectives for processing technologies, material characterization and future applications. *IEEE Transactions on Dielectrics and Electrical Insulation*, 11(5), 2004. 1, 3

[17] K. Kim Yong, A. F. Lewis, S. B. Warner, P. K. Patra, and P. D. Calvert. Nanocomposite fibers. Technical Report M00-MD08, National Textile Center, 2003. 1

[18] M. Ando, H. Miyamoto, H. Naito, and Y. Kanemitsu. Photoelectric properties of printed thin films of silicon nanocrystals dispersed in polymer binder. *Journal of Non-Crystalline Solids*, 299-302:1084–1089, 2002. 1, 4, 4.5.2, 4.5.3, 4.5.8

[19] Dinakar Ramadurai, Dwarakanath Geerpuram, Dimitri Alexson, Mitra Dutta, Nicholas A. Kotov, Zhiyong Tang, and Michael A. Stroscio. Electrical and optical properties of colloidal semiconductor nanocrystals in aqueous environments. *Superlattices and Microstructures*, 40:38–44, 2006. 1

[20] Henning. Sirringhaus, Nir. Tessler, and Richard H. Friend. Integrated optoelectronic devices based on conjugated polymers. *Science*, 280:1741 1744, 1998. 1

[21] Natalie Stutzmann, Richard H. Friend, and Henning Sirringhaus. Self-Aligned, Vertical-Channel, Polymer Field-Effect Transistors. *Science*, 299(5614):1881–1884, 2003. 1

University of Cape Town

[22] J. L. Bredas, J. P. Calbert, D. A. da Silva Filho, and J. Cornil. Organic semiconductors: A theoretical characterization of the basic parameters governing charge transport. *Proceedings of the National Academy of Sciences*, 99(9):5804–5809, 2002. 1

[23] Brent A. Ridley, Babak Nivi, and Joseph M. Jacobson. All-Inorganic Field Effect Transistors Fabricated by Printing. *Science*, 286(5440):746–749, 1999. 1

[24] S. Hernndez-Lopez, E. Vigueras-Santiago, J. Mercado-Posadas, and V. Sanchez-Mendieta. Electrical properties of acrylated epoxidized soybean oil polymers based composites. *Advances in Technology of Materials and Materials Processing*, 8:214–219, 2006. 1

[25] Robert Kelsall, Ian Hamley, and Mark Geoghegan. *Nanoscale Science and Technology*. John Wiley and Sons Ltd, 2005. 2, 2.1.1, 2.1.2, 2.1.2, 2.1.3, 2.2, 2.1.3, 2.1.3, 2.1.3, 2.1.3, 2.3.3, 2.17

[26] K. Tonokura, T. Murasaki, and M. Koshi. Formation mechanism of hydrogenated silicon clusters during thermal decomposition of disilane. *J. Phys. Chem. B.*, 106:555, 2002. 2

[27] V.G. Kravets, C. Meier, D. Konjhodzic, A. Lorke, and H. Wiggers. Infrared properties of silicon nanoparticles. *J. Appl. Phys.*, 97(8):084306, 2005. 2

[28] M. Ehbrecht and F. Huisken. Gas phase characterization of silicon nanoclusters produced by laser pyrolysis of silane. *Physical Review B*, 59:2975–2985, 1999. 2

[29] Nong-M. Hwang, Kim Doh-Y, and Jeon In-D. Charged cluster model as a new paradigm of crystal growth. *Journal of Ceramic Processing Research*, 1:34 – 44, 2000. 2

[30] H. Hofmeister, P. Kodderitzsch, and J. Dutta. Structure of nanometersized silicon particles prepared by various gas phase processes. *Journal of Non-Crystalline Solids.*, 232 - 234:182–187, 1998. 2

[31] T. Seto, T. Orii, M. Hirasawa, and N. Aya. Fabrication of silicon nanostructured films by deposition of size-selected nanoparticles generated by pulsed laser ablation. *Thin Solid Films*, 437(1):230–234, 2003. 2

[32] Qi Liu and M. Kauzlarich Susan. A new synthetic route for the synthesis of hydrogen terminated silicon nanoparticles. *Materials Science and Engineering B*, 96(2):72–75, 2002. 2

University of Cape Town

[33] J. P. Wilcoxon, G. A. Samara, and P. N. Provencio. Optical and electronic properties of SI nanoclusters synthesized in inverse micilles. *Physical Review B*, 60:2704–2714, 1999. 2

[34] D. T. Britton and M. Harting. Printed nanoparticulate composites for silicon thick-film electronics. *Pure Appl. Chem.*, 78(9):17231739, 2006. 2, 2.2.1, 3.3.1, 4

[35] A. S. Heintz, M. J. Fink, and B. S. Mitchell. Mechanochemical synthesis of blue luminescent alkyl/alkenyl-passivated silicon nanoparticles. *Advanced Materials*, 19:3984 – 3988, 2007. 2

[36] R. Radoi, P. Fernandez, J Piqueras, M S. Wiggins, and J. Solis. Luminescence properties of mechanically milled and laser irradiated zno. *Nanotechnology*, 14:794 –798, 2003. 2

[37] Claudio L. De Castro and Brian S. Mitchell. *Nanoparticles from Mechanical Attrition.* American Scientific Publishers, 2002. 2, 2.1.3, 2.5

[38] Jessica Elzea Kogel and Nikhil C. Trivedi. *Industrial Minerals and Rocks: Commodities, Markets, and Uses.* SME, 2006. 2

[39] Wikipedia. Nanocrystalline silicon — wikipedia, the free encyclopedia. 2.1.1

[40] Santiram Kal. *Basic Electronics: Devices, Circuits and IT Fundamentals.* Prentice Hall of India, 2004. 2.1

[41] C. Diaz-Guerra, A. Montone, J Piqueras, and F Cardellini. Structural and cathodoluminescence study of mechanically milled silicon. *Semiconductor Science and Technology*, 17:77–82, 2002. 2.1.1, 2.1.3, 2.3.1, 2.3.2, 2.3.3, 2.3.4

[42] J. Jakubowicz, K. Smardz, and L. Smardz. Characterisation of porous silicon prepared by powder technology. *Physica E*, 38:139–143, 2007. 2.1.1

[43] F. Villar, J. Escarr, A. Antony, M. Stella, F. Rojas, J.M. Asensi, J. Bertomeu, and J. Andreu. Nanocrystalline silicon thin films on PEN substrates. *Thin Solid Films*, 516:548–587, 2008. 2.1.1, 2.1.3

[44] V. M. Smirnov. Nanoscaled structuring as a way to constructing new solid substances and materials. *Russian Journal of General Chemistry*, 72(4):590–606, 2002. 2.1.1

[45] V. A. Pozdnyakov. Generalized size-dependent structural states of materials with an ultrafine structure. *Crystallography Reports*, 48(4):701–704, 2003. 2.1.1

University of Cape Town

[46] B.J. Hinds Yun, S. Hatatani, S. Oda, Q.X. Zhao, and M. Willander. Study of structural and optical properties of nanocrystalline silicon embedded in SiO_2. *Thin Sol. Films*, 375:137–141, 2000. 2.1.2

[47] Atif Mossad Ali, Takao Inokuma, and Seiichi Hasegawa. Structural and photoluminescence properties of nanocrystalline silicon films deposited at low temperature by plasma-enhanced chemical vapor deposition. *Applied Surface Science*, 253:1198–1204, 2006. 2.1.2

[48] Ngage Research Wiki. Quantum dots. Internet article, access on line January 2009. http://www.waterengage.com/researchwiki/index.php?title=Quantum_Dots. 2.1.2

[49] A. D. Yoffe. Low dimensional syatems: quantisation effect and electronic properties of semiconductor microcrystallites (zero-dimensional systems) and some quasi-two-dimensional systems. *Advances in Physics*, 42(2):173 – 266, 1993. 2.1.2

[50] Al. L. Efros and A. L. Efros. Interband absorption of light in a semiconductor sphere. *Sov. Phys. Semicond*, 16:772 – 775, 1982. 2.1.2

[51] H. Arizpe-Chavez, R. Ramirez-Bon, F. J. Espinoza-Beltran, O. Zelaya-Angel, J. L. Marn, and R. Riera. Quantum confinement effects in $CdTe$ nanostructured films prepared by the RF sputtering technique. *Journal of Physics and Chemistry of Solids*, 61(4):511–518, 2000. 2.1.2

[52] Al. L. Efros. Luminescence polarization of CdSe microcrystals. *Phys. Rev. B*, 46(-):7448 – 7458, 1992. 2.1.2

[53] A. Lipovskii, E. Kolobkova, V. Petrikov, I. A. Olkhovets Kang, T. Krauss, M. Thomas, J. Silcox, F. Wise, Q. Shen, and S. Kycia. Synthesis and characterization of pbse quantum dots in phosphate glass. *Appl. Phys. Lett.*, 71(23):3406, 1997. 2.1.2

[54] Toshihiko Toyama, Takashi Ouchida, Hiroaki Okamoto, and Yoshihiro Hamakawa. Optical and structural studies of nanocrystalline silicon thin film grown by rapid thermal annealing. *Applied Surface Science*, 113-114:130–134, 1997. 2.1.2

[55] Xinwei Zhao, Olaf Schoenfeld, Shuji Komuro, Yoshinobu Aoyagi, and Takuo Sugano. Quantum confinement in nanometer-sized silicon crystallites. *Phys. Rev. B*, 50(24):18654–18657, 1994. 2.1.2

University of Cape Town

[56] Germ Garcia-Belmonte and Juan Bisquert. Interpretation of the critical length scale determining the conductivity in ionically conducting silicate glasses. *Journal of Non-Crystalline Solids*, 337:272–275, 2004. 2.1.2

[57] Fernando Rinaldi. Basics of molecular beam epitaxy (mbe). Universitat ULM. Annual Research Report 2002, accessed online 15-February 2009. `www-opto.e-technik.uni-ulm.de/forschung/jahresbericht/2002/ar2002_fr.pdf`. 2.1.3

[58] Milton Ohring. *The materials science of thin films*. Academic Press, 1992. 2.1.3

[59] Christopher C. Striemer, Rishikesh Krishnan, and Philippe M. Fauchet. The development of nanocrystalline silicon for emerging microelectronic and nanoelectronic applications. *Journal of the Minerals, Metals and Materials Society*, 50:20–25, 2004. 2.1.3, 2.1.3

[60] B. Rau, T. Weber, B. Gorka, P. Dogan, F. Fenske, K.Y. Lee, S. Gall, and B. Rech. Development of a rapid thermal annealing process for polycrystalline silicon thin-film solar cells on glass. *Materials Science and Engineering B*, in press, 2008. 2.1.3

[61] Zhenghai Jin, Sungwook Jung, Nguyen Van Duy, Sunghyun Hwang, Kyungsoo Jang, Kwangsoo Lee, Jungin Lee, Park Hyungjun, Jaehon Kim, Hyukjoo Son, and Junsin Yi. Characterization of MONOS nonvolatile memory by solid phase crystallization on glass. *Surface and Coatings Technology*, 202:589–599, 2008. 2.1.3

[62] S. Holgado, J. Martinez, Garrido J., C. Morant, and J. Piqueras. Rapid solid phase crystallization of nanocrystalline silicon deposited by electron cyclotron plasma chemical vapor deposition. *Applied Physics Letters*, 69(13):271–277, 1996. 2.1.3

[63] G.G. Kirpilenko, V.D. Frolov, E.V. Zavedeev, S.M. Pimenov, V.I. Konov, E.Y. Shelukhin, and E.N. Loubnin. Synthesis, characterization and nanostructuring of (a-C:H):Si and (a-C:H):Si:metal films. *Diamond and Related Materials*, 15(4-8):1147–1150, 2006. 2.1.3

[64] H. Li, R.H. Franken, R.L. Stolk, C.H.M. van der Werf, J.K. Rath, and R.E.I. Schropp. Controlling the quality of nanocrystalline silicon made by hot-wire chemical vapor deposition by using a reverse H_2 profiling technique. *Journal of Non-Crystalline Solids*, 19-25:2087–2091, 2008. 2.1.3

[65] M.R. Scriba, C. Arendse, M. Härting, and D.T. Britton. Hot-wire synthesis of si nanoparticles. *Thin Solid Films*, 516:844846, 2008. 2.1.3, 2.3

University of Cape Town

[66] M. Fonrodona, D. Soler, J. M. Asensi, J. Bertomeu, and J. Andreu. Studies on grain boundaries in nanocrystalline silicon grown by hot-wire CVD. *Journal of Non-Crystalline Solids*, 299-302:14–19, 2002. 2.1.3

[67] Michael J. Bogan, W. Henry Benner, Stefan P. Hau-Riege, Henry N. Chapman, and Matthias Frank. Aerosol sample preparation methods for X-ray diffractive imaging: size-selected spherical nanoparticles on silicon nitride foils. *Aerosol Science*, 38:1119 1128, 2007. 2.1.3

[68] A. A. Onischuk, A. I. Levykin, V. P. Strunin, M. A. Ushakova, R. I. Samoilova, K. K. Sabelfeld, and V. N. Panfilov. Aerosol formation under heterogeneous/homogeneous thermal decomposition of silane: Experiment and numerical modeling. *J. Aerosol Sci.*, 31(8):879–906, 2000. 2.1.3

[69] Xiaoming Zhang, Doinita Neiner, Shizhong Wang, Angelique Y Louie, and Susan M . Kauzlarich. A new solution route to hydrogen-terminated silicon nanoparticles: synthesis, functionalization and water stability. *Nanotechnology*, 18:095601–07, 2007. 2.4, 2.1.3

[70] Jamie H Warner and Richard D Tilley. Synthesis of water-soluble photoluminescent germanium nanocrystals. *Nanotechnology*, 17:3745–3749, 2006. 2.1.3

[71] Wikipedia. Nanotechnology — wikipedia, the free encyclopedia. Internet article, accessed online 15-February 2009. `http://en.wikipedia.org/wiki/Nanotechnology`. 2.1.3

[72] A. Tanaka, G. Yamahata, Y. Tsuchiya, K. Usami, H. Mizuta, and S. Od. High-density assembly of nanocrystalline silicon quantum dots. *Current Applied Physics*, 6(3):344–347, 2006. 2.1.3

[73] P. Unifantowicz, S. Vaucher, M. Lewandowska, and K. J. Kurzydlowski. Structural changes of silicon upon high-energy milling investigated by raman spectroscopy. *Journal of Physics: Condensed Matter*, 20:025205, 2008. 2.1.3, 2.3.4, 2.3.4, 2.3.4

[74] H.W. Lau, O.K. Tan, B.C. Ooi, Y. Liu, T.P. Chen, and D. Lu. Characteristics of mechanically milled silicon nanocrystals embedded in teos thin films. *Journal of Crystal Growth*, 288(1, 2):92–95, 2006. 2.1.3

[75] Jun-ho Jeong, Ki-don Kim, Young-suk Sim, Hyonkee Sohn, and Eung-sug Lee. A step-and-repeat uv-nanoimprint lithography process using an elementwise patterned stamp. *Microelectronic Engineering*, 82(2):180–188, 2005. 2.1.3

University of Cape Town

[76] I Umezu, H Minami, H Senoo, and A Sugimura. Synthesis of photoluminescent colloidal silicon nanoparticles by pulsed laser ablation in liquids. *Journal of Physics: Conference Series*, 59:392–395, 2007. 2.1.3

[77] T. Makino, M. Inada, K. Yoshida, I. Mmezu, and A. Sugimura. Structural and optical properties of silicon nanoparticles prepared by pulsed laser ablation in hydrogen background gas. *Appl. Phys. A*, 79:13911393, 2004. 2.1.3

[78] M. Ben Rabha, M. Saadoun, B. Boujmil, M.F.and Bessas, H. Ezzaouia, and R. Bennaceur. Application of the chemical vapor-etching in polycrystalline silicon solar cells. *Applied Surface Science*, 252(2):488–493, 2005. 2.1.3

[79] J. Valenta, A. Fucikova, I. Pelant, K. Kusova, K. Dohnalova, A. Aleknavicius, O. Cibulka, A. Fojtik, and G. Kada. On the origin of the fast photoluminescence band in small silicon nanoparticles. *New Journal of Physics*, 10:1–6, 2008. 2.1.3

[80] Masato Ohmukai, Nobutomo Uehara, Tetsuya Yamasaki, and Yasuo Tsutsumi. The effects of chemical etching of porous silicon on raman spectra. *Czechoslovak Journal of Physics*, 54(7):781–784, 2004. 2.1.3

[81] R. J. Martin-Palma, L Vazquez, J. M. Martinez-Duart, M. Schnell, and S. Schaefer. Antireflective porous-silicon coatings for multicrystalline solar cells: the effects of chemical etching and rapid thermal processing. *Semicond. Sci. Technol.*, 16(8):657–661, 2001. 2.1.3

[82] Shinji Yae, Yukinori Kawamotoa, Hiroyuki Tanakaa, Naoki Fukumuroa, and Hitoshi Matsudaa. Formation of porous silicon by metal particle enhanced chemical etching in hf solution and its application for efficient solar cells. *Electrochemistry Communications*, 5(8):632–636, 2003. 2.1.3

[83] Siebtechnik. Laboratory disc mill. Internet article, accessed online 20-January 2009. `http://www.siebtechnik.com/index.php?ticket=WI1221137138W48c912f25788a&tname=default&node=355`. 2.2.1

[84] Wikipedia. X-ray scattering techniques — wikipedia, the free encyclopedia. Internet article, accessed online 20-January 2009. `http://en.wikipedia.org/w/index.php?title=X-ray_scattering_techniques&oldid=236064915`. 2.3.1

[85] Jim Connolly. Basics of x-ray diffraction. Internet article, accessed online 14-January 2009. `http://epswww.unm.edu/xrd/xrdbasics.pdf`, 1999. 2.3.1

University of Cape Town

[86] C.M. Kachhava. *Solid State Physics, Solid State Device and Electronics.* Mc Graw-Hill, 1987. 2.3.1

[87] G Beaucage. Class notes: Chapter 3. Internet article,accessed online 15-February 2009. `http://www.eng.uc.edu/~gbeaucag/Classes/XRD/Chapter3html/Chapter3.html`. 2.3.1, 2.3.1, 2.3.1

[88] C. Suryanarayana. *Mechanical Alloying and Milling.* CRC Press, 2004. 2.3.1, 2.3.1

[89] M.E. Rabanal, A. Vrez, B. Levenfeld, and J.M. Torralba. Magnetic properties of mg-ferrite after milling process. *Journal of Materials Processing Technology*, 143-144:470–474, 2003. 2.3.1

[90] Romyani Goswami, Biswajit Chowdhury, and Swati Ray. Solid phase crystallization of protocrystalline silicon films: Changes in structural and optical properties. *Thin Solid Films*, 516(8):2306–2313, 2008. 2.3.1

[91] T.D. Shen, C.C. Koch, T.L. McCormick, R.J. Nemanich, J.Y. Huang, and J.G. Huang. The structure and property characteristics of amorphous/nanocrystalline silicon produced by ball milling. *Journal of Materials Research*, 10:139–148, 1995. 2.3.1

[92] Wikipedia. Scanning electron microscope — wikipedia, the free encyclopedia. Internet article, accessed online 15-February 2009. `http://en.wikipedia.org/wiki/Scanning_electron_microscope`. 2.3.2

[93] Wikipedia. Energy-dispersive X-ray spectroscopy — Wikipedia, The Free Encyclopedia. Internet article, accessed online 15-February 2009. `http://en.wikipedia.org/wiki/Energy-dispersive_X-ray_spectroscopy`. 2.3.2

[94] Evans and Associates. Energy Dispersive X-ray Spectroscopy (EDS). Internet article, accessed online 15-February 2009. `www.eaglabs.com/techniques/analytical_techniques/eds.php`. 2.3.2

[95] Scientific Thermo. Energy Dispersive X-Ray Spectroscopy (EDS/EDX). Internet article, accessed online 20-January-2009. `www.thermo.com/com/cda/technology/detail/1,,12700,00.html`. 2.3.2

[96] Frank Schoonjans. Digimizer image analysis software, version 3.1.2.0, 2008. `http://www.digimizer.com/`. 2.3.2, 2.3.3

University of Cape Town

[97] Wikipedia. Transmission electron microscopy — wikipedia, the free encyclopedia. Internet article, accessed online 15-February 2009. http://en.wikipedia.org/wiki/Transmission_electron_microscopy. 2.3.3

[98] X. Z. Li. Jecp/pceda computer program for simulation of polycrystalline electron diffraction pattern and phase identification. *Ultramicroscopy*, 99(4):257–261, 2004. 2.3.3

[99] Wikipedia. Raman spectroscopy — wikipedia, the free encyclopedia. Internet article,accessed online 15-February 2009, 2008. http://en.wikipedia.org/wiki/Raman_spectroscopy. 2.3.4

[100] Md. N Islam and Kumar Satyendra. Influence of crystallite size distribution on microraman analysis of porous silicon. *Appllied Physics Letters*, 78(6), 2001. 2.3.4, 2.3.4

[101] E. Vallat-Sauvain, C. Droz, F. Meillaud, J. Bailat, A. Shah, and C. Ballif. Determination of raman emission cross-section ratio in hydrogenated microcrystalline silicon. *Journal of Non-Crystalline Solids*, 352(9-20):1200–1203, 2006. 2.3.4, 2.3.4

[102] C. Smit, R.A.CM.M. van Swaaij, H. Donker, A.M.H.N. Petit, W.M.M. Kessels, and M.C.M. van de Sanden. Determining the material structure of microcrystalline silicon from raman spectra. *Applied Physics*, 94(5):3582–3588, 2003. 2.3.4

[103] W. David Hahn. Raman scattering theory. 2007. Internet article, accessed online 15-February 2009. www.plaza.ufl.edu/dwhahn/Raman%20Scattering%20Theory.pdf,. 2.3.4

[104] Kaiser optical systems. 2007. Raman spectroscopy. Internet article, accessed online 15-February 2009. http://www.kosi.com/raman/resources/tutorial/index.html. 2.3.4, 2.23

[105] Alex Finnemore. Raman spectroscopic characterisation of silicon nanoparticles. Honours project, University of Cape Town, 2007. 2.3.4

[106] Lihe Zheng, Guangjun Zhao, Chengfeng Yan, Xiaodong Xu, Liangbi Su, Yongjun Dong, and Jun Xu. Raman spectroscopic investigation of pure and ytterbium-doped rare earth silicate crystals. *Journal of Raman Spectroscopy*, 38(11):1421 – 1428, 2007. 2.3.4

[107] M. Fanciulli, E. Bonera, E. Carollo, and L. Zanotti. EPR and UV-Raman study of BPSG thin films: structure and defects. *Microelectronic Engineering*, 55(1-4):65–71, 2001. 2.3.4

University of Cape Town

[108] Ch. Ossadnik, S. Veprek, and I. Gregora. Applicability of Raman scattering for the characterisation of nanocrystalline silicon. *Thin Solid Films*, 337:148–151, 1999. 2.3.4

[109] Giuseppe Faraci, Santo Gibilisco, Paola Russo, and Agata R. Pennisi. Modified raman confinement model for Si nanocrystals. *Physical Review B*, 73(033307):033307–1 – 4, 2006. 2.3.4

[110] Md. Nazrul Islam, Asima Pradhan, and Satyendra Kumar. Effects of crystallite size distribution on the raman-scattering profiles of silicon nanostructures. *Journal of Applied Physics*, 98(024309), 2005. 2.3.4

[111] Z.X. Zhaoa, R.Q. Cui, F.Y. Meng, B.C. Zhao, H.C. Yu, and Z.B. Zhou. Nanocrystalline silicon thin films prepared by rf sputtering at low temperature and heterojunction solar cell. *Materials Letters*, 58:3963– 3966, 2004. 2.3.4

[112] R.C. Teixeira, I. Doi, M.B.P. Zakia, J.A. Diniz, and J.W. Swart. Micro-raman stress characterization of polycrystalline silicon films grown at high temperature. *Materials Science and Engineering B*, 112(2-3):160–164, 2004. 2.3.4, 2.3.4

[113] Inc Global Information. Polymer nanocomposites. 2004. Internet article,accessed online 15-February 2009. `http://www.the-infoshop.com/study/bc5502_polymer_nanocomposites.html`. 3

[114] Mingqing Wang, Yanqing Lian, and Xiaogong Wang. Ppva/pva/zno nanocomposite prepared by complex precursor method and its photovoltaic application. *Current Applied Physics*, 9:189–194, 2009. 3

[115] N. Laidani, V. Micheli, R. Bartali, G. Gottardi, and M. Anderle. Optical and mechanical characterization of zirconiacarbon nanocomposite films. *Thin Solid Films*, 516:1553 – 1557, 2008. 3

[116] Guido Kickelbick. *Hybrid materioals, Synthesis, Characterisation and Application.* Cambridge University Press, 2002. 3

[117] P. M. Ajayan, L. S. Schadler, and P. V. Braun. *Nanocomposite Science and Technology.* WILEY-VCH Verlag GmbH Co., 2003. 3.1, 3.1, 3.3.1

[118] Sridhar Komarneni. *Chemical Processing of Ceramics Second Edition.* CRC Press, 2005. 3.1

[119] Joseph H. Koo. *Polymer Nanocomposites Processing, Characterization, and Applications.* McGraw-Hill, 2006. 3.1

University of Cape Town

[120] Luigi Nicolais and Gianfranco Carotenuto. *Metal-polymer nanocomposites*. John Wiley and Sons, Inc., 2005. 3.1, 3.1

[121] S. Srivastava, M Haridas, and J. K. Basu. Optical properties of polymer nanocomposites. *Bull. Mater. Sci.*, 31(3):213217, 2008. 3.1

[122] Youngchan Shin, Deokkyu Lee, Kangtaek Lee, Kyung Hyun Ahn, and Bumsang Kim. Surface properties of silica nanoparticles modified with polymers for polymer nanocomposite applications. *Journal of Industrial and Engineering Chemistry*, 14:515–519. 3.1

[123] L.L. Yang, X.D. He, F. He, and Y. Sun. Small angle X-ray scattering studies on structural evolution during calcination of sol-gel ITO nano-powder. *Alloys and Compounds*, page In press, 2008. 3.2

[124] A.F. Craievich. Synchrotron SAXS Studies of Nanostructured Materials and Colloidal Solutions. A Review. *Materials Research*, 5(1):1–11, 2002. 3.2, 3.2, 3.2, 3.3.1

[125] G Beaucage. Small angle x-ray scattering (saxs, internet resource tutorial. Internet article, accessed online 15-February 2009. `http://www.eng.uc.edu/~gbeaucag/Classes/XRD/SAXShtml/SAXS.pdf`. 3.2, 3.2, 3.2, 3.2

[126] D.T. Britton, E.A. Odo, G. Goro Gonfa, E.O. Jonah, J.F.Q. Rey, I.L. Torriani, Harvey A.J., and Harting M. Size distribution and surface characteristics of silicon nanoparticles. Sumitted to Journal of Appplied Crystallography, 2008. 3.2, 3.2, 3.3.1

[127] Luis A.S de A. Prado, M.L. Ponce, S.S Funari, K. Schulte, V.M. Garamus, R. Willumeit, and S.P. Nunes. SAXS/WAXS characterisation of proton-conducting polymer membranes containing phosphomolybdic acid. *Journal of Non-Crystalline Solids*, 351(1):2194–2199, 2005. 3.2, 3.2

[128] P. W. Schmidt. Small-angle scattering studies of disordered, porous and fractal systems. *J. Appl. Cryst*, 24:414–435, 1991. 3.2, 3.2, 3.2, 3.2

[129] E.O. Jonah. Charge transport in nanoparticle cluster network. Master's thesis, University of Cape Town, 2008. 3.2

[130] D.R. Vollet, D.A. Donatti, and A. Ibanez Ruiz. A SAXS study of the nanostructural characteristics of TEOS-derived sonogels upon heat treatment up to 1100^oC. *Journal of Non-Crystalline Solids*, 306(1):11–16, 2002. 3.2, 3.2, 3.2

University of Cape Town

[131] T. Hashimoto, M. Fujimura, and H. Kawai. Domain-boundary structure of styrene-isoprene block co-polymer films cast from solutions 5 molecular-weight dependence of spherical microdomains. *Macromolecules*, 13(6):1660–1669, 1980. 3.2

[132] J.E. Martin and B.J. Ackerson. Static and dynamic scattering from fractals. *Physical Review A*, 31(2):1180–1182, 1985. 3.2

[133] L. Rozes, G. Fornasieri, S. Trabelsi, C. Creton, N.E. Zafeiropoulos, M. Stamm, and C. Sanchez. Reinforcement of polystyrene by covalently bonded oxo-titanium clusters. *Progress in Solid State Chemistry*, 33:127–135, 2005. 3.2, 3.2

[134] A. Corina Geiculescu and H. J. Rack. X-ray scattering studies of polymeric zirconium species in aqueous xerogels. *Journal of Non-Crystalline Solids*, 306(1):30–41, 2002. 3.2, 3.2, 3.4.2, 3.4.2

[135] Rui Zhang, Yao X, Qinghan Meng, Liang Zhan, Kaixi Li, Dong Wu, Licheng Ling, Jun Wang, Hui Zhao, and Baozhong Dong. Small angle X-ray scattering study of microstructure changes of organic hydrogels from supercritical carbon dioxide drying. *J. of Supercritical Fluids*, 28(1):263–276, 2004. 3.2, 3.2, 3.2, 3.4.4, 3.4.4

[136] S. Pikus and E. Kobylas. Saxs studies of porous materials coated by organic layer. *Fibres and Textiles in Eastern Europe*, 11(5):70–74, 2003. 3.2, 3.4.4, 3.4.4

[137] G. Beaucage and D. W. Schaefer. Structural studies of complex systems using small-angle scattering: a unified guinier/power-law approach. *Journal of Non-Crystalline Solids*, 172 174(1):797–805, 1994. 3.2, 3.2

[138] G. Beaucage. Approximations leading to a unified exponential/power-law approach to small-angle scattering. *Journal of Applied Crystallography*, 28(6):717–728, 1995. 3.2, 3.2

[139] G. Kellermann, F. Vicentin, E. Tamura, M. Rocha, H. Tolentino, A. Barbosa, A. Craevich, and I. Torraini. The small-angle x-ray scattering beamline of the brazilian synchrotron light laboratory. *J. Appl. Cryst.*, 30(1):880–883, 1997. 3.3.1

[140] P.L. Guzzo, A.H. Shinohara, M.A. Pasquali, E. Gusken, C.K. Suzuki, V.M. Azevedo, and Y. Mikawa. Characterization of heterogeneities in new generation synthetic quartz crystal by small angle x-ray scattering. *J. Appl. Cryst*, 36(1):459–463, 2003. 3.4.2

[141] Bagchi Debjani and Menona Reghu. Conformational modification of conducting polymer chains by solvents: Small-angle x-ray scattering study. *Chemical Physics Letters*, 425(1-3):114–117, 2006. 3.4.2, 3.4.2

University of Cape Town

[142] N. Hiramatsu, A. Nakamura, M. Sugiyama, K. Hara, and Y. Maeda. Mesoscopic structure observation of egg white gel by small angle neutron scattering. *Physica B*, 241-243(1):987– 989, 1998. 3.4.2

[143] S.V. Chavan, P.U.M. Sastry, and A.K. Tyagi. Combustion synthesis of nano-crystalline nd-doped ceria and nd2o3 and their fractal behavior as studied by small angle x-ray scattering. *Journal of Alloys and Compounds*, 456(-):51–56, 2008. 3.4.3

[144] Man-Ho Kim. Modified porod's law estimate of the transition-layer thickness between two phases: test of triangular smoothing function. *Applied Crystallography*, 37:643–651, 2004. 3.4.4

[145] S.M. Sze. *Physics of Semiconductor Devices. Third Edition*. John Wiley and Son, 2007. 4, 4.1.1, 4.1.1, 4.1.1, 4.1.2, 4.4, 4.1.2, 4.1.2, 4.3, 4.7, 4.3.1, 4.3.1, 4.3.2, 4.3.2, 4.3.3, 4.8, 4.5.2, 4.5.5

[146] J. Barreto, J.A. Rodrguez, M. Perlvarez, A. Morales, B. Garrido, and C. Domnguez. Photoluminescence characterization of silicon nanostructures embedded in silicon oxide. *Superlattices and Microstructures*, 43:588–593, 2008. 4

[147] A. Fissel, A. Laha, E. Bugiel, D. Khne, M. Czernohorsky, R. Dargis, and H.J. Osten. Silicon in functional epitaxial oxides: A new group of nanostructures. *Microelectronics Journal*, 39:512–517, 2008. 4

[148] P N Vinod. Specific contact resistance of the porous silicon and silver metal ohmic contact structure. *Semicond. Sci. Technol*, 20:966 –971, 2005. 4.1

[149] Simon M. Sze. *Semiconductor Devices: Physics and Technology, 2nd Edition*. Wiley, 2001. 4.1, 4.1.1, 4.3.1, 4.3.1, 4.3.4, 4.5.5

[150] Raymond T. Tung. Recent advances in Schottky barrier concepts. *Material Science and Engineering R*, 35:1–138, 2001. 4.1.1, 4.1.2, 4.1.2, 4.1.2, 4.3.2, 4.3.2, 4.5.4, 4.5.4, 4.5.4, 4.5.4, 4.5.4, 4.5.5

[151] Dieter K. Schroder. *Semiconductor Material and Device Characterization*. Wiley-IEEE Press, 2006. 4.1.1, 4.2, 4.1.1, 4.3, 2, 4.3.2, 4.5.4

[152] Bart Van Zeghbroeck. Principle of semiconductor devices. 2004. E-book, accessed online 4-December 2008. `http://ece-www.colorado.edu/~bart/book`. 4.1.1, 4.1.1, 4.3.3

University of Cape Town

[153] Cetin Hidayet, Sahin Bunyamin, Ayyildiz Enise, and Turut Abdulmecit. The barrier-height inhomogeneity in identically prepared h-terminated ti/p-si schottky barrier diodes. *Semiconductor Science and Technology*, 19(9):1113–1116, 2004. 4.1.1

[154] Simon Ulrich. Charge transport in nanoparticle. *Adv. Mater.*, 10(17):1487–1492, 1998. 4.2, 4.5, 4.2, 4.2, 4.6

[155] Amir Zabet-Khosousi and Al-Amin Dhirani. Charge transport in nanoparticle assemblies. *Chem. Rev.*, 108(10):4072–4124, 2008. 4.2

[156] Sergei Baranovski. *Charge Transport in Disordered Solids with Applications in Electronics*. John Wiley and Sons Ltd, 2006. 4.2

[157] T.K.H. Starke, C. Johnston, and P.S. Grant. Evolution of percolation properties in nanocomposite films during particle clustering. *Scripta Materialia*, 56:425428, 2007. 4.2

[158] K. Varahramyan and E. J. Verret. A model for specific contact resistance applicable for titanium silicide-silicon contacts. *Solid-State Electronics*, 39:1601–1607, 1996. 2

[159] Shan Yu Quan, Feng Teng, DongDong Wang, DeAng Liu, Zheng Xu, YongSheng Wang, and XuRong Xu. Charge carrier injection and transport in polymer blend films. *Solid State Communications*, 134:291–294, 2005. 4.3

[160] S.M. Sze. *Physics of Semiconductor Devices. Second Edition.* John Wiley and Son, 1981. 4.3.1, 4.3.2

[161] F. Yakuphanoglu, Nihat Tugluoglu, and S. Karadeniz. Space charge-limited conduction in ag/p-si schottky diode. *Physica B: Condensed Matter*, 392:188–191, 2007. 4.3.4

[162] R. Singh, S. K. Tripathi, and S. Kumar. Space charge limited conduction in $a-(Ge_{20}Se_{80})1-xSn_x$ thin films. *Journal of Non-Crystalline Solids*, 352:3230–3235, 2006. 4.3.4

[163] S. P. Singh, A. Kumar, and S. Kumar. Non-ohmic behavior in $a-Se_{80-x}Te_{20}Cd_x$ thin films. *Materials Letters*, 60:1640–1645, 2006. 4.3.4

[164] A. M. A. EL-Barry. Photoinduced crystallization and space charge limited current through $Au/Se_{92.7}S_{7.3}/Au$ thin films. *Physica B: Condensed Matter*, 396:49–56, 2007. 4.3.4, 4.3.4, 4.5.5, 4.5.8, 5.7.2

University of Cape Town

[165] Ahmet Faruk Ozdemir, Aysegul Gok, and Abdulmecit Turut. The electrical measurements in poly(2-chloroaniline) based thin film sandwich devices. *Thin Solid Films*, 515:7253–7258, 2007. 4.3.4

[166] N. Arpatzanis, C. A. Dimitriadis, S. Siskos, A. A. Hatzopoulos, and G. Kamarinos. Determination of bulk and interface density of states in polycrystalline silicon thin film transistors. *Thin Solid Films*, 515:7581–7584, 2007. 4.3.4

[167] S. M. El-Sayed. Space-charge-limited current, trap distribution and optical energy gap in amorphous ($In_{13}Se_{87}$ and $In_{20}Se_{80}$) thin films. *Vacuum*, 65:177–184, 2002. 4.3.4

[168] R. Sathyamoorthy, J. Dheepa, and S. Velumani. Space charge limited current conduction in Bi_2Te_3 thin films. *Materials Characterization*, 58:842–846, 2007. 4.3.4

[169] DuPont. Dupont microcircuit materials, thick film composition 5000 silver paste. 2008. Internet article, accessed online 22-January 2009. http://www2.dupont.com/MCM/en_US/PDF/datasheets/5000.pdf. 4.4.1, 5.6.1

[170] S. Karatas, S. Altndal, A. Turut, and A. Ozmen. Temperature dependence of characteristic parameters of the H-terminated Sn/p-Si(1 0 0) Schottky contacts. *Applied Surface Science*, 217(1-4):250–260, 2003. 4.5.2, 4.5.5

[171] M. Ozer, D.E. Yildiz, S. Altindal, and M.M. Bulbul. Temperature dependence of characteristic parameters of the $Au/SnO_2/n-Si$ (MIS) Schottky diodes. *Solid-State Electronics*, 51(6):941–949, 2007. 4.5.2, 4.5.4

[172] M.E. Aydin, O. Gullu, and N. Yildirim. Temperature dependence of current-voltage characteristics of sn/p-si schottky contacts. *Physica B: Condensed Matter*, 403(1):131–138, 2008. 4.5.2, 4.5.4, 4.5.5

[173] Ilbilge Dokme and S. emsettin Altindal. On the intersecting behaviour of experimental forward bias current-voltage (I-V) characteristics of $Al/SiO_2/p-Si$ (MIS) Schottky diodes at low temperatures. *Semicond. Sci. Technol*, 21(8):1053–1058, 2006. 4.5.2

[174] S. Karatas and S. Altindalb. Analysis of IV characteristics on Au/n-type GaAs Schottky structures in wide temperature range. *Materials Science and Engineering: B*, 122:133–139, 2005. 4.5.2

[175] K. Akkilic, M. E. Aydin, I. Uzun, and T. Kilicoglu. The calculation of electronic parameters of an Ag/chitin/n-Si Schottky barrier diode. *Synthetic Metals*, 156:958–962, 2006. 4.5.4

University of Cape Town

[176] A. Altindal and S. Tataroglu. Analysis of interface states and series resistance of MIS Schottky diodes using the current-voltage (I-V) characteristics. *Microelectronic Engineering*, 85(1):233–237, 2008. 4.5.4

[177] S. Altindal, H. Kanbur, D.E. Yildiz, and M. Parlak. Current conduction mechanism in Al/p-Si Schottky barrier diodes with native insulator layer at low temperatures. *Applied Surface Science*, 253(11):5056–5061, 2007. 4.5.4

[178] S. K. Cheung and N. W. Cheung. Extraction of schottky diode parameters from forward current-voltage characteristics. *Applied Physics Letters*, 49(2):85–87, 1986. 4.5.4, 4.17

[179] I-Chun Cheng, Steven Allen, and Sigurd Wagner. Evolution of nanocrystalline silicon thin film transistor channel layers. *Journal of Non-Crystalline Solids*, 338-340(15):720–724, 2004. 4.5.4, 4.5.4, 5.4

[180] Myungsim Jun, Yarkyeon Kim, Cheljong Choi, Taeyoub Kim, Soonyoung Oh, and Moongyu Jang. Schottky barrier heights of n/p-type erbium-silicided schottky diodes. *Microelectronic Engineering*, 85(5-6):1395–1398, 2008. 4.5.4

[181] Department of Electrical Brigham Young University and Computer Engineering. Metal-semiconductor ohmic and Schottky contacts. Internet article, Online; accessed 10-January-2009. `http://www.ee.byu.edu/cleanroom/ohmic-schottky.phtml`. 4.5.4

[182] D.K. Aswal, S. Lenfant, D. Guerin, J.V. Yakhmi, and D. Vuillaume. Self assembled monolayers on silicon for molecular electronics. *Analytica Chimica Acta*, 568:84–108, 2006. 4.5.6

[183] Jeremy M. Beebe, BongSoo Kim, J.W. Gadzuk, C. Daniel Frisbie, and James G. Kushmerick. Transition from direct tunneling to field emission in metal-molecule-metal junctions. *Physical review letters*, 97:20680(1–4), 2006. 4.5.6, 4.5.6

[184] W. Wang, T. Lee, M. Kamdar, M.A. Reed, M.P. Stewart, J.-J. Hwang, and J.M. Tourb. Electrical characterization of metalmoleculesilicon junctions. *Superlattices and Microstructures*, 33:217 –226, 2003. 4.5.6, 4.5.6

[185] Wenyong Wang, Takhee Lee, and Mark A Reed. Electron tunnelling in self-assembled monolayers. *Rep. Prog. Phys.*, 68:523–544, 2005. 4.5.6

University of Cape Town

[186] A. I. K. Choudhury, M. R. R. Mazumder, K. Z. Ahmed, and Q. D. M. Khosru. Explanation for reduced fowler-nordheim tunneling current in ultrathin silicon nitride gate dielectric. *3rd International Conference on Electrical and Computer Engineering ICECE 2004 December 2004, Dhaka, Bangladesh*, 33:271–274, 2004. 4.5.6, 4.5.6

[187] Andreas Gehring. Simulation of tunneling in semiconductor devices. Ph.D Dissertation, Technische Universitat Wien. Austria, November 2003. `http://www.iue.tuwien.ac.at/phd/gehring/`. 4.22

[188] Y. Khlifi, K. Kassmi, L. Roubi, and R. Maimouni. Modeling of fowler-nordheim current of metal/ ultra-thin oxide/ semiconductor structures. *M.J. Condensed matter*, 3:271–274, 2000. 4.5.6

[189] M.N. Jones, Y.W. Knwon, and D.P. Norton. Dielectric constant and current transport for HFO_2 thin films on ITO. *Appl. Phys. A. Material Science and Processing*, 81:285–288, 2005. 4.5.7

[190] M.A. Gaffar, A Abu El-Fadl, and S. Bin Anooz. Mechanism of DC conduction in undoped and Sr_{2+} doped ammonium zinc crystal. *Solid State Communications*, 129:797–802, 2004. 4.5.7, 4.5.7

[191] M.M. El-Samanoudy. Modified Poole-Frenkel Mechanism in $Ge_{25}Bi_xSb_{15-x}$ Thin Fulms. *Applied Surface Science*, 207:219–226, 2003. 4.5.7

[192] A.A. Dakhel. DC-Conduction mechanism in lanthanum -manganese oxide films grown on p-Si substrate. *Microelectronics Reliability*, 48:395–400, 2007. 4.5.7

[193] A.A. Dakhel. DC electronic transport mechanisms in some manganese-oxide insulator thin films grown on Si substrates. *Journal of Alloys and Compounds*, 416(1-2):17–21, 2006. 4.5.7

[194] S. Senthilarasu, R. Sathyamoorthy, S. Lalitha, and A. Subbarayan. Electrical conduction properties of $ZnPc/TiO_2$ thin films. *Solar Energy Materials and Solar Cells*, 90:783 –797, 2006. 4.5.7, 4.5.7, 4.5.8, 4.5.8

[195] M.A. Gaffar, A Abu El-Fadl, and S. Bin Anooz. The non-isotropic character of electric and dielectric properties of ammonium zinc chloride crystal. *Journal of Physics and Chemistry of Solids*, 65:957–964, 2004. 4.5.7, 4.5.7, 4.5.7

[196] R. Maity, S. Kundoo, and Chattopadhyay K.K. Electrical characterization and Poole-Frenkel effect in sol-gel derived $ZnO : Al$ thin films. *Solar Energy Materials and Solar Cells*, 86:217 –227, 2005. 4.5.7

University of Cape Town

[197] Gorur G. Raju. *Dielectrics in Electric Fields*. CRC Press, 2003. 4.5.8, 4.5.8

[198] Mustafa Okutan, Halil I. Bakanb, Kemal Korkmaz, and Fahrettin Yakuphanoglu. Variable range hopping conduction and microstructure properties of semiconducting co-doped tio2. *Physica B*, 355:176 –181, 2005. 4.5.9

[199] Chen Ang, J. R. Jurado, Zhi Yu, M. T. Colomer, J. R. Frade, and J. L. Baptista. Variable-range-hopping conduction and dielectric relaxation in disordered $Sr_{0.97}Ti_{12x}Fe_xO_{32}$. *Physical Review B*, 57(19):1185811861, 1998. 4.5.9

[200] Woo-Hwan Jung. Variable range hopping conduction of polaron in n=2 Ruddlesden-Popper phase $Sr_3Fe_{1.5}Co_{0.5}O_{6.77}$. *Materials Letters*, 61:2274–2276, 2007. 4.5.9, 4.5.9

[201] Ajai K. Gupta, Vijay Kumar, and Neeraj Khare. Hopping conduction in double layered $La_{2-2x}Ca_{1+2x}Mn_2O_7$ manganite. *Solid State science*, 9(9):817–823, 2007. 4.5.9, 4.5.9, 4.5.9

[202] D. Sreekantha Reddy, B. Kang, S.C. Yu, K.R. Gunasekhar, and P. Sreedhara Reddy. Synthesis and characterization of zn1-xmnxs nanocrystalline films prepared on glass substrates. *Appl. Phys. A*, 91:627630, 2008. 5

[203] Gizmag electronic article. Breakthrough in printed electronics. 2008. internet article, accessed online 15-February 2009. `http://www.gizmag.com/go/4749/`. 5

[204] A NanoMarkets White Paper. Nanocrystalline silicon/silicon inks. 2008. Internet article, accessed online 23-January 2009. `http://www.nanomarkets.net/resources/NMNanocrystallineSilicon.pdf`. 5, 5.1

[205] Paul Andry and Cherie R. Kagan. *Thin-film transistors*. Marcel Dekker, Inc., 2003. 5.1, 5.3, 5.4, 5.5, 5.4, 5.5.3, 5.5

[206] Hyewon Kang, Keon kook Han, Jeong-Eun Park, and Hong H. Lee. High mobility, low voltage polymer transistor. *Organic Electronics Letters*, 8(4):460–464, 2007. 5.1

[207] C Y Lin, Y K Fang, S F Chen, C S Lin, and Et al. Investigation of structure and properties of nanocrystalline silicon on various buffer layers. *Journal of Electronic Materials*, 34(8):1123–1128, 2005. 5.2

[208] NRL. Nanoelectronic devices. internet article, accessed online 23-January 2009. `http://estd-www.nrl.navy.mil/code6870/nanodev/nanodev.html`. 5.2

University of Cape Town

[209] Fu-Cheng Wang, W. E. Zhang, C. H. Yang, M. J. Yang, B. R. Bennett, R. A. Wilson, and D. R. Stone. A tunneling field-effect transistor with 25 nm metallurgical channel length. *Applied Physics Letters*, 70:3005–3007, 1997. 5.2

[210] E.S. Snow, P.M. Campbell, R.W. Rendell, F.A. Buot, D. Park, C.R.K. Marrian, and R. Magno. A metal/oxide tunnelling transistor. *Semiconductor Science and Technology*, 13(8A):75–78, 1997. 5.2

[211] M. A. Kastner. The single electron transistor and artificial atoms. *Ann.Phys.*, 9(11 12):885–894, 2000. 5.2

[212] Michel Devoret and Christian Glattli. Single-electron transistors. *Physics World*, 11(9):29–34, 1998. 5.2

[213] Robert Kosik. *Numerical Challenges on the Road to NanoTCAD*. PhD thesis, Universitt Wien, 2004. `http://www.iue.tuwien.ac.at/phd/kosik/thesis.html`. 5.2

[214] G. F. Grom, D. J. Lockwood, J. P. McCaffrey, H. J. Labb, P. M. Fauchet, Jr B. White, J. Diener, D. Kovalev, F. Koch, and L. Tsybeskov. Ordering and self-organization in nanocrystalline silicon. *Nature*, 407(10):358–361, 2000. 5.2

[215] Hecheng Zou, Liangcai Wu, Xinfan Huang, Feng Qiao, Peigao Han, Xiaohui Zhou, Zhongyuan Ma, Yansong Liu, Wei Li, and Kunji Chen. Microstructure properties of nanocrystalline silicon/SiO_2 multilayers fabricated by laser-induced crystallization. *Thin Solid Films*, 491(1-2):212–216, 2005. 5.2

[216] R. D. Ott, P. Kadolkar, C. A. Blue, A. C. Cole, and G. B. Thompson. The pulse thermal processing of nanocrystalline silicon thin-films. *Journal of the Minerals, Metals and Materials Society*, 56(10):45–47, 2004. 5.2

[217] M. Fonrodona, D. Soler, J. Escarr, F. Villar, J. Bertomeu, J. Andreu, A. Saboundji, N. Coulon, and T. Mohammed-Brahimb. Low temperature amorphous and nanocrystalline silicon thin film transistors deposited by hot-wire cvd on glass substrate. *Thin Solid Films*, 501(1-2):303–306, 2006. 5.2

[218] George Cramer. Fabrication and Comparison of ZnO Thin Film Transistors with Various Gate Insulators. *National Nanotechnology Infrastructure Network, Research Experience for undergraduates program, Cornell University. 2006*, pages 34–35, 2006. 5.2

University of Cape Town

[219] C.M. Yu, H.C. Lin, C.Y. Lin, K.L. Yeh, T.Y. Huang, and T.F. Lei. Self-aligned fabrication of thin-film transistors with field-induced drain. *Solid-State Electronics*, 46:1091 –1095, 2002. 5.2

[220] Alex Z. Kattamis, Russell J. Holmes, I-Chun Ke Cheng, James Long, C. Sturm, Stephen R. Forrest, and Sigurd Wagner. High mobility nanocrystalline silicon transistors on clear plastic substrates. *IEEE Electron Device Letters*, 27(1):49–51, 2006. 5.2

[221] John Robertson. Materials science crystallization of silicon ideas. *Nature Materials*, 418(4):30–31, 2002. 5.2

[222] D. Dosev, B. Iguez, L. F. Marsala, J. Pallaresa, and T. Ytterdalb. Device simulations of nanocrystalline silicon thin-film transistors. *Solid-State Electronics*, 47(11):1917–1920, 2003. 5.2, 5.4

[223] Wikipedia. Printing — wikipedia, the free encyclopedia. Internet article, accessed online 23-January 2009. `http://en.wikipedia.org/wiki/Printing`. 5.3.1

[224] Hind Ali Ahmed. Deposition and characterization of nanoparticulate silicon layer. Project Report, African Institute of Mathematical Sciences, 2006. 5.3.1

[225] P. Holmes and Loasby R. *Handbook of thick film technology*. Electrochemical Publication Ltd., 1976. 5.3.1

[226] C. Johansson, X. Wang, and M. Robertsson. Printable rectifying device using si-composite. *Electronics Letters*, 44:53 – 55, 2008. 5.3.1

[227] Wikipedia. Flexography — wikipedia, the free encyclopedia. Internet article, accessed online 23-January 2009. `http://en.wikipedia.org/wiki/Flexography`. 5.3.1

[228] H H Lee, E. Menard, N. G. Tassi, J. A. Rogers, and G. B. Blanchet. Fabrication of large-area stamps, moulds, and conformable photomasks for soft lithography. *Proc. IMechE, Nanoengineering and Nanosystems*, 218:1–6, 2004. 5.3.1

[229] T. Makela, S. Jussila, Kosoneh H., Backlund T. G., Sandberg H. G. O., and Stubb H. Utilizing roll-to-roll techniques for manufacturing source-drain electrodes for all-polymer transistors. *Synthetic Metals*, 153(1-3):285–288, 2005. 5.3.1

[230] Joerg Puetz and Michel A. Aegerter. Direct gravure printing of indium tin oxide nanoparticle patterns on polymer foils. *Thin Solid Films*, 516:4495–4501, 2008. 5.3.1

University of Cape Town

[231] M. Lahti, S. Leppvuori, and V. Lantto. Gravure-offset-printing technique for the fabrication of solid films. *Applied Surface Science*, 142:367–370, 1999. 5.3.1

[232] Marko Pudas, Niina Halonen, Pivi Granat, and Jouko Vhkangas. Gravure printing of conductive particulate polymer inks on flexible substrates. *Progress in Organic Coatings*, 54:310–316, 2005. 5.3.1

[233] Wikipedia. Inkjet printer — wikipedia, the free encyclopedia. Internet article, accessed online 23-January 2009. `http://en.wikipedia.org/wiki/Inkjet_printer`. 5.3.1

[234] Cheong Min Hong and Sigurd Wagner. Inkjet printed copper source/drain metallization for amorphous silicon thin-film transistors. *IEEE Electron Device Letters*, 21(8):384–386, 2000. 5.3.1

[235] H. Sirringhaus, T. Kawase, R. H. Friend, T. Shimoda, M. Inbasekaran, W. Wu, and E. P. Woo. High-resolution inkjet printing of all-polymer transistor circuits. *Science*, 290(5499):2123 – 2126, 2000. 5.3.1

[236] Wikipedia. Screen-printing — wikipedia, the free encyclopedia. Internet article, accessed online 23-January 2009. `http://en.wikipedia.org/wiki/Screen-printing`. 5.3.1

[237] F. Duerinckx, P. Choulat, G. Beaucarne, R.J.S Young, M. Rose, and J.A. Raby. Improved screen printing process for very thin multicrystalline silicon solar cells. Presented at the 19th EPVSEC, 2004, Paris `http://www.nanoelektronica.be/wwwinter/energy/FILES/Duerinckx.pdf`, 2004. 5.3.1

[238] Marc Burgelman. Proceedings of the workshop on microtechnology and thermal problems in electronics, summer school. technical university of lodz. pages 129–135, 1998. 5.3.1

[239] A. Dodabalapur, Z. Bao, A. Makhija, J. G. Laquindanum, V. R. Raju, Y. Feng, H. E. Katz, and J. Rogers. Organic smart pixels. *Applied Physics Letters*, 73(2), 1998. 5.3.1

[240] Wikipedia. Pad printing — wikipedia, the free encyclopedia. Internet article, accessed online 23-January 2009. `http://en.wikipedia.org/wiki/Pad_printing`. 5.3.1, 5.3.2

[241] A. Knobloch, A. Bernds, and W. Clemens. Polymers and adhesives in microelectronics and photonics, 2001. first international IEEE conference on digital object identifier. pages 84–90, 2001. 5.3.1

University of Cape Town

[242] PDS Consulting. Principle of pad printing. Internet article, accessed online 23-January 2009. http://www.pdsconsulting.co.uk/Printing%20Process/Pad/Pad.htm. 5.3.2, 5.1, 5.2

[243] Proll. Pad printing theory and practice. Internet article, accessed online 23-January 2009. http://www.proell.de/_files/pdf/Pad%20Printing%20Theory%20and%20Practice.pdf. 5.3.2

[244] TAMPOPRINT. Hermetic tampon printing. Internet article, accessed online 23-January 2009. http://www.tampoprint.de/gb/3technikenen/pad_printing_hermetic_gb.html. 5.1

[245] Dosi Dosev. *Fabrication, characterisation and modelling of nanocrystalline Silicon thin Film Transistors obtained by Hit-Wire Chemical Vapour Deposition.* PhD thesis, Universitat Politecnica De Catalunya Spain: Ph.D. Thesis, 2003. 5.4, 5.3

[246] Ji-Hee Son, In-Nam Kang, Se-Young Oh, and Jong-Wook Park. Structure effects on organic thin-film transistor properties of dinaphthyl substituted pentacene derivatives. *Bull. Korean Chem. Soc*, 28(6):995–998, 2007. 5.4

[247] T. H. Lee. A Review of MOS Device Physics, Handout no 2: Harvard University EE214 Fall 2001. http://people.seas.harvard.edu/~jones/es154/lectures/lecture_4/pdfs/MOS_review.pdf, 2001. 5.5, 5.5.2

[248] Wikipedia. Mosfet — wikipedia, the free encyclopedia. Online; accessed 11-January-2009, 2009. http://en.wikipedia.org/w/index.php?title=MOSFET&oldid=262403238. 5.5.2

[249] IEEE Computer Society. 1620 IEEE standard test methods for the characterisation of Organic transistors and materials. *IEEE STD*, 2004. 5.5.3, 5.7

[250] Shiyang Zhu, J. Singh, Chunxiang Zhu, A. Du, and M.F. Li. Fabrication of poly-Si TFT with silicided Schottky barrier source/drain, high-K gate dielectric and metal gate. *Solid-State Electronics*, 50:232–236, 2006. 5.5.4

[251] Qing-Tai Zhao, Patrick Kluth, Stephan Winnerl, and Siegfried Mantl. Fabrication of schottky barrier mosfets on soi by a self-assembly cosi2-patterning method. *Solid-State Electronics*, 47:1183–1186, 2003. 5.5.4, 5.7.2

[252] M. Pourfath, E. Ungersboeck, A. Gehring, B.H. Cheong, W.J. Park, H. Kosina, and S. Selberherr. Optimization of schottky barrier carbon nanotube field effect transistors. *Microelectronic Engineering*, 81:428–433, 2005. 5.5.4

University of Cape Town

[253] M. Morana, P. Koers, C. Waldauf, M. Koppe, D. Muehlbacher, P. Denk, M. Scharber, D. Waller, and C. Brabec. Organic field-effect devices as tool to characterize the bipolar transport in polymer-fullerene blends: The case of p3ht-pcbm. *Advanced Functional Materials*, 17(16):3274 – 3283, 2007. 5.6.1, 5.7

[254] E. Minani, Z. Sigcau, O. Adegbite, F.L. Ramukosi, T.P. Ntoane, S. Harindintwari, D. Knoesen, C.M. Comrie, D.T. Britton, and M. Harting. Microstructure, optical characterisation and light induced degradation in a-si:h deposited at different temperatures. *Thin Solid Films*, 501:84–87, 2006. 5.6.1

[255] Kazuhihko Yamane, Hisao Yanagi, and Shu Hotta. Ambipolar field effect transistors with heterojunction of organic semiconductors. *Thin Solid Films*, 516:3157–3161, 2008. 5.7.1, 5.7.1, 5.7.2

[256] A. F. Qasrawi and N. M. Gasanly. Hall effect, space-charge limited current and photoconductivity measurements on $TlGaSe_2$ layered crystals. *Semicond. Sci. Technol.*, 19(3):505–509, 2004. 5.7.1

[257] Dolly Sinha, Niloufer Shroff, and P. C. Pillai. dc conduction mechanism in the composite system of lead zirconate titanate and polyvinylidene fluoride. *Ferroelectrics*, 103(1):49 – 56, 1990. 5.7.1

[258] P. Cosseddu, A. Bonfiglio, I. Salzmann, J.P. Rabe, and N. Koch. Ambipolar transport in transparent and flexible all-organic heterojunction field effect transistor at ambient conditions. *Organic Electronics*, 9:191–197, 2008. 5.7.1, 5.7.2

[259] J. Urban Jeffrey, V. Talapin Dmitri, V. Shevchenko Elena, R. Kagan Cherie, and B. Murray Christopher. Synergism in binary nanocrystal superlattices leads to enhanced p-type conductivity in self assembled $PbTe/Ag_2Te$ thin films. *Nature materials*, 6:115–121, 2007. 5.7.2

University of Cape Town

Appendix A. Appendices

University of Cape Town

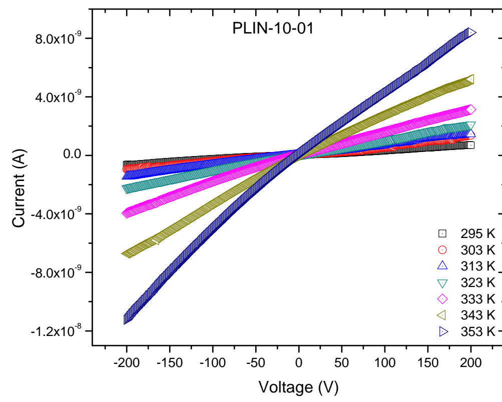

(a)

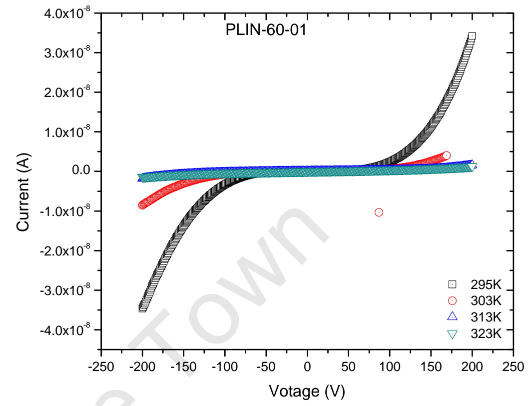

(b)

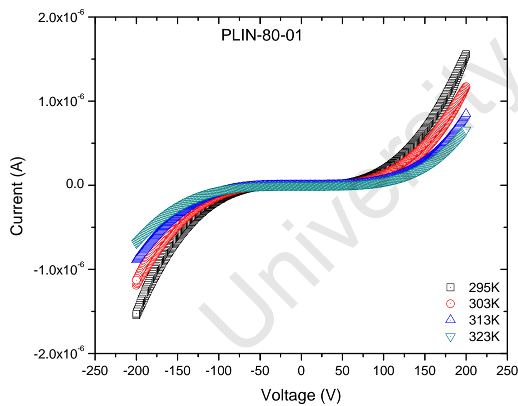

(c)

University of Cape Town

Fig. A.1: Temperature dependent forward and reverse bias I-V characteristics for samples (a)PLIN-10-01, (b)PLIN-60-01, (c) PLIN-80-01 in the temperature range specified on each plot.

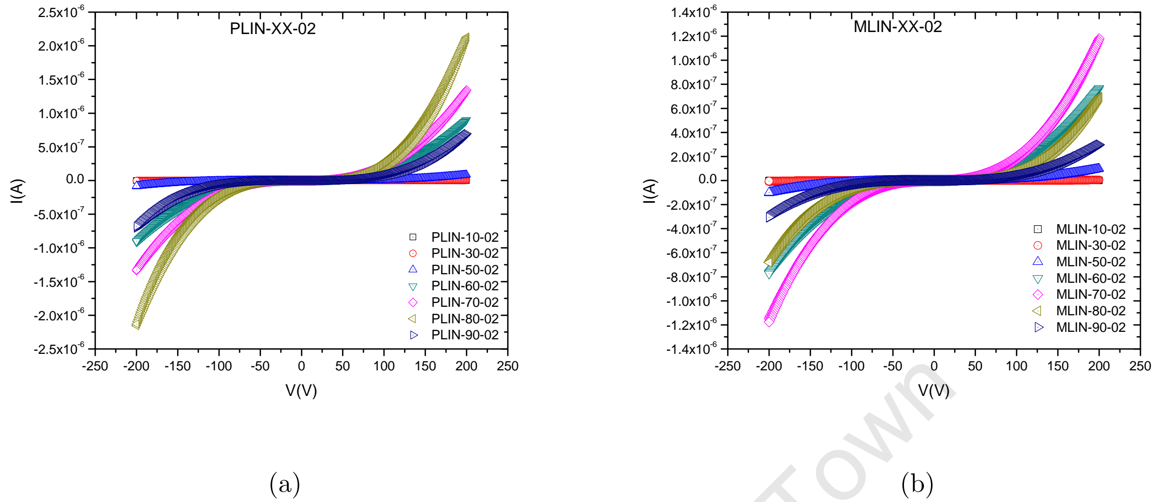

Fig. A.2: Forward and reverse bias $I-V$ characteristics for (a) PLIN-xx-02 (c) MLIN-xx-02, where xx stands for 10, 30, 50, 60, 70, 80 and 90 wt.% of the respective silicon powder type, namely P and M in linseed oil(LIN).

University of Cape Town

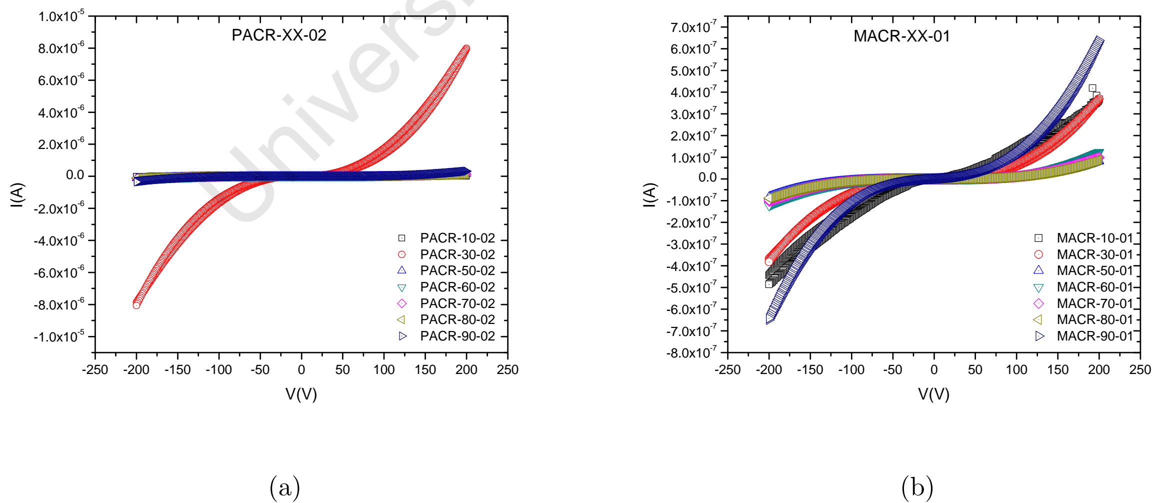

Fig. A.3: Forward and reverse bias $I-V$ characteristics for (a) PACR-xx-02 (b) MACR-xx-01, where xx stands for 10, 30, 50, 60, 70, 80 and 90 wt.% of the respective silicon powder type, namely P and M acrylic paste(ACR) respectively.

Table A.1: Concentration dependence of the Ideality factor, series resistance and Schottky barrier heights for (a) PLIN-XX-01 (b) MLIN-XX-01 (c) PACR-XX-01 and (d) MACR-XX-02 at temperature 295K. The different parameters was extracted using the direct method from a plot of $ln(I)$ versus V for the different forward dark I-V characteristics.

Concentration $(wt.\%)$	Ideality Factor (n)	Saturation Current $(I_0)A$	Barrier Height $\phi(eV)$	Resistance Ω
10	928.32 ± 24.32	$2.92 \pm 0.04 \times 10^{-11}$	0.85	2.74×10^{11}
30	1209.87 ± 28.44	$4.06 \pm 0.05 \times 10^{-11}$	0.85	3.35×10^{11}
50	339.66 ± 3.96	$2.44 \pm 0.07 \times 10^{-11}$	0.86	5.49×10^{8}
60	614.67 ± 2.96	$7.80 \pm 0.01 \times 10^{-12}$	0.89	2.62×10^{9}
70	153.14 ± 5.40	$3.99 \pm 0.34 \times 10^{-11}$	0.85	6.80×10^{7}
80	358.35 ± 3.23	$7.24 \pm 0.19 \times 10^{-11}$	0.83	6.23×10^{7}
90	644.486 ± 2.90	$2.20 \pm 0.04 \times 10^{-11}$	0.86	4.71×10^{8}

(a) PLIN-XX-01

Concentration $(wt.\%)$	Ideality Factor (n)	Saturation Current $(I_0)A$	Barrier Height $\phi(eV)$	Resistance Ω
10	703.75 ± 25.81	$1.03 \pm 0.03 \times 10^{-11}$	0.88	3.40×10^{10}
30	958.17 ± 29.41	$1.53 \pm 0.03 \times 10^{-11}$	0.87	5.46×10^{10}
50	209.82 ± 4.85	$7.16 \pm 0.40 \times 10^{-12}$	0.89	4.07×10^{8}
60	174.52 ± 3.57	$1.44 \pm 0.07 \times 10^{-11}$	0.87	1.95×10^{8}
70	215.01 ± 4.56	$6.68 \pm 0.30 \times 10^{-11}$	0.83	1.08×10^{8}
80	290.3 ± 4.0	$4.81 \pm 0.018 \times 10^{-11}$	0.84	8.34×10^{7}
90	340.58 ± 12.3	$1.71 \pm 0.10 \times 10^{-12}$	0.93	2.03×10^{9}

(b) MLIN-XX-01

Concentration $(wt.\%)$	Ideality Factor (n)	Saturation Current $(I_0)A$	Barrier Height $\phi(eV)$	Resistance Ω
10	366.78 ± 4.07	$3.23 \pm 0.08 \times 10^{-11}$	0.85	2.45×10^{9}
30	92.79 ± 9.23	$5.02 \pm 1.62 \times 10^{-11}$	0.84	2.00×10^{7}
50	217.8 ± 24.67	$5.14 \pm 1.41 \times 10^{-13}$	0.97	8.89×10^{8}
60	204.8 ± 10.71	$3.17 \pm 0.54 \times 10^{-13}$	0.97	7.32×10^{8}
70	167.06 ± 9.56	$1.04 \pm 0.16 \times 10^{-12}$	0.94	4.71×10^{8}
80	135.09 ± 8.82	$1.49 \pm 0.429 \times 10^{-13}$	0.99	3.49×10^{8}
90	406.84 ± 4.63	$2.47 \pm 9.66 \times 10^{-12}$	0.92	6.46×10^{8}

(c) PACR-XX-01

Concentration $(wt.\%)$	Ideality Factor (n)	Saturation Current $(I_0)A$	Barrier Height $\phi(eV)$	Resistance Ω
10	249.88 ± 17.68	$2.12 \pm 0.15 \times 10^{-9}$	0.75	6.24×10^{8}
30	76.7 ± 7.91	$1.22 \pm 0.35 \times 10^{-11}$	0.88	8.49×10^{7}
50	139.34 ± 4.76	$2.22 \pm 0.23 \times 10^{-12}$	0.92	4.96×10^{8}
60	324.85 ± 4.91	$2.12 \pm 0.09 \times 10^{-12}$	0.92	1.73×10^{9}
70	175.37 ± 6.06	$1.56 \pm 0.14 \times 10^{-12}$	0.93	1.10×10^{9}
80	169.31 ± 5.89	$5.21 \pm 0.44 \times 10^{-12}$	0.90	4.08×10^{8}
90	693.7 ± 2.93	$1.97 \pm 0.02 \times 10^{-11}$	0.86	2.67×10^{9}

(d) MACR-XX-02

University of Cape Town

Table A.2: Theoretical calculated characteristics tunneling energy E_{00} dependence on concentration, and type of composite.

Concentration	Characteristic Tunneling Energy E_{00} (eV)			
	PLIN-XX-01	MLIN-XX-01	PACR-XX-01	MACR-XX-02
10	23.60 ± 0.62	17.89 ± 0.66	9.32 ± 0.10	6.35 ± 0.45
30	30.73 ± 0.72	24.36 ± 0.75	2.36 ± 0.24	1.95 ± 0.20
50	8.63 ± 0.10	5.33 ± 0.12	5.54 ± 0.63	3.54 ± 0.12
60	15.63 ± 0.08	4.44 ± 0.09	5.21 ± 0.27	8.26 ± 0.13
70	3.89 ± 0.14	5.47 ± 0.12	4.25 ± 0.24	4.46 ± 0.15
80	9.11 ± 0.08	7.38 ± 0.10	3.43 ± 0.22	4.30 ± 0.15
90	16.38 ± 0.07	8.66 ± 0.31	10.34 ± 0.12	17.63 ± 0.08

University of Cape Town

Table A.3: Table showing derived values for V_{trans} and barrier potential derived from the negative slope value of the Fowler-Nordheim plots for (a)PLIN (b)MLIN (c)PACR and (d)MACR based inks.

Ink	concentration of particles (wt.%)	V_{trans}	Barrier Potential $\phi(meV)$
PLIN-10-01	10	NA	NA
PLIN-30-01	30	NA	NA
PLIN-50-01	50	16.05	1.80 ± 0.01
PLIN-60-01	60	24.88	2.69 ± 0.10
PLIN-70-01	70	8.95	1.53 ± 0.07
PLIN-80-01	80	14.99	2.30 ± 0.01
PLIN-90-01	90	30.00	2.80 ± 0.10

(a)

Ink	concentration of particles (wt.%)	V_{trans}	Barrier Potential $\phi(meV)$
MLIN-10-01	10	83.48	2.14 ± 0.18
MLIN-30-01	30	66.60	3.98 ± 0.38
MLIN-50-01	50	19.05	1.52 ± 0.06
MLIN-60-01	60	8.00	1.48 ± 0.07
MLIN-70-01	70	11.00	1.44 ± 0.07
MLIN-80-01	80	11.00	2.00 ± 0.09
MLIN-90-01	90	15.98	2.17 ± 0.11

(b)

Ink	concentration of particles (wt.%)	V_{trans}	Barrier Potential $\phi(meV)$
PACR-10-01	10	16.12	0.31 ± 0.02
PACR-30-01	30	5.00	1.00 ± 0.07
PACR-50-01	50	10.04	2.13 ± 0.12
PACR-60-01	60	13.99	2.32 ± 0.12
PACR-70-01	70	10.00	2.14 ± 0.11
PACR-80-01	80	NA	2.20 ± 0.12
PACR-90-01	90	19.02	3.00 ± 0.10

(c)

Ink	concentration of particles (wt.%)	V_{trans}	Barrier Potential $\phi(meV)$
MACR-10-01	10	NA	NA
MACR-30-01	30	5.96	1.11 ± 0.05
MACR-50-01	50	6.16	1.77 ± 0.10
MACR-60-01	60	11.90	2.38 ± 0.10
MACR-70-01	70	9.16	2.02 ± 0.10
MACR-80-01	80	8.12	1.83 ± 0.08
MACR-90-01	90	35.13	2.87 ± 0.08

(d)

University of Cape Town

Table A.4: Table showing the experimental obtained field lowering coefficient $\beta_{RS/PF}$, barrier height $\phi_{RS/PF}$ and an estimated dielectric constant for different concentration for (a) PLIN (b) MLIN (c) PACR and (d) MACR nanocomposite.

Conc	High field region			Medium field region		
	$\beta \times 10^{-5}(V/m)^{1/2}$	$\phi(eV)$	diel const (ϵ)	$\beta \times 10^{-5}(V/m)^{1/2}$	$\phi(eV)$	diel. const (ϵ)
10	7.86 ± 0.05	0.84	0.23	12.76 ± 0.04	0.87	0.09
30	6.74 ± 0.16	0.83	0.32	9.43 ± 0.04	0.85	0.16
50	22.91 ± 0.12	0.82	0.03	41.16 ± 0.22	0.90	0.01
60	27.36 ± 0.11	0.90	0.02	37.88 ± 0.1	0.96	0.01
70	21.28 ± 0.11	0.75	0.03	35.77 ± 0.36	0.82	0.01
80	26.82 ± 0.14	0.79	0.02	39.97 ± 0.26	0.87	0.01
90	28.3 ± 0.01	0.86	0.018	43.37 ± 0.01	0.96	0.01

(a)

Conc	High field region			Medium field region		
	$\beta \times 10^{-5}(V/m)^{1/2}$	$\phi(eV)$	diel const (ϵ)	$\beta \times 10^{-5}(V/m)^{1/2}$	$\phi(eV)$	diel. const (ϵ)
10	23.06 ± 0.16	0.93	0.03	15.18 ± 0.08	0.89	0.06
30	22.48 ± 0.16	0.93	0.03	12.61 ± 0.01	0.88	0.09
50	21.64 ± 0.11	0.80	0.03	33.41 ± 0.23	0.86	0.01
60	21.61 ± 0.16	0.78	0.03	34.88 ± 0.26	0.85	0.01
70	21.76 ± 0.11	0.76	0.03	33.83 ± 0.23	0.82	0.01
80	24.68 ± 0.11	0.78	0.02	34.67 ± 0.18	0.84	0.01
90	27.89 ± 0.13	0.89	0.02	45.71 ± 0.18	0.99	0.01

(b)

Conc	High field region			Medium field region		
	$\beta \times 10^{-5}(V/m)^{1/2}$	$\phi(eV)$	diel const (ϵ)	$\beta \times 10^{-5}(V/m)^{1/2}$	$\phi(eV)$	diel. const (ϵ)
10	14.36 ± 0.09	0.78	0.07	23.06 ± 0.18	0.83	0.03
30	19.68 ± 0.09	0.70	0.04	13.2 ± 0.29	0.77	0.08
50	27.46 ± 0.12	0.87	0.02	41.62 ± 0.33	0.95	0.01
60	28.7 ± 0.12	0.87	0.02	45.48 ± 0.34	0.96	0.01
70	25.88 ± 0.1	0.84	0.02	41.44 ± 0.38	0.92	0.01
80	28.6 ± 0.15	0.85	0.02	47.85 ± 0.42	0.96	0.01
90	30.74 ± 0.15	0.89	0.02	48.69 ± 0.34	0.99	0.01

(c)

Conc	High field region			Medium field region		
	$\beta \times 10^{-5}(V/m)^{1/2}$	$\phi(eV)$	diel const (ϵ)	$\beta \times 10^{-5}(V/m)^{1/2}$	$\phi(eV)$	diel. const (ϵ)
10	8.11 ± 0.07	0.68	0.22	15.51 ± 0.11	0.73	0.06
30	19.98 ± 0.12	0.74	0.04	37.35 ± 0.45	0.82	0.01
50	22.3 ± 0.07	0.81	0.03	40.00 ± 0.07	0.89	0.01
60	25.6 ± 0.08	0.87	0.02	39.81 ± 0.31	0.95	0.01
70	23.21 ± 0.06	0.83	0.03	36.76 ± 0.33	0.91	0.01
80	22.88 ± 0.11	0.81	0.03	38.21 ± 0.04	0.89	0.01
90	26.14 ± 0.1	0.89	0.02	33.43 ± 0.06	0.93	0.01

(d)

University of Cape Town

Table A.5: Table showing variation of slope values for the (a) PLIN (b) MLIN (c) PACR and (d) MACR systems for the three regions, A, B and C

Conc	Low Bias		Medium Bias		High Bias	
	m_A	Range(V)	m_B	Range(V)	m_C	Range(V)
10	0.20	$V < 10.81$	0.68	$10.81 < V < 36.97$	1.15	$36.97 < V$
30	0.16	$V < 13.32$	0.65	$13.32 < V < 64.72$	1.03	$64.72 < V$
50	0.26	$V < 6.96$	1.70	$6.96 < V < 23.57$	2.87	$23.57 < V$
60	0.52	$V < 16.28$	1.92	$16.28 < V < 43.82$	3.73	$43.82 < V$
70	0.72	$V < 4.39$	1.94	$4.39 < V < 12.81$	2.68	$12.81 < V$
80	0.39	$V < 8.59$	1.92	$8.59 < V < 26.31$	3.44	$26.31 < V$
90	0.26	$V < 15.64$	1.82	$15.64 < V < 44.70$	4.26	$44.70 < V$

(a)

Conc	Low Bias		Medium Bias		High Bias	
	m_A	Range(V)	m_B	Range(V)	m_C	Range(V)
10	0.47	$V < 14.73$	0.94	$14.73 < V < 83.93$	2.46	$83.93 < V$
30	0.47	$V < 26.31$	0.94	$26.31 < V < 75.94$	2.99	$75.94 < V$
50	0.83	$V < 5.05$	1.84	$5.05 < V < 12.18$	2.68	$12.18 < V$
60	0.45	$V < 3.10$	1.43	$3.10 < V < 8.33$	2.72	$8.33 < V$
70	0.55	$V < 5.93$	1.79	$5.93 < V < 15.48$	2.66	$15.48 < V$
80	0.54	$V < 9.21$	2.47	$8.59 < V < 26.03$	3.21	$26.03 < V$
90	0.86	$V < 16.61$	2.45	$15.64 < V < 30.57$	3.71	$30.57 < V$

(b)

Conc	Low Bias		Medium Bias		High Bias	
	m_A	Range(V)	m_B	Range(V)	m_C	Range(V)
10	0.20	$V < 3.60$	0.61	$3.60 < V < 11.71$	2.16	$11.71 < V$
30	–	–	1.97	$V < 10.70$	2.50	$10.70 < V$
50	–	–	0.10	$V < 11.82$	3.82	$11.82 < V$
60	–	–	0.07	$V < 13.87$	3.97	$13.87 < V$
70	–	–	0.88	$V < 9.68$	3.28	$9.68 < V$
80	–	–	–	–	3.81	$0 < V$
90	0.75	$V < 18.17$	2.49	$18.17 < V < 28.22$	4.21	$28.22 < V$

(c)

Conc	Low Bias		Medium Bias		High Bias	
	m_A	Range(V)	m_B	Range(V)	m_C	Range(V)
10	0.44	$V < 3.49$	0.84	$3.49 < V < 13.743$	1.18	$13.73 < V$
30	–	–	1.84	$V < 7.92$	2.43	$7.92 < V$
50	–	–	1.23	$V < 5.75$	2.90	$5.75 < V$
60	0.45	$V < 7.93$	2.11	$7.93 < V < 19.49$	3.35	$19.49 < V$
70	0.93	$V < 6.96$	2.31	$6.96 < V < 14.59$	2.98	$14.58 < V$
80	1.29	$V < 8.09$	2.37	$8.09 < V < 22.08$	2.97	$29.08 < V$
90	0.48	$V < 12.81$	1.50	$12.81 < V < 49.91$	3.43	$48.91 < V$

(d)

University of Cape Town